MODELING AND IDENTIFICATION IN STRUCTURAL DYNAMICS

Dissertation by
Paramsothy Jayakumar

In Partial Fulfillment of the Requirements
for the Degree of
Doctor of Philosophy

California Institute of Technology
Pasadena, California

1987

(Submitted May 21, 1987)

To my parents

ACKNOWLEDGMENTS

My most sincere thanks to my advisor, Professor Jim Beck, without whose help, guidance, and encouragement this study would not have been possible. He was always available to advise and guide my research. It is because of his concern and efforts that my graduate study at Caltech has been such a memorable experience. And his help was most crucial in completing this dissertation on time.

Professors P.C. Jennings (Caltech), D.A. Foutch (University of Illinois at Urbana–Champaign), R.D. Hanson and S.C. Goel (University of Michigan, Ann Arbor), and C.W. Roeder (University of Washington) provided much valuable information and many records on the pseudo-dynamic testing carried out at the Building Research Institute in Tsukuba, Japan. Professor Erik Antonsson allowed me to use the computational facilities at his Engineering Design and Research Laboratory. Caltech generously provided me with tuition awards and graduate teaching and research assistantships during my study. This research was funded by the National Science Foundation through Grant No. CEE–8119962. Norbert Arndt translated Masing's paper (1926) from German to 'English.' Crista Potter, Arun Vedhanayagam, and Truong Nguyen typed and Gracia Vedhanayagam proof read various parts of this dissertation. Cecilia Lin drew the illustrations. My office-mate Ravi Thyagarajan was available whenever I needed help. I am grateful and appreciative for all the help and assistance of the above people and institutions. Furthermore, I enjoyed working in the quiet and pleasant atmosphere of the Earthquake Engineering Research Library and my thanks to Donna Covarrubias for her assistance.

To Nanthikesan and Thayaparan, I am deeply thankful for their friendship and constant encouragement despite the miles of separation between us.

Finally, I am grateful to Arun and Gracia Vedhanayagam and David Koilpillai for all the wonderful Sundays we shared together which provided me much relaxation amidst the demands and rigour of research life. Without their love, constant encouragement and help, I would not have met any of the deadlines concerning this dissertation and my graduation this year.

ABSTRACT

Analytical modeling of structures subjected to ground motions is an important aspect of fully dynamic earthquake-resistant design. In general, linear models are only sufficient to represent structural responses resulting from earthquake motions of small amplitudes. However, the response of structures during strong ground motions is highly nonlinear and hysteretic.

System identification is an effective tool for developing analytical models from experimental data. Testing of full-scale prototype structures remains the most realistic and reliable source of inelastic seismic response data. Pseudo-dynamic testing is a recently developed quasi-static procedure for subjecting full-scale structures to simulated earthquake response. The present study deals with structural modeling and the determination of optimal linear and nonlinear models by applying system identification techniques to elastic and inelastic pseudo-dynamic data from a full-scale, six-story steel structure.

It is shown that the feedback of experimental errors during the pseudo-dynamic tests significantly affected the higher modes and led to an effective negative damping for the third mode. The contributions of these errors are accounted for and the small-amplitude modal properties of the test structure are determined. These properties are in agreement with the values obtained from a shaking table test of a 0.3 scale model.

The nonlinear hysteretic behavior of the structure during strong ground motions is represented by a general class of Masing models. A simple model belonging to this class is chosen with parameters which can be estimated theoretically, thereby making this type of model potentially useful during the design stages. The above model is identified from the experimental data and then its prediction capability and application in seismic design and analysis are examined.

TABLE OF CONTENTS

PAGE

PAGE

CHAPTER 1

INTRODUCTION

Modeling of structures subjected to ground motions is an important aspect of earthquake-resistant design. Also, system identification is an effective tool for developing models from experimental data. This dissertation deals with structural modeling and the determination of optimal linear and nonlinear-hysteretic models by applying system identification techniques to experimental data from a full-scale structure.

Since the acquisition of response data from structures during earthquakes is infrequent, it becomes necessary to complement the field data by means of analysis and/or experiments. Many analytical methods are questionable because of their simplified modeling of structural and material behavior, and they need to be assessed using real structural data. Also, because of disadvantages associated with the testing of small-scale models and full-scale structural components and subassemblages, testing of full-scale prototype structures remains the most realistic and reliable method for evaluating the inelastic seismic performance of structures.

The pseudo-dynamic test method is a recently developed quasi-static procedure for subjecting full-scale structures to simulated earthquake response by means of on-line computer control of hydraulic actuators. In contrast to the usual quasi-static test procedures, the relation between the interstory forces and deformations is not prescribed prior to the test. Instead, feedback from displacement and load transducers is used to force the appropriate earthquake behavior on the structure in an interactive manner as the experiment proceeds. Hence, full-scale structures can be tested at strong-motion amplitude levels without making any assumptions about the stiffness and damping characteristics of the structure. The pseudo-dynamic method, its advantages and the sources of errors are described in Chapter 2. An analysis of experimental errors in pseudo-dynamic testing shows that these errors act as effective excitations of the structure in addition to the ground motion.

A six-story, two-bay, full-scale steel structure was tested by the pseudo-dynamic method at low amplitudes to give nominally elastic response and at larger amplitudes to excite the structure into the inelastic range. These tests were carried out in 1984 as part of a U.S.—Japan Cooperative Earthquake Research Program Utilizing Large-Scale Testing

Facilities, at the Building Research Institute in Tsukuba, Japan. A major portion of this study is devoted to analysis of these test data.

Linear models are, in general, sufficient to represent structural responses resulting from earthquake motions of small amplitudes. In addition, Beck [1] recommends that if linear models are to be used in system identification, the parameters of the lower modes whose contributions dominate the response, and not the stiffness and damping matrices, should be estimated from the records for reasons of uniqueness and measurement noise. Linear modal models are used to study the elastic response of the pseudo-dynamic test structure in Chapters 3 and 4.

A single-input single-output structural identification technique has been developed by Beck [2] which is applicable when the input and output consist only of one component of ground motion and a parallel component of response at some point in the structure, respectively. This method is used to estimate the modal properties of the full-scale six-story steel structure from the 'elastic' pseudo-dynamic test data, in Chapter 3.

The surprising result is that the third-mode damping is negative. This is then attributed to the cumulative effect of feedback of control and measurement errors during the pseudo-dynamic test in which each of these errors acted as an effective excitation to the structure in addition to the ground motion, as shown in Chapter 2. In Chapter 4, these additional excitations are treated explicitly in order to get more reliable estimates of the modal properties of the test structure.

A multiple-input multiple-output structural identification technique, namely MODE-ID [3], which is applicable to any number of simultaneous input excitations and structural response measurements used in conjunction with a linear modal model, is used to determine the optimal modal properties of the test structure from the elastic pseudo-dynamic test data, while accounting for the experimental errors as additional excitations to the test structure. It then becomes possible to estimate the actual structural damping effective during the test and also the apparent equivalent viscous damping effect of the feedback errors on the structural modes. The identification results of modal parameters from the full-scale structural test data are compared with the Berkeley shaking table test results of a 0.3 scale model of the same prototype test structure.

The response of a structure during strong earthquake ground motions, as described by its dynamic force-deflection relationship, is highly nonlinear and hysteretic. The modeling

of such behavior is a difficult task. This subject is dealt with in detail in Chapter 5.

A class of Masing models is discussed in which Masing [4] assumed that a system consists of a collection of elasto-plastic elements each with the same elastic stiffness but different yield limits. He asserted that if the load-deflection curve for the entire system at virgin loading is given, then the branches of the hysteresis loops for steady-state response are geometrically similar to the virgin loading curve and are described by the same basic equation but scaled with two-fold magnification. It is shown that Masing's hypothesis results in a continuous distribution of constant stiffness surfaces in the region of the restoring force space, an idea similar to the concept of multiple yield surfaces with kinematic hardening in the incremental theory of plasticity. The Ramberg-Osgood model [5], Iwan's model [6], Pisarenko's model [7] and Rosenblueth-Herrera's model [8] are a few examples of nonlinear, hysteretic relations which belong to the class of Masing models describing steady-state response.

It has been contended by previous researchers [6,9-11] that Masing's hypothesis is of no help for cases of transient loading. It is shown in the present study that this problem can be eliminated by defining the transient response by two simple hysteresis rules. It is also proved that Iwan's distributed-element formulation [6,10] is mathematically equivalent to this general class of Masing models. However, the implementation of the latter class of models is much simpler as compared with the computation of the force-deformation relationship for Iwan's model which requires keeping track of element behavior involving several integral terms. Finally, a simple hysteretic restoring force-deformation relationship belonging to the general class of Masing models is chosen to represent the inelastic response of the pseudo-dynamic test structure.

A hysteretic system identification program, HYSID, is developed in Chapter 6 to determine the optimal estimates of the hysteretic model parameters from experimental data. The optimal estimates for the structural parameters resulting from the hysteretic modeling of the full-scale six-story steel structure are then obtained by applying HYSID to the inelastic pseudo-dynamic test data. The hysteretic model chosen in Chapter 5 is used to represent the story shear-deformation relationship. The predictive capability of the model and the prospects of using the hysteretic model in the seismic analysis of structures are also examined.

Conclusions and directions for further exploration of the nonlinear model are given in Chapter 7.

REFERENCES

[1] Beck, J.L., "System Identification Applied to Strong Motion Records from Structures," *Earthquake Ground Motion and Its Effects on Structures*, Datta, S.K. (ed.), ASME, AMD–Vol. 53, 109–133, New York, 1982.

[2] Beck, J.L., "Determining Models of Structures from Earthquake Records," Report No. EERL 78–01, Earthquake Engineering Research Laboratory, California Institute of Technology, Pasadena, California, June, 1978.

[3] Werner, S.D., Beck, J.L. and Levine, M.B., "Seismic Response Evaluation of Meloland Road Overpass Using 1979 Imperial Valley Earthquake Records," *Earthquake Engineering and Structural Dynamics*, Vol. 15, 249–274, 1987.

[4] Masing, G., "Eigenspannungen und Verfestigung beim Messing," *Proceedings of the 2nd International Congress for Applied Mechanics*, Zurich, Switzerland, 332–335, 1926. (German)

[5] Jennings, P.C., "Response of Simple Yielding Structures to Earthquake Excitation," Ph.D. Dissertation, California Institute of Technology, Pasadena, California, June, 1963.

[6] Iwan, W.D., "A Distributed-Element Model for Hysteresis and Its Steady-State Dynamic Response," *Journal of Applied Mechanics*, ASME, Vol. 33(4), 893–900, December, 1966.

[7] Pisarenko, G.S., "Vibrations of Elastic Systems Taking Account of Energy Dissipation in the Material," Technical Documentary Report No. WADD TR 60–582, February, 1962.

[8] Rosenblueth, E. and Herrera, I., "On a Kind of Hysteretic Damping," *Journal of the Engineering Mechanics Division*, ASCE, Vol. 90(4), 37–48, August, 1964.

[9] Iwan, W.D., "On a Class of Models for the Yielding Behavior of Continuous and Composite Systems," *Journal of Applied Mechanics,* ASME, Vol. 34(3), 612–617, September, 1967.

[10] Iwan, W.D., "The Distributed-Element Concept of Hysteretic Modeling and Its Application to Transient Response Problems," *Proceedings of the 4th World Conference on Earthquake Engineering*, Vol. II, A–4, 45–57, Santiago, Chile, 1969.

[11] Jennings, P.C., "Earthquake Response of a Yielding Structure," *Journal of the Engineering Mechanics Division*, ASCE, Vol. 91(4), 41–68, August, 1965.

CHAPTER 2

PSEUDO-DYNAMIC TESTING OF FULL-SCALE STRUCTURES TO SIMULATE EARTHQUAKE DYNAMICS

2.1 Introduction

It is well recognized that an earthquake can be viewed as a full-scale, large-amplitude experiment on a structure, and that if the structural motion is recorded, it offers an opportunity to make a quantitative study of the behavior of the structure at dynamic force and deflection levels directly relevant to earthquake-resistant design. However, the time and location of a strong-motion earthquake cannot be predicted with confidence so that the acquisition of such data is very infrequent [1]. Hence, it becomes necessary to complement the field data by means of analysis and/or experiments.

Although various analytical methods are available to predict the inelastic response of a structure, the confidence that can be placed in results obtained with them is severely limited by the uncertainties associated with the simplified modeling processes of structures and of their nonlinear material and member behaviors [2-6]. For these reasons, experimental testing remains the most reliable means to evaluate the inelastic behavior of structural systems and to devise structural details to improve their seismic performance.

Small-scale models of structures, full-scale structural components and subassemblages have been tested in the past as economical and efficient means of predicting the response of prototype structures. However, the scale effects which usually arise in small-scale model testing may prevent good correlation of the model response with the prototype structural behavior [7,8], whereas any results obtained from full-scale tests can be applied in practice almost directly. Also, it is not always possible to scale material properties.

Component tests provide useful information on the individual characteristics of these members, but do not provide much information on the overall behavior of building structures in which many members are connected. Although the subassemblage test is a useful approach to investigate closely the behavior of a structure as a unit, on many occasions it is difficult to perfectly simulate the boundary conditions which are present in the real structure [9]. The ultimate validity of the adopted boundary conditions can only be checked by comparison with the behavior of the real structure. Often engineering judgement is needed

to incorporate member and assembly test data into structural design. Therefore, testing of full-scale prototype structures remains the most realistic and reliable experimental method for evaluating the inelastic seismic performance of structures. Some of the available testing methods of structures for earthquake dynamics are listed in Table 2.1.

2.2 Pseudo-Dynamic Testing

The pseudo-dynamic test method is a recently developed quasi-static procedure [11-15] for subjecting full-scale structures to simulated earthquake response by means of on-line computer control of hydraulic actuators. The inertial effects of the structure are modeled in an on-line computer, but in contrast to the usual quasi-static test procedures the relation between the interstory forces and deformations is not prescribed prior to the test. Instead, feedback from displacement and load transducers is used to force the appropriate earthquake behavior on the structure in an interactive manner as the experiment proceeds. Hence, full-scale structures can be tested at strong-motion amplitude levels without making any assumptions about the stiffness and damping characteristics of the structure. Also, it is relatively inexpensive to test full-scale structures by the pseudo-dynamic method compared with the construction and instrumentation of a big shaking table facility.

In the pseudo-dynamic method, a multi-story building structure is modeled as a lumped-mass discrete system using the following assumptions:

(a) Floor slabs are rigid in their own planes.

(b) Mass of the building is lumped at each floor level.

(c) Rotational inertias are negligible.

(d) Both horizontal translational degrees-of-freedom are uncoupled.

The equation of motion of such a system when excited by earthquake ground accelerations $\ddot{z}(t)$ (Fig. 2.1) is given by:

$$\mathrm{M}\underset{\sim}{\ddot{x}} + \mathrm{C}\underset{\sim}{\dot{x}} + \underset{\sim}{\mathrm{R}} = \underset{\sim}{\mathrm{F}}(t) = -\mathrm{M}\ddot{z}(t)\,\underset{\sim}{1} \quad , \tag{2.1}$$

where
$\mathrm{M,C}$ = mass and viscous damping matrices, respectively,
$\underset{\sim}{\mathrm{R}}$ = restoring force, a function of the displacement history,
$\underset{\sim}{\mathrm{F}}(t)$ = excitation due to earthquake accelerations $\ddot{z}(t)$,
$\underset{\sim}{x}$ = vector of floor displacements relative to the ground, $[x_1, x_2, \ldots, x_N]^T$,
$\underset{\sim}{\dot{x}}, \underset{\sim}{\ddot{x}}$ = floor velocities and accelerations relative to the ground, and
$\underset{\sim}{1}$ = $[1, 1, \ldots, 1]^T$.

The $C\underset{\sim}{\dot{x}}$ term represents the viscous damping added artificially by the on-line data processing computer which is part of the pseudo-dynamic testing facility (Fig. 2.2) during the tests.

Equation 2.1 is solved for the displacements by a direct step-by-step numerical integration scheme. At each time step, the calculated displacements are imposed on the structure and the resulting story restoring forces are then measured. The nature of the pseudo-dynamic test procedure prevents the possibility of employing implicit integration schemes since they require the knowledge of stiffness characteristics to solve the equation of motion for displacements. Implicit integration methods involve iterations which are highly undesirable for pseudo-dynamic testing of history-dependent inelastic systems. Therefore, Eq. 2.1 should be integrated using explicit integration schemes which are, in general, only conditionally stable but are computationally more efficient.

Therefore, for an explicit integration scheme, Eq. 2.1 becomes:

$$M\underset{\sim}{\ddot{x}}_i + C\underset{\sim}{\dot{x}}_i + \underset{\sim}{R}_i = \underset{\sim}{F}_i \qquad i = 1, 2, \cdots, N \quad , \tag{2.2}$$

where $\underset{\sim}{x}_i = \underset{\sim}{x}(t_i)$

$t_i = i(\Delta t)$ and

Δt = discretization time of the ground motion.

Japanese researchers [11] chose to use the central-difference method for which:

$$\underset{\sim}{\dot{x}}_i = (\underset{\sim}{x}_{i+1} - \underset{\sim}{x}_{i-1}) \Big/ (2\,\Delta t) \tag{2.3}$$

$$\underset{\sim}{\ddot{x}}_i = (\underset{\sim}{x}_{i-1} - 2\,\underset{\sim}{x}_i + \underset{\sim}{x}_{i+1}) \Big/ (\Delta t)^2 \quad . \tag{2.4}$$

Substitution of Eqs. 2.3 and 2.4 in Eq. 2.2 gives:

$$[M + C\,\Delta t/2]\,\underset{\sim}{x}_{i+1} = (\Delta t)^2\,[\underset{\sim}{F}_i - \underset{\sim}{R}_i] + 2\,M\underset{\sim}{x}_i + [C\,\Delta t/2 - M]\,\underset{\sim}{x}_{i-1} \quad . \tag{2.5}$$

The mass matrix is prescribed from the known mass distribution of the test structure so that the on-line computer can simulate its inertial effects, and the viscous damping matrix is set equal to that derived from the preliminary free and forced vibration tests of the structure at low amplitudes assuming Rayleigh damping. From the knowledge of measured restoring forces and calculated displacements at the previous time steps, the displacement at the time step (i+1) is calculated using Eq. 2.5 in the data processing computer. This

displacement is first transformed to a voltage change in the servo-controller (Fig. 2.2) and the resulting electrical command signal is then converted by means of the servo-valve to a regulated flow of high pressure hydraulic fluid to the actuators [16]. The actuators in turn force the structure quasi-statically to deflect to the calculated position. When the desired displacement is achieved, the load cells mounted on the actuators measure the restoring forces and the displacement transducers on the structure measure the final displacements achieved. This information is fed back to the on-line data processing computer to calculate the displacements to be imposed at the next time step. The basic operations of the pseudo-dynamic test procedure are given as a flow diagram in Fig. 2.3.

By the pseudo-dynamic testing method, a full-scale structure can be tested quasi-statically using a given earthquake ground motion so that the deformation and restoring force history will be close to that the structure would have experienced during the actual earthquake. This method is a more cost-effective procedure for achieving this realism than construction and operation of a sufficiently large shaking table facility to test structures which are large and massive. The large scale structure test laboratory at the Building Research Institute in Tsukuba, Japan which houses the pseudo-dynamic testing facility (Fig. 2.2) can accommodate a building specimen as large as 300 m^2 in floor area and 25 m in height on each side of a reaction wall, with the floor bearing capacity being 1 MN/m^2. But the world's largest shaking table, a counterpart of this laboratory, is 15 m$\times$15 m in table dimensions and can carry at most 10 MN weight [16]. There is therefore a sizable difference between the allowable maximum scale of structures which can be tested on a shaking table and by the pseudo-dynamic method.

Another advantage of the pseudo-dynamic method is that it is possible to keep track of the localized behavior and damage propagation while loading because of the quasi-static nature of the test.

Behavior of structural foundations is very difficult to evaluate because of the complexity of soil properties and soil–structure interaction. Considering that soils are difficult to scale down properly, a full-scale test can be performed pseudo-dynamically.

In the traditional quasi-static tests, to select a proper load sequence, a simplified mathematical model is first assumed, and the earthquake response of the test component is calculated. Based on test results obtained by the use of this calculated load sequence, a new mathematical model is formulated and the analysis is repeated, this sequence being

followed until satisfactory convergence is achieved [9]. Hence, the most important advantage of pseudo-dynamic testing over these traditional quasi-static test methods is that no assumption is made regarding the stiffness or restoring force characteristics of the test system. This makes it a very powerful means of analyzing the dynamical behavior of structures in the inelastic region, since the actual restoring forces developed are measured during the test and used to compute the deformation response, in contrast to the *a priori* prediction of these forces using analytical models during ordinary quasi-static tests. Indeed, a better understanding of the inelastic behavior of structures gained from the pseudo-dynamic tests can be used to improve the current analytical modeling techniques, as has been done in this study.

2.3 Sources of Errors in Pseudo-Dynamic Testing

As in all experimental methods, the pseudo-dynamic method has errors inherently associated with it. These errors occur mainly in the following three stages:

(a) Modeling of mass distribution and damping.

(b) Numerical algorithm used to integrate the equation of motion.

(c) Experimental errors arising from displacement control and force measurements.

By prescribing a diagonal mass matrix, it is assumed that masses exist only at a few selected degrees-of-freedom. This assumption is reasonable for structures like multi-story buildings where the masses can be lumped at the floors whose horizontal motion constitutes the degrees-of-freedom. But structures whose distributed mass can significantly influence local failure modes are not suitable for pseudo-dynamic testing, such as dams.

Energy dissipation due to friction and hysteresis is taken care of since the actual restoring forces developed are measured during the test and used in the computation of the displacement response [18]. However, because of the quasi-static nature of the test, energy radiation due to soil–structure interaction will be negligibly small in a pseudo-dynamic test compared to that of the same structure during an actual earthquake. This can be conveniently modeled by prescribing viscous damping in the on-line control algorithm. The viscous damping matrix may be constructed using the modal damping values estimated from the preliminary free and forced vibration tests and the mode shapes obtained from a pre-test finite element analysis of the test structure. Viscous damping is not a realistic damping model for structures, since they appear to exhibit rate-independent damping over

a range of strain-rates expected during earthquake response. For structures with significant inelastic deformations, the energy loss due to hysteresis will be very large compared to the energy loss due to radiation, so that the error made by prescribing a viscous damping matrix in the on-line computer will be negligible.

Solutions obtained by numerical integration are, in general, approximate. However, if the numerical integration scheme is convergent, the numerical solution should approach the exact solution of the differential equation as the time step Δt tends to zero. Therefore, the time integration step Δt should be as small as possible for solutions to be accurate enough. In addition, the algorithm should be stable. The central-difference scheme used to integrate Eq. 2.2 is stable if and only if $\Delta t < 2/\omega_m$ where ω_m is the largest natural frequency of the system in rad/sec and the accuracy of the solution is of the order $(\Delta t)^2$. One-sixth of the above time interval is recommended to guarantee sufficient accuracy [16]. For example, if the natural frequency of the sixth mode of a six-story test structure is 17 Hz, the required Δt would be 0.003 sec. The very small Δt results in considerable limitations and difficulties such as creep of concrete in reinforced concrete structures and error accumulation problems, in implementing the pseudo-dynamic technique.

The most serious error comes from the experimental control system itself. Since it is impossible to make the structure deform precisely to the computed displacement levels, an allowable error bound is set for each actuator. This results in the structure always undershooting the desired displacements, which leads to displacement-control errors adding energy into all the modes of the structure. To correct this, an overshoot is added to the calculated displacement. Hence, the restoring forces measured and fed back to the data processing computer for further computations do not correspond to the displacements computed for the time step, but instead to the actual deformation that was realized by the structure. In addition, errors can also occur in the measurements of these displacements and forces. The displacement errors, which include both the control and measurement errors, are plotted in Fig. 2.4 against the increment in the calculated displacements at every step. These data are from the inelastic test of a concentrically braced six-story full-scale steel structure tested at the pseudo-dynamic testing facility in Tsukuba, Japan. Although the control and measurement errors may be small at every time step, being of the order of 0.1 mm, the cumulative effect of the feedback of these errors seems to be very severe. In multi-degree-of-freedom systems, the higher-mode contributions are highly vulnerable to

the cumulative effect of the feedback of experimental errors and this can even make the test system unstable [20,21]. One possible scheme to avoid the instability is to suppress the higher degrees-of-freedom by employing very high viscous dampings in the computer algorithm corresponding to these modes. Aktan [22] has proposed a modification to the pseudo-dynamic method which makes use of classical control theory to ease the constraints on the time interval Δt and to include higher modes, but under the assumption that the structure behaves linearly during each loading step. For the success of the pseudo-dynamic test, the most critical requirements are, therefore, the capability of the actuators to control the specimen deformation with sufficient accuracy and the accurate measurement of restoring force values which should be transferred to the computer for the computation of the next step. In the next section, the experimental errors in the pseudo-dynamic method are analyzed and a method of treatment of these errors is proposed by which the structural properties can be reliably estimated from the pseudo-dynamic test data.

The strain rates during the pseudo-dynamic tests will be very much different from those during an actual earthquake because of the quasi-static nature of these tests. Materials do behave differently under different strain-rate conditions. For example, dynamic tension and bending tests on steel beams of section H 200×100×5.5×8 at increasing strain rates show a modest increase in yield strength (Fig. 2.5). However, for most steel structures the strain-rate effects are insignificant if the natural frequencies of interest are below 10 Hz [24]. This may not be the case for reinforced concrete structures. For this reason, a 'rapid computer-actuator on-line system' has been proposed by Takanashi and Ohi [23] to improve the pseudo-dynamic testing system explained in Section 2.2, so that structural responses can be simulated as near as possible to the actual dynamic rates.

2.4 Analysis of Experimental Errors in Pseudo-Dynamic Testing

The displacements to be imposed on the test structure during the pseudo-dynamic testing are calculated from the equation of motion 2.5 in Section 2.2:

$$[\mathrm{M} + \mathrm{C}\,\Delta\mathrm{t}/2]\,\underset{\sim}{x}_{i+1} = (\Delta\mathrm{t})^2\,[\underset{\sim}{\mathrm{F}}_i - \underset{\sim}{\mathrm{R}}_i] + 2\mathrm{M}\underset{\sim}{x}_i + [\mathrm{C}\,\Delta\mathrm{t}/2 - \mathrm{M}]\,\underset{\sim}{x}_{i-1} \quad , \tag{2.6}$$

where $\underset{\sim}{x}_{i-1}$, $\underset{\sim}{x}_i$ = displacements calculated at the previous time steps i-1 and i,

$\underset{\sim}{R}_i$ = restoring force measured at time step i,

$\underset{\sim}{F}_i$ = exciting force due to ground acceleration at time step i, and

$\underset{\sim}{x}_{i+1}$ = displacement to be imposed on the test structure at the next time step.

However, as discussed in the previous section, it is not possible to control the testing apparatus precisely so that the exact displacements calculated from Eq. 2.6 can be imposed on the test structure.

Let the displacement-control errors and force-measurement errors at time step i be $\underset{\sim}{x}_i^{ec}$ and $\underset{\sim}{R}_i^{em}$, respectively; then the restoring forces measured in the elastic tests will be:

$$\underset{\sim}{R}_i = K(\underset{\sim}{x}_i + \underset{\sim}{x}_i^{ec}) + \underset{\sim}{R}_i^{em} \quad , \tag{2.7}$$

where K is the stiffness matrix corresponding to the elastic behavior of the test structure.

Also, if $\underset{\sim}{x}_i^{em}$ is the displacement-measurement error at the i-th time step, then the measured displacement $\underset{\sim}{x}_i^m$ will be:

$$\underset{\sim}{x}_i^m = \underset{\sim}{x}_i + \underset{\sim}{x}_i^{ec} + \underset{\sim}{x}_i^{em} \quad , \tag{2.8}$$

where $\underset{\sim}{x}_i$ is the displacement calculated from Eq. 2.6. Figure 2.6 summarizes the experimental errors and shows the feedback of these errors in a flow diagram.

Substitution of Eq. 2.7 in Eq. 2.6 gives:

$$\begin{aligned}[M + C\Delta t/2]\,\underset{\sim}{x}_{i+1} = (\Delta t)^2\,\underset{\sim}{F}_i + [2M - (\Delta t)^2 K]\,\underset{\sim}{x}_i \\ + [C\Delta t/2 - M]\,\underset{\sim}{x}_{i-1} - (\Delta t)^2\,[K\underset{\sim}{x}_i^{ec} + \underset{\sim}{R}_i^{em}] \quad .\end{aligned} \tag{2.9}$$

If the cumulative displacement error at time step i is $\underset{\sim}{x}_i^e$, then the calculated displacement $\underset{\sim}{x}_i$ can be written as:

$$\underset{\sim}{x}_i = \underset{\sim}{x}_i^* + \underset{\sim}{x}_i^e \quad , \tag{2.10}$$

where $\underset{\sim}{x}_i^*$ is the ideal displacement in the absence of experimental errors which satisfies the following equation:

$$[M + C\Delta t/2]\,\underset{\sim}{x}_{i+1}^* = (\Delta t)^2\,\underset{\sim}{F}_i + [2M - (\Delta t)^2 K]\,\underset{\sim}{x}_i^* + [C\Delta t/2 - M]\,\underset{\sim}{x}_{i-1}^* \quad . \tag{2.11}$$

Subtraction of Eq. 2.11 from Eq. 2.9 and the use of Eq. 2.10 lead to:

$$\begin{aligned}[M + C\Delta t/2]\,\underset{\sim}{x}_{i+1}^e = (\Delta t)^2\,[-K\underset{\sim}{x}_i^{ec} - \underset{\sim}{R}_i^{em}] + [2M - (\Delta t)^2 K]\,\underset{\sim}{x}_i^e \\ + [C\Delta t/2 - M]\,\underset{\sim}{x}_{i-1}^e \quad .\end{aligned} \tag{2.12}$$

Comparing Eq. 2.12 with Eq. 2.11, it is evident that the cumulative displacement error $\underset{\sim}{x}^{e}(t)$ is the response of the linear structure to an equivalent exciting force $[-K\underset{\sim}{x}^{ec}(t) - \underset{\sim}{R}^{em}(t)]$.

2.4.1 Modal Analysis of Experimental Errors

If the damping matrix C used in the computer algorithm is symmetric and 'classical,' then the modal column matrix Φ, whose columns are the modeshapes of the structure, satisfies the following orthogonality relationships:

$$\Phi^T M \Phi = I\,, \qquad \Phi^T K \Phi = \Omega^2 \quad \text{and} \qquad \Phi^T C \Phi = 2\,Z\Omega \quad . \tag{2.13}$$

Premultiplication of Eq. 2.12 by the modal row matrix Φ^T gives:

$$\begin{aligned}[\Phi^T M + \Phi^T C\,\Delta t/2]\,\underset{\sim}{x}^{e}_{i+1} = (\Delta t)^2\,[-\Phi^T K\,\underset{\sim}{x}^{ec}_{i} - \Phi^T\,\underset{\sim}{R}^{em}_{i}] \\ + [2\,\Phi^T M - (\Delta t)^2\,\Phi^T K]\,\underset{\sim}{x}^{e}_{i} + [\Phi^T C\,\Delta t/2 - \Phi^T M]\,\underset{\sim}{x}^{e}_{i-1} \quad .\end{aligned} \tag{2.14}$$

Furthermore, the cumulative displacement error, the displacement-control and force-measurement errors may be modally decomposed in the following manner:

$$\begin{aligned}\underset{\sim}{x}^{e}_{i} &= \Phi\,\underset{\sim}{\xi}_{i} \\ \underset{\sim}{x}^{ec}_{i} &= \Phi\,\underset{\sim}{\eta}_{i} \\ M^{-1}\,\underset{\sim}{R}^{em}_{i} &= \Phi\,\underset{\sim}{f}_{i} \quad ,\end{aligned} \tag{2.15}$$

where $\underset{\sim}{\xi}$, $\underset{\sim}{\eta}$ and $\underset{\sim}{f}$ are the modal coordinates, respectively.
Substituting Eq. 2.15 into Eq. 2.14 and using Eq. 2.13 gives:

$$[I + \Delta t\,Z\Omega]\,\underset{\sim}{\xi}_{i+1} = [2\,I - (\Delta t\,\Omega)^2]\,\underset{\sim}{\xi}_{i} + [\Delta t\,Z\Omega - I]\,\underset{\sim}{\xi}_{i-1} - (\Delta t)^2\,[\Omega^2\,\underset{\sim}{\eta}_{i} + \underset{\sim}{f}_{i}] \quad ,$$

or in component form: (2.16)

$$\begin{aligned}(1 + \Delta t\,\zeta_r\,\omega_r)\,\xi^{(r)}_{i+1} = \left(2 - (\Delta t\,\omega_r)^2\right)\,\xi^{(r)}_{i} + (\Delta t\,\zeta_r\,\omega_r - 1)\,\xi^{(r)}_{i-1} \\ - (\Delta t)^2\,(\omega_r^2\,\eta^{(r)}_{i} + f^{(r)}_{i}) \quad .\end{aligned}$$

Equation 2.16 can also be written as:

$$\xi_{i+1}^{(r)} - \phi_1^{(r)}\,\xi_i^{(r)} + \phi_2^{(r)}\,\xi_{i-1}^{(r)} = a_i^{(r)} \quad ,$$

where
$$\phi_1^{(r)} = \frac{2-(\Delta t\,\omega_r)^2}{1+\Delta t\,\zeta_r\,\omega_r} \quad , \quad \phi_2^{(r)} = \frac{1-\Delta t\,\zeta_r\,\omega_r}{1+\Delta t\,\zeta_r\,\omega_r} \quad ; \tag{2.17}$$

and
$$a_i^{(r)} = -\alpha^{(r)}\,\eta_i^{(r)} - \beta^{(r)}\,f_i^{(r)} \quad ,$$

where
$$\alpha^{(r)} = \frac{(\Delta t\,\omega_r)^2}{1+\Delta t\,\zeta_r\,\omega_r} \qquad \text{and} \qquad \beta^{(r)} = \frac{(\Delta t)^2}{1+\Delta t\,\zeta_r\,\omega_r} \quad .$$

The transient and steady-state response statistics of the difference equation 2.17 are obtained by the method of operational calculus in Appendix A, in which the steady-state response variance for the cumulative error (Eq. A.25) is shown to be:

$$\sigma^2_{\xi_\infty^{(r)}} = \frac{\Delta t}{\zeta_r\,[4-(\Delta t\,\omega_r)^2]}\;\left[\omega_r\,\sigma^2_{\eta^{(r)}} + \frac{1}{\omega_r^3}\,\sigma^2_{f^{(r)}}\right] \quad . \tag{2.18}$$

Equation 2.18 shows that the control errors have a greater effect in the higher modes whereas the response of the lower modes is affected more by the measurement errors, provided σ_η and σ_f are of the same order for different modes.

2.5 BRI Testing Program

A six-story, two-bay, full-scale steel structure (Figs. 2.7 and 2.8) was tested by the pseudo-dynamic method at the Building Research Institute (BRI) in Tsukuba, Japan during November, 1983–March, 1984. This structure, which represented Phase II of the steel program under the U.S.—Japan Cooperative Earthquake Research Program Utilizing Large-Scale Testing Facilities, was designed to satisfy the requirements of both the 1979 Uniform Building Code (UBC) of U.S. and the 1981 Architectural Institute of Japan code, using eccentric K-bracings [25]. It was 15 m×15 m in plan and 21.5 m high. The two exterior frames A and C are unbraced moment-resisting frames with one column in each oriented for weak-axis bending in order to increase the torsional stiffness, and the interior frame B is a braced moment-resisting frame with eccentric K-bracing in its north bay. All the girder-to-column connections have been designed as moment connections in the loading

direction and shear connections in the transverse direction. The floor system consisted of a formed metal decking with cast-in-place light-weight concrete acting compositely with the girders and floor beams (Figs. 2.9 and 2.10). No non-structural component was attached to the frame system.

The eccentric-braced frame is a new type of structural system for earthquake resistant design [27] which has a high elastic lateral stiffness as in concentric braced frames but in addition has a good energy dissipation capacity due to active shear links, whereas concentric braces can buckle under compressive cyclic loading and so suffer a drastic decrease in their buckling strength and their ability to dissipate energy.

The BRI tests were performed at low amplitudes to give nominally elastic response and at larger amplitudes to excite the structure into the inelastic range. The uni-directional loading in the elastic and inelastic tests was produced by an early digitized version (not the Caltech Vol. II A004 version) of the Taft S21W component from the 1952 Kern County, California, earthquake (Fig. 2.11) scaled to peak accelerations of 6.5% g and 50% g, respectively. The Fourier amplitude spectrum of the ground accelerations is shown in Fig. 2.12 [28].

During the inelastic test, yielding in shear links, brace gusset plates and some columns was observed. Overall, the structure performed very well without much visible damage, so additional three large-amplitude tests were performed using sinusoidal ground acceleration pulses of one cycle each in order to explore the ultimate strength, ductility and failure mechanism of the structure [29]. Table 2.2 summarizes some of the elastic and inelastic test details.

REFERENCES

[1] Beck, J.L., "Determining Models of Structures from Earthquake Records," Report No. EERL 78–01, Earthquake Engineering Research Laboratory, California Institute of Technology, Pasadena, California, June, 1978.

[2] Charney, F.A. and Bertero, V.V., "An Evaluation of the Design and Analytical Seismic Response of a Seven-Story Reinforced Concrete Frame-Wall Structure," Report No. UCB/EERC–82/08, Earthquake Engineering Research Center, University of California, Berkeley, California, 1982.

[3] Chavez, J.W., "Study of the Seismic Behavior of Two-Dimensional Frame Buildings: A Computer Program for the Dynamic Analysis—INDRA," *Bulletin of the International Institute of Seismology & Earthquake Engineering*, Vol. 18, Building Research Institute, Tsukuba, Japan, 1980.

[4] Bertero, V.V. and Moazzami, S., "U.S.—Japan Cooperative Earthquake Research Program: General Implications of Research Results for the 7-Story Reinforced Concrete Test Structure on the State of U.S. Practice in Earthquake Resistant Design of Frame–Wall Structural Systems, " *Proceedings of the 6th Joint Technical Coordinating Committee Meeting*, U.S.—Japan Cooperative Research Program Utilizing Large-Scale Testing Facilities, Maui, Hawaii, June, 1985.

[5] Boutros, M.K. and Goel, S.C., "Pre-Test Analysis of the Six-Story Eccentric Braced Steel Test Building," *Proceedings of the 5th Joint Technical Coordinating Committee Meeting*, U.S.—Japan Cooperative Research Program Utilizing Large-Scale Testing Facilities, Tsukuba, Japan, February, 1984.

[6] Goel, S.C. and Boutros, M.K., "Analytical Study of the Response of an Eccentrically Braced Steel Structure," *Proceedings of the ASCE Structural Engineering Congress '85*, Chicago, Illinois, September, 1985.

[7] Wallace, B.J. and Krawinkler, H., "Small-Scale Model Experimentation on Steel Assemblies: U.S.—Japan Research Program," Report No. 75, The John A. Blume Earthquake Engineering Center, Department of Civil Engineering, Stanford University, Stanford, California, June, 1985.

[8] Bertero, V. et al., "Earthquake Simulator Tests and Associated Experimental, Analytical and Correlation Studies of One-Fifth Scale Model, " *Earthquake Effects on Reinforced Concrete Structures: U.S.—Japan Research*, Wight, J.K. (ed.), American Concrete Institute, Detroit, Michigan, 375–424, 1985.

[9] Clough, R.W. and Bertero, V.V., "Laboratory Model Testing for Earthquake Loading," *Journal of the Engineering Mechanics Division*, ASCE, Vol. 103(6), 1105–1124, December, 1977.

[10] Beck, J.L., "System Identification Analysis Applied to Full Scale Test Data," *Earthquake Research Affliates Conference*, California Institute of Technology, Pasadena, California, February, 1985.

[11] Takanashi, K. et al., "Non-Linear Earthquake Response Analysis of Structures by

a Computer-Actuator On-Line System," *Bulletin of Earthquake Resistant Structure Research Center*, No. 8, Institute of Industrial Science, University of Tokyo, Japan, 1–17, December, 1974.

[12] Takanashi, K., Udagawa, K. and Tanaka, H., "A Simulation of Earthquake Response of Steel Buildings," *Proceedings of the 6th World Conference on Earthquake Engineering*, New Delhi, India, 3156–3162, January, 1977.

[13] Takanashi, K., Udagawa, K. and Tanaka, H., "Earthquake Response Analysis of a 1-Bay 2-Story Steel Frame by Computer-Actuator On-Line System," *Bulletin of Earthquake Resistant Structure Research Center*, No. 11, Institute of Industrial Science, University of Tokyo, Japan, 55–60, December, 1977.

[14] Takanashi, K., Udagawa, K. and Tanaka, H., "Pseudo-Dynamic Tests on a 2-Story Steel Frame by Computer-Load Test Apparatus Hybrid System," *Proceedings of the 7th World Conference on Earthquake Engineering*, Istanbul, Turkey, 225–232, September, 1980.

[15] Takanashi, K. and Taniguchi, H., "Pseudo-Dynamic Tests on Frames Including High Strength Bolted Connections," *Proceedings of the 7th World Conference on Earthquake Engineering*, Istanbul, Turkey, 445–448, September, 1980.

[16] Okamoto, S. et al., "Techniques for Large Scale Testing at BRI Large Scale Structure Test Laboratory," Research Paper No. 101, Building Research Institute, Ministry of Construction, Japan, May, 1983.

[17] Shing, P.B. and Mahin, S.A., "Experimental Error Propagation in Pseudodynamic Testing," Report No. UCB/EERC–83/12, Earthquake Engineering Research Center, University of California, Berkeley, California, June, 1983.

[18] Mahin, S.A. and Shing, P.B., "Pseudodynamic Method for Seismic Testing," *Journal of Structural Engineering*, ASCE, Vol. 111(7), 1482–1503, July, 1985.

[19] B.R.I. Steel Group, "Inelastic Behavior of the Structural Members in the Phase I Test," *Proceedings of the 6th Joint Technical Coordinating Committee Meeting*, U.S.—Japan Cooperative Research Program Utilizing Large-Scale Testing Facilities, Maui, Hawaii, June, 1985.

[20] Kaminosono, T. et al., "Trial Tests on Full Scale Six Story Steel Structure," *Proceedings of the 4th Joint Technical Coordinating Committee Meeting*, U.S.—Japan Cooperative Research Program Utilizing Large-Scale Testing Facilities, Tsukuba, Japan, June, 1983.

[21] Yamazaki, Y., Nakashima, M. and Kaminosono, T., "Note on High Frequency Error in MDOF Pseudo Dynamic Testing," *Proceedings of the 4th Joint Technical Coordinating Committee Meeting*, U.S.—Japan Cooperative Research Program Utilizing Large-Scale Testing Facilities, Tsukuba, Japan, June, 1983.

[22] Aktan, H.M., "Pseudo-Dynamic Testing of Structures," *Journal of Engineering Mechanics*, Vol. 112(2), 183–197, February, 1986.

[23] Takanashi, K. and Ohi, K., "Earthquake Response Analysis of Steel Structures by

Rapid Computer-Actuator On-Line System," *Bulletin of Earthquake Resistant Structure Research Center*, No. 16, Institute of Industrial Science, University of Tokyo, Japan, 103–109, March, 1983.

[24] Shing, P.B. and Mahin, S.A., "Pseudodynamic Test Method for Seismic Performance Evaluation: Theory and Implementation," Report No. UCB/EERC–84/01, Earthquake Engineering Research Center, University of California, Berkeley, California, January, 1984.

[25] Askar, G., Lee, S.J. and Lu, L.-W., "Design Studies of the Six Story Steel Test Building: U.S.—Japan Cooperative Earthquake Research Program," Report No. 467.3, Fritz Engineering Laboratory, Lehigh University, Bethlehem, Pennsylvania, June, 1983.

[26] Ricles, J.M. and Popov, E.P., "Cyclic Behavior of Composite Floor Systems in Eccentrically Braced Frames," *Proceedings of the 6th Joint Technical Coordinating Committee Meeting*, U.S.—Japan Cooperative Research Program Utilizing Large-Scale Testing Facilities, Maui, Hawaii, June, 1985.

[27] Roeder, C.W. and Popov, E.P., "Eccentrically Braced Steel Frames for Earthquakes," *Journal of the Structural Division*, ASCE, Vol. 104(3), 391–412, March, 1978.

[28] Hall, J.F., "An FFT Algorithm for Structural Dynamics," *Earthquake Engineering and Structural Dynamics*, Vol. 10, 797–811, 1982.

[29] Goel, S.C. and Foutch, D.A., "Preliminary Studies and Test Results of Eccentrically Braced Full-Size Steel Structure," *Proceedings of the 16th Joint Meeting*, U.S.—Japan Panel on Wind and Seismic Effects, National Bureau of Standards, Washington, D.C., May, 1984.

Type	Excitation	Amplitudes	Scale	Cost/Time	Comments
Ambient Vibrations	Microtremors, Wind, Cultural Noise	Small	Full	Cheap/Short	Limited Information
Building Shaker	Harmonic force	Small—medium	Full	Cheap/Short	Not at Earthquake Levels
Shaking Table	Earthquake Record	Large	Reduced	Expensive/ Long	Validity of Scaling, Structure/Table Interaction
Pseudo-Dynamic	Earthquake Record	Large	Full	Expensive/ Long	Inertia Modeling Errors, Unstable Control
Natural	Earthquake	Large	Full	Cheap/ Unscheduled	Extensive Instrumentation not Practical

Table 2.1 Testing Structures for Earthquake Dynamics [10]

Input Motion	Test	Peak Acceleration (% g)	Input Duration (sec)	Time Step (sec)	Peak Roof Displacement (cm)	Peak Interstory Drift (cm)
Taft S21W Component, 1952 Kern County, California, Earthquake	Elastic	6.5	17.92	0.01	1.41	0.31
	Inelastic	50	17.10	0.005	8.84	3.00

Table 2.2 Some Details on Phase II Testing and Results

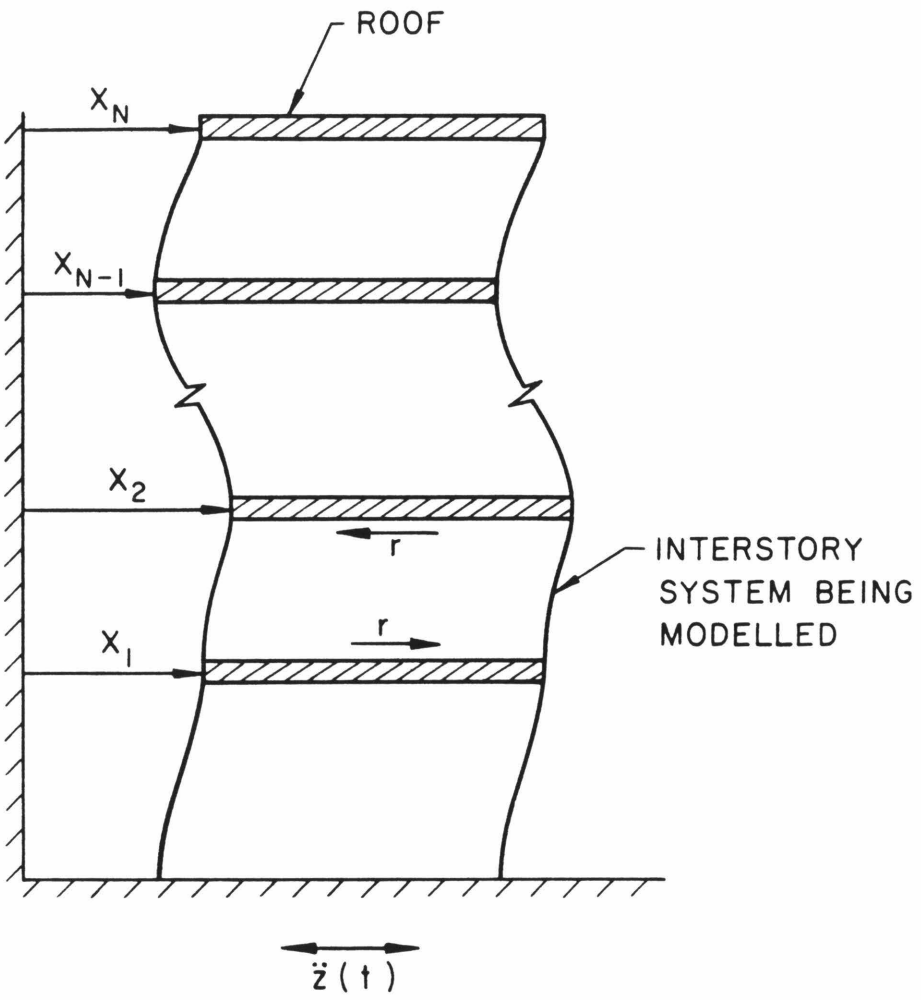

Fig. 2.1 A Multi-Story Building Structure Excited by Ground Accelerations

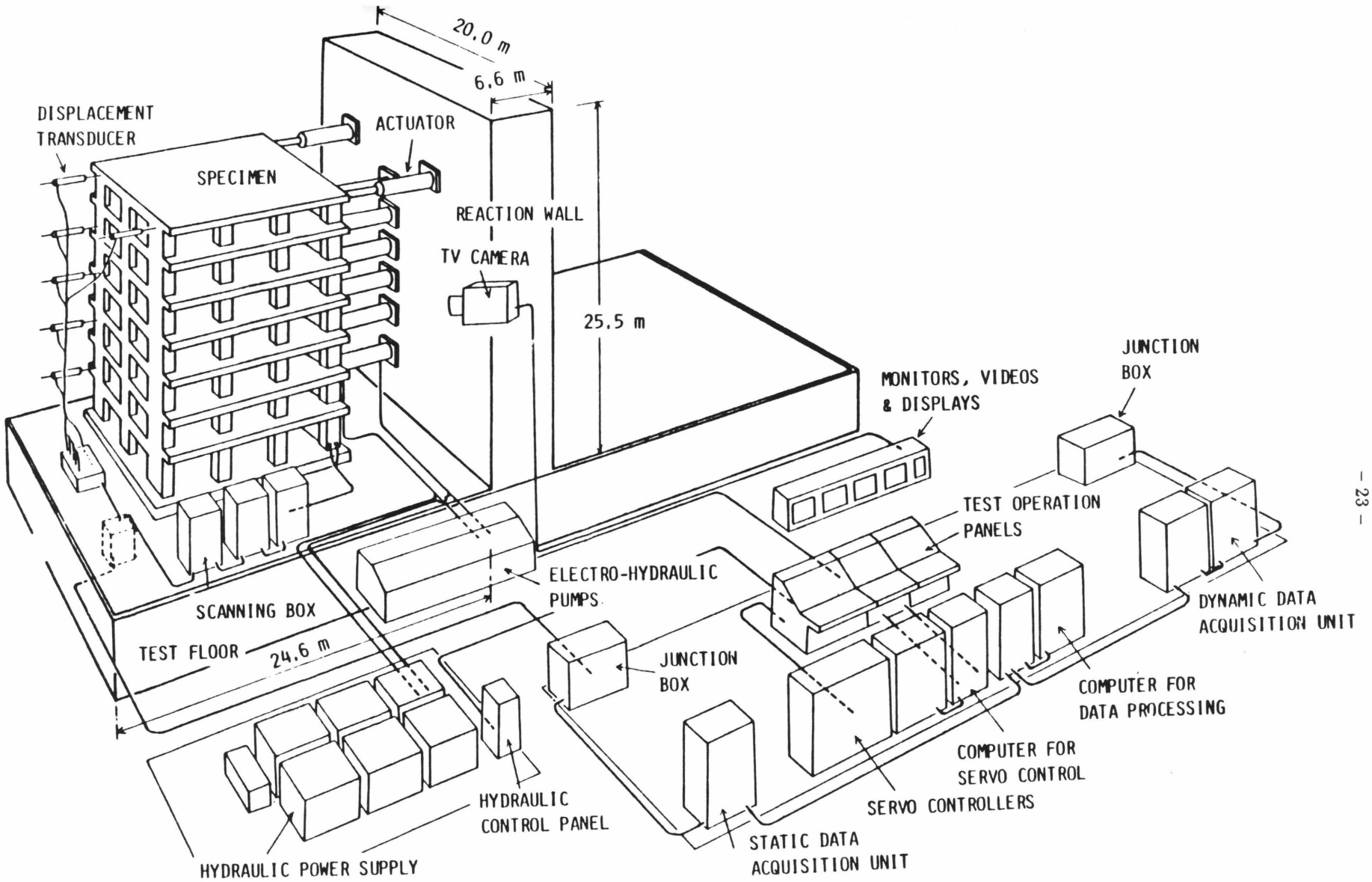

Fig. 2.2 Pseudo-Dynamic Testing Facility at the Building Research Institute in Tsukuba, Japan [16]

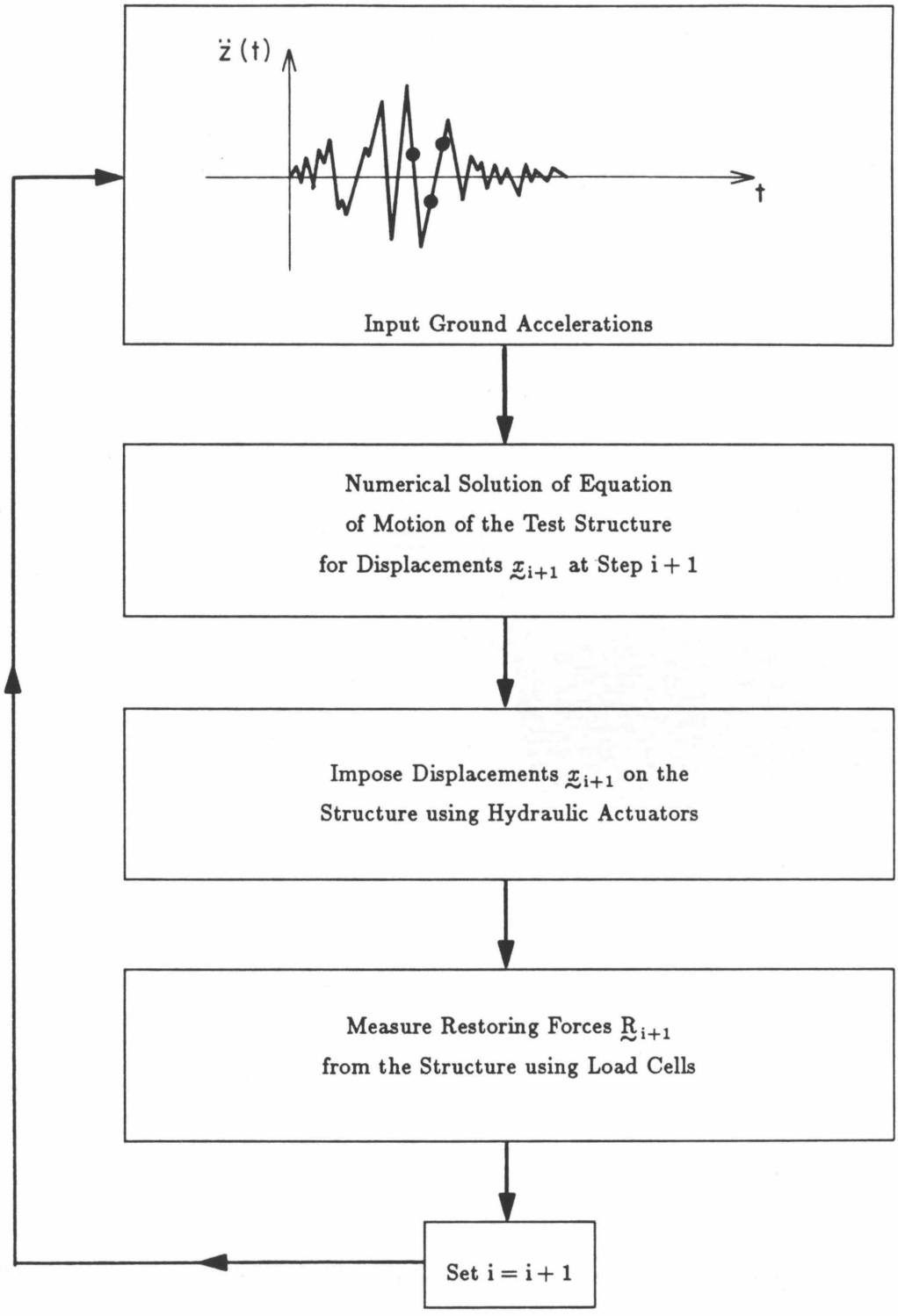

Fig. 2.3 A Simplified Flow Diagram for Pseudo-Dynamic Test Operation [17]

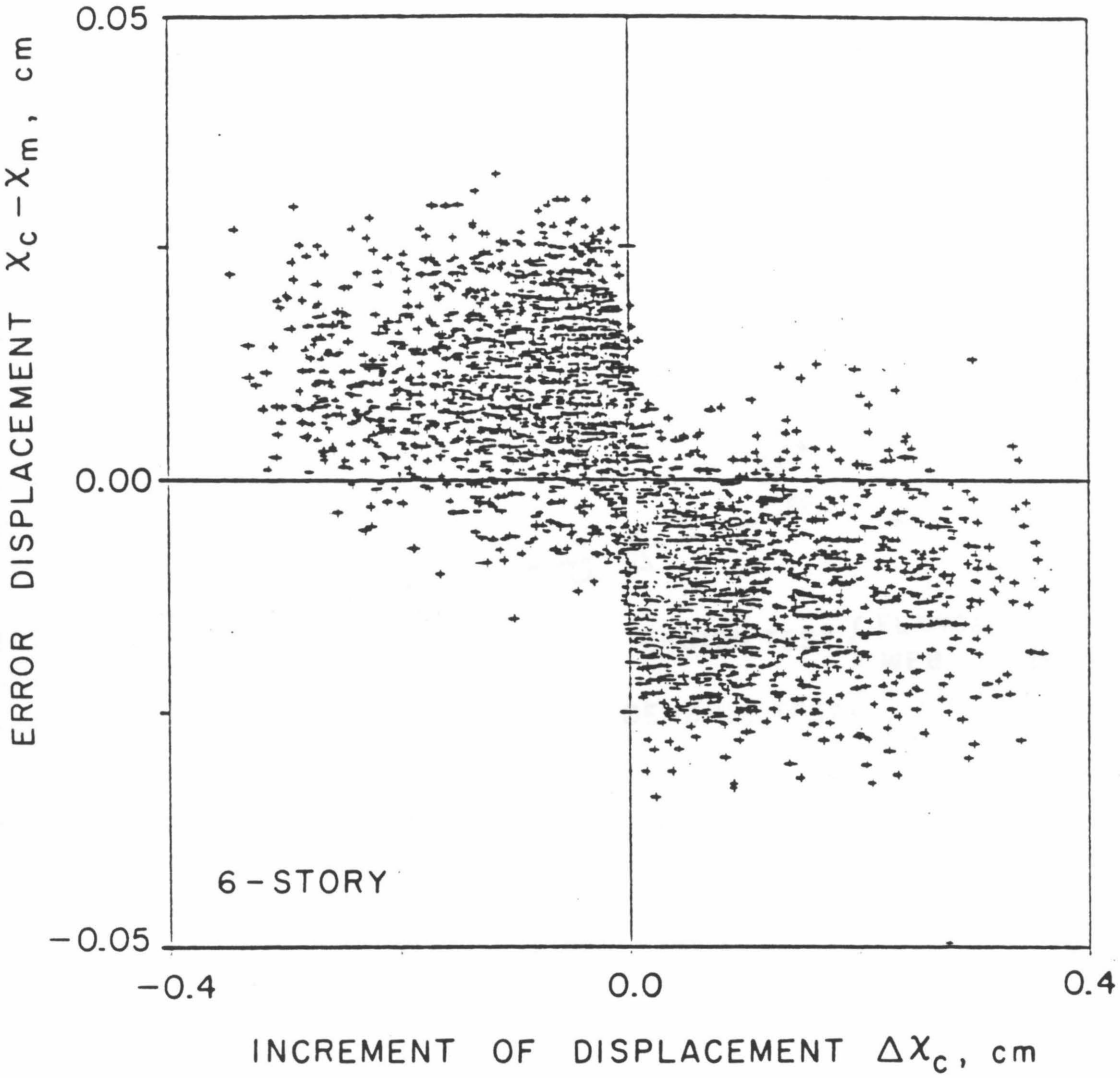

Fig. 2.4 A Typical Plot Showing Displacement Errors During Pseudo-Dynamic Testing [19]

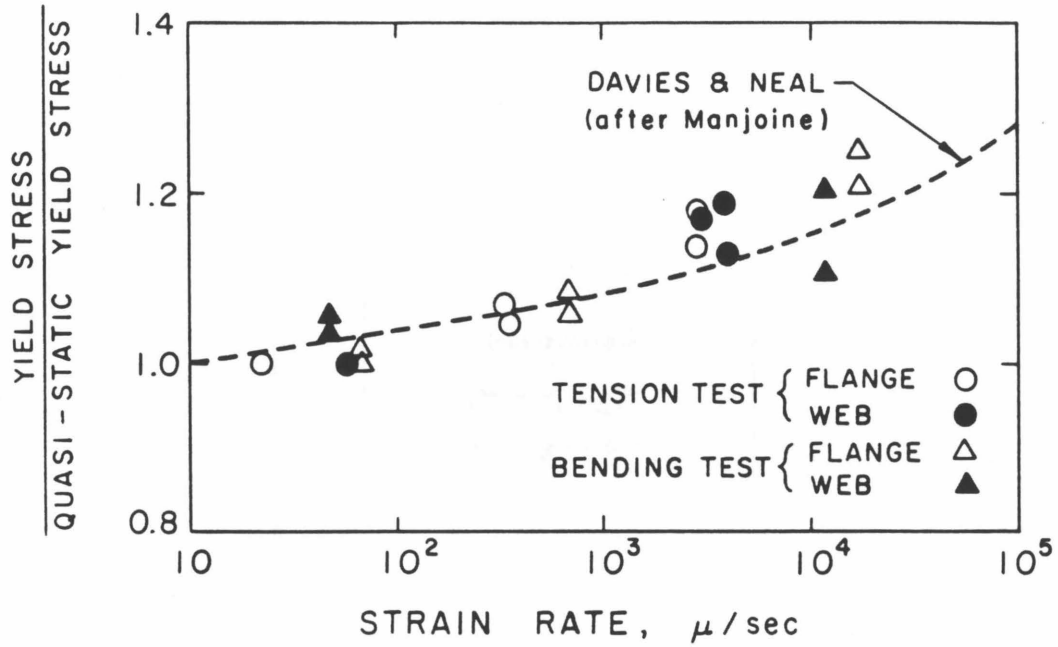

Fig. 2.5 Increase of Yield Stress due to Strain Rate [23]

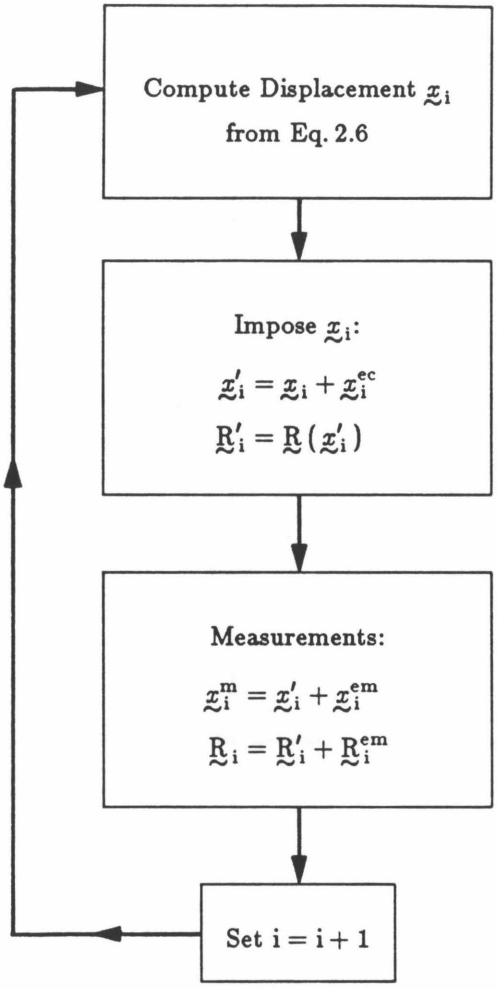

Fig. 2.6 Feedback of Experimental Errors in Pseudo-Dynamic Testing

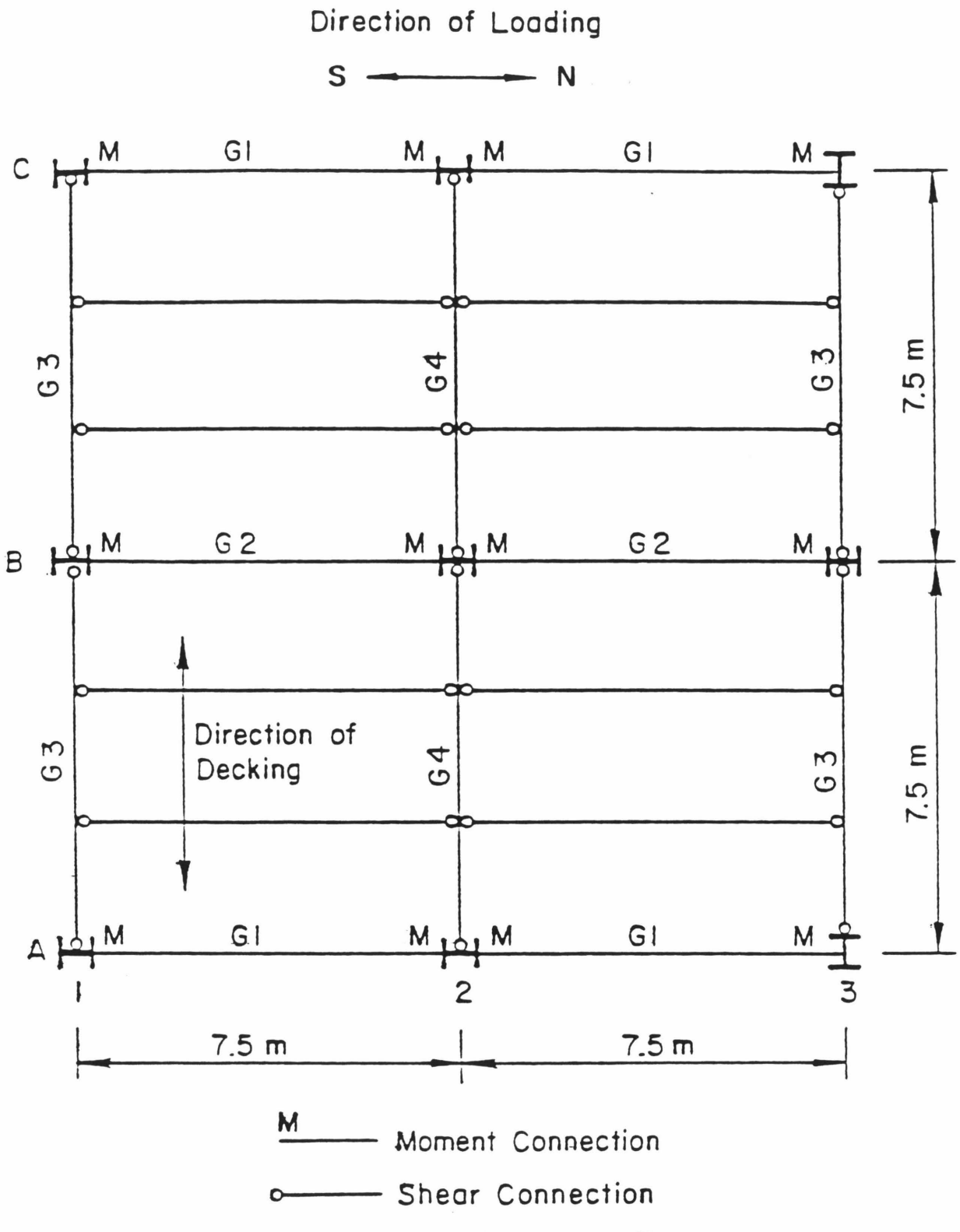

Fig. 2.7 Plan of Test Structure [25]

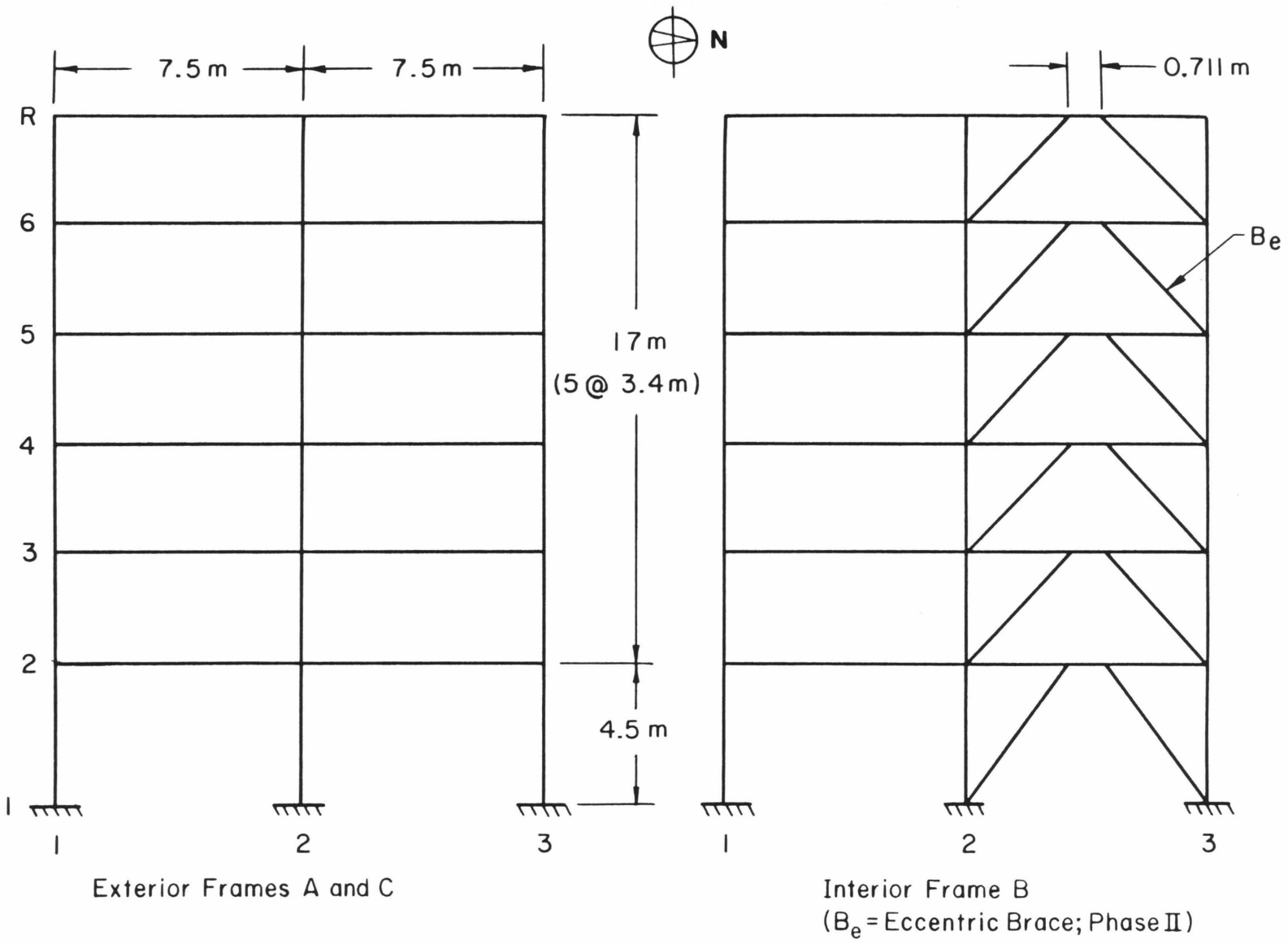

Fig. 2.8 Elevation Views of Exterior and Interior Frames of Test Structure [25]

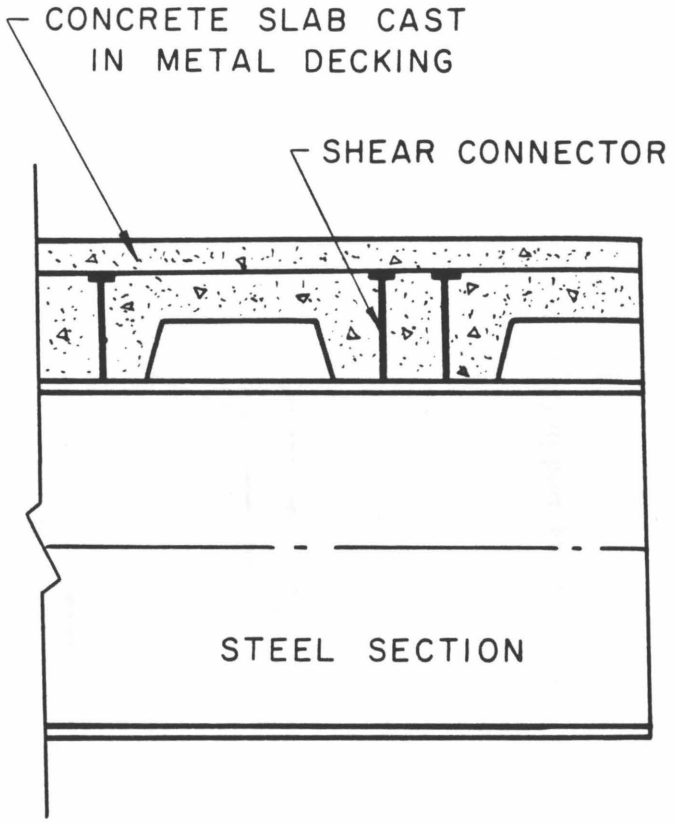

Fig. 2.9 Section of a Composite Girder [26]

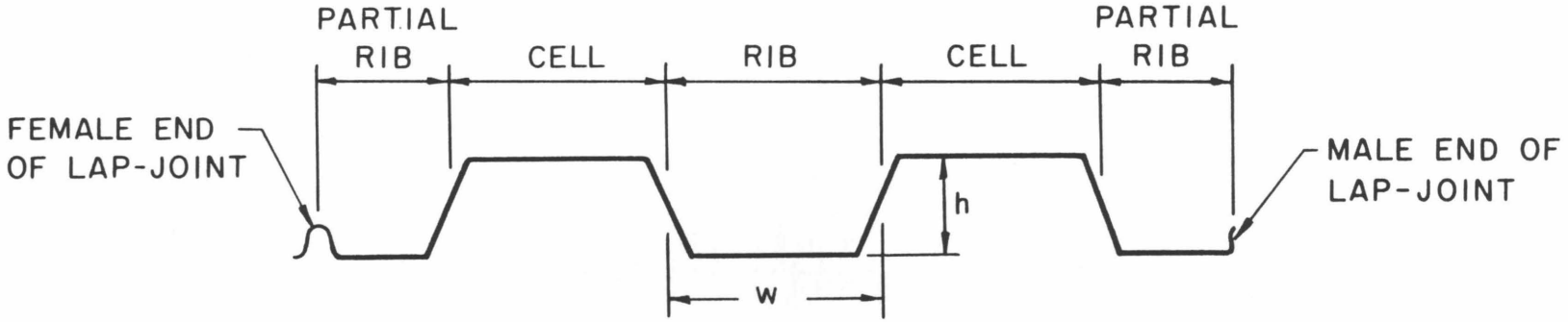

Fig. 2.10 Typical Metal Decking used in Composite Construction [26]

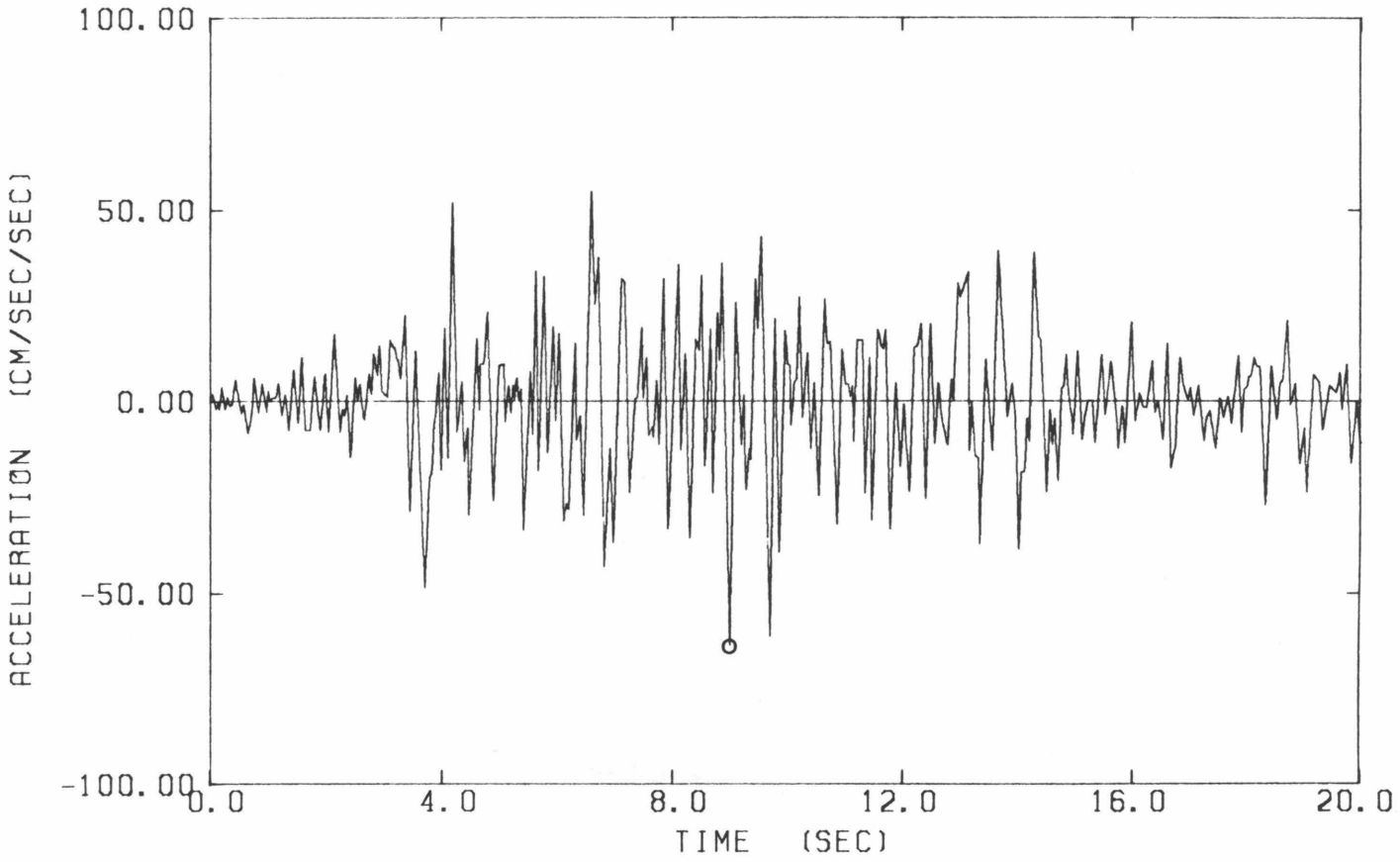

Fig. 2.11 Taft S21W Accelerogram, 1952 Kern County, California, Earthquake (peak scaled to 6.5% g)

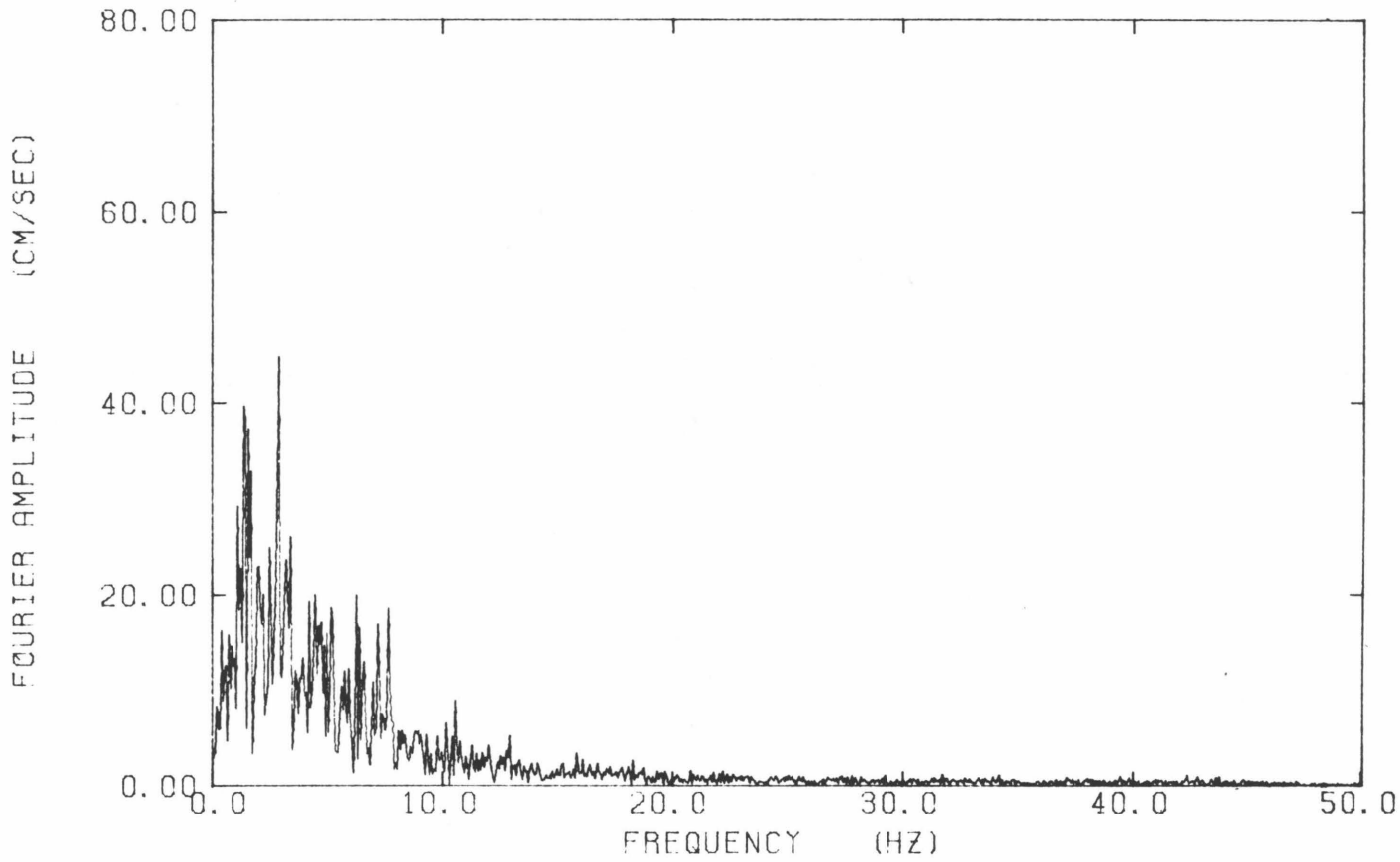

Fig. 2.12 Fourier Amplitude Spectrum of Scaled Taft S21W Accelerogram in Fig. 2.11

CHAPTER 3

SYSTEM IDENTIFICATION APPLIED TO THE ELASTIC PSEUDO-DYNAMIC TEST DATA —IGNORING FEEDBACK OF EXPERIMENTAL ERRORS

3.1 Introduction

In system identification, we are concerned with the determination of system models from records of system operation [1,10]. The problem can be represented diagrammatically as Fig. 3.1 in which

$\underset{\sim}{u}(t)$ = known input

$\underset{\sim}{z}(t)$ = system output

$\underset{\sim}{w}(t)$ = process noise (e.g., unknown inputs)

$\underset{\sim}{n}(t)$ = observation noise

$\underset{\sim}{y}(t)$ = measured output.

Thus, the problem of system identification is the determination of a system model from records of $\underset{\sim}{u}(t)$ and $\underset{\sim}{y}(t)$. In other words, given the input-output data set for a real system, we want to obtain a mathematical model which describes a certain behavior of the system.

We will be concerned with parametric system identification in this study, in which a particular mathematical form is chosen to describe the essential features of the system and then the unknown parameters of the model are estimated from the input and output data. In contrast, in nonparametric system identification, functions rather than parameters are estimated, such as a transfer function or impulse response function. In practice, only discrete values of the functions can be estimated and so, in effect, a model with a very large number of parameters must be estimated. This makes the results very sensitive to model error and measurement noise. Nonparametric models have been discussed by Beck [2].

3.2 Output-Error Method for Parameter Estimation

In this section, the output-error approach to parameter estimation is described, following Beck [2]. In this method, the parameters of a model are estimated by determining those values which give an optimal match of the output of the model and the measured output of the real system, when both are subjected to nominally the same input. The quality of the output match is determined by some scalar function J of the output-error called the measure-of-fit. The parameter adjustment algorithm shown in Fig. 3.2 selects the optimal parameter values by minimizing the measure-of-fit J in a systematic manner.

The output-error $\underset{\sim}{e}$ is the difference between the output measurements $\underset{\sim}{y}$ of the system and the model output $\underset{\sim}{m}$:

$$\underset{\sim}{e}(t;\underset{\sim}{\theta}) = \underset{\sim}{y}(t) - \underset{\sim}{m}(t;\underset{\sim}{\theta}) \quad . \tag{3.1}$$

In structural identification, the output vector $\underset{\sim}{y}$ will be the recorded response such as displacement, velocity or acceleration at various points in the structure.

For a given observed input $\ddot{z}(t)$ and measured output $\underset{\sim}{y}$ over a time interval $[t_s\ ,\ t_e]$, the optimal estimates of the parameters are defined to be the values which minimize the measure-of-fit:

$$J(\underset{\sim}{\theta}) = \int_{t_s}^{t_e} < \underset{\sim}{e}(t;\underset{\sim}{\theta})\ ,\ V\underset{\sim}{e}(t;\underset{\sim}{\theta}) > \quad dt \quad , \tag{3.2}$$

where $<\ .\ ,\ .\ >$ is the Euclidean scalar product and V is a prescribed positive definite diagonal matrix which allows weighting of the output-error.

The problem of identifying the optimal model from system data has been now reduced to minimizing the function $J(\underset{\sim}{\theta})$ in Eq. 3.2. This minimization could be achieved by directly solving the stationarity condition of J with respect to $\underset{\sim}{\theta}$:

$$\nabla J\Big|_{\underset{\sim}{\theta}=\underset{\sim}{\hat{\theta}}} = \underset{\sim}{0} \quad , \tag{3.3}$$

where $\underset{\sim}{\hat{\theta}}$ is the vector of optimal parameter estimates. This usually leads to a set of simultaneous nonlinear algebraic equations in $\underset{\sim}{\theta}$ which cannot be solved analytically. The nonlinearity arises because the model response is, in general, a nonlinear function of the parameters, even if the model itself is linear in the state and linear in the parameters.

Some descent methods for optimization which have been used in structural identification include the Gauss–Newton method, the method of steepest descent and the conjugate

gradient method. The Gauss–Newton method is equivalent to applying to Eq. 3.3 a modification of the classical Newton–Raphson method for finding the zeros of a multi-variable vector function.

A descent method called the modal minimization method, developed by Beck and Jennings [3] to provide a reliable technique for the identification of linear modal models, is used in this study.

3.3 Linear Structural Model

3.3.1 Analytical Model

A discrete analytical model which has the following equation of motion:

$$\mathrm{M}\underset{\sim}{\ddot{x}} + \mathrm{D}\underset{\sim}{\dot{x}} + \mathrm{K}\underset{\sim}{x} = -\mathrm{M}\ddot{z}(t)\,\underset{\sim}{1} \quad , \tag{3.4}$$

with the initial conditions

$$\underset{\sim}{x}(\mathrm{t_s}) = \underset{\sim}{x}_0 \qquad \text{and} \qquad \underset{\sim}{\dot{x}}(\mathrm{t_s}) = \underset{\sim}{\mathrm{v}}_0 \quad ,$$

represents a physical model consisting of a distribution of lumped masses linked by linear, massless springs and dashpots, with the base being rigid and moving in only one direction. The vector $\underset{\sim}{x} = [\, x_1, x_2, \cdots, x_{\mathrm{N}} \,]^{\mathrm{T}}$ then consists of horizontal displacement relative to the base of each degree of freedom of each lumped mass of the model, and $\ddot{z}$ is taken to be the horizontal component of acceleration of the base motion. All the components of $\underset{\sim}{1}$ are unity. M,D and K are mass, damping and stiffness matrices, respectively, and along with the initial conditions, form the parameters of the model.

With respect to the inverse problem, Beck [2] showed that the stiffness and damping matrices are not determined uniquely in typical situations. The first limitation arises from the fact that seismic response is usually measured at only a few points in a structure while 'local' uniqueness of K and D requires measurement of response at $\frac{1}{2}$N or more of the coordinates. Another important limitation is due to the deterioration of the signal-to-noise ratio at higher frequencies, implying that the higher mode information in the stiffness and damping matrices will be unreliable if attempts are made to estimate these matrices from seismic records.

On the other hand, modal parameters for the structure can theoretically be determined which contain all the information about the structural properties that can be estimated

directly from the input and output records, although the small signal-to-noise ratio at higher frequencies implies that only the dominant modes of the response can be estimated reliably from earthquake data. Beck [2] then concluded that when linear models are to be estimated from seismic excitation and response time-histories, they should be based on the dominant modes in the records of the response and not on the stiffness and damping matrices. If estimation of structural parameters is of interest, this may be done in a separate stage using the identified modal parameters.

3.3.2 Modal Model

If the mass matrix M is assumed symmetric and positive definite, then a real inner-product in $\mathbf{R}^N$ can be defined as :

$$< \underset{\sim}{x}, \underset{\sim}{y} > = \underset{\sim}{x}^T \mathrm{M} \underset{\sim}{y} \qquad \forall \underset{\sim}{x}, \underset{\sim}{y} \in \mathbf{R}^N \quad , \tag{3.5}$$

where $\mathbf{R}^N$ is an N-dimensional Euclidean vector space. Also, the stiffness matrix K and the damping matrix D being assumed symmetric matrices and K also being assumed a positive definite matrix [i.e., self-adjoint and positive definite operators with respect to the usual innerproduct $(\underset{\sim}{x}, \underset{\sim}{y}) = \underset{\sim}{x}^T \underset{\sim}{y}$], it can be shown that $\mathrm{M}^{-1}\mathrm{K}$ and $\mathrm{M}^{-1}\mathrm{D}$ are self-adjoint operators and $\mathrm{M}^{-1}\mathrm{K}$ is also a positive definite operator, but with respect to the innerproduct defined in Eq. 3.5. Furthermore, if the damping is assumed to be classical, then $\mathrm{M}^{-1}\mathrm{K}$ and $\mathrm{M}^{-1}\mathrm{D}$ are commutative.

The above properties of $\mathrm{M}^{-1}\mathrm{K}$ and $\mathrm{M}^{-1}\mathrm{D}$ ensure that they have a common set of N orthonormal eigenvectors [4] such that:

$$\begin{aligned} \mathrm{M}^{-1}\mathrm{K}\,\Phi &= \Phi\,\Omega^2 \\ \mathrm{M}^{-1}\mathrm{D}\,\Phi &= \Phi\,(2\mathrm{Z}\,\Omega) \quad , \end{aligned} \tag{3.6}$$

where $\Phi = [\underset{\sim}{\phi}^{(1)}, \underset{\sim}{\phi}^{(2)}, \cdots, \underset{\sim}{\phi}^{(N)}]$ denotes the modeshape matrix whose columns are the eigenvectors of $\mathrm{M}^{-1}\mathrm{K}$ and $\mathrm{M}^{-1}\mathrm{D}$. Also

$$\Omega = \begin{bmatrix} \omega_1 & & 0 \\ & \ddots & \\ & \omega_r & \\ & & \ddots \\ 0 & & \omega_N \end{bmatrix} \quad \text{and} \quad \mathrm{Z} = \begin{bmatrix} \varsigma_1 & & 0 \\ & \ddots & \\ & \varsigma_r & \\ & & \ddots \\ 0 & & \varsigma_N \end{bmatrix} \quad ,$$

where the ω_r and ς_r are the modal frequencies and modal damping factors, respectively.

Since Φ gives an orthonormal basis for $\mathbf{R}^N$ with respect to the innerproduct defined in Eq. 3.5,

$$\Phi^T M \Phi = I \quad . \tag{3.7}$$

Premultiplying Eq. 3.6 by Φ^T and using Eq. 3.7:

$$\Phi^T K \Phi = \Omega^2 \qquad \text{and} \qquad \Phi^T D \Phi = 2Z\Omega \quad . \tag{3.8}$$

Since the eigenvectors $\underset{\sim}{\phi}^{(r)}$ are a basis for the N-dimensional space $\mathbf{R}^N$, $\underset{\sim}{x}$ can be written as:

$$\begin{aligned} \underset{\sim}{x}(t) &= \Phi \underset{\sim}{\xi}(t) \qquad\qquad \forall \underset{\sim}{x} \in \mathbf{R}^N \\ &= \sum_{r=1}^{N} \xi_r(t) \underset{\sim}{\phi}^{(r)} \quad , \end{aligned} \tag{3.9}$$

where $\underset{\sim}{\xi}$ is the vector of coordinates of $\underset{\sim}{x}$ with respect to the basis of eigenvectors. Substituting Eq. 3.9 into Eq. 3.4:

$$M\Phi \ddot{\underset{\sim}{\xi}} + D\Phi \dot{\underset{\sim}{\xi}} + K\Phi \underset{\sim}{\xi} = -M\ddot{z}(t) \underset{\sim}{1} \quad . \tag{3.10}$$

Premultiplying Eq. 3.10 by Φ^T and using Eqs. 3.7 and 3.8:

$$\begin{aligned} \ddot{\underset{\sim}{\xi}} + 2Z\Omega \dot{\underset{\sim}{\xi}} + \Omega^2 \underset{\sim}{\xi} &= -\Phi^T M \ddot{z}(t) \underset{\sim}{1} \\ &= -\underset{\sim}{\alpha} \ddot{z}(t) \quad , \end{aligned} \tag{3.11}$$

where $\underset{\sim}{\alpha}$ is the vector of modal participation factors whose magnitude in general depends on the normalization used for Φ, such as Eq. 3.7. Hence it is useful to express Eqs. 3.9 and 3.11 in forms which are invariant with respect to any particular normalization introduced for Φ.

Equation 3.9 can also be written as:

$$x_i(t) = \sum_{r=1}^{N} x_i^{(r)}(t) \quad , \tag{3.12}$$

where

$$x_i^{(r)}(t) = \phi_i^{(r)} \xi_r(t) \tag{3.13}$$

and is the contribution from the r-th mode to the response at degree-of-freedom i. From Eqs. 3.11 and 3.13, the following equation can be deduced:

$$\ddot{x}_i^{(r)} + 2\zeta_r \omega_r \dot{x}_i^{(r)} + \omega_r^2 x_i^{(r)} = -p_i^{(r)} \ddot{z}(t) \quad , \tag{3.14}$$

where $p_i^{(r)} = \phi_i^{(r)} \alpha_r$, is called the effective participation factor for the r-th mode at the i-th degree-of-freedom, and it is independent of the normalization chosen for the $\underset{\sim}{\phi}^{(r)}$.
The corresponding initial conditions for Eq. 3.14 are:

$$\begin{aligned} x_i^{(r)}(t_s) &= \phi_i^{(r)} \xi_r(t_s) = \phi_i^{(r)} \sum_{j,k=1}^{N} \phi_j^{(r)} m_{jk} x_k(t_s) \\ \dot{x}_i^{(r)}(t_s) &= \phi_i^{(r)} \dot{\xi}_r(t_s) = \phi_i^{(r)} \sum_{j,k=1}^{N} \phi_j^{(r)} m_{jk} \dot{x}_k(t_s) \quad . \end{aligned} \tag{3.15}$$

Summary:

$$\ddot{x}_i^{(r)} + 2\zeta_r \omega_r \dot{x}_i^{(r)} + \omega_r^2 x_i^{(r)} = -p_i^{(r)} \ddot{z}(t)$$

with the initial conditions $x_i^{(r)}(t_s)$ and $\dot{x}_i^{(r)}(t_s)$; (3.16)

and $$x_i(t) = \sum_{r=1}^{N} x_i^{(r)}(t) .$$

Hence the parameters of the modal model to be estimated are:

$$\{\omega_r,\ \zeta_r,\ p_i^{(r)},\ x_i^{(r)}(t_s),\ \dot{x}_i^{(r)}(t_s) \ :\ i,\ r = 1,2,\cdots,N\} .$$

3.4 Single-Input Single-Output (SI-SO) System Identification Technique

A single-input single-output system identification technique may be used to estimate the modal parameters when the input and output consist only of one component of ground motion and a parallel component of response at some point in the structure, respectively.

The parameters to be estimated are the modal parameters:

$$\underset{\sim}{\theta}^{(r)} = [\,\theta_1^{(r)},\ \theta_2^{(r)},\ \theta_3^{(r)},\ \theta_4^{(r)},\ \theta_5^{(r)}\,]^T \qquad r = 1,2,\cdots,R \quad ,$$

where each modal contribution, $x^{(r)}(t)$, is governed by the standard equation of motion:

$$\ddot{x}^{(r)} + \theta_2^{(r)} \dot{x}^{(r)} + \theta_1^{(r)} x^{(r)} = -\theta_3^{(r)} \ddot{z}(t)$$

with the initial conditions (3.17)

$$x^{(r)}(t_s) = \theta_4^{(r)} \quad \text{and} \quad \dot{x}^{(r)}(t_s) = \theta_5^{(r)} \quad .$$

Comparing Eqs. 3.16 and 3.17:

$$\theta_1^{(r)} = \omega_r^2 \,, \quad \theta_2^{(r)} = 2\zeta_r\,\omega_r \,, \quad \theta_3^{(r)} = p_i^{(r)} \quad ,$$

and R is the number of dominant modes in the structure contributing at the point of consideration.

Let the measured output history be:

$$\underset{\sim}{y} = [\,K_1\,x_0, K_2\,v_0, K_3\,a_0\,]^T \tag{3.18}$$

over some time interval $[t_s\ ,\ t_e]$, then any combination of displacement, velocity or acceleration records of one component of the structural response at a point can be used by choosing each K_i as either 1 or 0.

The corresponding model output is:

$$\underset{\sim}{m} = [\,K_1\,x, K_2\,\dot{x}, K_3\,\ddot{x}\,]^T \quad , \tag{3.19}$$

where the response at each floor is modelled as a superposition of the contributions of a small number, R, of classical modes so that:

$$x(t;\underset{\sim}{\theta}) = \sum_{r=1}^{R} x^{(r)}\,(t;\underset{\sim}{\theta}^{(r)})$$

and (3.20)

$$\underset{\sim}{\theta} = [\,\underset{\sim}{\theta}^{(1)}, \underset{\sim}{\theta}^{(2)}, \cdots, \underset{\sim}{\theta}^{(R)}\,]^T \quad .$$

From Eq. 3.1, the output-error is:

$$\underset{\sim}{e}(t;\underset{\sim}{\theta}) = [\,K_1\,(x_0 - x),\ K_2\,(v_0 - \dot{x}),\ K_3\,(a_0 - \ddot{x})\,]^T \quad . \tag{3.21}$$

The measure-of-fit can be obtained by substituting Eq. 3.21 into Eq. 3.2:

$$J(\underset{\sim}{\theta}) = K_1V_1 \int_{t_s}^{t_e} (x_0 - x)^2\,dt \;+\; K_2V_2 \int_{t_s}^{t_e} (v_0 - \dot{x})^2\,dt \;+\; K_3V_3 \int_{t_s}^{t_e} (a_0 - \ddot{x})^2\,dt \quad ,$$

where (3.22)

$$V_1 = 1\Big/\int_{t_s}^{t_e} x_0^2\,dt\,, \qquad V_2 = 1\Big/\int_{t_s}^{t_e} v_0^2\,dt\,, \qquad V_3 = 1\Big/\int_{t_s}^{t_e} a_0^2\,dt \quad .$$

The diagonal weighting matrix V has been chosen to normalize each integral in Eq. 3.22 in order to give a meaningful comparison between the optimal values of J for different time

segments and for different response quantities. The optimal estimates of the parameters are obtained by minimizing the above measure-of-fit by the modal minimization method. This method, which is explained in detail by Beck in his thesis dissertation [2], is given very briefly in the following section.

3.4.1 Modal Minimization Method

The method consists of three parts:

(a) Modal Sweeps

(b) Single-Mode Minimizations

(c) One-Dimensional Minimizations

(a) Modal Sweeps

Initial estimates are made for $\underset{\sim}{\theta} = [\underset{\sim}{\theta}^{(1)}, \underset{\sim}{\theta}^{(2)}, \cdots, \underset{\sim}{\theta}^{(R)}]^T$. Then the following sequence of minimizations, which is called a modal sweep, is applied:

$$\begin{aligned}
J(\hat{\underset{\sim}{\theta}}^{(1)}, \underset{\sim}{\theta}^{(2)}, \cdots, \underset{\sim}{\theta}^{(R)}) &= \min_{\underset{\sim}{\theta}^{(1)}} \; J(\underset{\sim}{\theta}^{(1)}, \underset{\sim}{\theta}^{(2)}, \cdots, \underset{\sim}{\theta}^{(R)}) \\
J(\hat{\underset{\sim}{\theta}}^{(1)}, \hat{\underset{\sim}{\theta}}^{(2)}, \cdots, \underset{\sim}{\theta}^{(R)}) &= \min_{\underset{\sim}{\theta}^{(2)}} \; J(\hat{\underset{\sim}{\theta}}^{(1)}, \underset{\sim}{\theta}^{(2)}, \cdots, \underset{\sim}{\theta}^{(R)}) \\
&\vdots \\
J(\hat{\underset{\sim}{\theta}}^{(1)}, \hat{\underset{\sim}{\theta}}^{(2)}, \cdots, \hat{\underset{\sim}{\theta}}^{(R)}) &= \min_{\underset{\sim}{\theta}^{(R)}} \; J(\hat{\underset{\sim}{\theta}}^{(1)}, \hat{\underset{\sim}{\theta}}^{(2)}, \cdots, \hat{\underset{\sim}{\theta}}^{(R-1)}, \underset{\sim}{\theta}^{(R)}) \quad .
\end{aligned} \tag{3.23}$$

Each of the above steps involves minimization at the modal level and is called a single-mode minimization. Successive sweeps are performed until the change in J is insignificant.

(b) Single-Mode Minimizations

The minimization of $J(\underset{\sim}{\theta})$ in Eq. 3.22 with respect to $\underset{\sim}{\theta}^{(r)}$ is equivalent to minimizing the function:

$$\begin{aligned}
J_r(\underset{\sim}{\theta}^{(r)}) = K_1 V_1 \int_{t_s}^{t_e} (x_0^{(r)} - x^{(r)})^2 \, dt \; + \; K_2 V_2 \int_{t_s}^{t_e} (v_0^{(r)} - \dot{x}^{(r)})^2 \, dt \\
+ \; K_3 V_3 \int_{t_s}^{t_e} (a_0^{(r)} - \ddot{x}^{(r)})^2 \, dt \quad ,
\end{aligned} \tag{3.24}$$

where $\quad x_0^{(r)} = x_0 - \sum_{\substack{s=1 \\ \neq r}}^{R} x^{(s)} \; , \quad v_0^{(r)} = v_0 - \sum_{\substack{s=1 \\ \neq r}}^{R} \dot{x}^{(s)} \; , \quad a_0^{(r)} = a_0 - \sum_{\substack{s=1 \\ \neq r}}^{R} \ddot{x}^{(s)} \; .$

Let $s_k^{(r)}$, k = 3,4,5, satisfy the following differential equations:

$$D^{(r)}\, s_3^{(r)} = -\ddot{z}(t) \qquad s_3^{(r)}(t_s) = 0 \qquad \dot{s}_3^{(r)}(t_s) = 0$$

$$D^{(r)}\, s_4^{(r)} = 0 \qquad s_4^{(r)}(t_s) = 1 \qquad \dot{s}_4^{(r)}(t_s) = 0$$

$$D^{(r)}\, s_5^{(r)} = 0 \qquad s_5^{(r)}(t_s) = 0 \qquad \dot{s}_5^{(r)}(t_s) = 1$$

where
$$D^{(r)} = \frac{d^2}{dt^2} + \theta_2^{(r)} \frac{d}{dt} + \theta_1^{(r)} \quad . \tag{3.25}$$

Comparing Eq. 3.25 with Eq. 3.17 yields:

$$x^{(r)}(t; \underset{\sim}{\theta}^{(r)}) = \sum_{k=3}^{5} \theta_k^{(r)}\, s_k^{(r)}(t; \theta_1^{(r)}, \theta_2^{(r)}) \quad . \tag{3.26}$$

For a fixed $\theta_1^{(r)}$ and $\theta_2^{(r)}$, the minimum of $J_r(\underset{\sim}{\theta}^{(r)})$ is given by:

$$\frac{\partial J_r}{\partial \theta_k^{(r)}} = 0 \qquad k = 3,4,5 \quad . \tag{3.27}$$

Applying the stationarity condition in Eq. 3.27 to Eq. 3.24 and using Eq. 3.26 gives a linear system of equations:

$$H^{(r)}\, \underset{\sim}{\hat{\theta}}^{(r)} = \underset{\sim}{c}^{(r)} \quad , \tag{3.28}$$

whose solutions, $\underset{\sim}{\hat{\theta}}^{(r)}$ are the optimal estimates

$$\underset{\sim}{\hat{\theta}}^{(r)} = [\, \hat{\theta}_3^{(r)},\ \hat{\theta}_4^{(r)},\ \hat{\theta}_5^{(r)} \,]^T$$

for a given $\theta_1^{(r)}$ and $\theta_2^{(r)}$, and where

$$H_{ij}^{(r)} = K_1 V_1 \int_{t_s}^{t_e} s_i^{(r)}\, s_j^{(r)}\, dt \;+\; K_2 V_2 \int_{t_s}^{t_e} \dot{s}_i^{(r)}\, \dot{s}_j^{(r)}\, dt \;+\; K_3 V_3 \int_{t_s}^{t_e} \ddot{s}_i^{(r)}\, \ddot{s}_j^{(r)}\, dt$$

and

$$c_i^{(r)} = K_1 V_1 \int_{t_s}^{t_e} s_i^{(r)}\, x_0^{(r)}\, dt \;+\; K_2 V_2 \int_{t_s}^{t_e} \dot{s}_i^{(r)}\, v_0^{(r)}\, dt \;+\; K_3 V_3 \int_{t_s}^{t_e} \ddot{s}_i^{(r)}\, a_0^{(r)}\, dt \quad .$$

Hence the original problem of minimizing $J_r(\underset{\sim}{\theta}^{(r)})$ with respect to $\underset{\sim}{\theta}^{(r)}$ reduces to finding the minimum of J_r^* where

$$J_r^*(\theta_1^{(r)}, \theta_2^{(r)}) \;=\; J_r(\theta_1^r, \theta_2^r, \underset{\sim}{\hat{\theta}}^{(r)}) \;=\; \min_{\underset{\sim}{\theta}^{(r)}} \; J_r(\theta_1^{(r)}, \theta_2^{(r)}, \underset{\sim}{\theta}^{(r)}) \quad . \tag{3.29}$$

This is achieved by applying a series of one-dimensional minimizations of J_r^* alternately with respect to $\theta_1^{(r)}$ and $\theta_2^{(r)}$.

(c) One-Dimensional Minimizations

J_r^* is minimized alternately with respect to $\theta_1^{(r)}$ and $\theta_2^{(r)}$ as shown in Fig. 3.3. This process is continued until a consecutive pair of one-dimensional minimizations results in a fractional decrease in J_r^* of less than a specified tolerance. This technique for minimizing J_r^* with respect to $\theta_1^{(r)}$ and $\theta_2^{(r)}$ turns out to be equivalent to the method of steepest descent, after the first step, as seen in Fig. 3.3, but with the advantage that the gradients of J_r^* with respect to $\theta_1^{(r)}$ and $\theta_2^{(r)}$ need not be computed.

To evaluate J_r^* in Eq. 3.29, first the linear differential equations in 3.25 are solved for the 'sensitivity coefficients' using the transition-matrix method of Nigam and Jennings [5]. This method gives exact solutions at each time step for a linear variation of the ground accelerations $\ddot{z}(t)$ within each time step. Equation 3.28 is then solved using Gaussian elimination for $\underset{\sim}{\hat{\theta}}^{(r)}$ and the contribution of the r-th mode to the response is calculated from Eq. 3.26. The value of J_r^* can then be obtained from Eq. 3.24 using Simpson's rule for numerical integration.

3.5 A SI-SO Analysis of Pseudo-Dynamic Elastic Test Data

Using the single-input single-output structural identification method explained in the previous section, the data from the Phase II 'elastic' test at Tsukuba, Japan, described in Chapter 2, are analyzed. The principal objectives are:

(a) to examine the validity of the pseudo-dynamic method, within the elastic range of the structure,

(b) to ascertain how well a linear model with classical normal modes is capable of reproducing the measured response, and

(c) to determine what damping levels were operative during the elastic test.

As explained in Section 2.3, the higher modes in multi-degree-of-freedom systems are susceptible to becoming unstable due to the cumulative effects of feedback of experimental errors in the computer control system. This led to artificial suppression during the test of the higher structural modes beyond the first three. This was done by effectively adding large viscous damping factors of 90% of critical to the computer model used to calculate the experimental displacements to be imposed on the structure during the test. However, the Fourier amplitude spectrum of the Taft record in Fig. 2.12 shows that these higher modes would not be significantly excited by the earthquake accelerations since their natural frequencies lie above 10 Hz where the ground motions are negligibly small and, in addition,

these modes have relatively small participation factors. It should be noted that since only three modes can be determined from the test data, it is not possible to use these data for an inverse calculation to compute the stiffness and damping matrices uniquely for a six-degree-of-freedom model corresponding to the horizontal motions of each floor, unless a chain model is assumed.

3.5.1 Identification Results: Two-Mode Models

The results of applying the SI-SO system identification procedure independently to each of the displacement histories measured at each floor level are given in Table 3.1. In this application, the model response is computed from a modal model consisting of just the first two modes. It is seen from Table 3.1 that the period and damping for the fundamental mode are estimated as 0.553 sec and 1.2% of critical, respectively, and these estimates are remarkably consistent from floor to floor. This is again observed for the period of the second mode, which is estimated as 0.191 sec. However, the damping of the second mode shows some scatter about a mean value of 2.1% of critical damping. This scatter is probably due to the fact that the response of a mode is much less sensitive to changes in damping than to changes in its period, so that the damping is more difficult to estimate reliably, again confirming the observation made by Beck and Jennings [3]. The above difficulty is accentuated by a low signal-to-noise ratio when the second mode is estimated from the displacement records, since this mode makes a relatively small contribution to the displacement. Overall, the estimates from each floor and the small values of J, in Table 3.1, suggest that the structural displacement is approximated well by two classical modes of vibration, each giving structural motions in which all the floors move in phase.

The estimates in Table 3.2 are obtained by the application of SI-SO technique to the pseudo-velocity record at each floor, again using a two-mode model. The pseudo-velocity is the velocity calculated by the on-line computer (Fig. 2.2) using the central difference method and displacement history. Since the second mode has a relatively stronger signal in the velocity, the damping can be estimated more reliably in this case. Hence, much less variation in the damping estimates is observed for the second mode in Table 3.2 compared with Table 3.1. The estimates for the periods and dampings in Table 3.2 are again consistent from floor to floor and the values of J are small, showing the validity of an approximation of the pseudo-velocity by two classical modes of vibration.

Comparing Tables 3.1 and 3.2, it is seen that the estimates of the periods from the

two sources, measured displacements and pseudo-velocities, are identical, to within the precision specified in the tables, for both modes. The damping and effective participation factors for the fundamental mode are also identical, but there are small differences in the corresponding values for the second mode in Tables 3.1 and 3.2. Since the second-mode signal is stronger in the pseudo-velocities than in the measured displacements, a signal-to-noise argument suggests that the effective participation factors in Table 3.2 are the more reliable estimates.

The small values of the measure-of-fit J shown in Tables 3.1 and 3.2 indicate that a two-mode model is capable of reproducing the test displacement and velocity responses very well. This is again demonstrated by the time-history comparisons in Figs. 3.4 and 3.5. Figure 3.4 compares the velocities of the test structure and the optimal two-mode model at the roof, mid-height (floor 4) and floor 2 using the parameters estimated from the pseudo-velocity records (Table 3.2). The corresponding displacements are also compared in Fig. 3.5. Note the larger J-value for floor 2 in Table 3.2. This suggests high frequency components in the pseudo-velocity record at this floor which require a higher mode model approximation. A three-mode model is now examined.

3.5.2 Identification Results: Three-Mode Models

In this section, the SI-SO system identification method is applied to the pseudo-velocity and pseudo-acceleration responses independently, using a linear model consisting of three modes. The results are shown in Tables 3.3 and 3.4, respectively. The estimates for the first two modes are again consistent from floor to floor and they are essentially the same as the estimates for the two-mode model in Table 3.2. The estimates of the third-mode parameters from both the pseudo-velocity (Table 3.3) and pseudo-acceleration (Table 3.4) responses are also very nearly identical. The values of measure-of-fit J in Table 3.3 are smaller than the corresponding values in Table 3.2, where the pseudo-velocity response was used to estimate the parameters in both cases, as expected.

However, the surprising results in Tables 3.3 and 3.4 are:

(a) the third-mode damping is negative, and

(b) the measure-of-fit J is relatively large for the optimal three-mode model which would be expected to be capable of giving a very good match of the pseudo-accelerations since the higher modes beyond the first three were suppressed in the test (Table 3.4).

The response time-history comparisons from the test and the optimal three-mode model obtained from the pseudo-velocity records are shown in Figs. 3.6 and 3.7. The velocities of the test structure and the three-mode model are compared at the roof, mid-height and floor 2 in Fig. 3.6 and the corresponding displacement comparisons are given in Fig. 3.7. The roof pseudo-acceleration from the test and that calculated from the three-mode model identified from the roof pseudo-acceleration record are plotted in Fig. 3.8 for successive six-second segments at a larger time scale so that the nature of the high-frequency differences is easier to observe.

An examination of the Fourier amplitude spectrum of the roof pseudo-acceleration record (Fig. 3.9) shows that the 'third-mode' signal near a frequency of 10 Hz is much too large relative to the first- and second-mode signals. This anomaly is also demonstrated in Fig. 3.10 where the Fourier amplitude spectra for the roof pseudo-accelerations and the accelerations of the three-mode model identified from the pseudo-acceleration record at the roof are compared. Both spectra agree very well over a frequency range of the first two modes, but the third mode from the system identification procedure underestimates the apparent resonant amplitude from the test, despite the fact that the system identification procedure has tried to make the third-mode response of the model larger by selecting a negative damping.

It is concluded that this strong signal around 10 Hz is not entirely due to the excitation of the third mode by the Taft acceleration record but is partly due to the cumulative effect of feedback of control and measurement errors during the test, as discussed in Chapter 2. This unstable growth in the third mode produced the apparent negative damping when the system identification procedure tried to account for the strong signal solely from the earthquake excitation.

The equation of motion used to control the test structure is:

$$\mathbf{M}\ddot{\underset{\sim}{x}} + \mathbf{C}\dot{\underset{\sim}{x}} + \underset{\sim}{\mathrm{R}}(\underset{\sim}{x}) = -\mathbf{M}\ddot{z}(t)\,\underset{\sim}{1} \quad , \tag{3.30}$$

where C represents the nominal damping used in the on-line computer algorithm. But the linear model used in the system identification procedure can be represented by the equation:

$$\mathbf{M}\ddot{\underset{\sim}{x}} + \mathbf{D}\dot{\underset{\sim}{x}} + \mathbf{K}\underset{\sim}{x} = -\mathbf{M}\ddot{z}(t)\,\underset{\sim}{1} \quad . \tag{3.31}$$

If the cumulative effect of feedback of the measurement and control errors in the pseudo-

dynamic test is approximated by an equivalent viscous damping, then D in Eq. 3.31 represents the total viscous damping which is the sum of the viscous damping from the computer algorithm (C), the structural damping due to some hysteretic action and the apparent damping due to feedback of experimental errors.

From Table 3.5, the algorithmic dampings used in the pseudo-dynamic test for the first three modes are 0.35%, 0.35% and 2.00%, respectively. Hence, a negative damping of -0.05% for the third mode from the linear model of the system identification method suggests that the experimental errors introduced an equivalent negative viscous damping in the third mode which is greater than 2% in magnitude. This phenomenon of adding energy into the third mode explains why the third-mode signal appears very strong in the Fourier amplitude spectrum in Fig. 3.9.

3.5.3 Conclusions

(a) For similar amplitudes to those in the elastic test (peak relative acceleration and displacement of 30% g and 1.4 cm respectively at the roof), a linear model based on just two classical modes should give an excellent approximation to the real dynamic response of the structure.

(b) At these amplitude levels, the overall equivalent viscous damping factors for the first two modes are 1.2% and 2.1% of critical. The damping of the fundamental mode is consistent with the value of 1.25% reported for a pseudo-dynamic free-vibration test performed after the elastic test [8]. Part of the damping was artificially introduced as numerical viscous damping in the computer model used to produce the experimental displacements (Table 3.5). The cumulative effect of feedback of control and measurement errors also contributed some damping.

Assuming the latter damping is small for the lower modes, especially the first two modes, the energy dissipated by the structure itself produced equivalent viscous damping factors of about 0.9% and 1.8%, respectively, for the first and second modes. These low values of damping, compared with the values of 3% to 8% from the earthquake response of tall buildings in the field [9], are most likely due to the absence of both energy dissipation by nonstructural components and by radiation damping, the latter because of the quasi-static nature of the test.

(c) The feedback of control and measurement errors into the computer model used to produce the experimental displacements in the elastic test produced a cumulative error

of large amplitude in the pseudo-acceleration at the frequency of the third mode. This addition of energy into the test structure is further demonstrated by an equivalent negative viscous damping of at least 2% estimated for the feedback effect in the third mode. However, these errors have an insignificant effect on the displacements and pseudo-velocities, where the high-frequency content is greatly reduced. Chapter 4 deals with the estimation of the actual structural damping and the effect of the experimental errors on the response of the test structure.

REFERENCES

[1] Sinha, N.K. and Kuszta, B., *Modeling and Identification of Dynamic Systems*, Van Nostrand Reinhold Company Inc., New York, 1983.

[2] Beck, J.L., "Determining Models of Structures from Earthquake Records," Report No. EERL 78–01, Earthquake Engineering Research Laboratory, California Institute of Technology, Pasadena, California, June, 1978.

[3] Beck, J.L. and Jennings, P.C., "Structural Identification Using Linear Models and Earthquake Records," *Earthquake Engineering and Structural Dynamics*, Vol. 8, 145–160, 1980.

[4] Lectures by Professor J.L. Beck on Engineering Mathematical Principles, California Institute of Technology, Pasadena, California, 1983–84.

[5] Nigam, N.C. and Jennings, P.C., "Calculation of Response Spectra from Strong-Motion Earthquake Records," *Bulletin of Seismological Society of America*, Vol. 59, 909–922, 1969.

[6] Beck, J.L. and Jayakumar, P., "Analysis of Elastic Pseudo-Dynamic Test Data from a Full-Scale Steel Structure Using System Identification," *Proceedings of the 6th Joint Technical Coordinating Committee Meeting*, U.S.—Japan Cooperative Research Program Utilizing Large-Scale Testing Facilities, Maui, Hawaii, June, 1985.

[7] Beck, J.L. and Jayakumar, P., "Application of System Identification to Pseudo-Dynamic Test Data from a Full-Scale Six-Story Steel Structure," *Proceedings of the International Conference on Vibration Problems in Engineering*, Xian, China, June, 1986.

[8] Midorikawa, M., et al., "Preliminary Test in Phase II," *Proceedings of the 5th Joint Technical Coordinating Committee Meeting*, U.S.—Japan Cooperative Research Program Utilizing Large-Scale Testing Facilities, Tsukuba, Japan, February, 1984.

[9] Beck, J.L., "System Identification Applied to Strong Motion Records from Structures," *Earthquake Ground Motion and Its Effects on Structures*, S.K. Datta (ed.), ASME, AMD–Vol. 53, New York, 1982.

[10] Eykhoff, P., *System Identification*, John Wiley & Sons, New York, 1977.

Floor	Mode 1			Mode 2			J
	Period (sec)	Damping (%)	Effective Participation Factor	Period (sec)	Damping (%)	Effective Participation Factor	(%)
Roof	0.553	1.2	1.39	0.191	2.3	-0.57	1.2
6	0.553	1.2	1.22	0.191	2.6	-0.25	0.57
5	0.553	1.2	1.00	0.192	1.6	0.13	0.51
4	0.553	1.2	0.77	0.191	1.9	0.39	0.35
3	0.553	1.2	0.53	0.191	2.0	0.47	0.48
2	0.553	1.2	0.30	0.191	2.1	0.37	1.3

Table 3.1 Modal Parameters Estimated from the Measured Displacement Records Using a Two-Mode Model and the SI-SO Technique [6]

Floor	Mode 1			Mode 2			J
	Period (sec)	Damping (%)	Effective Participation Factor	Period (sec)	Damping (%)	Effective Participation Factor	(%)
Roof	0.553	1.2	1.39	0.191	2.2	-0.53	1.3
6	0.553	1.2	1.22	0.191	2.2	-0.21	0.34
5	0.553	1.2	1.00	0.191	2.0	0.16	2.8
4	0.553	1.2	0.77	0.191	2.1	0.42	0.93
3	0.553	1.2	0.53	0.191	2.1	0.48	4.3
2	0.553	1.2	0.30	0.191	2.1	0.36	18.7

Table 3.2 Modal Parameters Estimated from the Pseudo-Velocity Records Using a Two-Mode Model and the SI-SO Technique [6]

Floor	Mode 1			Mode 2			Mode 3			J
	$\hat{T}$ (sec)	$\hat{\varsigma}$ (%)	$\hat{p}$	$\hat{T}$ (sec)	$\hat{\varsigma}$ (%)	$\hat{p}$	$\hat{T}$ (sec)	$\hat{\varsigma}$ (%)	$\hat{p}$	(%)
Roof	0.553	1.2	1.39	0.191	2.2	-0.53	0.106	-0.05	0.03	0.75
6	0.553	1.2	1.22	0.191	2.2	-0.21	0.106	-0.04	-0.01	0.24
5	0.553	1.2	1.00	0.191	2.0	0.16	0.106	-0.05	-0.05	1.4
4	0.553	1.2	0.77	0.191	2.1	0.42	0.106	-0.06	-0.02	0.62
3	0.553	1.2	0.53	0.191	2.1	0.47	0.106	-0.05	0.02	2.4
2	0.553	1.2	0.30	0.191	2.1	0.36	0.106	-0.05	0.04	9.5

Table 3.3 Modal Parameters Estimated from the Pseudo-Velocity Records Using a Three-Mode Model and the SI-SO Technique [7]

Floor	Mode 1			Mode 2			Mode 3			J
	$\hat{T}$ (sec)	$\hat{\varsigma}$ (%)	$\hat{p}$	$\hat{T}$ (sec)	$\hat{\varsigma}$ (%)	$\hat{p}$	$\hat{T}$ (sec)	$\hat{\varsigma}$ (%)	$\hat{p}$	(%)
Roof	0.553	1.2	1.39	0.191	2.2	-0.53	0.106	-0.05	0.03	11.2
6	0.553	1.2	1.23	0.191	2.2	-0.21	0.106	-0.03	-0.01	5.0
5	0.553	1.3	1.01	0.191	2.2	0.17	0.106	-0.05	-0.04	21.0
4	0.553	1.3	0.78	0.191	2.1	0.43	0.106	-0.05	-0.02	8.0
3	0.553	1.2	0.53	0.191	2.1	0.48	0.106	-0.04	0.02	19.6
2	0.553	1.2	0.30	0.191	2.1	0.36	0.106	-0.05	0.04	35.8

Table 3.4 Modal Parameters Estimated from the Pseudo-Acceleration Records Using a Three-Mode Model and the SI-SO Technique [7]

Test	Critical Damping Ratio (%)						Comments
	Mode 1	2	3	4	5	6	
Preliminary Free and Forced Vibration Tests	0.354	0.311	—	—	—	—	Calculated from Test Response
Elastic Pseudo-Dynamic Test	0.35	0.35	2.00	90.0	90.0	90.0	Selection Based on Vibration Test Values and Stability Considerations

Table 3.5 Damping Values for Tests in Phase II [8]

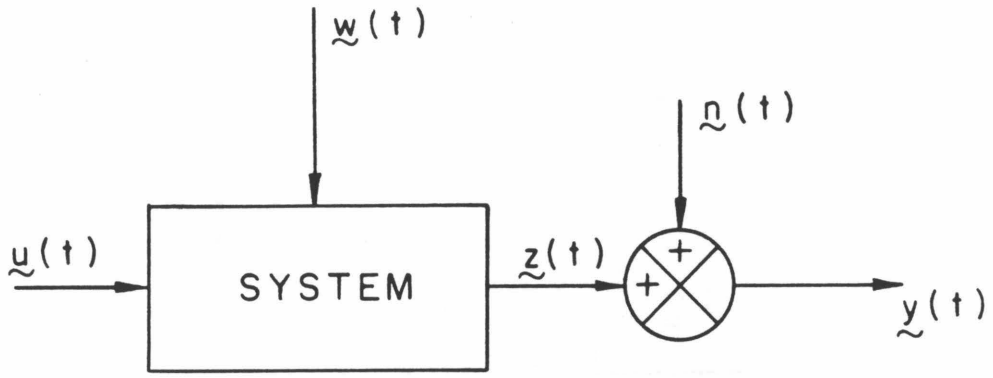

Fig. 3.1 Block Diagram Illustrating the System Identification Method [1]

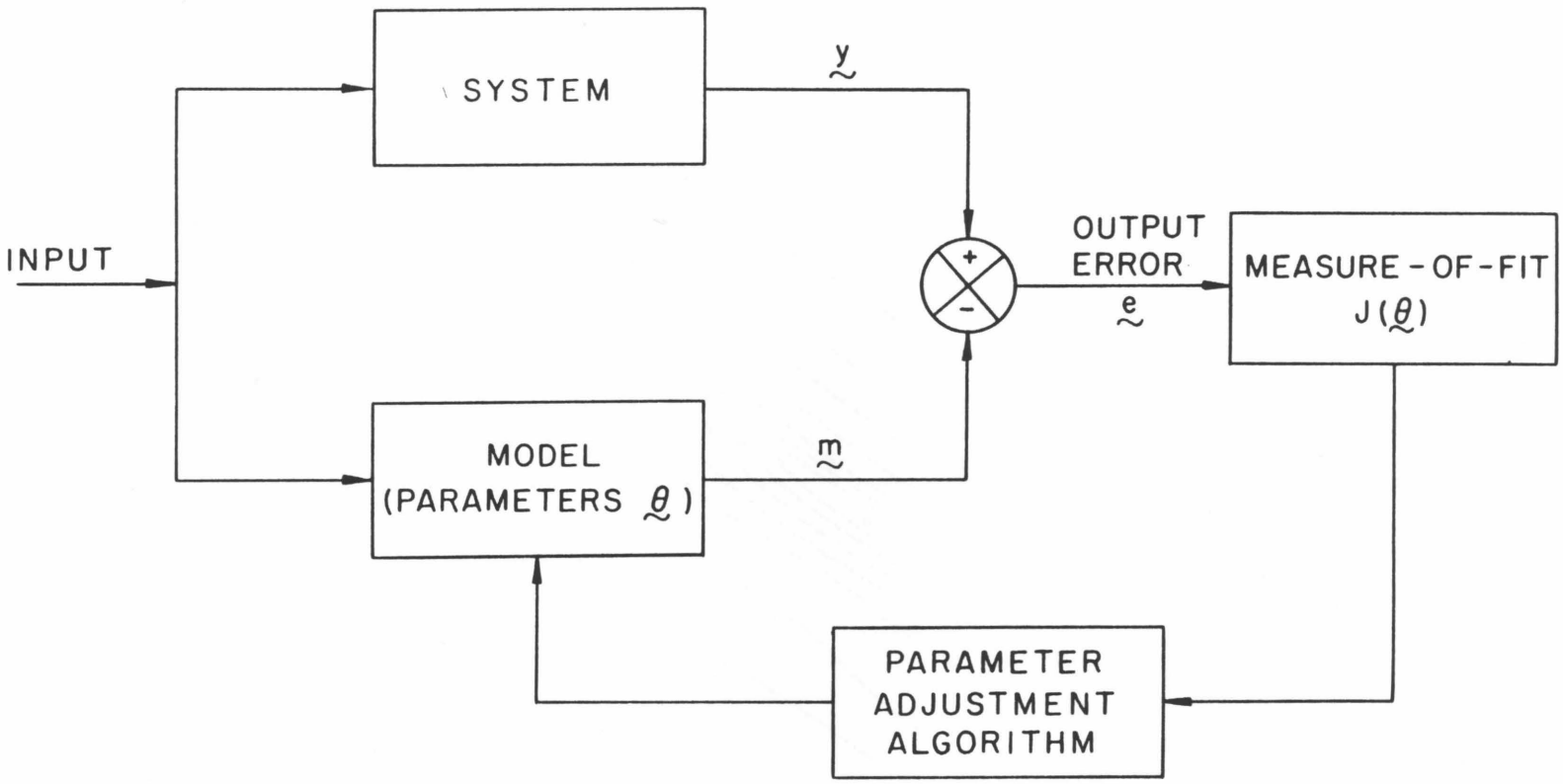

Fig. 3.2 Block Diagram Illustrating the Output-Error Method

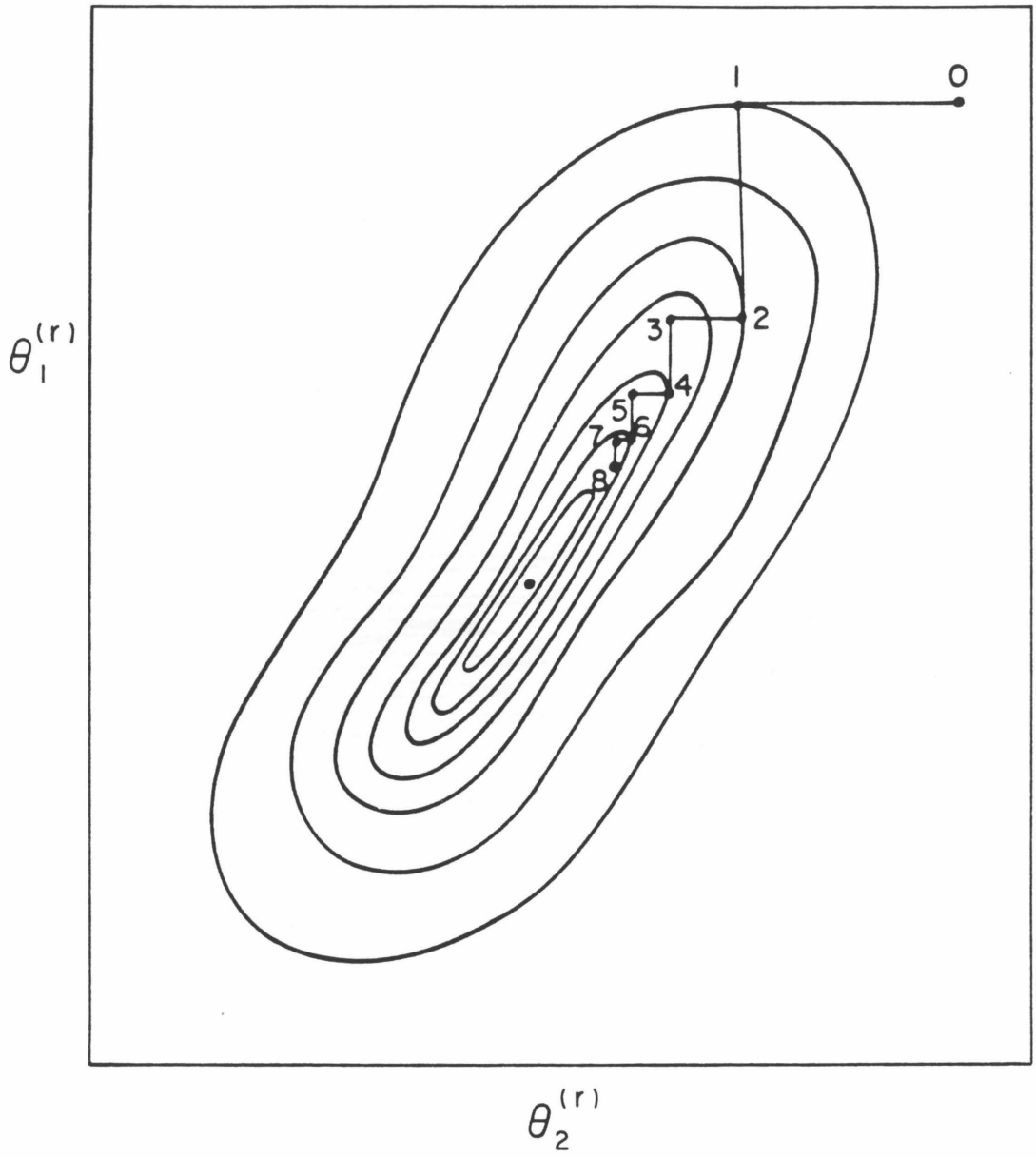

Fig. 3.3 Schematic Diagram of Contours of $J_r^*(\theta_1^{(r)}, \theta_2^{(r)})$ Showing a Path of Convergence [2]

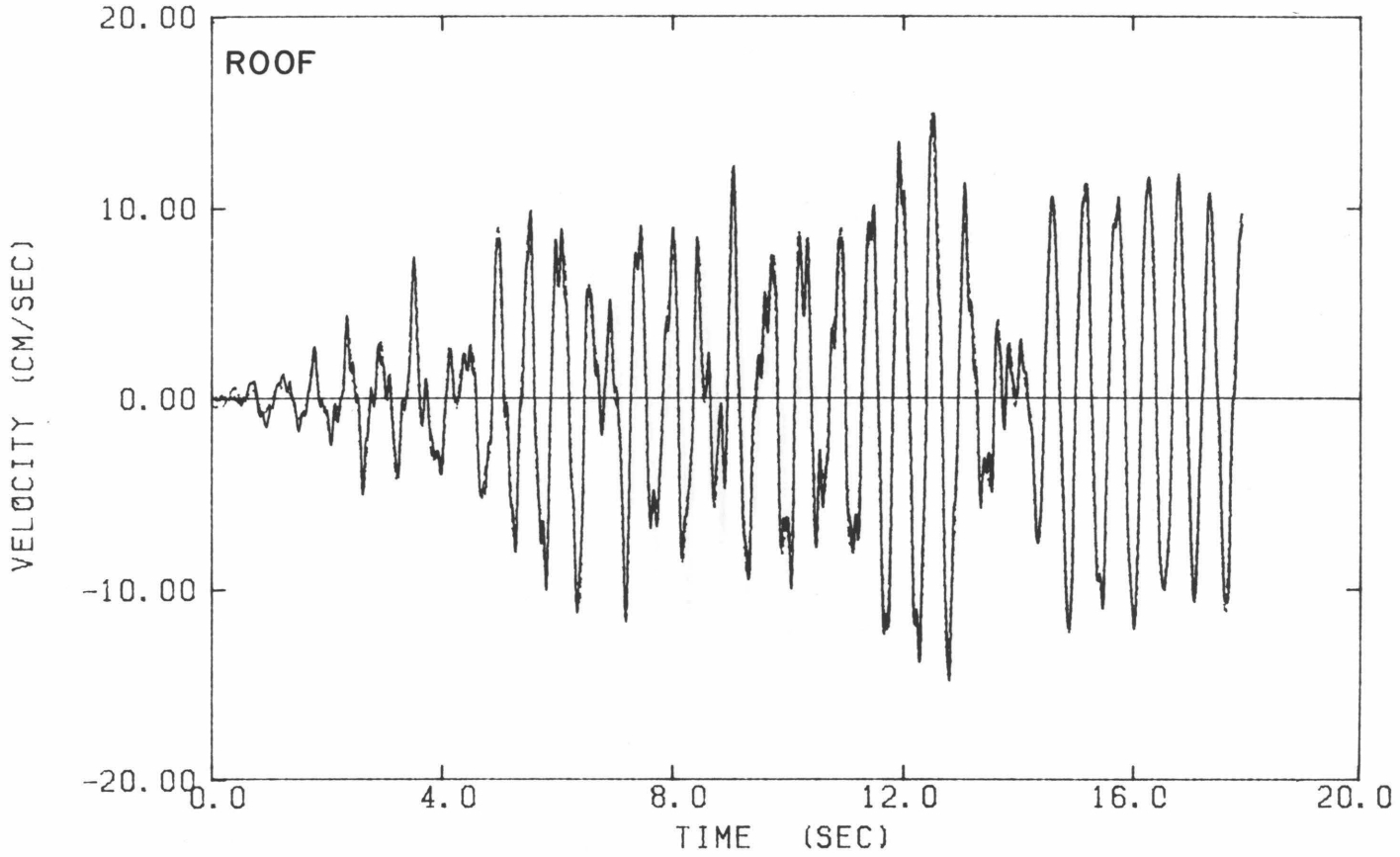

Fig. 3.4 Pseudo-Velocities of the Test Structure (——) and Calculated Velocities of a Two-Mode Model (- - -), at the Roof, Mid-Height and Floor 2;
Model Identified from Velocity Records

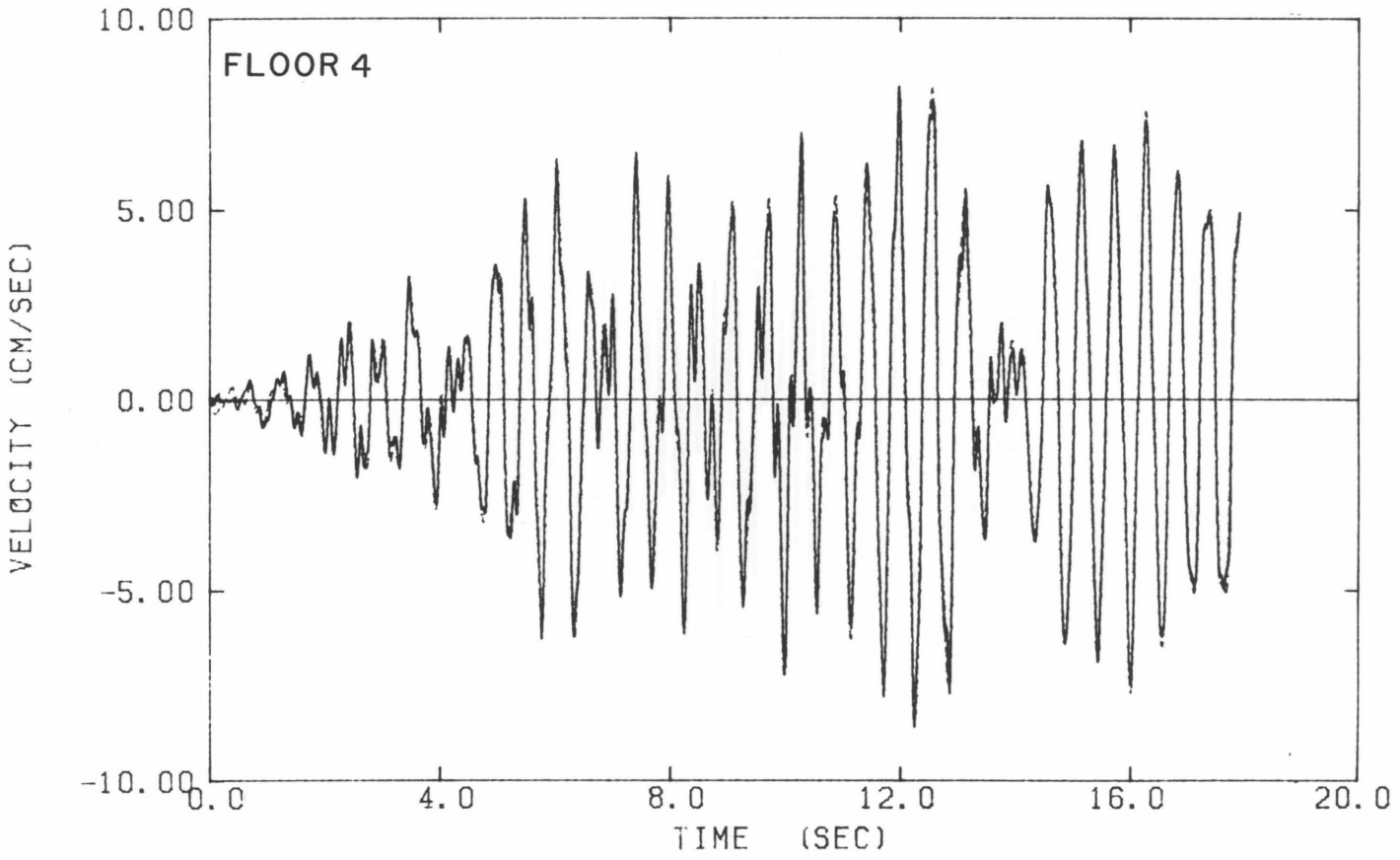

Fig. 3.4 (continued)
Pseudo-Velocities of the Test Structure (——) and Calculated Velocities of a Two-Mode Model (- - -), at the Roof, Mid-Height and Floor 2;
Model Identified from Velocity Records

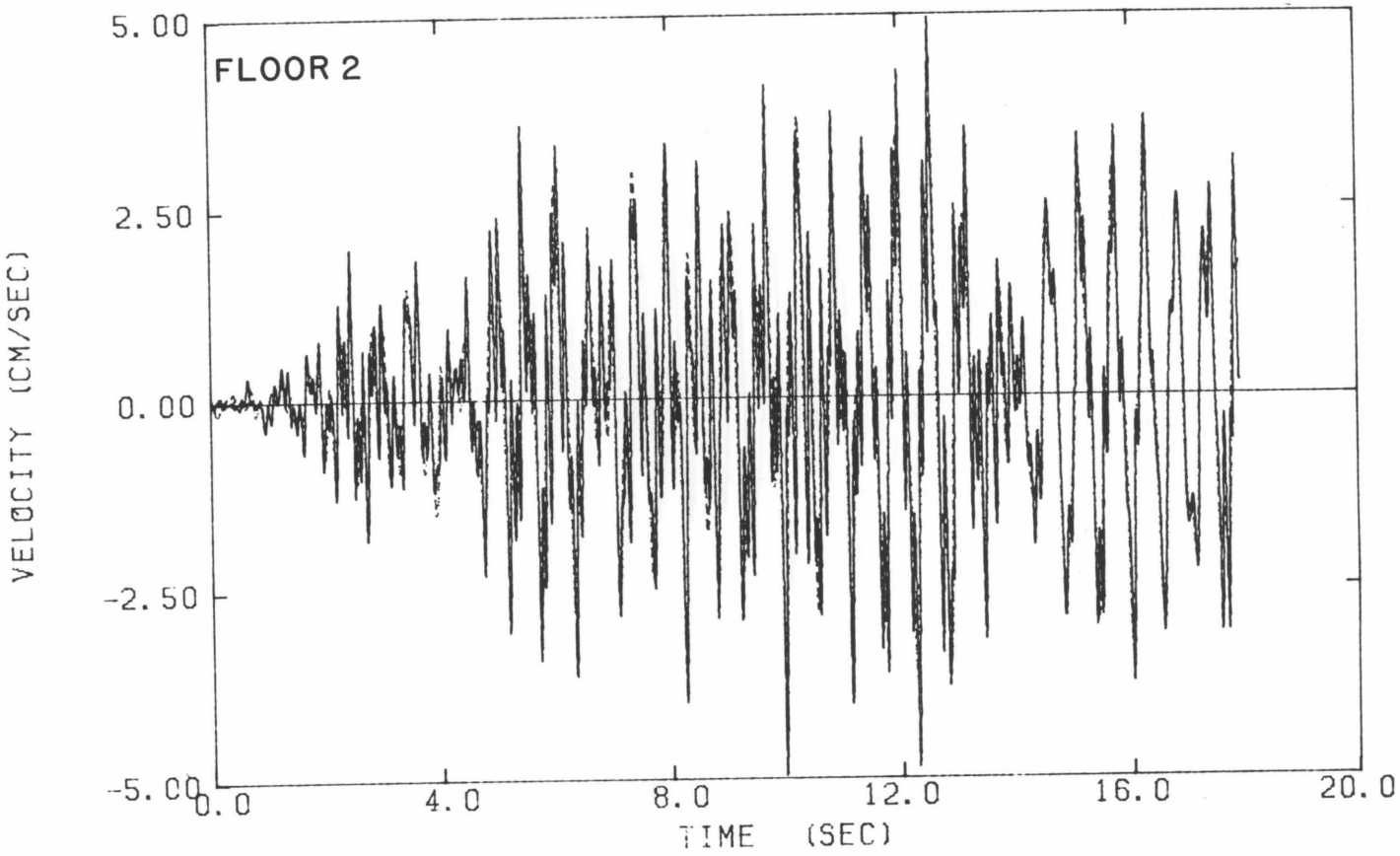

Fig. 3.4 (continued)
Pseudo-Velocities of the Test Structure (——) and Calculated Velocities of a Two-Mode Model (- - -), at the Roof, Mid-Height and Floor 2;
Model Identified from Velocity Records

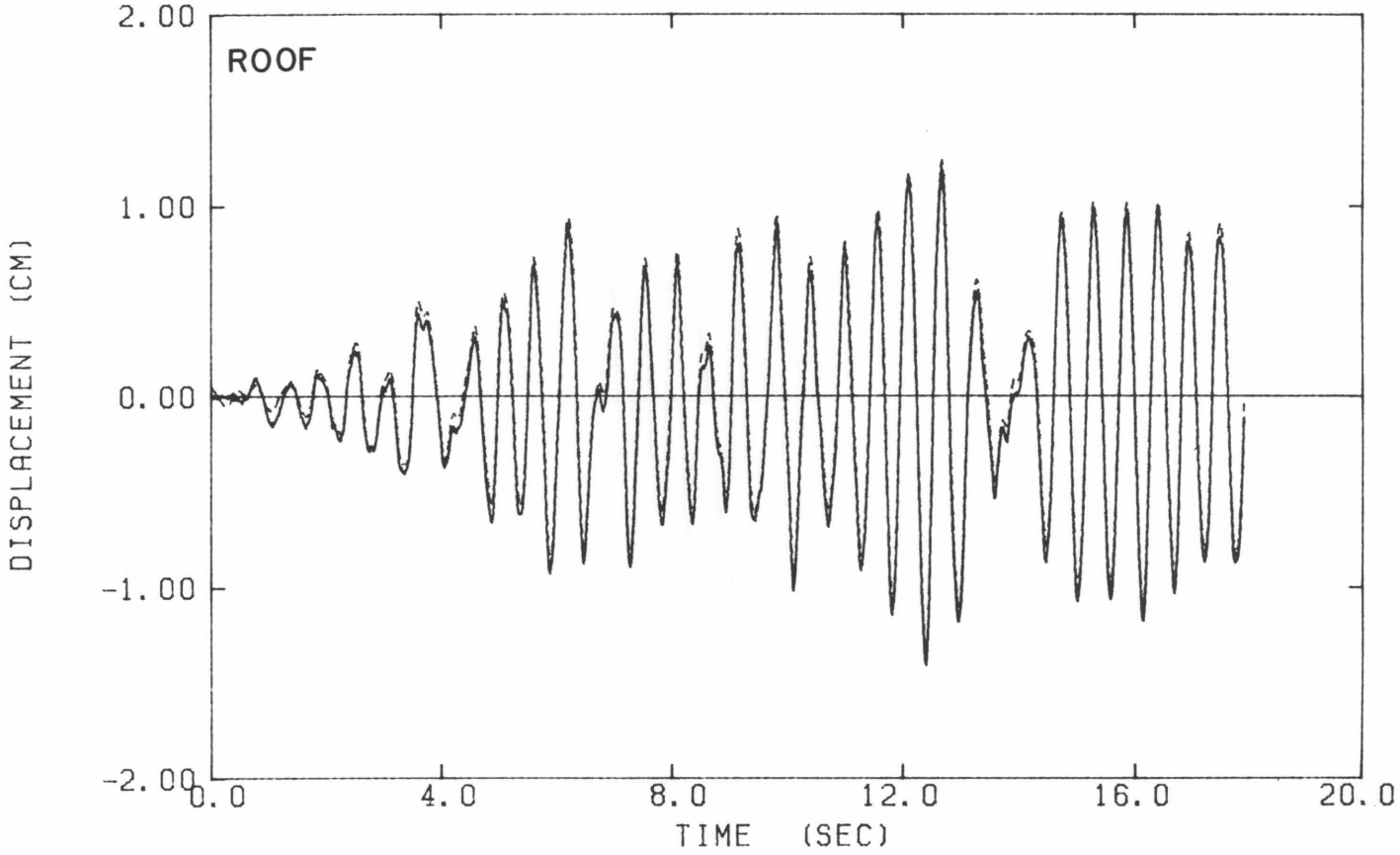

Fig. 3.5 Measured Displacements of the Test Structure (——) and Calculated Displacements for the Same Two-Mode Model as in Fig. 3.4 (- - -), at the Roof, Mid-Height and Floor 2

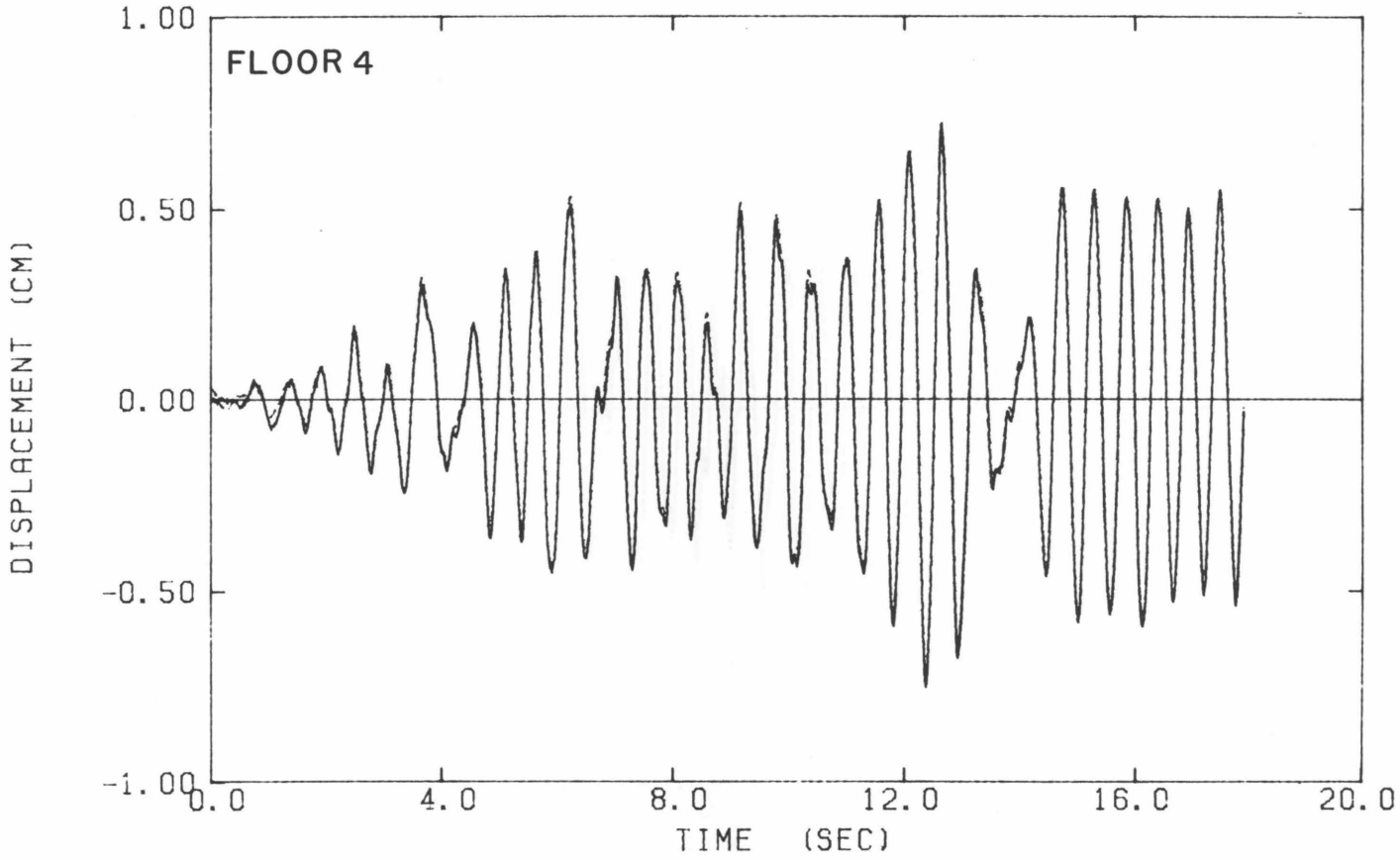

Fig. 3.5 (continued)
Measured Displacements of the Test Structure (——) and Calculated Displacements for the Same Two-Mode Model as in Fig. 3.4 (- - -), at the Roof, Mid-Height and Floor 2

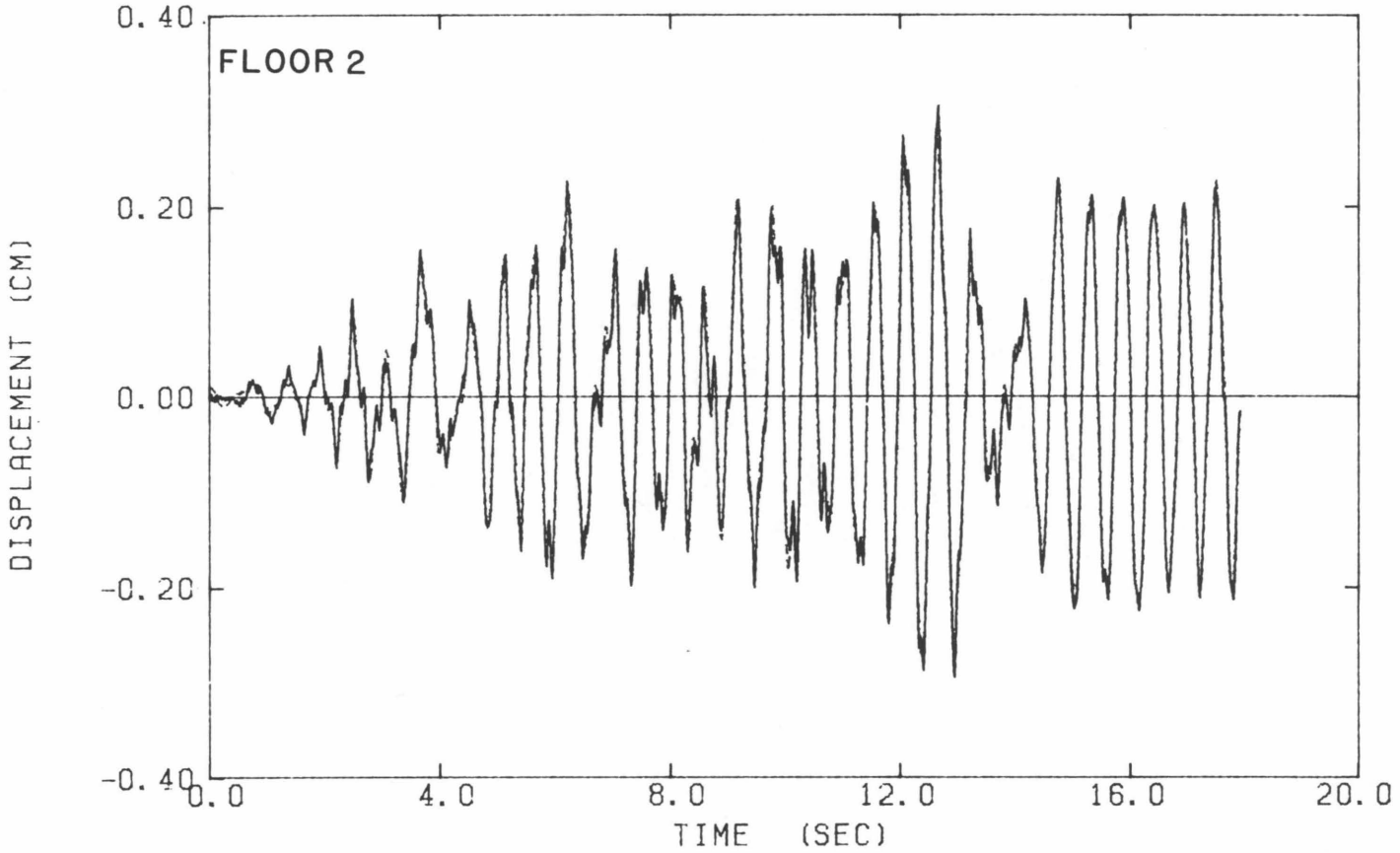

Fig. 3.5 (continued)
Measured Displacements of the Test Structure (——) and Calculated Displacements for the Same Two-Mode Model as in Fig. 3.4 (- - -), at the Roof, Mid-Height and Floor 2

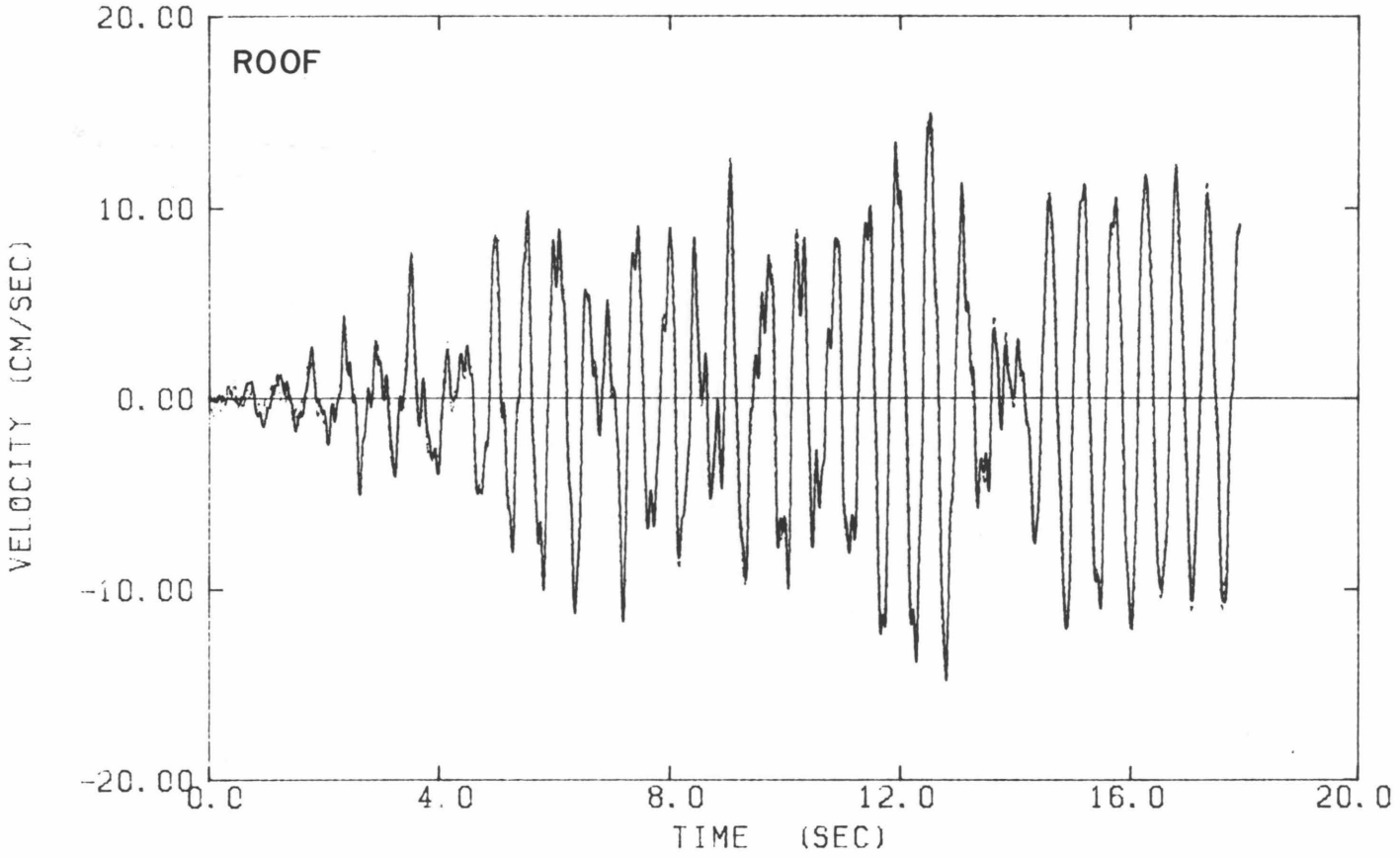

Fig. 3.6 Pseudo-Velocities of the Test Structure (——) and Calculated Velocities of a Three-Mode Model (- - -), at the Roof, Mid-Height and Floor 2; Model Identified from Velocity Records

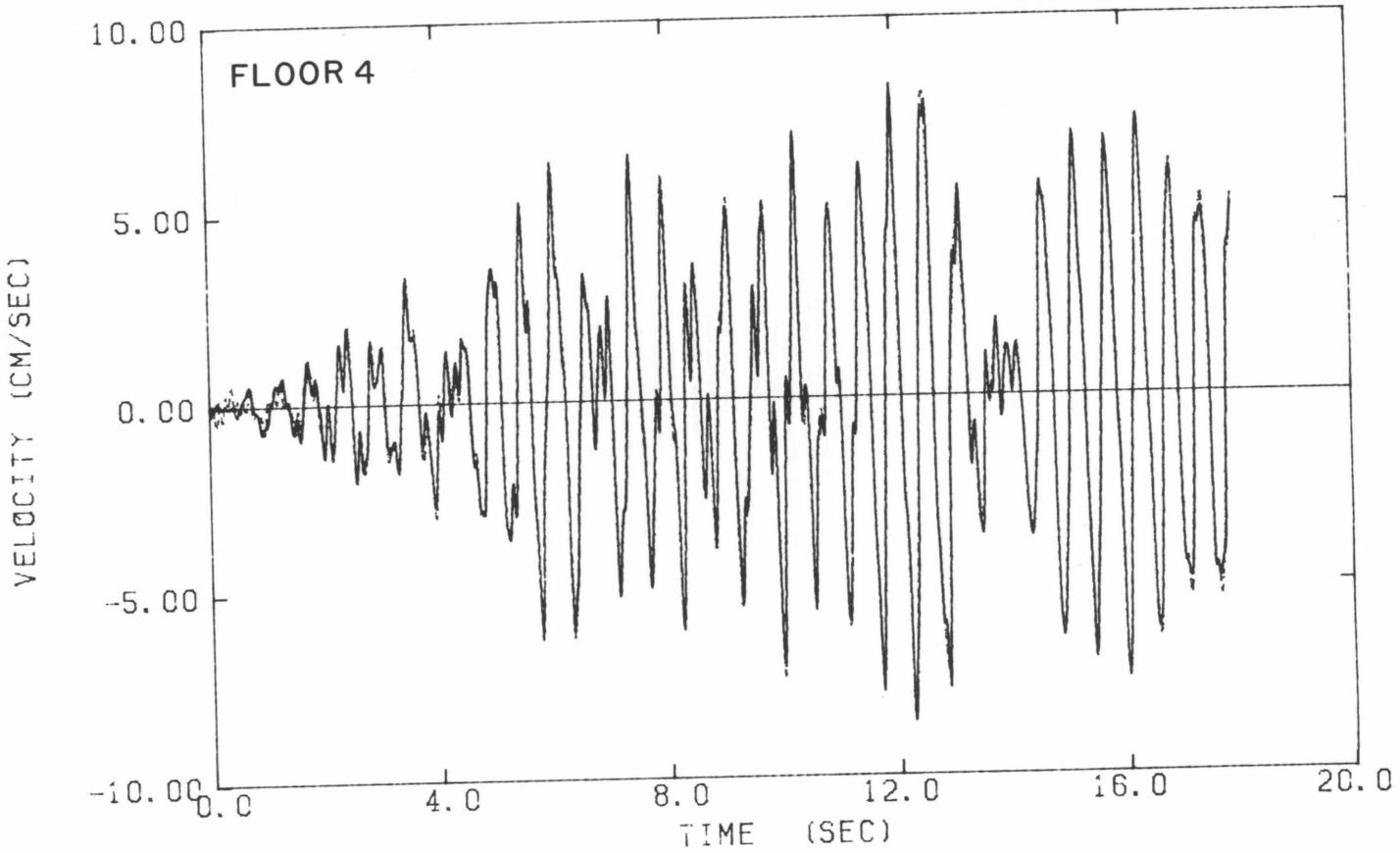

Fig. 3.6 (continued)
Pseudo-Velocities of the Test Structure (——) and Calculated Velocities of a Three-Mode Model (- - -), at the Roof, Mid-Height and Floor 2;
Model Identified from Velocity Records

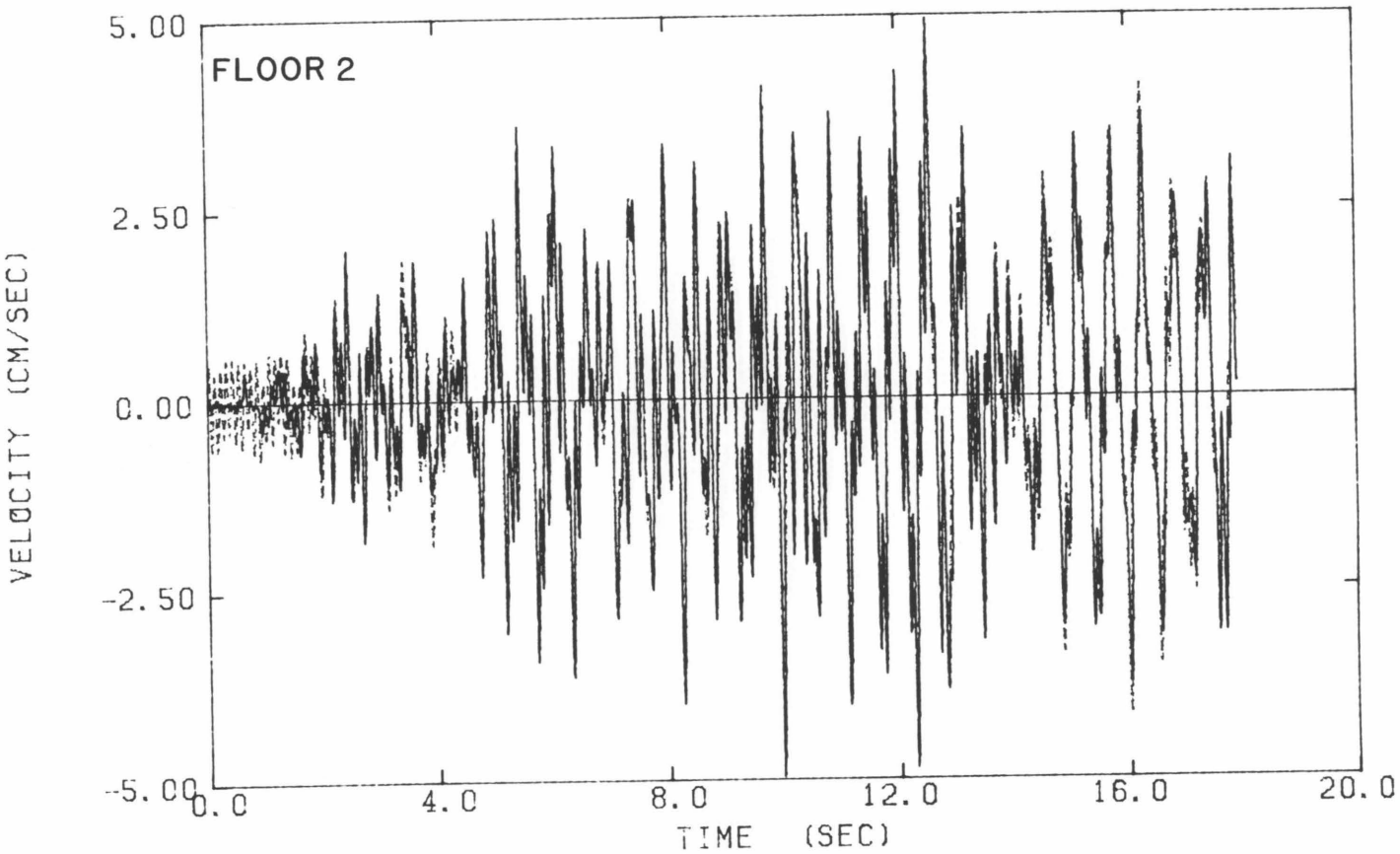

Fig. 3.6 (continued)
Pseudo-Velocities of the Test Structure (——) and Calculated Velocities of a Three-Mode Model (- - -), at the Roof, Mid-Height and Floor 2;
Model Identified from Velocity Records

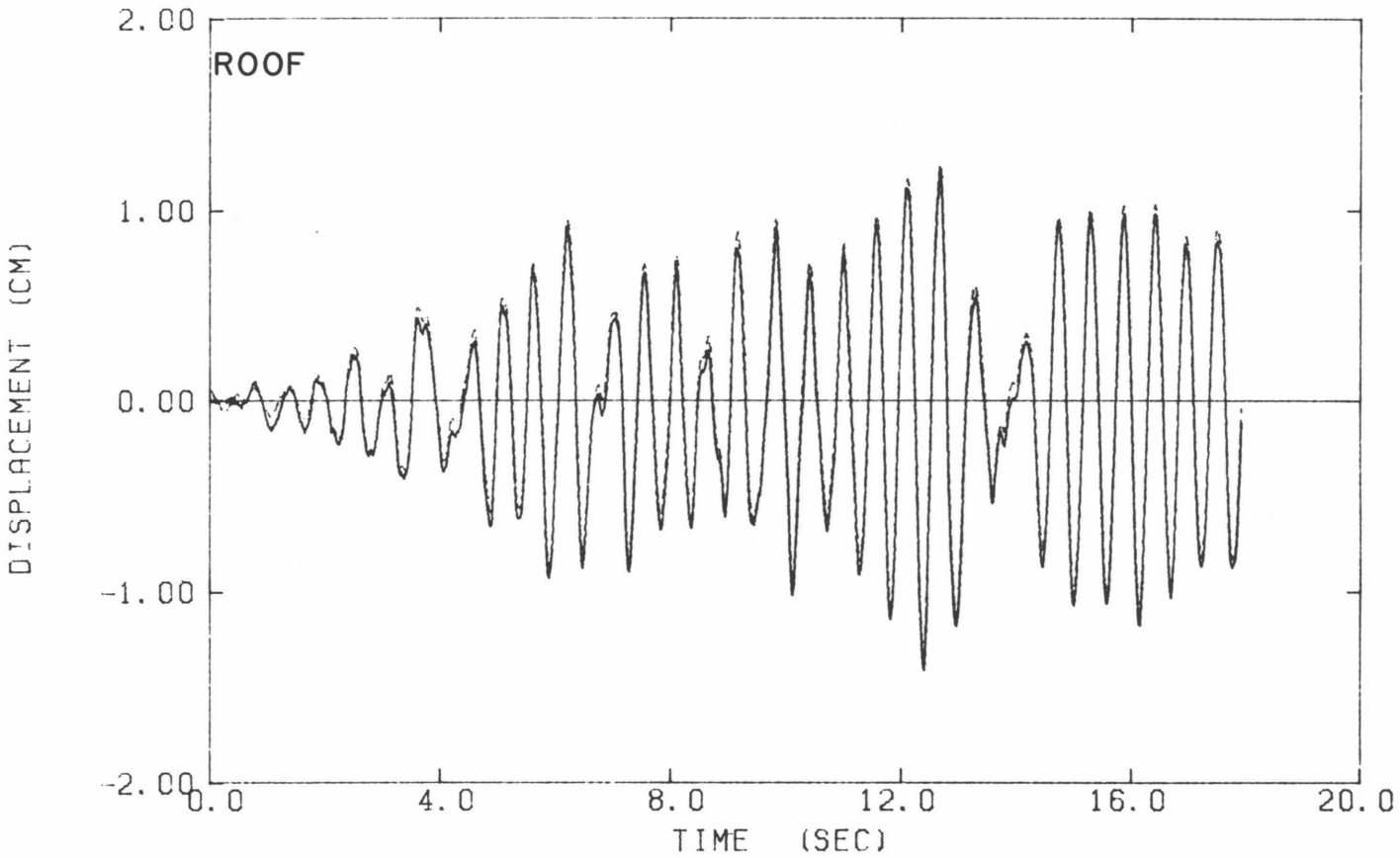

Fig. 3.7 Measured Displacements of the Test Structure (——) and Calculated Displacements for the Same Three-Mode Model as in Fig. 3.6 (- - -), at the Roof, Mid-Height and Floor 2

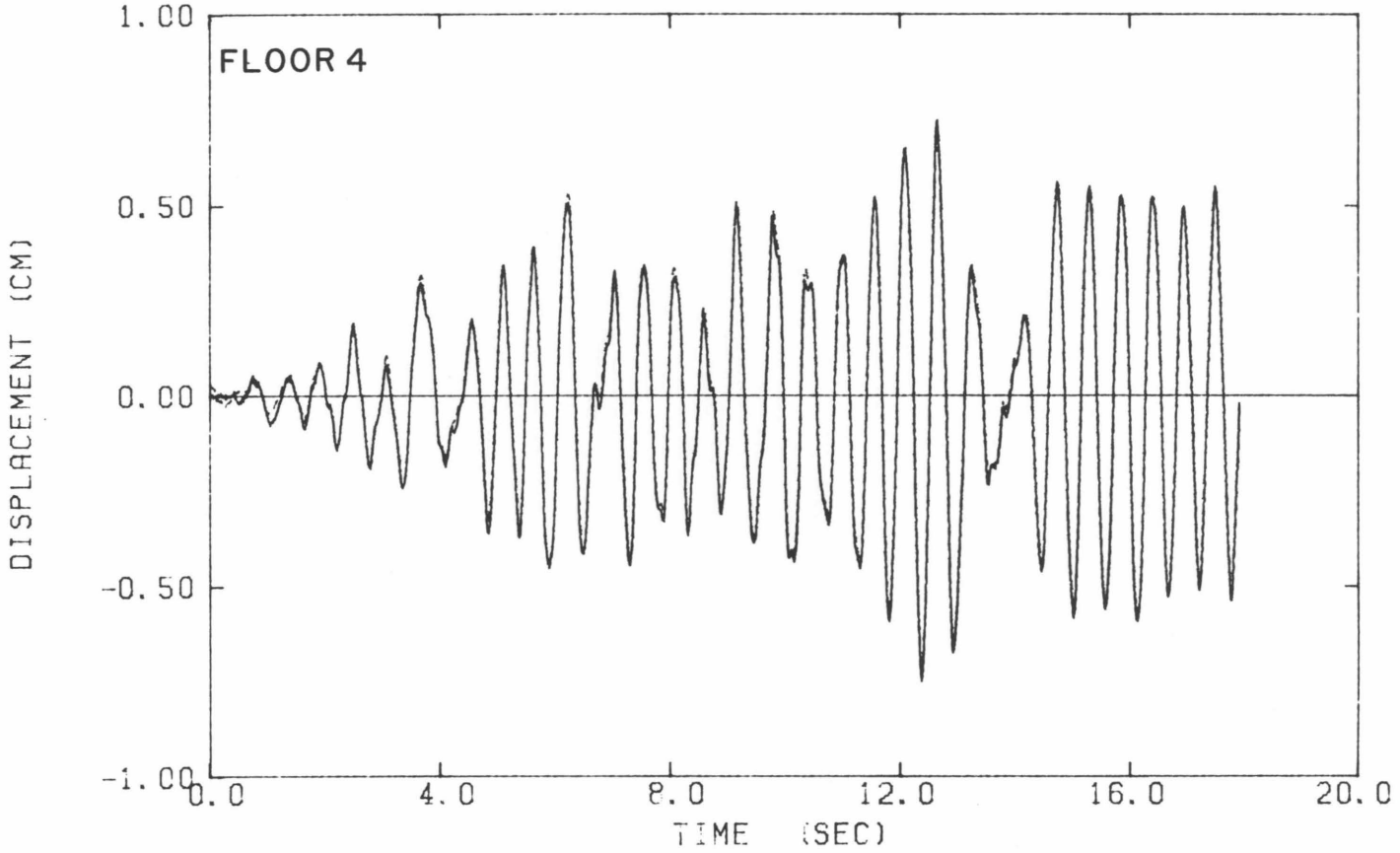

Fig. 3.7 (continued)
Measured Displacements of the Test Structure (——) and Calculated Displacements for the Same Three-Mode Model as in Fig. 3.6 (- - -), at the Roof, Mid-Height and Floor 2

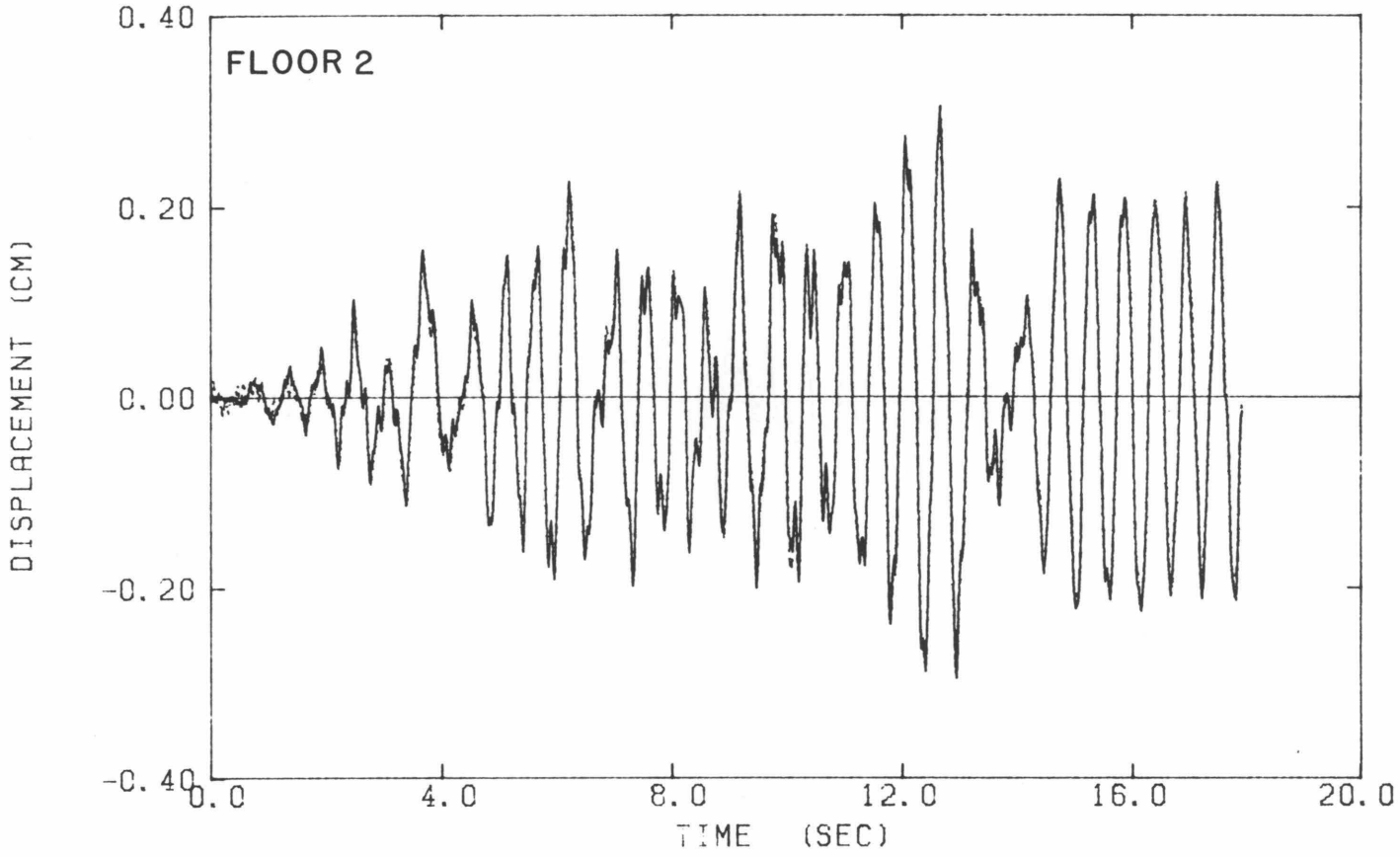

Fig. 3.7 (continued)
Measured Displacements of the Test Structure (——) and Calculated Displacements for the Same Three-Mode Model as in Fig. 3.6 (- - -), at the Roof, Mid-Height and Floor 2

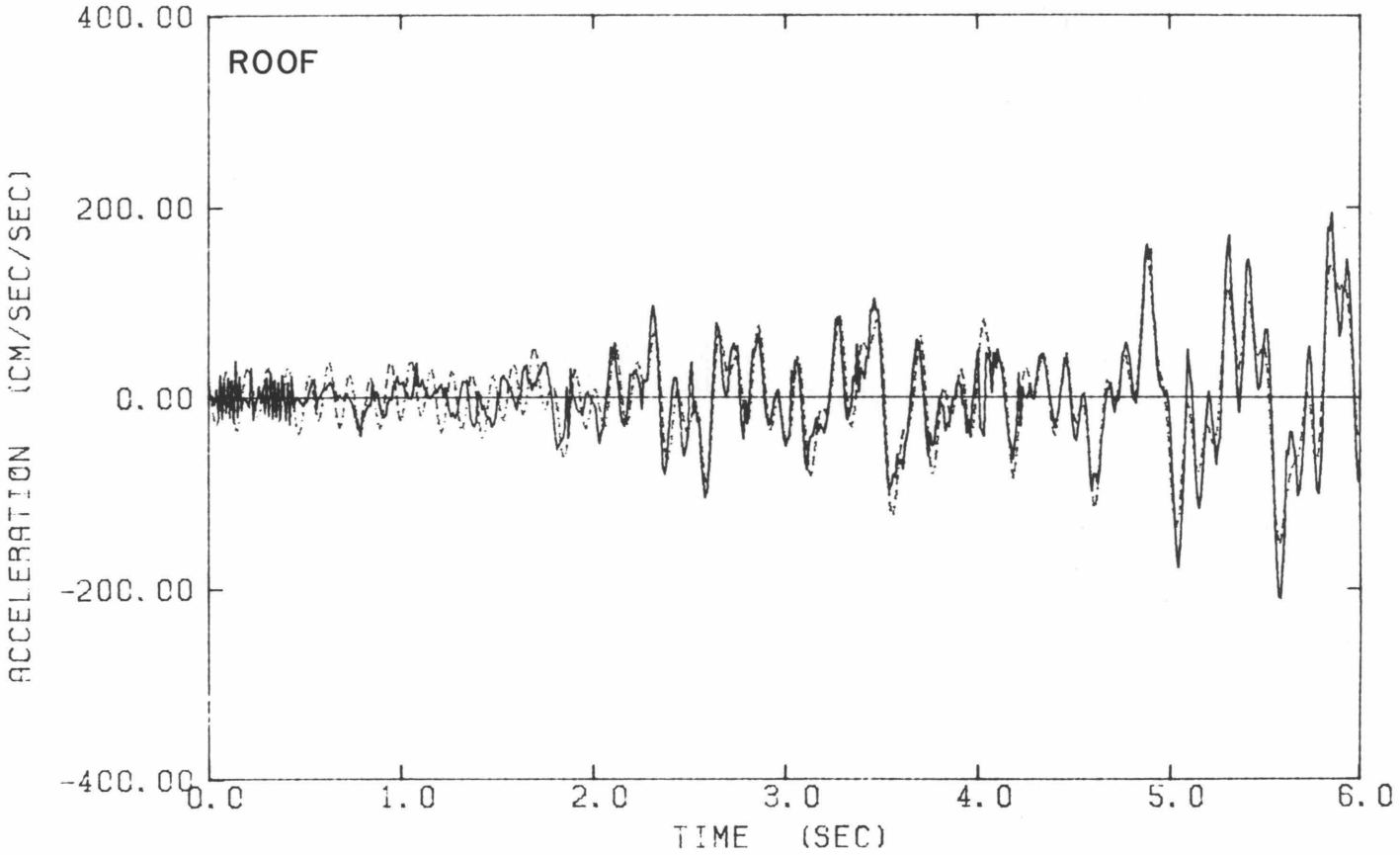

Fig. 3.8 Six-Second Segments of the Pseudo-Acceleration (——) and Calculated Acceleration Using a Three-Mode Model Identified from Pseudo-Acceleration Record (- - -), at Roof

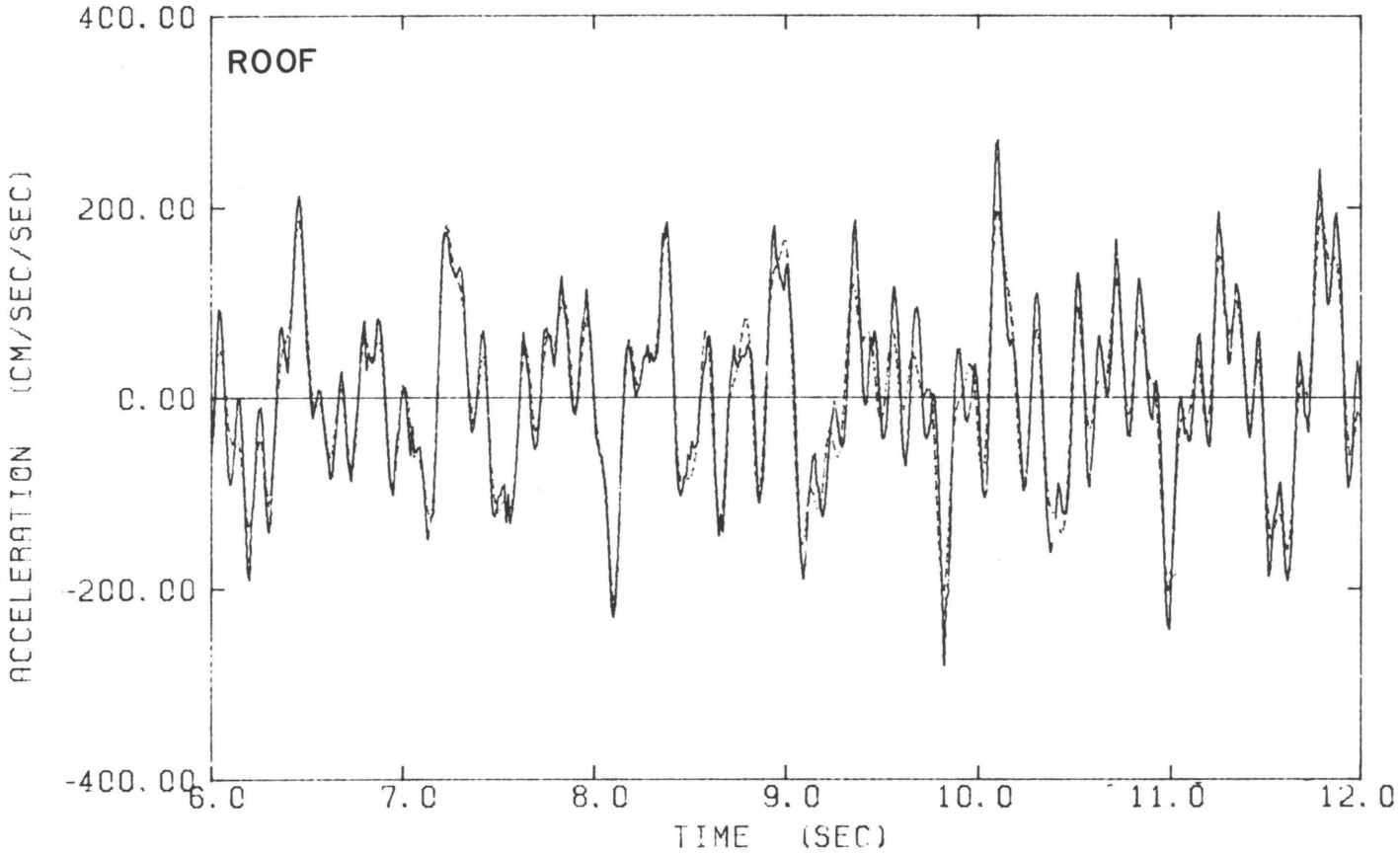

Fig. 3.8 (continued)
Six-Second Segments of the Pseudo-Acceleration (——) and Calculated Acceleration Using a Three-Mode Model Identified from Pseudo-Acceleration Record (- - -), at Roof

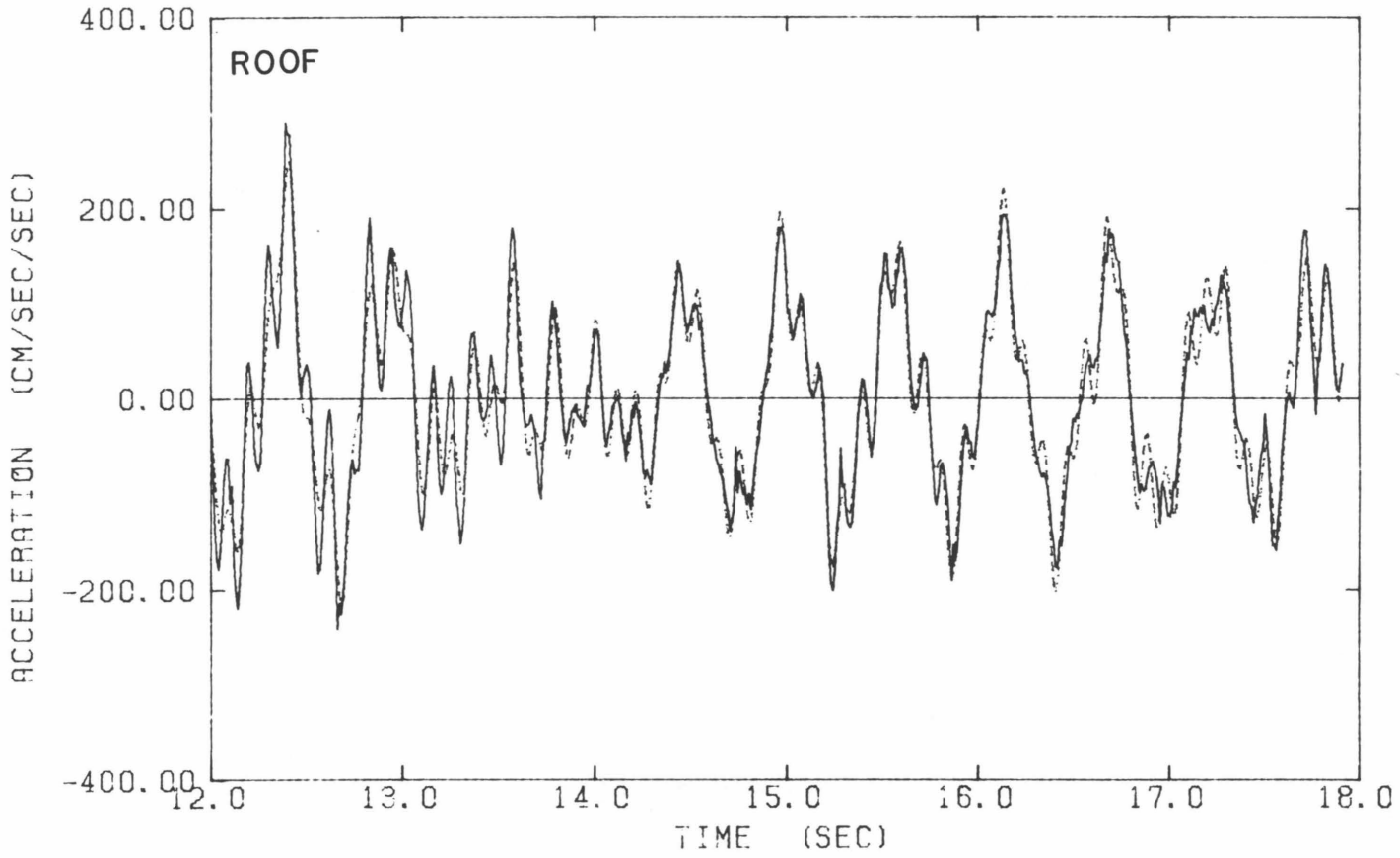

Fig. 3.8 (continued)
Six-Second Segments of the Pseudo-Acceleration (——) and Calculated Acceleration Using a Three-Mode Model Identified from Pseudo-Acceleration Record (- - -), at Roof

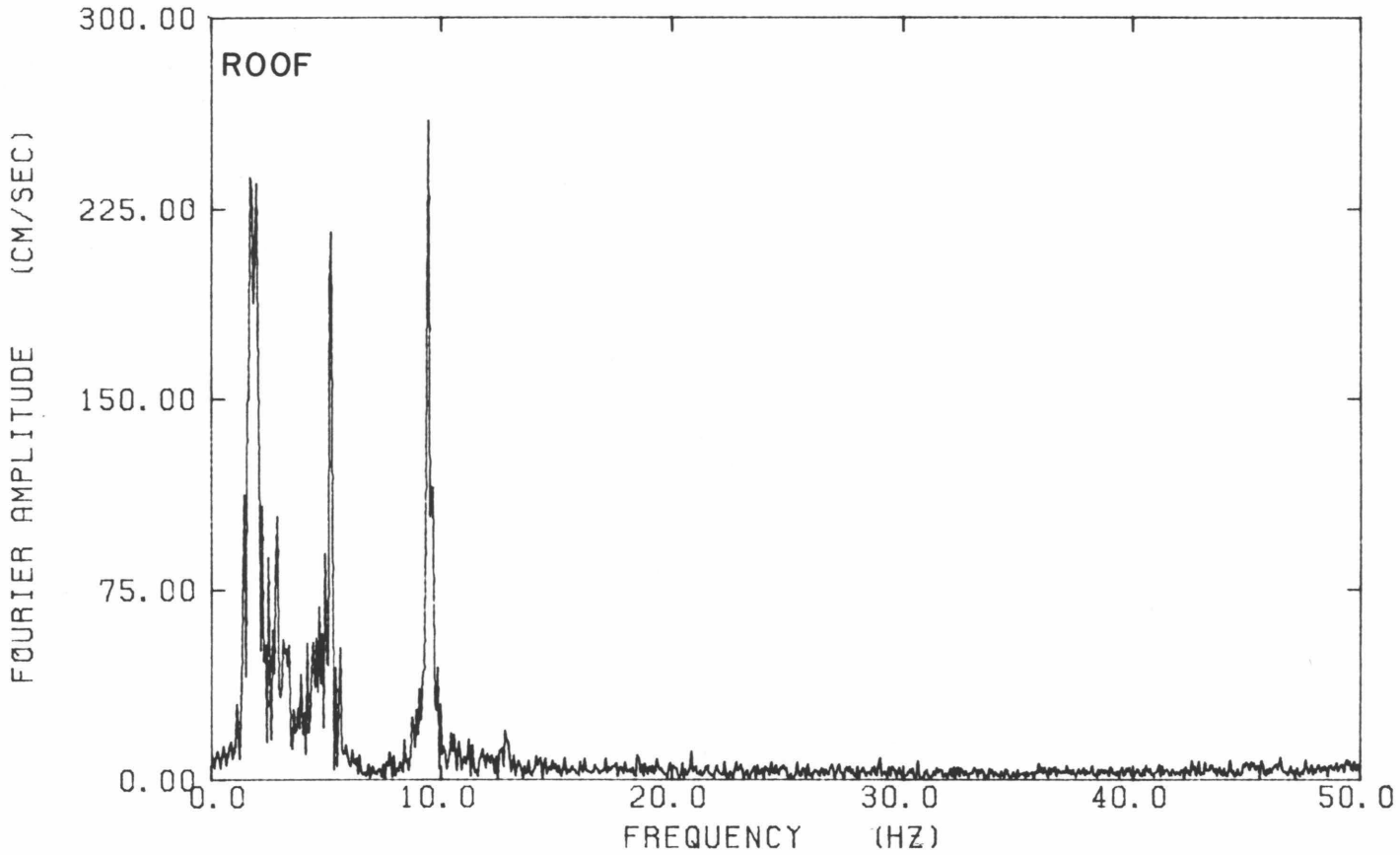

Fig. 3.9 Fourier Amplitude Spectrum of Pseudo-Accelerations at Roof

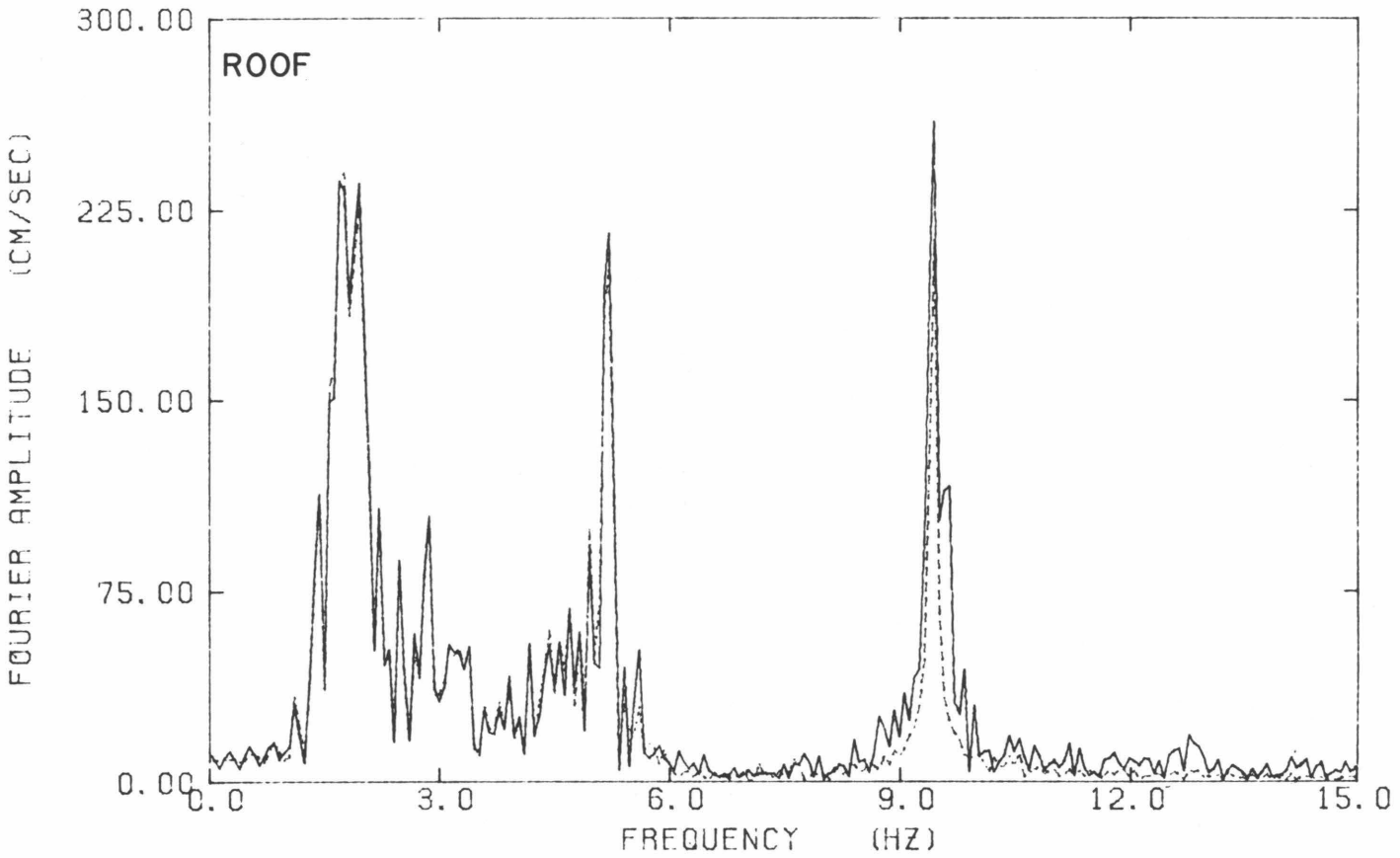

Fig. 3.10 Fourier Amplitude Spectra of Pseudo-Acceleration (——) and Calculated Acceleration Using the Same Three-Mode Model as in Fig. 3.8 (- - -), at Roof

CHAPTER 4

SYSTEM IDENTIFICATION APPLIED TO THE ELASTIC PSEUDO-DYNAMIC TEST DATA —TREATING FEEDBACK OF EXPERIMENTAL ERRORS

4.1 Introduction

As discussed in the previous chapter, a straightforward application of a single-input single-output system identification technique to estimate the modal properties of the full-scale six-story steel structure tested within its elastic range revealed negative damping for the third mode. This was attributed to the cumulative effect of feedback of control and measurement errors during the pseudo-dynamic testing. These experimental errors were analyzed in Chapter 2 and were shown to act as excitations to the structure in addition to the ground motion.

In this chapter, these additional excitations are treated explicitly. For the purpose of system identification, this requires a multiple-input multiple-output technique. An output-error technique, namely MODE-ID [1,2], was used, which is applicable to any number of simultaneous input excitations and structural response measurements used in conjunction with a linear model. By accounting for the cumulative effect of the feedback of the experimental errors during the estimation of the modal parameters of the structure from the 'elastic' test data, it is possible to estimate the actual structural damping effective during the test and also the apparent equivalent viscous damping produced by the feedback errors. The identification results from the full-scale structural test data are in good agreement with the shaking table test results of a 0.3 scale model of the same prototype structure.

4.2 Modification of the Linear Structural Model

4.2.1 Analytical Model

It was shown in Chapter 2 that the cumulative displacement error $\underset{\sim}{x}^e$ is the response of the structure to an excitation $[-\mathrm{K}\underset{\sim}{x}^{ec}(t) - \underset{\sim}{\mathrm{R}}^{em}(t)]$ (Eq. 2.12), while the ideal (error-free) displacement $\underset{\sim}{x}^*$ is the response of the structure to a ground excitation force $[-\mathrm{M}\ddot{z}(t)\,\underset{\sim}{1}]$ (Eq. 2.11). The total response $\underset{\sim}{x}$ being the sum of both $\underset{\sim}{x}^*$ and $\underset{\sim}{x}^e$ (Eq. 2.10) suggests using

the following differential equation as a structural model:

$$\mathrm{M}\underset{\sim}{\ddot{x}} + \mathrm{E}\underset{\sim}{\dot{x}} + \mathrm{K}\underset{\sim}{x} = -\mathrm{M}\ddot{z}(t)\,\underset{\sim}{1} - \mathrm{K}\underset{\sim}{x}^{ec}(t) - \underset{\sim}{\mathrm{R}}^{em}(t) \quad , \tag{4.1}$$

where E is the equivalent viscous damping in the model.

If the force measurement errors are negligible in comparison with the force effects of displacement control errors as expected for a stiff structure, that is,

$$\| \underset{\sim}{\mathrm{R}}^{em}(t) \| \quad \ll \quad \| \mathrm{K}\underset{\sim}{x}^{ec}(t) \| \quad , \tag{4.2}$$

where $\| \cdot \|$ is the Euclidean vector norm, then the structural model in Eq. 4.1 can be rewritten as:

$$\mathrm{M}\underset{\sim}{\ddot{x}} + \mathrm{E}\underset{\sim}{\dot{x}} + \mathrm{K}\underset{\sim}{x} = -\mathrm{M}\ddot{z}(t)\,\underset{\sim}{1} - \mathrm{K}\underset{\sim}{x}^{ec}(t) \quad . \tag{4.3}$$

If it is assumed, in addition, that the measurement errors in the displacements, $\underset{\sim}{x}^{em}$, are much smaller than the displacement control errors, $\underset{\sim}{x}^{ec}$, that is,

$$\| \underset{\sim}{x}^{em}(t) \| \quad \ll \quad \| \underset{\sim}{x}^{ec}(t) \| \quad , \tag{4.4}$$

then from Eq. 2.8, $\underset{\sim}{x}^{ec}$ can be calculated from known quantities, the measured and calculated displacements, as:

$$\underset{\sim}{x}^{ec}(t) = \underset{\sim}{x}^{m}(t) - \underset{\sim}{x}(t) \quad . \tag{4.5}$$

The time-histories of these displacement control errors during the Phase II elastic test are plotted in Fig. 4.1. At the roof, the peak displacement errors are about 1% of the peak displacements and also the errors tend to oscillate at the fundamental frequency of the structure.

For the reasons discussed in Section 3.3.1, a linear model based on the dominant modes in the records of the response, and not on the stiffness and damping matrices as in Eq. 4.3, is preferred. This modal formulation is explained in the following section.

4.2.2 Modal Model

If the damping matrix E in Eq. 4.3 is assumed to be symmetric and also classical, then arguments similar to the ones in Section 3.3.2 will ensure that $\mathrm{M}^{-1}\mathrm{K}$ and $\mathrm{M}^{-1}\mathrm{E}$ have a common set of N orthonormal eigenvectors such that

$$\begin{aligned} \mathrm{M}^{-1}\mathrm{K}\,\Phi &= \Phi\,\Omega^2 \\ \mathrm{M}^{-1}\mathrm{E}\,\Phi &= \Phi\,(2\mathrm{Z}\,\Omega) \quad , \end{aligned} \tag{4.6}$$

where $\Phi = [\underset{\sim}{\phi}^{(1)}, \underset{\sim}{\phi}^{(2)}, \cdots, \underset{\sim}{\phi}^{(N)}]$, the modal column matrix of the structure normalized to satisfy the following orthogonality relationships:

$$\Phi^T M \Phi = I, \quad \Phi^T K \Phi = \Omega^2 \quad \text{and} \quad \Phi^T E \Phi = 2Z\Omega \quad . \tag{4.7}$$

Since the eigenvectors $\underset{\sim}{\phi}^{(r)}$ are a basis for N-dimensional vector space $\mathbf{R}^N$, $\underset{\sim}{x}$ can be written as

$$\underset{\sim}{x}(t) = \Phi \underset{\sim}{\xi}(t) \quad , \tag{4.8}$$

where $\underset{\sim}{\xi}$ is the vector of modal response amplitudes, that is the coordinates of $\underset{\sim}{x}$ with respect to the basis of eigenvectors.

Substituting Eq. 4.8 into Eq. 4.3:

$$M\Phi \underset{\sim}{\ddot{\xi}} + E\Phi \underset{\sim}{\dot{\xi}} + K\Phi \underset{\sim}{\xi} = -M\ddot{z}(t) \underset{\sim}{1} - K\underset{\sim}{x}^{ec}(t) \quad . \tag{4.9}$$

Premultiplying Eq. 4.9 by Φ^T and using Eq. 4.7:

$$\begin{aligned} \underset{\sim}{\ddot{\xi}} + 2Z\Omega \underset{\sim}{\dot{\xi}} + \Omega^2 \underset{\sim}{\xi} &= -\Phi^T M \ddot{z}(t) \underset{\sim}{1} - \Phi^T K \underset{\sim}{x}^{ec}(t) \\ &= -\underset{\sim}{\alpha}\, \ddot{z}(t) - B \underset{\sim}{x}^{ec}(t) \quad , \end{aligned} \tag{4.10}$$

or in component form:

$$\ddot{\xi}^{(r)} + 2\varsigma^{(r)} \omega^{(r)} \dot{\xi}^{(r)} + \omega^{(r)^2} \xi^{(r)} = -\alpha^{(r)} \ddot{z}(t) - \underset{\sim}{\beta}^{(r)^T} \underset{\sim}{x}^{ec}(t) \quad ,$$

where $\alpha^{(r)}$ and $\underset{\sim}{\beta}^{(r)}$ are the modal participation factors corresponding to the ground accelerations and control-errors in displacements, respectively.

Equation 4.8 can also be written as:

$$\underset{\sim}{x}(t) = \sum_{r=1}^{N} \underset{\sim}{x}^{(r)}(t) \quad , \tag{4.11}$$

where

$$\underset{\sim}{x}^{(r)}(t) = \xi^{(r)}(t) \underset{\sim}{\phi}^{(r)} \tag{4.12}$$

and $\underset{\sim}{x}^{(r)}(t)$ is the contribution of the r-th mode to the response vector $\underset{\sim}{x}(t)$.

From Eqs. 4.10 and 4.12 the following equation can be deduced:

$$\begin{aligned} \underset{\sim}{\ddot{x}}^{(r)} + 2\varsigma^{(r)} \omega^{(r)} \underset{\sim}{\dot{x}}^{(r)} + \omega^{(r)^2} \underset{\sim}{x}^{(r)} &= -\underset{\sim}{\phi}^{(r)} \left(\alpha^{(r)} \ddot{z}(t) + \underset{\sim}{\beta}^{(r)^T} \underset{\sim}{x}^{ec}(t) \right) \\ &= -P^{(r)} \underset{\sim}{f}(t) \quad , \end{aligned} \tag{4.13}$$

where

$$\underset{\sim}{f}(t) = \begin{bmatrix} \ddot{z}(t) \\ - - - - \\ \underset{\sim}{x}^{ec}(t) \end{bmatrix}$$

and (4.14)

$$\mathrm{P}^{(r)} = \underset{\sim}{\phi}^{(r)} \left[\alpha^{(r)}, \underset{\sim}{\beta}^{(r)^{\mathrm{T}}} \right]$$

is the effective participation factor matrix for the r-th mode.

In summary, the model used is Eqs. 4.13 and 4.14 in conjunction with Eq. 4.11. Hence the parameters of the modal model to be estimated are:

$$\{ \omega^{(r)}, \varsigma^{(r)}, \mathrm{P}^{(r)} \ : \ r = 1, 2, \cdots, \mathrm{N} \} \quad .$$

The effective participation factors and hence the mode shapes can be determined from the first column of the matrices $\mathrm{P}^{(r)}$.

4.3 Multiple-Input Multiple-Output (MI-MO) System Identification Technique

The modal parameters corresponding to the linear model in Eq. 4.13 are estimated using a multiple-input multiple-output system identification technique which is applicable to any elastic structure with any arbitrary configuration, classical normal modes, any number of simultaneous excitations and structural response measurements, and an initial at-rest position. This output-error technique was developed by Beck [1,2] to identify the pseudo-static and normal mode parameters of a linear model that characterized the measured response of the Meloland Road Overpass during the 1979 Imperial Valley earthquake.

The modal parameters $\underset{\sim}{\theta}^{(r)}$ to be estimated are:

$\omega^{(r)}$ = natural frequency of mode r ,
$\varsigma^{(r)}$ = damping ratio of mode r ,
$\mathrm{p}_{ij}^{(r)}$ = effective participation factor for mode r corresponding to the i-th response degree of freedom and the j-th excitation degree of freedom : $i = 1, \cdots, \mathrm{NR}$, $j = 1, \cdots, \mathrm{NI}$

where NR = no. of degrees of freedom at which the response is measured,
and NI = no. of degrees of freedom at which the input excitation forces are measured.

Each modal contribution $\underset{\sim}{x}^{(r)}(t)$ is governed by the following equation of motion:

$$\ddot{\underset{\sim}{x}}^{(r)} + 2\varsigma^{(r)}\omega^{(r)}\dot{\underset{\sim}{x}}^{(r)} + \omega^{(r)^2}\underset{\sim}{x}^{(r)} = -\mathrm{P}^{(r)}\underset{\sim}{f}(t) \qquad r = 1, \cdots, \mathrm{NM} \quad . \tag{4.15}$$

NM is the number of dominant modes in the structure because the response is modelled as a superposition of the contributions of the significant modes:

$$\underset{\sim}{x}(t; \underset{\sim}{\theta}) = \sum_{r=1}^{\mathrm{NM}} \underset{\sim}{x}^{(r)}(t; \underset{\sim}{\theta}^{(r)}) \quad . \tag{4.16}$$

An output-error $\underset{\sim}{e}$ is now defined in terms of the pseudo-accelerations[1] $\underset{\sim}{a}$ and model accelerations $\ddot{\underset{\sim}{x}}$ as:

$$\underset{\sim}{e}(t;\underset{\sim}{\theta}) = \underset{\sim}{a}(t) - \ddot{\underset{\sim}{x}}(t;\underset{\sim}{\theta}) \quad . \tag{4.17}$$

The accelerations are used in this study since they have the richest high-frequency content and they therefore allow more reliable estimation of the parameters of the higher modes.

The measure-of-fit to be used in conjunction with the above output-error $\underset{\sim}{e}$ is obtained by substituting Eq. 4.17 into Eq. 3.2 which yields:

$$\mathrm{J}(\underset{\sim}{\theta}) = \mathrm{V} \sum_{i=1}^{\mathrm{NR}} \int_0^{\mathrm{T}} [\, a_i(t) - \ddot{x}_i(t;\underset{\sim}{\theta})\,]^2 \quad dt \quad ,$$

where

$$\mathrm{V} = 1 \Big/ \sum_{i=1}^{\mathrm{NR}} \int_0^{\mathrm{T}} [\, a_i(t)\,]^2 \quad dt \quad . \tag{4.18}$$

The integrals are replaced by summations to give:

$$\mathrm{J}(\underset{\sim}{\theta}) = \mathrm{V} \sum_{i=1}^{\mathrm{NR}} \sum_{j=0}^{\mathrm{T}/\Delta t} [\, a_i(j\Delta t) - \ddot{x}_i(j\Delta t\,;\,\underset{\sim}{\theta})\,]^2 \quad ,$$

where the normalizing constant (4.19)

$$\mathrm{V} = 1 \Big/ \sum_{i=1}^{\mathrm{NR}} \sum_{j=0}^{\mathrm{T}/\Delta t} [\, a_i(j\Delta t)\,]^2$$

---

[1] Pseudo-accelerations are calculated during the test by the on-line computer from the pseudo-dynamic test displacements which appear in Eq. 2.5, using the central difference method.

and a_i, $\ddot{x}_i$ = pseudo-acceleration response of the structure and the model acceleration, respectively, at degree of freedom i,

Δt = discretization time step of the records,

T = length of the response records considered.

Therefore, from Eq. 4.19, J may be interpreted as the ratio of the mean-square model error to the mean square of the measured response. The best estimates of the modal parameters are identified from the measured excitation and response by minimizing the measure-of-fit J with respect to the modal parameters using a modification of the modal minimization method of the single-input single-output system identification technique explained in Section 3.4.1.

4.4 A MI-MO Analysis of Pseudo-Dynamic Elastic Test Data

The data from the 'elastic' test of Phase II is analyzed using the multiple-input multiple-output structural identification method explained in the previous section, in order to estimate the modal properties of the structure and also to quantify the apparent equivalent viscous damping effect of the feedback errors on the structural modes. The displacement control errors at all six floors calculated using Eq. 4.5 and the specified ground motion record serve as inputs (i.e., NI = 7), and the outputs to be matched are the pseudo-accelerations from all six floors (i.e., NR = 6). A linear model is constructed from three classical modes (i.e., NM = 3).

4.4.1 Identification Results

Modal periods, damping ratios and effective participation factors estimated from the nominally elastic test data using the MI-MO system identification method are given in Table 4.1. The linear model response is based on the contribution from the first three classical modes of a modal model since the higher modes, which would have contributed little to the earthquake response, were artificially suppressed during the test.

The estimated modal periods have the same values as in the case of the SI-SO system identification results from each floor of the test structure (Table 3.3), except for the third mode where the MI-MO method estimated the period as 0.104 sec while the SI-SO value was 0.106 sec at every floor.

The identified mode shapes in Table 4.1 are checked for orthogonality in the following

manner:

$$\text{Let} \quad \varepsilon_{rs} \equiv \frac{< \underset{\sim}{\phi}^{(r)} , \underset{\sim}{\phi}^{(s)} >}{\| \underset{\sim}{\phi}^{(r)} \| \; \| \underset{\sim}{\phi}^{(s)} \|} \quad , \tag{4.20}$$

where $< \underset{\sim}{\phi}^{(r)} , \underset{\sim}{\phi}^{(s)} > = \underset{\sim}{\phi}^{(r)^T} \mathrm{M} \underset{\sim}{\phi}^{(s)}$

and $\| \underset{\sim}{\phi}^{(r)} \| = < \underset{\sim}{\phi}^{(r)} , \underset{\sim}{\phi}^{(r)} >^{1/2} = [\underset{\sim}{\phi}^{(r)^T} \mathrm{M} \underset{\sim}{\phi}^{(r)}]^{1/2}$;

then, for orthogonal modes r and s,

$$\varepsilon_{rs} = 0 \quad .$$

The mass distribution of the test structure from Boutros and Goel [4] is:

$$\mathrm{M} = \begin{bmatrix} 0.095 & & & & & \\ & 0.090 & & & \bigcirc & \\ & & 0.090 & & & \\ & & & 0.090 & & \\ & \bigcirc & & & 0.090 & \\ & & & & & 0.077 \end{bmatrix} \text{ton} \quad .$$

Using the above mass matrix and the identified mode shapes in Table 4.1, the ε's are calculated to be:

$$\varepsilon_{12} = -0.3\% \quad , \quad \varepsilon_{13} = 0.6\% \quad \text{and} \quad \varepsilon_{23} = 1.6\% \quad .$$

Hence, the identified modes are almost orthogonal to each other, which is consistent with the theory of classical normal modes of vibration. The reasons for the above ε's being not exactly zero could be that the structure might not exhibit an exact linear behavior, any presence of noise in the experimental data, and also the damping might not be 'classical.'

The time-histories of pseudo-accelerations of the test structure agree very well with the acceleration predictions of the three-mode linear model corresponding to the optimal parameters, as seen in Fig. 4.2 where the time-histories are compared at the roof, mid-height and floor 2. The time-history comparisons are divided into six-second time-segments because of the dense high-frequency content in the acceleration records. The value of measure-of-fit corresponding to these comparisons is calculated as only 2.2%, which again demonstrates quantitatively the capability of linear models consisting of a few classical normal modes to reproduce the measured response for low amplitude tests.

The analytical model used to represent the structure during the MI-MO system identification procedure is:

$$\mathrm{M}\underset{\sim}{\ddot{x}} + \mathrm{E}\underset{\sim}{\dot{x}} + \mathrm{K}\underset{\sim}{x} = -\mathrm{M}\ddot{z}(t)\,\underset{\sim}{1} - \mathrm{K}\underset{\sim}{x}^{ec}(t) \quad . \tag{4.21}$$

Since the effects of the experimental errors are now explicitly taken into account as excitations to the structure in addition to the ground accelerations, the viscous damping matrix E in Eq. 4.21 will represent the sum of the viscous damping from the computer algorithm (C in Eq. 3.30), and the structural damping effective during the test. These various damping values are estimated in the following section.

4.4.2 Estimation of Structural Damping and Equivalent Viscous Damping Effect of Experimental Errors

The following is summarized from the previous sections in order to estimate damping values corresponding to both the structure and the effect of experimental errors.

The equation of motion of the test structure used in the pseudo-dynamic method is:

$$\mathrm{M}\underset{\sim}{\ddot{x}} + \mathrm{C}\underset{\sim}{\dot{x}} + \underset{\sim}{\mathrm{R}}(\underset{\sim}{x}) = -\mathrm{M}\ddot{z}(t)\,\underset{\sim}{1} \quad , \tag{4.22}$$

where

$$[\,\mathrm{C}\,] = [\,\text{Algorithmic Damping}\,] \quad . \tag{4.23}$$

The analytical model used in the SI-SO system identification method is:

$$\mathrm{M}\underset{\sim}{\ddot{x}} + \mathrm{D}\underset{\sim}{\dot{x}} + \mathrm{K}\underset{\sim}{x} = -\mathrm{M}\ddot{z}(t)\,\underset{\sim}{1} \quad , \tag{4.24}$$

where

$$[\,\mathrm{D}\,] = [\,\mathrm{C}\,] + [\,\text{Structural Damping}\,] + [\,\text{Feedback Error 'Damping'}\,] \quad . \tag{4.25}$$

Similarly, the analytical model used in the MI-MO system identification method is:

$$\mathrm{M}\underset{\sim}{\ddot{x}} + \mathrm{E}\underset{\sim}{\dot{x}} + \mathrm{K}\underset{\sim}{x} = -\mathrm{M}\ddot{z}(t)\,\underset{\sim}{1} - \mathrm{K}\underset{\sim}{x}^{ec}(t) \quad , \tag{4.26}$$

where

$$[\,\mathrm{E}\,] = [\,\mathrm{C}\,] + [\,\text{Structural Damping}\,] \quad . \tag{4.27}$$

Therefore, from Eqs. 4.25 and 4.27,

$$[\text{Structural Damping}] = [\text{E}] - [\text{C}] \tag{4.28}$$

$$[\text{Feedback Error Damping}] = [\text{D}] - [\text{E}] \quad . \tag{4.29}$$

The algorithmic damping C used in the on-line computer calculations during the actual pseudo-dynamic test was constructed using the specified diagonal modal damping matrix Z_1 based on Table 3.5, and the modal frequencies Ω_1 and modeshapes Φ_1 obtained from a pre-test finite element analysis of the test structure [4] as follows:

$$C = (M\,\Phi_1)\,(2Z_1\,\Omega_1)\,(\Phi_1{}^T\,M\,\Phi_1)^{-1}\,(M\,\Phi_1)^T \quad . \tag{4.30}$$

Since the effective natural frequencies Ω and modeshapes Φ of the structure during the test, as identified by the MI-MO method, are different from the pre-test analytical values, the effective modal damping matrix Z_2 corresponding to the algorithmic damping is reconstructed as follows:

$$Z_2 = \frac{1}{2}\,(\Phi^T\,M\,\Phi)^{-1}\,(\Phi^T\,C\,\Phi)\,\Omega^{-1} \quad . \tag{4.31}$$

Although Z_1 is a diagonal matrix, Z_2 need not be, since the stiffness matrix effective during the elastic pseudo-dynamic test is different from its pre-test analytical value. Z_2 calculated as above is shown in Table 4.2 and is approximated by its diagonal elements alone. Since only the first three modes were identified using the MI-MO method, the pre-test modeshapes were used in Φ for the last three modes. This is why the diagonal modal damping values above the third mode remain unchanged.

The above modal damping values for C which are different from the values in Table 3.5 for the first three modes, and modal damping values for D and E from SI-SO and MI-MO results, respectively, are shown in the first three columns of Table 4.3. The structural damping and feedback error damping values of the first three modes calculated using Eqs. 4.28 and 4.29, respectively, are shown in the last two columns of Table 4.3.

The low structural damping values of less than 1% as shown in Table 4.3, compared to field observations of 3% to 8% for the earthquake response of actual buildings, are mainly due to the absence of nonstructural components in the test structure and the absence of radiation damping during the pseudo-dynamic test because of its quasi-static nature.

Feedback errors have produced positive damping values of 0.3% and 0.9% in the first two modes, and a negative damping value of 2.4% in the third mode, confirming the fact that higher modes are affected significantly by the feedback of experimental errors in pseudo-dynamic testing. More than 2% of negative feedback damping in the third mode, which is about 4 times larger than the positive structural damping in that mode, explains the extraordinarily strong third-mode signal seen in Fig. 3.9.

4.4.3 Comparisons of Full-Scale and Scale-Model Test Results

The full-scale structural identification results of natural frequencies, damping ratios and modeshapes using MI-MO technique are compared in Table 4.4 and Fig. 4.3, with the corresponding results from a 0.305 scale-model of the same prototype structure tested on a shaking table at the University of California, Berkeley by Bertero, et al. [5].

In Table 4.4, model periods have already been scaled up by $1/\sqrt{0.305}$ so that they can be compared with the full-scale structural values. Also, the plotted mode shape vectors for the full-scale structure are just the effective participation factors in Table 4.1 , which in turn are the first column of each modal participation factor matrix $P^{(r)}$, r =1,2,3, appearing in Eq. 4.13.

The periods and modeshapes of both the full-scale structure and the scale model are in good agreement and the small difference in the damping values could be attributed to radiation and table-structure interaction effects present in the shaking table test. Overall, the scale-model test proved to be a viable alternative to full-scale testing, at least with regard to reproducing the modal properties of the full-scale structure.

4.4.4 Conclusions

A linear model consisting of three classical normal modes was shown to be capable of reproducing the measured structural response with a mean-square acceleration error of 2% of the mean-square pseudo-acceleration. Also, it was shown that the effect of feedback errors may be accounted for when estimating the modal parameters. By using the control errors, in addition to the ground motion, as inputs to a multiple-input multiple-output system identification technique, the equivalent viscous dampings for energy dissipated by the structure and for the apparent damping from the feedback errors were estimated. The identification results showed that the feedback errors added energy to the test structure in its third mode but damped the contributions of the first two modes during the nominally elastic test of Phase II.

The estimates for the modal parameters of the full-scale structure are in very good agreement with those from a 0.3 scale model tested on a shaking table, suggesting that scale-model testing is in fact a reliable technique for reproducing the dynamic properties of full-scale structures.

REFERENCES

[1] Werner, S.D., Levine, M.B. and Beck, J.L.,"Seismic Response Characteristics of Meloland Road Overpass During 1979 Imperial Valley Earthquake," Report No. R–8222–5603, Agbabian Associates, El Segundo, California, March, 1985.

[2] Beck, J.L., "Users Guide for MODE-ID," Report No. R–8222–5931, Agbabian Associates, El Segundo, California, March, 1985.

[3] Beck, J.L. and Jayakumar, P., "System Identification Applied to Pseudo-Dynamic Test Data: A Treatment of Experimental Errors," *Proceedings of the 3rd ASCE Engineering Mechanics Specialty Conference on Dynamic Response of Structures*, University of California, Los Angeles, California, April, 1986.

[4] Boutros, M.K. and Goel, S.C., "Pre-Test Analysis of the Six-Story Eccentric-Braced Steel Test Building," *Proceedings of the 5th Joint Technical Coordinating Committee Meeting*, U.S.—Japan Cooperative Research Program Utilizing Large-Scale Testing Facilities, Tsukuba, Japan, February, 1984.

[5] Bertero, V., et al., "Progress Report on the Earthquake Simulation Tests and Associated Studies of 0.3 Scale Models of the 6-story Steel Test Structure," *Proceedings of the 6th Joint Technical Coordinating Committee Meeting*, U.S.—Japan Cooperative Research Program Utilizing Large-Scale Testing Facilities, Maui, Hawaii, June, 1985.

Mode	Period (sec)	Damping (%)
1	0.553	0.90
2	0.191	1.19
3	0.104	2.32

Mode	Effective Participation Factor at Floor					
	2	3	4	5	6	Roof
1	0.30	0.53	0.78	1.01	1.22	1.40
2	0.37	0.48	0.42	0.16	-0.19	-0.53
3	0.15	0.11	-0.05	-0.17	-0.05	0.15

Table 4.1 Modal Parameters Estimated from the Pseudo-Acceleration Records Using a Three–Mode Model and the MI-MO Technique (J=2.2%) [3]

$$Z_2 = \begin{bmatrix} 0.33 & 0.00 & 0.00 & 0.00 & 0.00 & 0.00 \\ 0.03 & 0.31 & 0.01 & 0.00 & 0.00 & 0.00 \\ 0.37 & 0.35 & 1.75 & 0.00 & 0.00 & 0.00 \\ -1.12 & 2.55 & -0.33 & 90.00 & 0.00 & 0.00 \\ 4.64 & -1.00 & -0.85 & 0.00 & 90.00 & 0.00 \\ -0.67 & -3.33 & -0.66 & 0.00 & 0.00 & 90.00 \end{bmatrix}$$

Table 4.2 The Effective Modal Damping Matrix Z_2 Corresponding to the Algorithmic Damping C, as in Eq. 4.31 (values in percent of critical)

Mode	Damping (%)				
	Numerical [C]	SI-SO [D]	MI-MO [E]	Feedback Errors	Structural
1	0.33	1.23	0.90	0.33	0.58
2	0.31	2.11	1.19	0.92	0.88
3	1.75	-0.05	2.32	-2.37	0.56

Table 4.3 Estimated Damping Values

Mode	Period (sec)		Damping (%)	
	Structure	Scale Model	Structure	Scale Model
1	0.553	0.572	0.58	0.67
2	0.191	0.190	0.88	0.90
3	0.104	0.105	0.56	—

Table 4.4 Comparison of Modal Period and Damping Values for Full-Scale Structure and Scale-Model Specimen

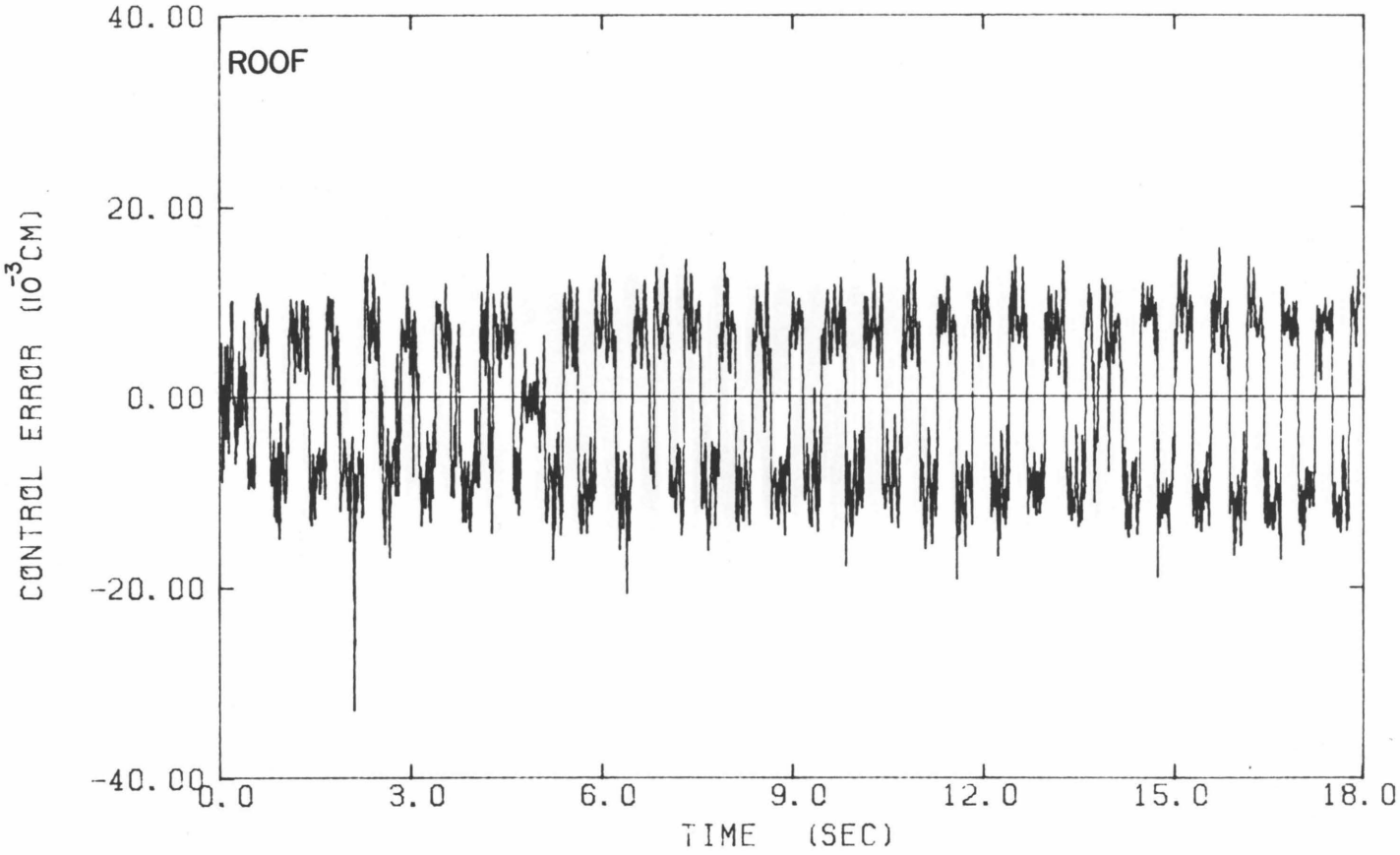

Fig. 4.1 Time-Histories of Displacement Control Errors at the Roof, Mid-Height and Floor 2

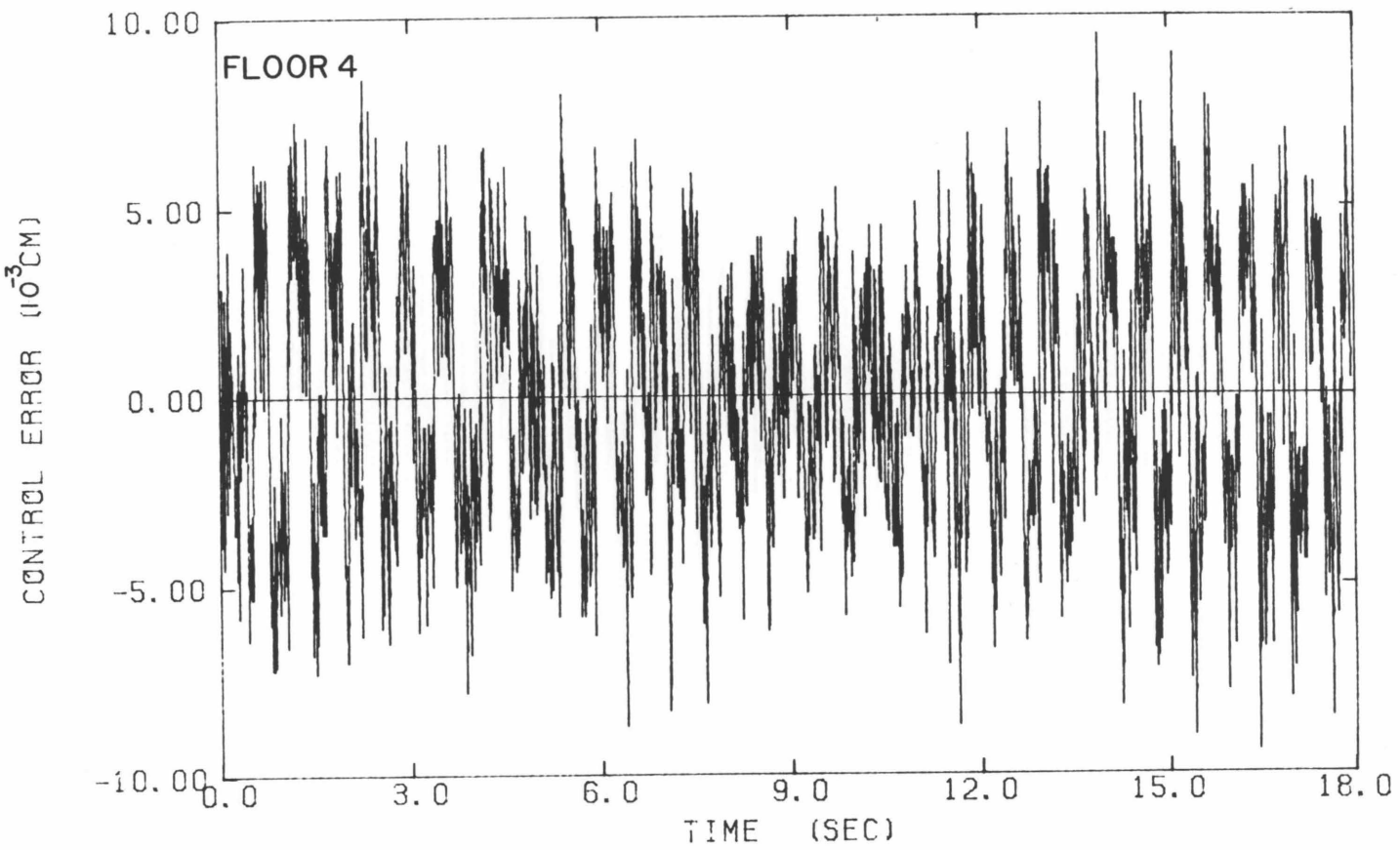

Fig. 4.1 (continued)
Time-Histories of Displacement Control Errors at the Roof, Mid-Height and Floor 2

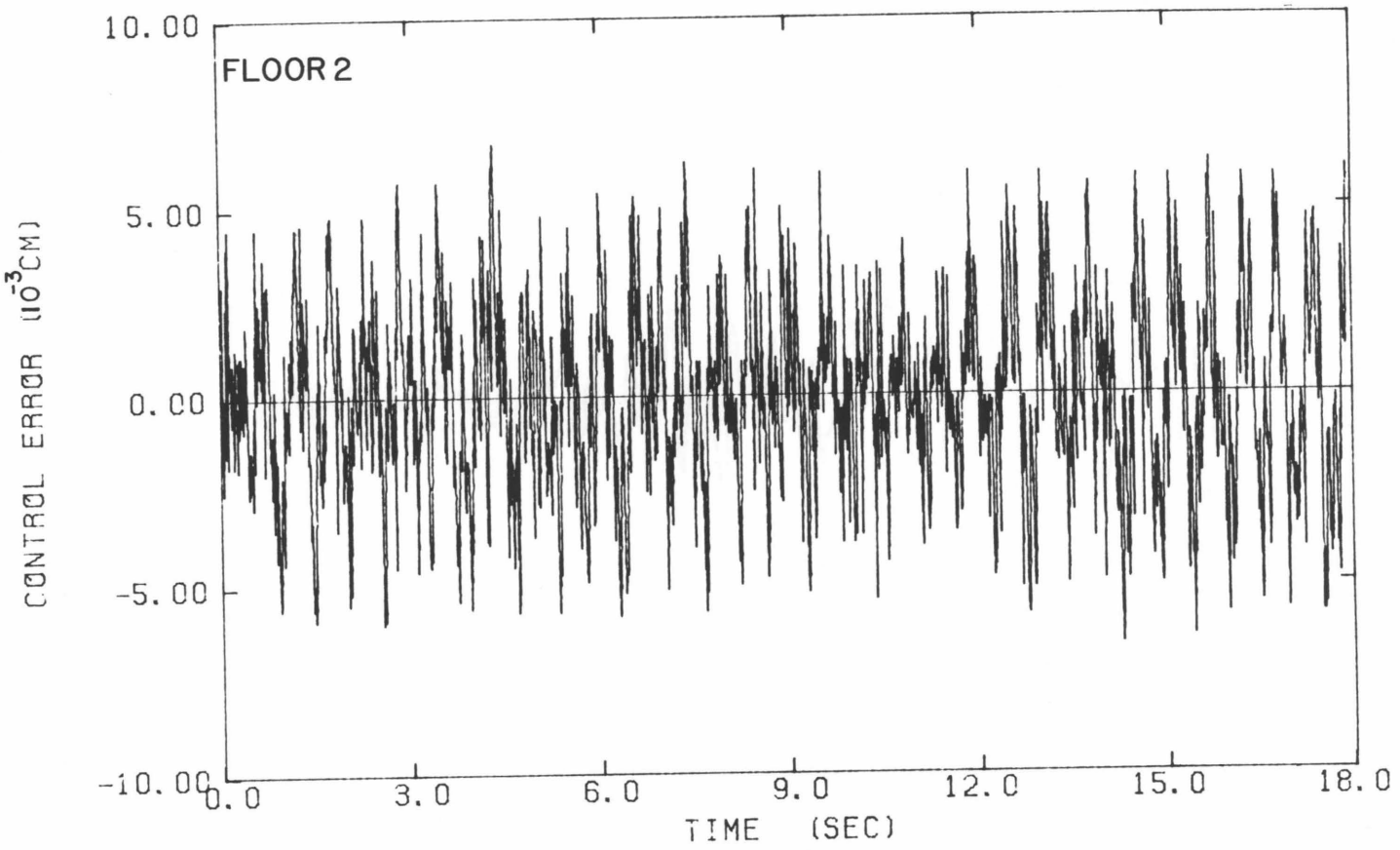

Fig. 4.1 (continued)
Time-Histories of Displacement Control Errors at the Roof, Mid-Height and Floor 2

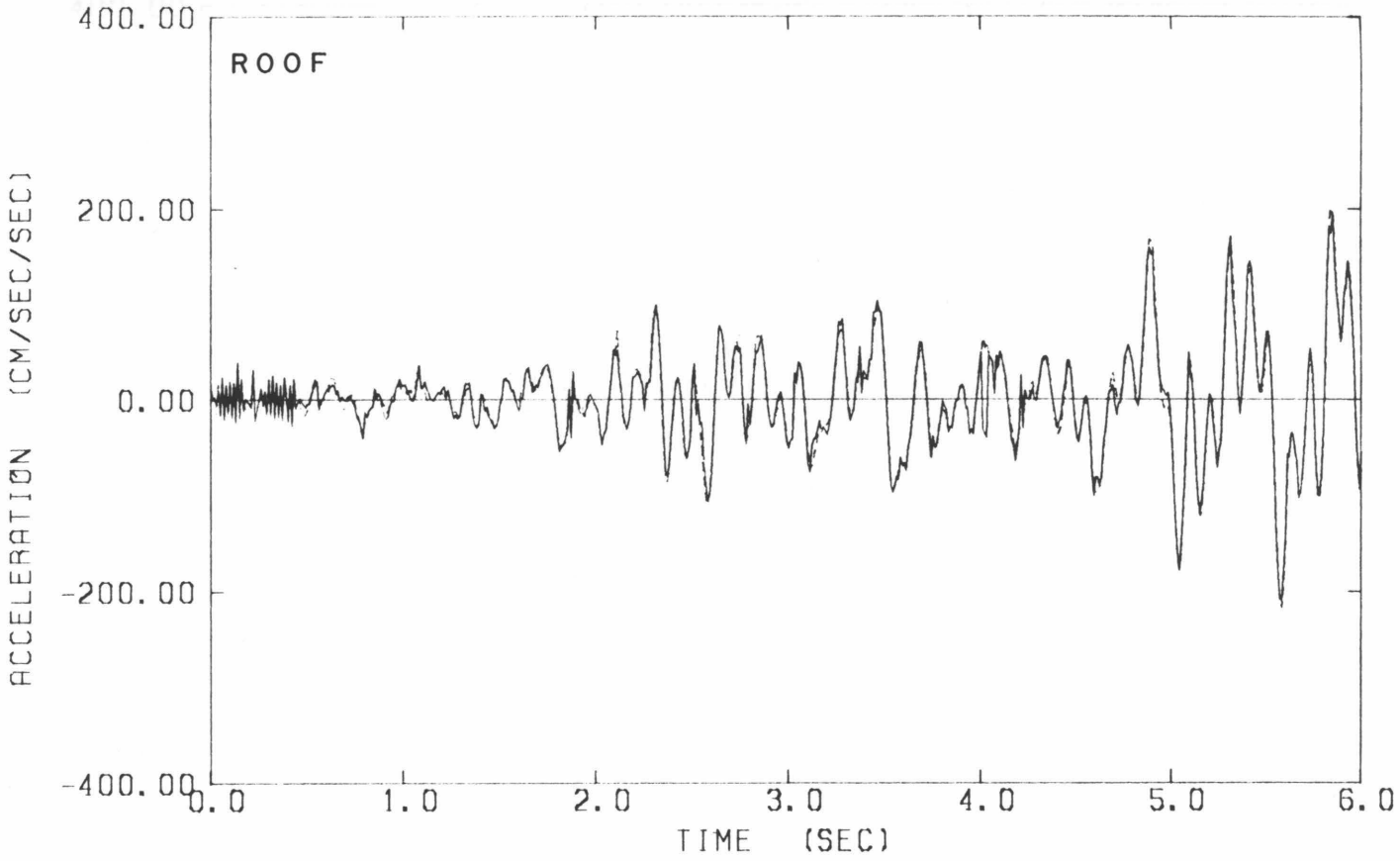

Fig. 4.2 Pseudo-Accelerations of the Test Structure (——) and Calculated Accelerations of a Three-Mode Model (- - -), at the Roof, Mid-Height and Floor 2; Model Identified from Pseudo-Acceleration Records

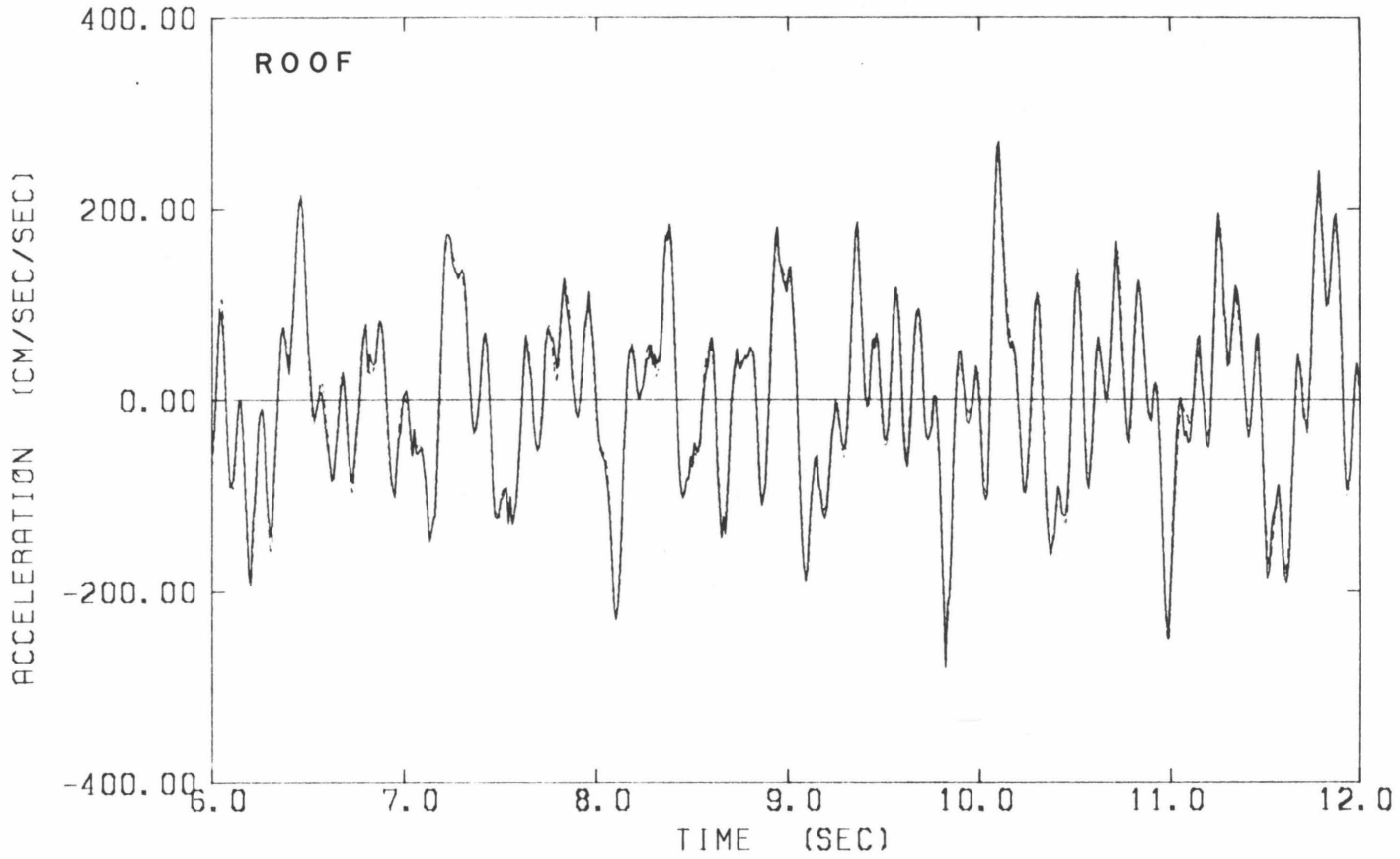

Fig. 4.2 (continued)
Pseudo-Accelerations of the Test Structure (——) and Calculated Accelerations of a Three-Mode Model (- - -), at the Roof, Mid-Height and Floor 2;
Model Identified from Pseudo-Acceleration Records

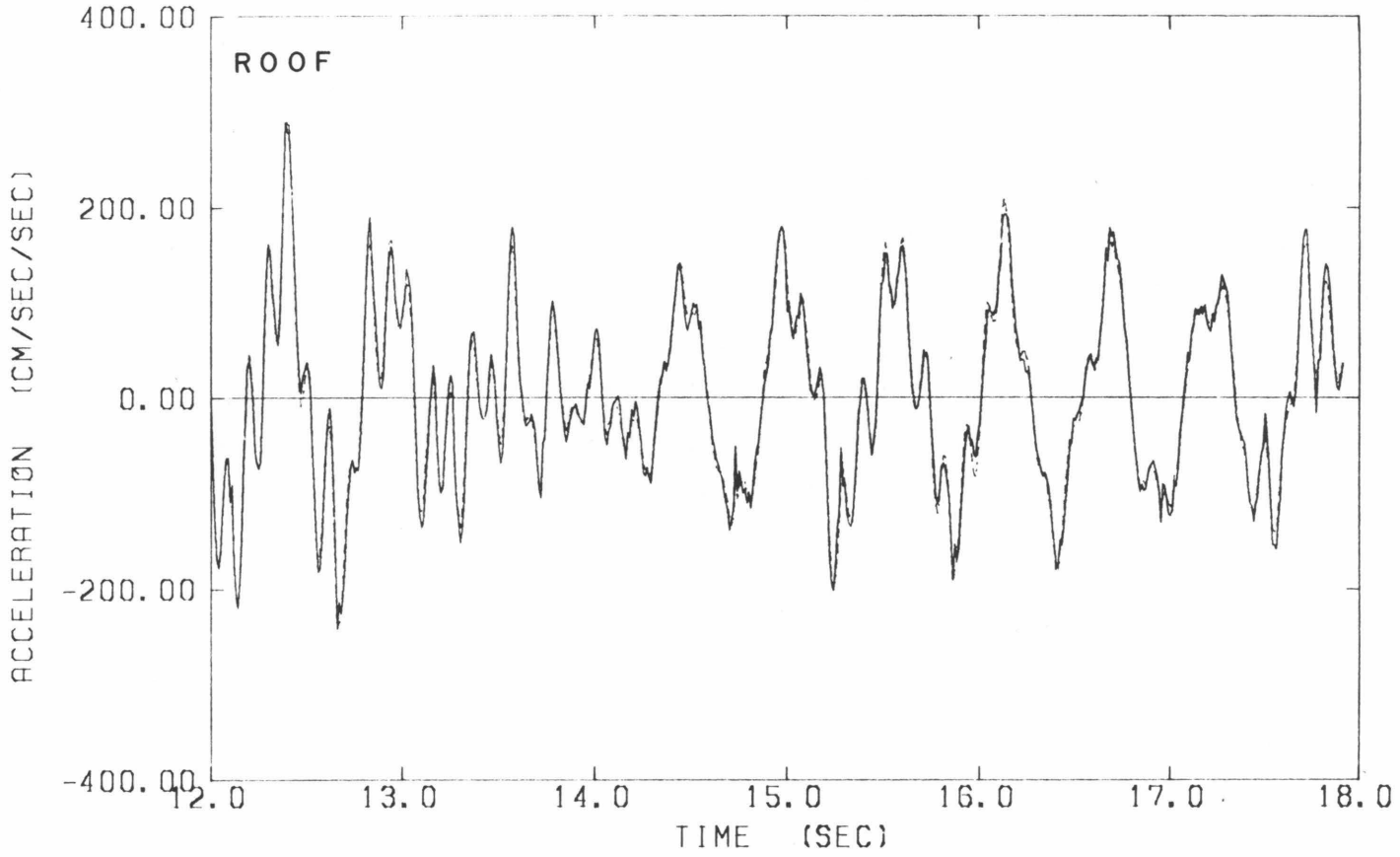

Fig. 4.2 (continued)
Pseudo-Accelerations of the Test Structure (——) and Calculated Accelerations of a Three-Mode Model (- - -), at the Roof, Mid-Height and Floor 2;
Model Identified from Pseudo-Acceleration Records

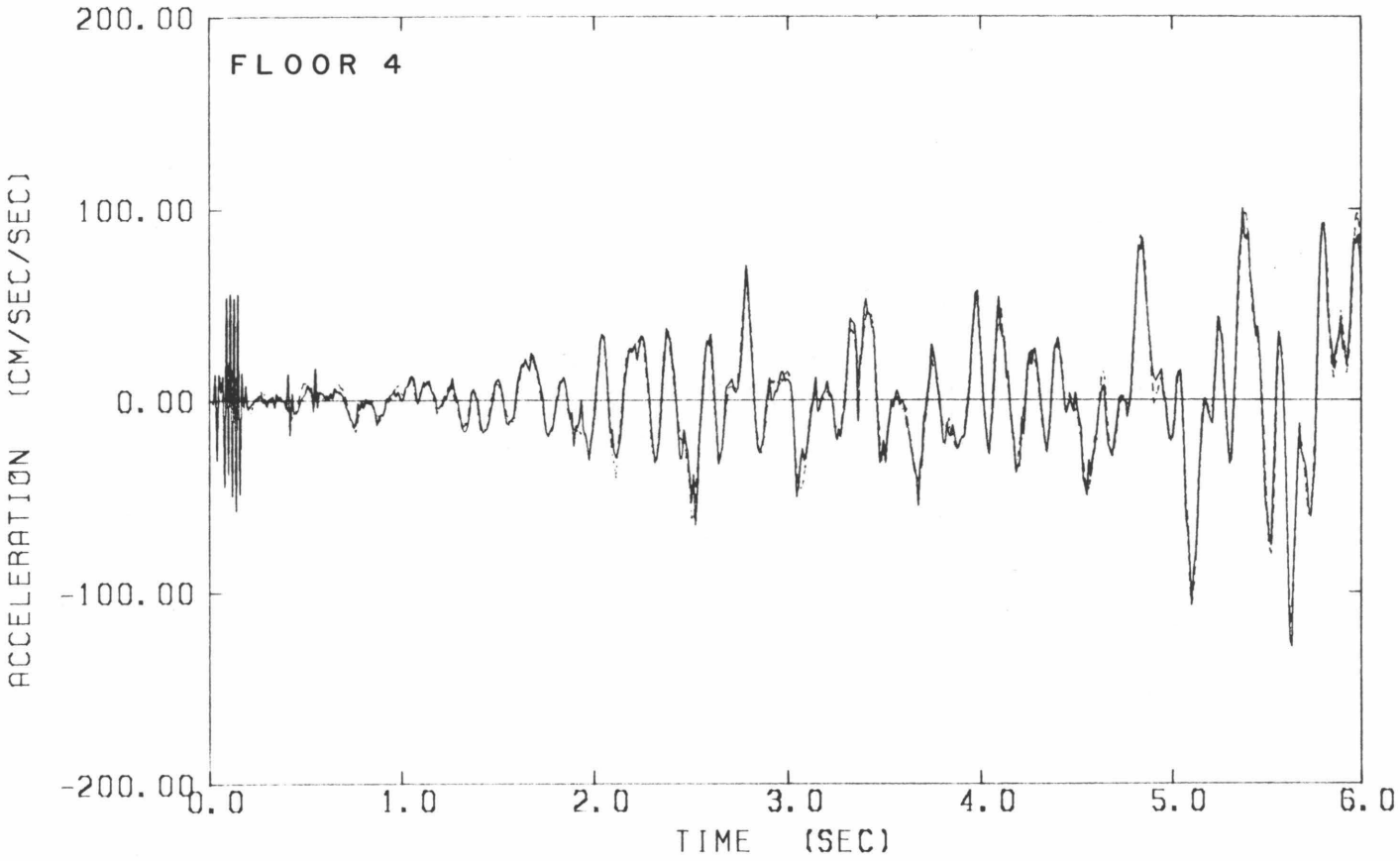

Fig. 4.2 (continued)
Pseudo-Accelerations of the Test Structure (——) and Calculated Accelerations of a Three-Mode Model (- - -), at the Roof, Mid-Height and Floor 2;
Model Identified from Pseudo-Acceleration Records

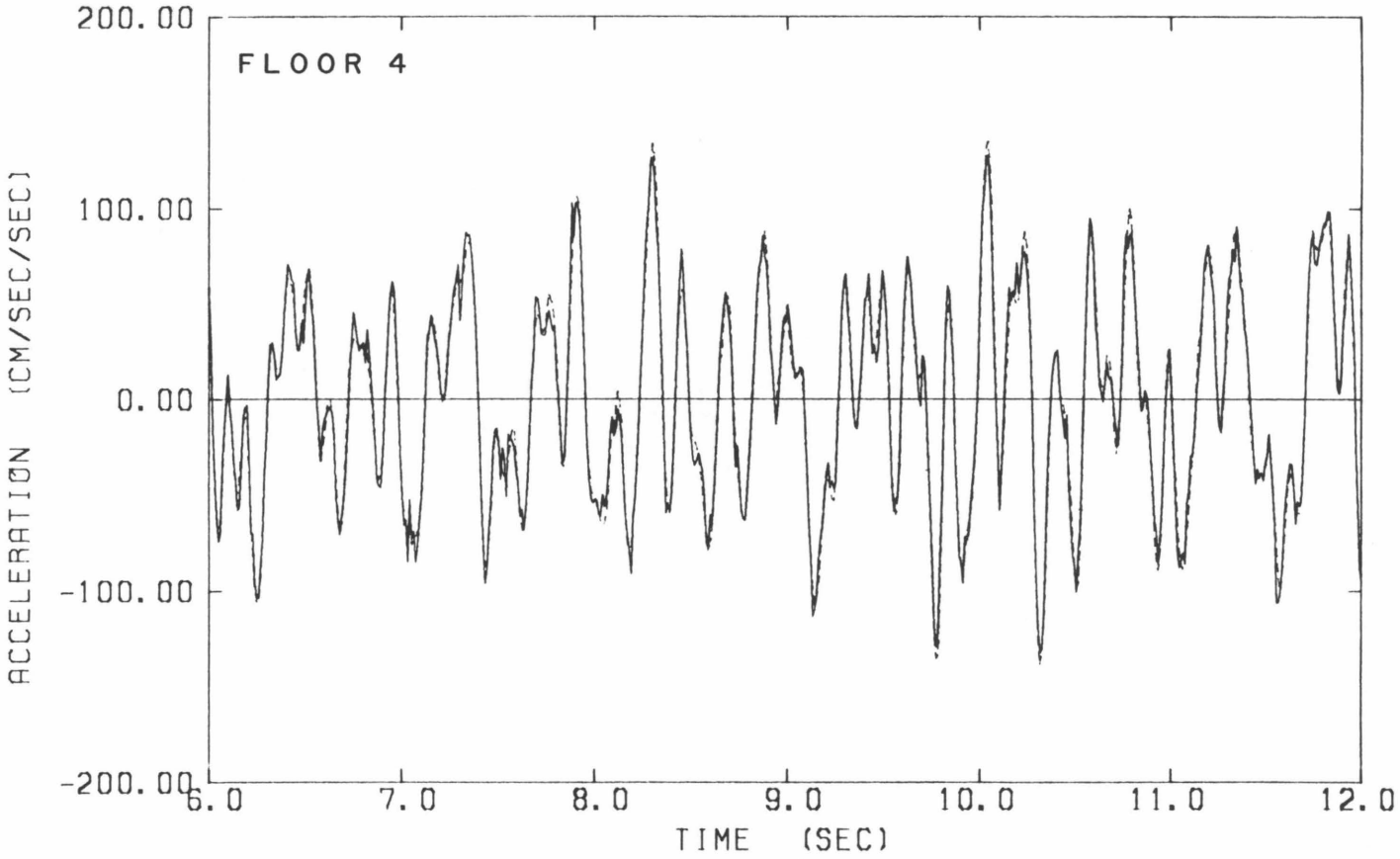

Fig. 4.2 (continued)
Pseudo-Accelerations of the Test Structure (——) and Calculated Accelerations of a Three-Mode Model (- - -), at the Roof, Mid-Height and Floor 2;
Model Identified from Pseudo-Acceleration Records

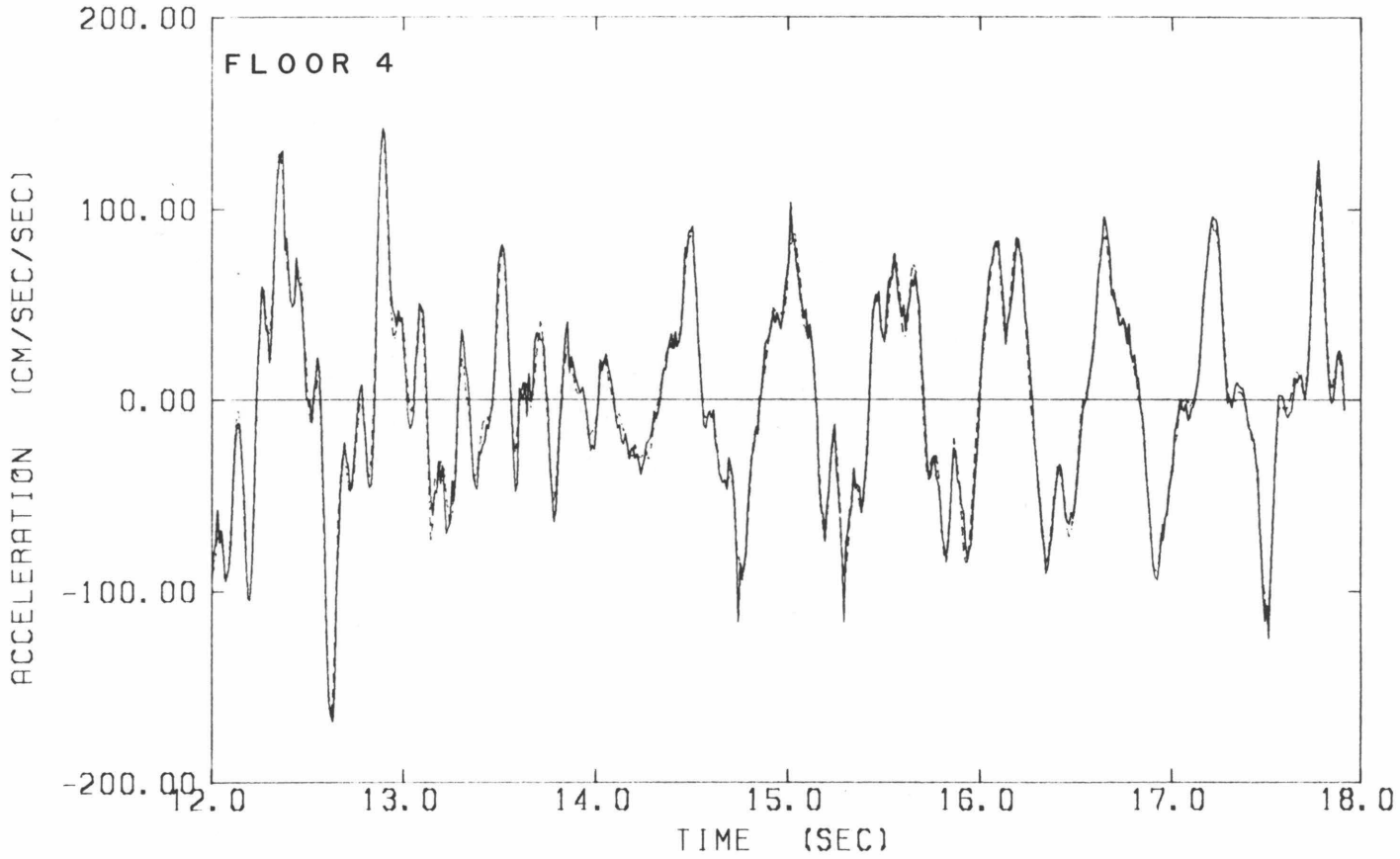

Fig. 4.2 (continued)
Pseudo-Accelerations of the Test Structure (——) and Calculated Accelerations of a Three-Mode Model (- - -), at the Roof, Mid-Height and Floor 2;
Model Identified from Pseudo-Acceleration Records

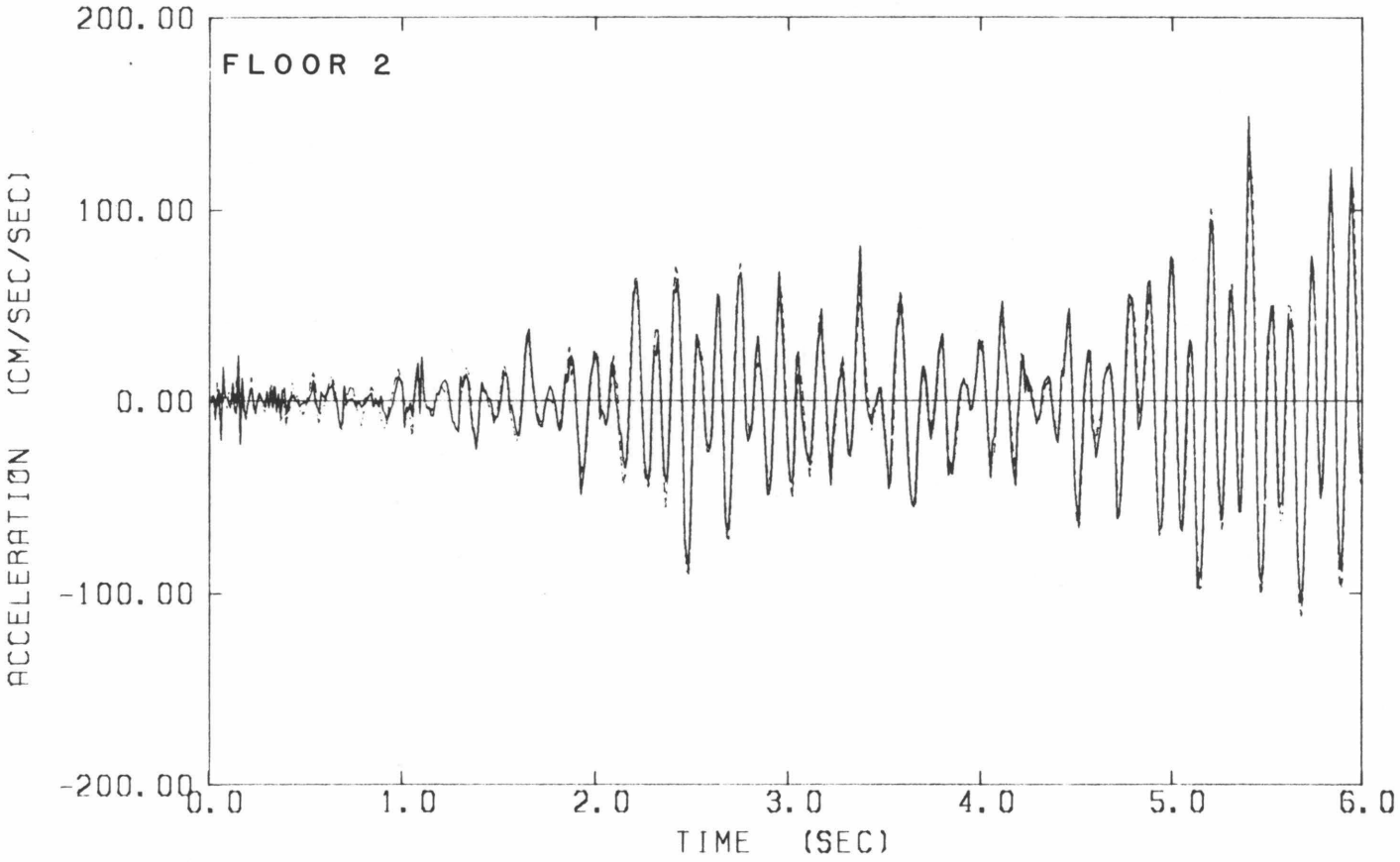

Fig. 4.2 (continued)
Pseudo-Accelerations of the Test Structure (——) and Calculated Accelerations of a Three-Mode Model (- - -), at the Roof, Mid-Height and Floor 2;
Model Identified from Pseudo-Acceleration Records

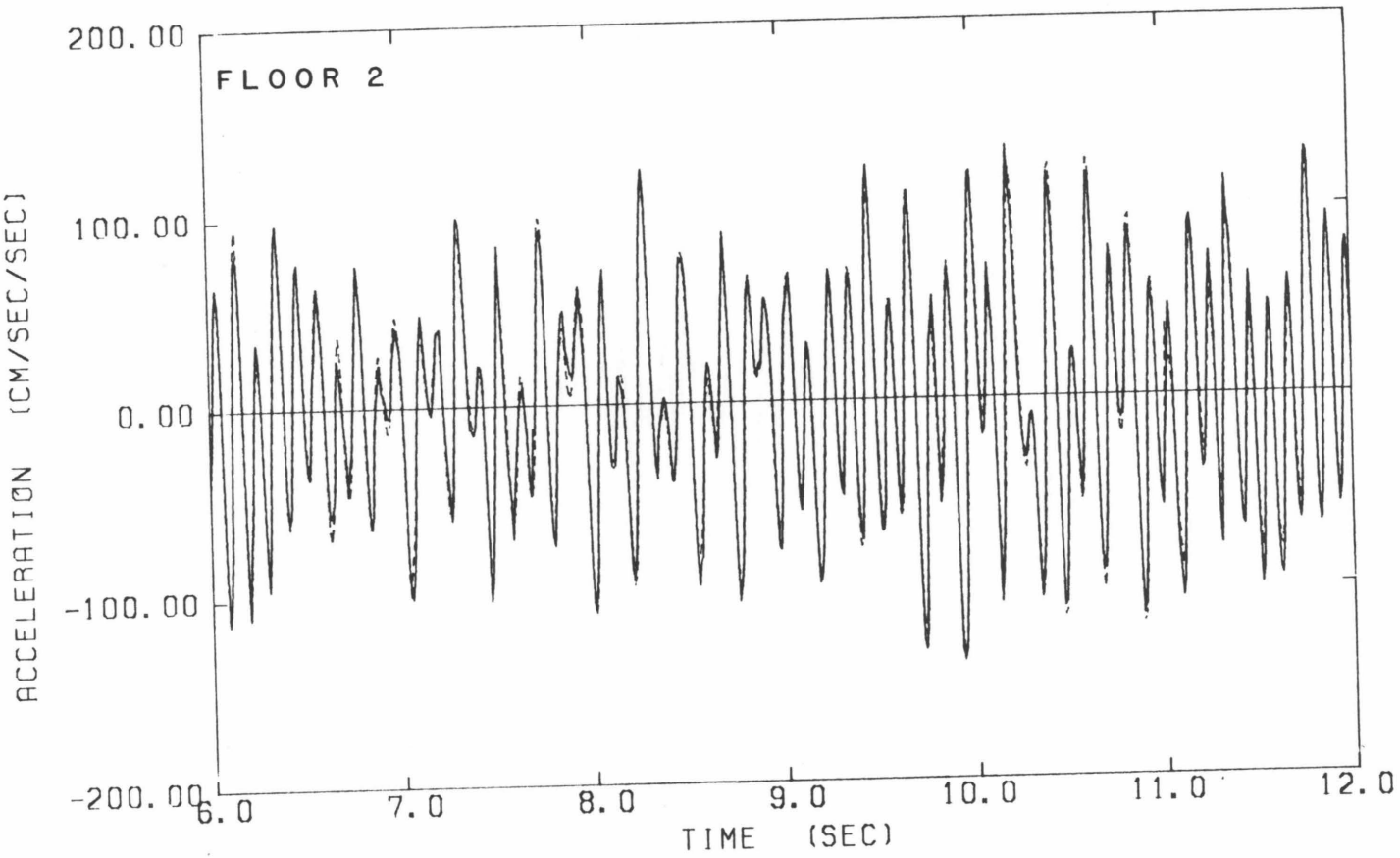

Fig. 4.2 (continued)
Pseudo-Accelerations of the Test Structure (——) and Calculated Accelerations of a Three-Mode Model (- - -), at the Roof, Mid-Height and Floor 2;
Model Identified from Pseudo-Acceleration Records

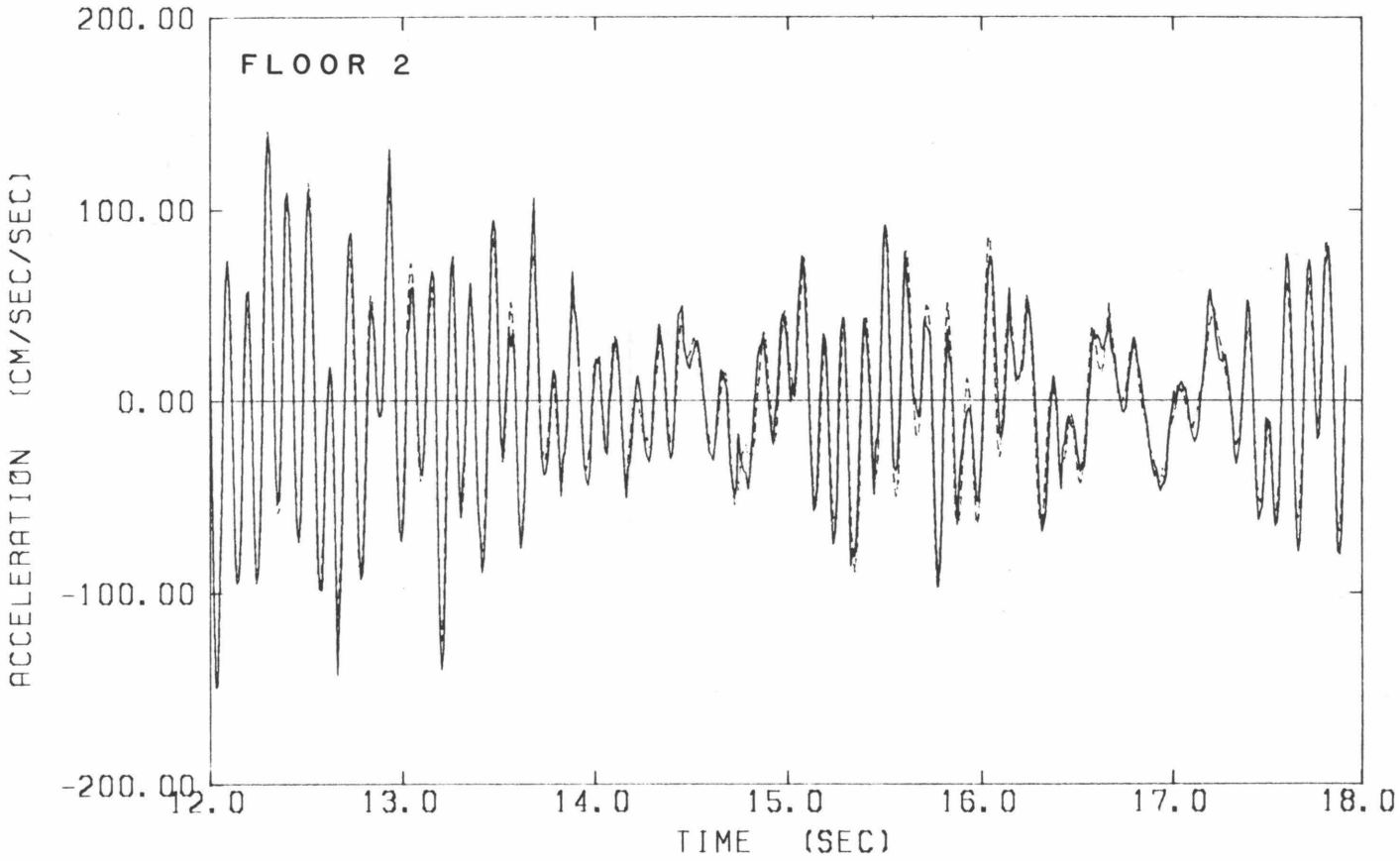

Fig. 4.2 (continued)
Pseudo-Accelerations of the Test Structure (——) and Calculated Accelerations of a Three-Mode Model (- - -), at the Roof, Mid-Height and Floor 2;
Model Identified from Pseudo-Acceleration Records

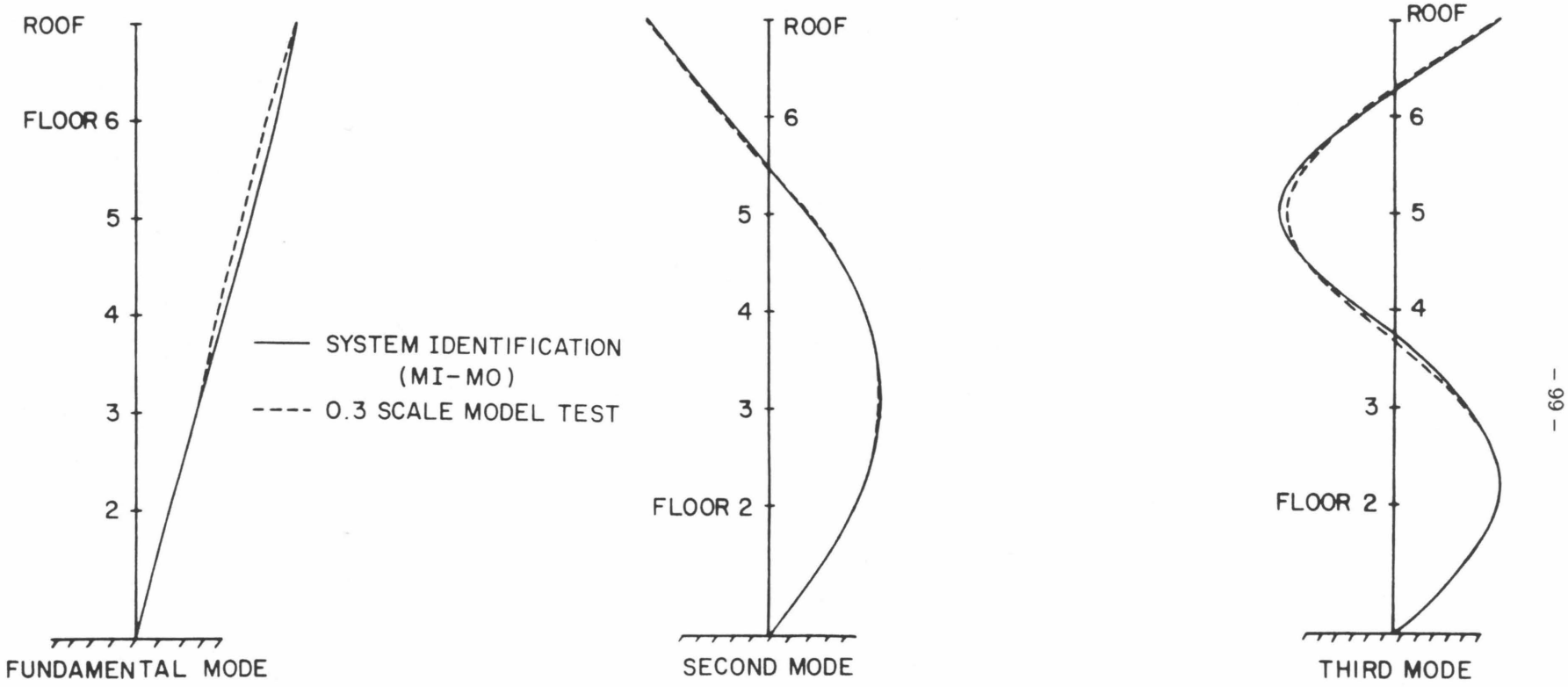

Fig. 4.3 Comparison of Modeshapes for Full-Scale Structure and Scale-Model Specimen

CHAPTER 5

MODELING OF HYSTERETIC SYSTEMS

5.1 Introduction

The problem of designing structures to resist the vibratory forces developed by strong earthquake ground motions leads naturally to the investigation of the response of structures that are stressed beyond the yield point into the nonlinear range [1]. In essence, this requires a method for describing the dynamic force-deflection relation of the structural members right up to their ultimate strength. Because the restoring force of such a system is highly nonlinear and depends not only on the instantaneous displacement, but also on its past history, analytical modeling of such a system under arbitrary excitation has been a challenging and interesting subject [2].

Force-deformation relations can be obtained from the constitutive equations which govern material behavior at a point, but complex stress distributions and material inhomogeneities render such an approach impractical. In addition, there is not a common agreement on the choice of such constitutive models. On the other hand, force-deformation relationships tend to be different in character from the underlying constitutive equations, as they reflect the behavior of the member as a whole and also include geometrical effects [3].

Elastic-perfectly plastic and bilinear hysteretic models have been studied extensively in the past, mainly because of their simplicity. But for dynamic studies it would be desirable to use a yielding relation that has a deviation from linearity which is smooth and yet is general enough to describe yielding behavior varying within a wide range. Such a relation would be a more realistic model for most practical applications, since even materials with a sharply pronounced yield point in tension exhibit smooth force-deflection relations when formed into structural shapes. Furthermore, an assemblage of structural shapes can, in general, be expected to exhibit a rounded force-deflection curve [1].

In this chapter, various nonlinear hysteretic models are discussed within this context and finally a simple model which is consistent with the real behavior of several materials and structures under dynamic loading conditions is presented.

5.2 A General Class of Masing Models

5.2.1 Masing's Hypothesis

Masing, in a paper titled "Self Stretching and Hardening for Brass" in 1926 [4], assumed that a metal body consists of a system of body elements each with the same elastic stiffness but different yield limits, and that the force-deformation curve of such an element, as shown in Fig. 5.1, consists of two straight lines.

Masing then asserted that if the load-deflection curve for the entire system at the virgin loading is symmetric about the origin and is given by

$$f(x, r) = 0 \tag{5.1}$$

where x is the displacement and r is the restoring force, then the unloading and reloading branches of the hysteresis loops for steady-state response are geometrically similar to the virgin loading curve and are described by the same basic equation except for a two-fold magnification. Applying this to a hysteretic loop describing cyclic loading between (x_0, r_0) and $(-x_0, -r_0)$ as shown in Fig. 5.2, each branch of the hysteresis loop is given by:

$$f\left(\frac{x - x^*}{2}, \frac{r - r^*}{2}\right) = 0 \quad , \tag{5.2}$$

where (x^*, r^*) is the load reversal point for that particular branch curve. Therefore, the descending (unloading) branch of the hysteresis loop becomes

$$f\left(\frac{x_0 - x}{2}, \frac{r_0 - r}{2}\right) = 0 \quad ,$$

while the ascending (reloading) branch of the hysteresis loop becomes (5.3)

$$f\left(\frac{x + x_0}{2}, \frac{r + r_0}{2}\right) = 0 \quad .$$

To experimentally test these equations, brass rods of different preliminary treatment were first plastically extended and then compressed. The overall result of Masing's experiment was that the compression curve obtained fron the experiment deviated only a little from the compression curve computed from Eq. 5.2, with $f(x, r)$ based on the initial tension curve. This showed that the model is in agreement with the well known Bauschinger effect occurring in a metal, which describes the weakening of the metal in one loading direction due to plastic yielding in the opposite direction during cyclic loading as observed in his experiment.

The Bauschinger effect, also observed in soils, is usually attributed to damage caused in the material by the initial stressing (slips along crystal planes in a solid; slips between grains in a soil). Prager devised a simple mechanical model to demonstrate this; it is a kinematic model, and the increased strength on straining and the Bauschinger effect are therefore sometimes referred to as kinematic hardening [5].

5.2.2 Properties of Masing Hysteresis Loops for Steady-State Response

The following are some of the important properties of the Masing hysteresis loops which were discussed in the previous section. Some of them (a-c) have been pointed out by Jennings [1] with regard to his formulation of the Ramberg-Osgood model. The Ramberg-Osgood model, which is included within the Masing class of models, is described later in this chapter.

(a) Since the virgin loading curve is symmetric about the origin, if (x, r) is a point on the virgin loading curve, then so is the point $(-x, -r)$.

(b) The branch curve originating from (x_0, r_0) or $(-x_0, -r_0)$ on the virgin curve will intersect the virgin curve again at $(-x_0, -r_0)$ or (x_0, r_0), respectively. Therefore, it can be concluded that Eq. 5.3 can describe a closed hysteresis loop whose upper and lower points lie on the virgin curve.

(c) The initial slopes of the ascending and descending branches of the hysteresis loop are the same as the slope of the virgin curve at the origin (the 'small-amplitude' slope). By comparing the slopes of the hysteretic curves at their other points of contact with the virgin curve, it can be shown that the ascending and descending branches are tangent to the virgin curve at these points.

(d) In general, because of the two-fold magnification of the branch curves in Eq. 5.3 compared to the virgin curve in Eq. 5.1, it can be shown that the tangent stiffness dr/dx at any point P(x, r) on the virgin curve (Fig. 5.3(a)) is the same as the tangent stiffness at Q$(x_0 - 2x, r_0 - 2r)$ on the unloading branch curve and again at R$(2x - x_0, 2r - r_0)$ on the reloading branch curve. This property of the hysteresis loop curves can be well understood with the help of a continuous distribution of constant 'stiffness' surfaces in the region of the restoring force space as shown in Fig. 5.3(b). Hence the overall stiffness characteristic will also be continuous and nonlinear. This idea was first introduced by Iwan [6] and Mróz [7] under the context of multiple yield surfaces with kinematic hardening in the incremental theory of plasticity. This concept of nested

yield surface representation has been used to study the earthquake response of earth dams by Prévost and his co-workers [8–10].

5.2.3 Masing's Rules Extended for Transient Response

For steady-state cyclic response or loading between fixed limits, Masing's hypothesis will suffice. However, for cases of transient loading or loading between variable limits, the hypothesis was considered to be of no help [6,11–13]. However, Masing's original hypothesis can be extended to transient loading in a manner which is simple and has a physical basis, as follows:

- **Rule 1: Incomplete Loops**

The equation of any hysteretic response curve, irrespective of steady-state or transient response, can be obtained simply by applying the original Masing's rules to the virgin loading curve using the latest point of loading reversal.

For example, let the virgin loading curve OA in Fig. 5.4 be characterized by Eq. 5.1. Applying Rule 1, the equation for the branch curve CD in Fig. 5.4 becomes:

$$f\left(\frac{x - x_c}{2}, \frac{r - r_c}{2}\right) = 0 \quad . \tag{5.4}$$

Based on Eq. 5.4 applied to the Ramberg-Osgood model, Jennings [14] has shown that if the reloading curve CD in Fig. 5.4 had been continued, it would have formed a closed hysteresis loop ABCDA.

- **Rule 2: Completed Loops**

The ultimate fate of an interior curve under continued loading or unloading can be determined by choosing one of the following two interpretations [15]:

(i) Force-deflection values are given by a hysteretic curve originating from the point of most recent loading reversal until either the upper or lower boundary is contacted. Thereafter, the force-deflection values are given by that boundary until the direction of loading is again reversed.

(ii) If an interior curve crosses a curve described in a previous load cycle, the load-deformation curve follows that of the previous cycle.

The first interpretation is due to Jennings [14] and has also been used by Matzen and McNiven [15] in their system identification study using the Ramberg-Osgood model. Fan [16] and Prévost, et al. [8–10] have used the second interpretation to analyze earthquake

response of steel frames and earth dams, respectively. Based on observations made from experimental hysteresis loops as explained below, the second interpretation is chosen for the present study.

Özdemir [3] in testing mild steel for energy-absorbing devices under earthquake-type loading, obtained the hysteresis loops shown in Fig. 5.5. The closed hysteresis loops in Fig. 5.5 numbered as 4–5–7–8–4, 5–6–5, 8–9–8, 11–12–13–11 and 13–14–13 reinforce the implication of Rule 1, according to which every loop, irrespective of whether it corresponds to steady-state or transient response, forms a closed loop if continued long enough. More importantly, from the loops 5–6–5, 8–9–8, 4–5–7–8–4 and 13–14–13, it can be seen that they continue along 4–5–7, 7–8–4, 3–4–10 and 12–13–15, respectively, once they complete their respective inner loops. Hence it is assumed hereafter that an interior hysteresis curve at its completion of an inner loop starts to continue the load-deformation curve from a previous cycle just outside the completed loop (Rule 2).

5.2.4 Summary of A General Class of Masing Models

A general class of Masing models may, therefore, be defined which consists of all those hysteretic models with a virgin loading curve, or skeleton curve, defined in general by

$$f(x,r) = 0 \quad , \tag{5.1}$$

and for which any other hysteretic response curve is described by the following equation:

$$f\left(\frac{x - x^*}{2}, \frac{r - r^*}{2}\right) = 0 \quad , \tag{5.5}$$

where (x^*, r^*) is the load reversal point chosen appropriately using Rules 1 and 2.

It is important to note that to specify any particular model in this class, only its initial loading curve need be prescribed. These models give a complete description of hysteretic behavior for every possible loading type. It will be shown in subsequent sections that this class of models provides a unifying framework which incorporates other previously proposed hysteretic models.

- **Differential Form of the Model**

If the initial loading curve in Eq. 5.1 is written in terms of the instantaneous stiffness:

$$\frac{dr}{dx} = g(x,r) \quad , \tag{5.6}$$

then any branch curve is given by:

$$\frac{dr}{dx} = g\left(\frac{x - x^*}{2}, \frac{r - r^*}{2}\right) \quad , \tag{5.7}$$

where (x^*, r^*) is the point of load reversal chosen appropriately, using Rules 1 and 2.

5.2.5 Physical Interpretation and Some Applications of Masing's Model

A conceptual model of a single Masing-type element, as interpreted by Tanabashi and Kaneta [17], Herrera [18] and Iwan [6], is shown in Fig. 5.6. They have also shown that structural behavior can be modeled by combinations of coulomb friction and linearly elastic elements.

The behavior of dry or very permeable granular material is close to that of a Masing solid, provided the stress level is not so high as to cause extensive grain damage, as experimental evidence confirms this contention [19]. Masing's hysteresis model can also be used to explain characteristics of the hysteresis loop observed in the load-deformation curve, under alternate plus and minus loading, for complete steel girders, as well as structures with welded steel skeletons or monolithic reinforced concrete frames [17].

5.3 Ramberg-Osgood Model

A general nonlinear hysteretic force-deflection relation which is a smooth function and describes yielding behavior varying between the limits of linear and elasto-plastic cases was developed by Jennings [14]. He based his model on a formula first proposed by Ramberg and Osgood [20] to describe stress-strain relations in terms of three parameters for monotonic loading starting from the origin.

The skeleton (virgin) curve of this general force-deflection relation, which is of the softening type, symmetric about the origin and can be considered linear for small deflections, is described by the following equation:

$$\frac{x}{x_y} = \frac{r}{r_y} + \alpha\left(\frac{r}{r_y}\right)^n \quad , \tag{5.8}$$

where x is the displacement of the structure, x_y is a characteristic displacement, r is the restoring force, r_y is a characteristic force, α is a positive constant, and $n > 1$ is a positive odd integer to assure symmetry about the origin. A linear structure is described by $\alpha = 0$, and an elasto-plastic structure is approached as n tends to ∞ with α greater than zero.

Using tensile and compressive data on aluminum alloy, stainless steel and carbon-steel sheets, Ramberg and Osgood showed that their formula was adequate for most of these materials. Similar expressions have been used for static analysis of structures loaded into the plastic range [21].

The hysteretic behavior of the structure with a skeleton curve given by Eq. 5.8 is formulated using Masing's idea described in Section 5.2, so that the branches of the hysteresis loop are described by the same basic equation as the skeleton curve, except that the branch curves are scaled by a factor of 2 as follows:

$$\frac{x - x_i}{2x_y} = \frac{r - r_i}{2r_y} + \alpha\left(\frac{r - r_i}{2r_y}\right)^n \quad , \tag{5.9}$$

where $(x_i/x_y, r_i/r_y)$ is the most recent point at which the direction of the loading has been reversed. A typical hysteretic loop resulting from Eqs. 5.8 and 5.9 is shown in Fig. 5.7.

Skeleton curves and steady-state hysteresis loops of yielding structures are adequate for determining static response and steady-state response to periodic forces, but however are incapable of describing the response to random earthquake excitations. For this purpose, Jennings [14] defined the following two additional properties which specify the way in which the branch curves are linked together to represent arbitrary loading patterns:

(i) lower and upper bounding curves,

(ii) fate of an interior curve.

In his approach, force-deflection values are given by the hysteresis curve originating from the point of most recent loading reversal until either the upper or lower boundary is contacted. Thereafter the force-deflection values are given by that boundary until the direction of loading is again reversed.

It was thought that the above law was a reasonable approximation to the behavior of many actual structures, but insufficient experimental data were available to verify this at the time of Jennings' research. But based on the experimental evidence given for Masing models in Section 5.2.3, it is now clear that this law is not necessarily supported by real systems.

Difficulties associated with the Ramberg-Osgood representation include:

(1) An explicit expression for the force in terms of the displacement is not possible.

(2) For the transient response of yielding structures, Jennings' formulation of the hysteretic equation is difficult.

(3) Intersections of the upper and lower bounding curves with the skeleton curve sometimes must be found by iterative techniques.

(4) Model parameters α and n in Eq. 5.8 do not represent any physical quantities. Hence the direct estimation of these parameters from material properties and structural plans would be impossible.

(5) From Fig. 5.8 it can be seen that the Ramberg-Osgood model parameter n controls:

   (a) the mode of transition into the plastic range, and also

   (b) the hardening beyond the yield point.

   Therefore it is not possible to:

   (a) obtain an elasto-plastic model with a rounded knee, and

   (b) build into Ramberg-Osgood equations some other form of hardening [3].

Matzen and McNiven [15] tested a single story steel frame structure on a shaking table for an array of moderate and severe earthquake excitations. Computed hysteretic loops given by the Ramberg-Osgood model do not match the test hysteretic loops for the entire duration of the test. Also the displacement predictions were not good, primarily because of an offset between the test and model displacements. They concluded that two sets of Ramberg-Osgood model parameters are required to predict the response time-histories and hysteretic loops well, where one set is used for the brief initial phase during which the structure responds approximately elasto-plastically, and the other set is used for the second phase in which the hysteretic behavior is stabilized.

As a final remark, it should be noted that the Ramberg-Osgood model can be absorbed in the general class of Masing models by using Eq. 5.8 to define the skeleton curve.

5.4 Iwan's Model

As did Masing [4], Iwan [11] assumed that a general hysteretic system may be thought of as consisting of a large number of ideal elasto-plastic elements, each with the same elastic stiffness but having different yield levels. He examined the behavior of a system composed of a series of N elements in which each element consists of a linear spring with stiffness K/N in series with a coulomb or slip damper which has a maximum allowable force r_i^*/N. This arrangement of linear springs and coulomb dampers is shown in Fig. 5.9. Each element is therefore an ideal elasto-plastic unit and will have a force-deflection diagram as shown in Fig. 5.10 when cycled between fixed deflection limits. Because of its physical constituents, the model is considered to be physically motivated.

Based on contributions from the elements which have yielded and those which have not as yet yielded, the force-deflection relation for the entire system shown in Fig. 5.9, on initial loading, is given by

$$\tau = \sum_{i=1}^{n} r_i^*/\mathrm{N} + \mathrm{K}x(\mathrm{N}-n)/\mathrm{N}, \qquad \dot{x} > 0 \quad , \tag{5.10}$$

assuming that the elements are arranged in order of increasing yield force and where n is the number of elements in a positive yielded state. If the total number of elements N becomes very large, Eq. 5.10 may be written in an equivalent integral form:

$$r = \int_0^{\mathrm{K}x} r^*\phi(r^*)dr^* + \mathrm{K}x\int_{\mathrm{K}x}^{\infty} \phi(r^*)dr^* \qquad \dot{x} > 0 \tag{5.11}$$

where $\phi(r^*)dr^*$ is the fraction of the total number of elements with strengths in the range $r^* \le r_i^* \le r^* + dr^*$.

If $\mathrm{K}x\int_{\mathrm{K}x}^{\infty} \phi(r^*)dr^* \to 0$ as $x \to \infty$, then the ultimate strength of the system is given by:

$$r_u = \int_0^{\infty} r^*\phi(r^*)dr^* \quad . \tag{5.12}$$

For a continuous yield distribution function $\phi(r^*)$ and a finite r_u, the initial loading force-deflection curve of the system will have a general shape similar to that of curve OA in Fig. 5.11.

When the direction of loading is reversed after initial loading, as along curve ABC of Fig. 5.11, the total force will result from three different groups of elements: Those elements which were in a positive yield state after initial loading and have now changed to a negative

yield state; those elements which were in a positive yield state after the initial loading but have not yet changed to a negative yield state; and those elements which were unyielded on initial loading and are still unyielded. Thus the restoring force along the path ABC will be given by:

$$r = \int_0^{\mathrm{K}(x_a - x)/2} -r^*\phi(r^*)dr^* + \int_{\mathrm{K}(x_a-x)/2}^{\mathrm{K}x_a} [\mathrm{K}x - (\mathrm{K}x_a - r^*)]\phi(r^*)dr^* + \mathrm{K}x\int_{\mathrm{K}x_a}^{\infty} \phi(r^*)dr^* \qquad \dot{x} < 0,\ -x_a \le x \le x_a \quad . \tag{5.13}$$

In order to perform a dynamic analysis of the transient response of a yielding system, it is necessary to be able to describe the force-displacement relation of the system for arbitrary loading such as cyclic loading between variable limits. Recognizing this fact, Iwan [12] explains the manner in which the force-deflection relationship between C and D of Fig. 5.4 can be obtained, as follows:

If the fraction of elements in any given yielded or unyielded state is known at C, one need only determine what happens to each of these separate groups as the loading is reversed. This will lead to an expression for the force-displacement curve between C and D of the form:

$$r = \int_0^{\mathrm{K}(x-x_c)/2} r^*\phi(r^*)dr^* + \int_{\mathrm{K}(x-x_c)/2}^{\mathrm{K}(x_a-x_c)/2} (\mathrm{K}x - \mathrm{K}x_c - r^*)\phi(r^*)dr^* + \int_{\mathrm{K}(x_a-x_c)/2}^{\mathrm{K}x_a} (\mathrm{K}x - \mathrm{K}x_a + r^*)\phi(r^*)dr^* + \mathrm{K}x\int_{\mathrm{K}x_a}^{\infty} \phi(r^*)dr^* \qquad |x_c| < |x_a|, \quad x_c \le x \le x_a \quad . \tag{5.14}$$

The above procedure could be carried on indefinitely by keeping track of the fraction of elements in each of the yielded or unyielded category after each reversal in the direction of loading. In this way, the entire history of the hysteresis loops may be traced out without introducing any additional mathematical assumptions about the manner in which the loop curves change after each reversal of the direction of loading, which is in contrast to the situation in the case of purely mathematically motivated models such as the Ramberg-Osgood model discussed earlier. Iwan [6,11,12] considers that one of the important advantages of the distributed-element formulation is its ready adaptability to transient loading problems;

as in the case of steady-state loading, no additional assumptions need be made and the physics of the model itself dictates the history dependence of the loading behavior.

A review of Iwan's model shows that Eq. 5.13, which defines the steady-state response curve ABC of Fig. 5.11 (an unloading branch curve starting from virgin loading curve), and Eq. 5.14, specifying the transient response curve CD of Fig. 5.4 (a reloading branch curve not starting from the virgin curve), can be obtained using Masing's rules. All that is required is specification of the skeleton curve OA of Fig. 5.11 or Fig. 5.4 respectively, as in Eq. 5.11. Thus, Iwan's model falls within the general class of Masing models.

The above claims can be proved as follows: The stiffness of the entire system at any instant is given by the stiffness contributions from those elements which have not yet yielded. Therefore, for the virgin loading curve in Eq. 5.11,

$$\frac{dr}{dx} = \mathrm{K}\int_{\mathrm{K}x}^{\infty} \phi(r^*)dr^* \triangleq g(x) \qquad \dot{x} > 0 \quad . \tag{5.15}$$

Using similar arguments, the instantaneous (or tangent) stiffness corresponding to the steady-state response curve described by Eq. 5.13 is given by:

$$\frac{dr}{dx} = \mathrm{K}\int_{\mathrm{K}(x_a - x)/2}^{\mathrm{K}x_a} \phi(r^*)dr^* \; + \; \mathrm{K}\int_{\mathrm{K}x_a}^{\infty} \phi(r^*)dr^* \quad .$$

Therefore,

$$\frac{dr}{dx} = \mathrm{K}\int_{\mathrm{K}(x_a - x)/2}^{\infty} \phi(r^*)dr^* = g\left(\frac{x_a - x}{2}\right) \qquad \dot{x} < 0, \; -x_a \leq x \leq x_a \quad . \tag{5.16}$$

It is clear that Eq. 5.16 can be directly obtained from the skeleton curve of Eq. 5.15 by applying Masing's rules. Similarly, from the transient loading curve in Eq. 5.14,

$$\frac{dr}{dx} = \mathrm{K}\int_{\mathrm{K}(x - x_c)/2}^{\mathrm{K}(x_a - x_c)/2} \phi(r^*)dr^* \; + \; \mathrm{K}\int_{\mathrm{K}(x_a - x_c)/2}^{\mathrm{K}x_a} \phi(r^*)dr^* \; + \; \mathrm{K}\int_{\mathrm{K}x_a}^{\infty} \phi(r^*)dr^* \quad .$$

Therefore,

$$\frac{dr}{dx} = \mathrm{K}\int_{\mathrm{K}(x - x_c)/2}^{\infty} \phi(r^*)dr^* = g\left(\frac{x - x_c}{2}\right) \qquad |x_c| < |x_a|, \; x_c \leq x \leq x_a \quad . \tag{5.17}$$

Again Eq. 5.17 can be deduced from the initial loading curve of Eq. 5.15 by using Masing's rules. In addition, the implementation of the Masing model is much simpler, as indicated in Eqs. 5.15–17, compared with computing the force-deformation relationship for Iwan's

model by keeping track of element behavior, which involves several integral terms as shown in Eqs. 5.11, 5.13 and 5.14. It can also be shown that the fate of an interior curve leaving a completed loop is predicted by Iwan's model to be the same as specified by Rule 2 of the Masing model.

This confirms that Iwan's model falls within the general class of Masing models and that prescribing the yield distribution function $\phi(r^*)$ along with K is one way of prescribing the skeleton curve for the corresponding Masing model. This also shows that the Masing models are in accordance with the physics of a particular class of mechanical systems, namely those consisting of a collection of elastic springs and slip dampers in the manner described by Iwan. Therefore, the Masing models will not exhibit any nonphysical properties such as the ability of self-generating energy.

An application of Iwan's model using system identification was made by Cifuentes [32], to model the restoring force behavior of reinforced concrete structures subjected to earthquake-type dynamic loading. He modified Iwan's model to include stiffness and strength deterioration. This was done by assuming that all but one of the elasto-plastic elements in the model can break after they begin yielding at certain specified displacements, and they do not regain their stiffness and strength afterwards, thereby causing a permanent loss of stiffness and strength.

5.5 Other Models

5.5.1 Pisarenko's Model

Pisarenko [22] investigated the oscillations of elastic systems allowing for dissipation of energy in the material due to 'incomplete' elasticity. The need for such a study arose due to the demand for higher standards in the calculation of the dynamic strength of the components of high-speed machines such as turbines and motors. He adopted a relation proposed by Davidenkov [23] as the fundamental relation between forces and deformations which characterizes the very slight departure from Hooke's law for the majority of materials used in machine construction.

The expressions for the tangent stiffnesses in a symmetrical cycle as shown in Fig. 5.12 are given by:

$$\frac{dr}{dx} = \mathrm{K}[1 - \nu(x_0 + x)^{n-1}]$$

and (5.18)

$$\frac{dr}{dx} = \mathrm{K}[1 - \nu(x_0 - x)^{n-1}],$$

for the loading and unloading paths, respectively. The following final equations of the contour curves of the hysteresis loop were obtained by integrating Eq. 5.18 taking account of the boundary conditions of the branches of the hysteresis loop:

$$\begin{aligned} r &= \mathrm{K}\left\{x - \frac{\nu}{n}\left[(x_0 + x)^n - 2^{n-1}x_0^n\right]\right\} \quad \text{(loading)} \\ r &= \mathrm{K}\left\{x + \frac{\nu}{n}\left[(x_0 - x)^n - 2^{n-1}x_0^n\right]\right\} \quad \text{(unloading)} \quad . \end{aligned} \tag{5.19}$$

Pisarenko did not specify the virgin loading curve in his report. However, it can be shown that the above set of equations, 5.18 and 5.19, could also be obtained with an assumed virgin loading curve of

$$r = \mathrm{K}x\left[1 - \frac{\nu}{n}|2x|^{n-1}\right] \tag{5.20}$$

or, equivalently, with a tangent stiffness relation at the virgin loading of

$$\frac{dr}{dx} = \mathrm{K}\left[1 - \nu|2x|^{n-1}\right] \quad , \tag{5.21}$$

and then using Masing's rules. Equation 5.21 shows clearly that for larger displacements, the model possesses unstable characteristics.

5.5.2 Rosenblueth and Herrera's Model

Rosenblueth and Herrera [24] attempted to establish mildly nonlinear load-deformation, or stress-strain curves, for structures and materials with purely hysteretic damping, so that the model gives an equivalent degree of viscous damping which is independent of amplitude and of frequency under steady-state sinusoidal oscillations. The equivalent viscous damping ς of the nonlinear system is defined so that the energy lost per cycle by an equivalent linear system equals the energy lost per cycle by the nonlinear system.

The above conditions imply that the resulting load-deformation or stress-strain relationship should be

$$r = \mathrm{A}\, x^{\alpha} \tag{5.22}$$

on virgin loading, where A, α are material constants and

$$\alpha = (2 - \pi\varsigma)/(2 + \pi\varsigma) \;\leq\; 1 \quad . \tag{5.23}$$

In this derivation, Masing's rules are used to obtain the curves on unloading and reloading (Fig. 5.13). The model leads to a behavior very near to that of a linear viscoelastic material, except that the equivalent damping ratio does not depend on frequency or amplitude.

According to Rosenblueth and Herrera, very accurate measurements taken in a large triaxial machine showed that confined sands, gravels and broken rock behave in this manner almost up to failure. However, a much wider class of materials, including granular soils, have a different stress-strain behavior on first loading, although their unloading and reloading curves can still be modelled satisfactorily in accordance with Masing's rules. Also, the infinite stiffness at $x = 0$ resulting from Eq. 5.22 is objectionable on several counts, including the implied infinite velocity of small amplitude waves. Therefore, Eq. 5.29 can only be accepted as an idealization valid within a certain range of variables and for the calculation of certain phenomena.

5.5.3 A Group of Similar Models

In this section, three models which are similar in their description of hysteresis, namely Wen's model, the Endochronic model and a model developed by Özdemir, are discussed.

5.5.3.1 Wen's Model

A hysteretic restoring force model that allows analytical treatment was constructed by Wen [2,25] by requiring the displacement x and the force r to satisfy the following first-order nonlinear differential equation:

$$\dot{r} = -\gamma|\dot{x}|\, r\, |r|^{n-1} - \beta\dot{x}|r|^{n} + A\dot{x} \tag{5.24}$$

where n, γ, β and A are model parameters. Equation 5.24 can be integrated in closed form and one can show that a hysteretic relationship exists between r and x. Also, by adjusting the values of the model parameters, one can construct a large class of hysteretic systems, such as hardening or softening, and narrow- or wide-band systems. The case $n = 1$ in Eq. 5.24 was first proposed by Bouc [26].

Wen [27,28] later extended Eq. 5.24 to obtain a differential equation model for system hysteresis that admits stiffness and strength degradation, and he studied some important problems in civil engineering, such as the damage evaluation of buildings, soil-structure interaction and liquefaction of soil deposits. However, the hysteresis curves corresponding to Wen's model as shown in Figs. 5.14–16 indicate some inconsistencies, such as nonclosure and drift, with the real behavior of most materials and structures.

5.5.3.2 Endochronic Model

Endochronic theory [30] was originated by Valanis for the description of mechanical behavior of metals, such as strain hardening, unloading and reloading, cross-hardening, continued cyclic strainings and sensitivity to strain rate. Using Valanis' concept, Bazant extended the theory to describe the behavior of rock, sand, concrete, and reinforced concrete, under various conditions; for example, liquefaction of sand, and inelasticity and failure of concrete. The theory appears to have the capability of characterizing a broad range of inelastic behaviors and loading conditions without recourse to additional yield conditions and hardening rules.

A simple endochronic model for uniaxial behavior of metals is given by the following equation:

$$d\epsilon = \frac{1}{\mathrm{E}}\, d\sigma + \frac{\sigma}{\mathrm{ZE}}\, |d\epsilon| \quad , \tag{5.25}$$

where E is the elastic modulus and ZE is the limit stress of the material. This model is rate-independent and exhibits stress-strain behavior in a manner shown in Fig. 5.17.

Sandler [31] published a very interesting paper in which he demonstrated that such behavior violates Drucker's stability postulate and Ilyushin's postulate. Although the postulates of Drucker and Ilyushin are not strict physical or thermodynamical requirements for the behavior of real materials, they do play an important role in the construction of rational theories or models of material behavior for use in general dynamic problems. Through the construction of some simple examples, he showed that the endochronic models are unsuitable for numerical solution of dynamical problems, for reasons such as nonunique solutions for a physical problem with unique solution, and small errors in initial and/or boundary conditions leading to rapid deterioration in the accuracy of the subsequent computations.

5.5.3.3 Özdemir's Model

Özdemir's [3] objective was to obtain a mathematical model capable of describing the force-deformation relationship for energy absorbers under gross plastic deformations induced by random cyclic loading. He derived the following rate-independent model from a rate-dependent model for metals:

$$\frac{\dot{r}}{r_0} = \frac{\dot{x}}{x_0} - \left|\frac{\dot{x}}{x_0}\right| \left(\frac{r}{r_0}\right)^n \quad . \tag{5.26}$$

A typical hysteresis loop corresponding to Özdemir's model is shown in Fig. 5.18 which indicates that the loops are not necessarily closed.

5.5.3.4 Conclusion

From Eqs. 5.24–26, the following can be deduced for the case $\dot{x}$, $\dot{\varepsilon} > 0$ and r, $\sigma > 0$:

$$\begin{aligned}
&\text{Wen's model:} && \dot{r} = \mathrm{A}\dot{x}\left[1 - \left(\frac{r}{\left(\mathrm{A}/(\beta+\gamma)\right)^{1/n}}\right)^n\right] \\
&\text{Endochronic model:} && \dot{\sigma} = \mathrm{E}\dot{\varepsilon}\left[1 - \frac{\sigma}{\mathrm{ZE}}\right] \\
&\text{Özdemir's model:} && \dot{r} = \left(\frac{r_0}{x_0}\right)\dot{x}\left[1 - \left(\frac{r}{r_0}\right)^n\right]
\end{aligned} \tag{5.27}$$

Eq. 5.27 shows that all three models describe essentially the same hysteretic relationship. The inconsistent and unrealistic characteristics discussed for each class of models are therefore shared by all the models described by any one of the differential equations

5.24–26. The problems with these models are associated with the way they handle initial loading, unloading and reloading, although each model defines an acceptable virgin loading curve.

5.6 Model Used in the Present Study

Because of the wide range of engineering applications of Wen's, the endochronic and Özdemir's models, a similar hysteretic model is used in the present study, but the inconsistencies and difficulties associated with those models are eliminated because of better modeling of both the steady-state response and transient-loading response behavior.

The restoring force-deformation relation for the virgin loading is given by the differential equation:

$$\dot{r} = \mathrm{K}\dot{x}\left[1 - \left|\frac{r}{r_u}\right|^n\right] \quad ,$$

or, equivalently,

$$\frac{dr}{dx} = \mathrm{K}\left[1 - \left|\frac{r}{r_u}\right|^n\right] \quad , \tag{5.28}$$

where K, r_u and n are three model parameters which are sufficient to capture the essential features of the hysteretic behavior being modeled. The initial stiffness of the model is given by K, and the ultimate strength of the system is r_u, while the smoothness of the transition from elastic to plastic response of the force-displacement curve is controlled by n as seen in Fig. 5.19.

For the cases $n = 1$ and 2, Eq. 5.28 results in the following simple relationships when $r > 0$:

$$\frac{r}{r_u} = 1 - e^{-\mathrm{K}x/r_u}$$

and (5.29)

$$\frac{r}{r_u} = \tanh\left(\frac{\mathrm{K}x}{r_u}\right) \quad ,$$

respectively.

The inconsistent behavior of the previous three models described in Section 5.5.3 is eliminated by supplementing the model in Eq. 5.28 with Masing's rules to define the response to any loading situation. Therefore, the force-deflection relation for any loading other than at the virgin loading is defined by the differential equation:

$$\frac{dr}{dx} = \mathrm{K}\left[1 - \left|\frac{r - r_0}{2r_u}\right|^n\right] \quad , \tag{5.30}$$

where r_0 is the restoring force at the point of load reversal chosen according to Rules 1 and 2.

The relation above is simple and practical, and yet is general enough to be useful as a model for the dynamic, hysteretic behavior of a wide range of softening materials and structures. As shown in Figs. 5.20 and 5.21, the hysteresis loops for the model introduced are closed and exhibit no drift. An important feature of a model is our ability to select its parameters in a manner that is physically meaningful. This objective is easily achieved with the present formulation, since two of the parameters, namely K and r_u, are the initial stiffness and the ultimate strength of the system under investigation. This means, for example, that these parameters could be determined during structural design from material properties and the plans of a structure. Application of this model in system identification of hysteretic structures is discussed in the next chapter.

REFERENCES

[1] Jennings, P.C., "Periodic Response of a General Yielding Structure," *Journal of the Engineering Mechanics Division*, ASCE, Vol. 90(2), 131–166, April, 1964.

[2] Wen, Y.-K., "Method for Random Vibration of Hysteretic Systems," *Journal of the Engineering Mechanics Division,* ASCE, Vol. 102(2), 249–263, April, 1976.

[3] Özdemir, H., "Nonlinear Transient Dynamic Analysis of Yielding Structures," Ph.D. Dissertation, Division of Structural Engineering and Structural Mechanics, Department of Civil Engineering, University of California, Berkeley, California, June, 1976.

[4] Masing, G., "Eigenspannungen und Verfestigung beim Messing," *Proceedings of the 2nd International Congress for Applied Mechanics,* Zurich, Switzerland, 332–335, 1926. (German)

[5] Scott, R.F., *Foundation Analysis*, Prentice–Hall, Inc., Englewood Cliffs, New Jersey, 1981.

[6] Iwan, W.D., "On a Class of Models for the Yielding Behavior of Continous and Composite Systems," *Journal of Applied Mechanics*, ASME, Vol. 34(3), 612–617, September, 1967.

[7] Mróz, Z., "On the Description of Anisotropic Workhardening," *Journal of the Mechanics and Physics of Solids*, Vol. 15, 163–175, 1967.

[8] Prévost, J.-H., Abdel-Ghaffar, A.M. and Elgamal, A.-W.M. "Nonlinear Hysteretic Dynamic Response of Soil Systems," *Journal of Engineering Mechanics*, ASCE, Vol. 111(5), 696–713, May, 1985.

[9] Prévost, J.-H., Abdel-Ghaffar, A.M. and Lacy, S.J., "Nonlinear Dynamic Analyses of an Earth Dam," *Journal of Geotechnical Engineering*, ASCE, Vol. 111(7), 882–897, July, 1985.

[10] Elgamal, A.-W.M., Abdel-Ghaffar, A.M. and Prévost, J.-H., "Elasto-Plastic Earthquake Shear-Response of One-Dimensional Earth Dam Models," *Earthquake Engineering and Structural Dynamics*, Vol. 13, 617–633, 1985.

[11] Iwan, W.D., "A Distributed-Element Model for Hysteresis and Its Steady-State Dynamic Response," *Journal of Applied Mechanics*, ASME, Vol. 33(4), 893–900, December, 1966.

[12] Iwan, W.D. "The Distributed-Element Concept of Hysteretic Modeling and Its Application to Transient Reponse Problems," *Proceedings of the 4th World Conference on Earthquake Engineering*, Vol. II, A-4, 45–57, Santiago, Chile, 1969.

[13] Jennings, P.C., "Earthquake Response of a Yielding Structure, " *Journal of the Engineering Mechanics Division*, ASCE, Vol. 91(4), 41–68, August, 1965.

[14] Jennings, P.C., "Response of Simple Yielding Structures to Earthquake Excitation," Ph.D. Dissertation, California Institute of Technology, Pasadena, California, June, 1963.

[15] Matzen, V.C. and McNiven, H.D., "Investigation of the Inelastic Characteristics of a Single Story Steel Structure using System Identification and Shaking Table Experiments," Report No. EERC 76–20, Earthquake Engineering Research Center, University of California, Berkeley, California, August, 1976.

[16] Fan, W.R.-S., "The Damping Properties and the Earthquake Response Spectrum of Steel Frames," Ph.D. Dissertation, University of Michigan, 1968.

[17] Tanabashi, R. and Kaneta, K., "On the Relation Between the Restoring Force Characteristics of Structures and the Pattern of Earthquake Ground Motions," *Proceedings of the Japan National Symposium on Earthquake Engineering*, Tokyo, Japan, 57–62, 1962.

[18] Herrera, I., "Modelos Dinámicos para Materiales y Estructuras del Tipo Masing," *Bol. Soc. Mex. Ing. Sism.*, Vol. 3(1), 1–8, 1965. (Spanish)

[19] Newmark, N.M. and Rosenblueth, E., *Fundamentals of Earthquake Engineering*, Prentice Hall, Inc., Englewood Cliffs, New Jersey, 1971.

[20] Ramberg, W. and Osgood, W.R., "Description of Stress-Strain Curves by Three Parameters," Technical Note No. 902, National Advisory Committee on Aeronautics, July, 1943.

[21] Ang, A.H., "Analysis of Frame with Non-Linear Behavior," *Journal of the Engineering Mechanics Division* , ASCE, Vol. 86(3), 1–24, June, 1960.

[22] Pisarenko, G.S., "Vibrations of Elastic Systems Taking Account of Energy Dissipation in the Material," Technical Documentary Report No. WADD TR 60–582, February, 1962.

[23] Davidenkov, N.N., "On Energy Dissipation in Vibrations," *Journal of Technical Physics*, Vol. VIII(6), 483, 1938. (Russian)

[24] Rosenblueth, E. and Herrera, I., "On a Kind of Hysteretic Damping," *Journal of the Engineering Mechanics Division,* ASCE, Vol. 90(4), 37–48, August, 1964.

[25] Wen, Y.-K., "Equivalent Linearization for Hysteretic Systems Under Random Excitation," *Journal of Applied Mechanics*, ASME, Vol. 47(1), 150–154, March, 1980.

[26] Bouc, R., "Forced Vibration of Mechanical Systems with Hysteresis," Abstract, *Proceedings of the 4th Conference on Nonlinear Oscillation*, Prague, Czechoslovakia, 1967.

[27] Baber, T.T. and Wen, Y.-K., "Random Vibration of Hysteretic Degrading Systems," *Journal of the Engineering Mechanics Division*, ASCE, Vol. 107(6), 1069–1087, December, 1981.

[28] Wen, Y.-K., "Stochastic Response and Damage Analysis of Inelastic Structures," *Probabilistic Engineering Mechanics*, Vol. 1(1), 49–57, 1986.

[29] Spencer, Jr., B.F. and Bergman, L.A. "On the Reliability of a Simple Hysteretic System," *Journal of Engineering Mechanics*, Vol. 111(12), 1502–1514, December, 1985.

[30] Chen, W.-F., and Ting, E.C., "Constitutive Models for Concrete Structures," *Journal of the Engineering Mechanics Division*, ASCE, Vol. 106(1), 1–19, February, 1980.

[31] Sandler, I.S., "On the Uniqueness and Stability of Endochronic Theories of Material Behavior," *Journal of Applied Mechanics*, ASME, Vol. 45(2), 263–266, June, 1978.

[32] Cifuentes, A.O., "System Identification of Hysteretic Structures," Report No. EERL 84–04, Earthquake Engineering Research Laboratory, California Institute of Technology, Pasadena, California, 1984.

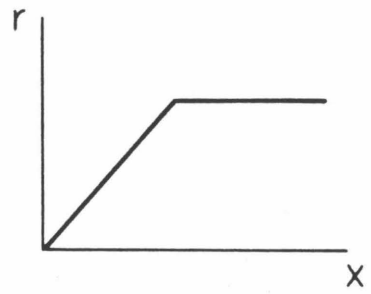

Fig. 5.1 Force-Deformation Curve of a Masing Element

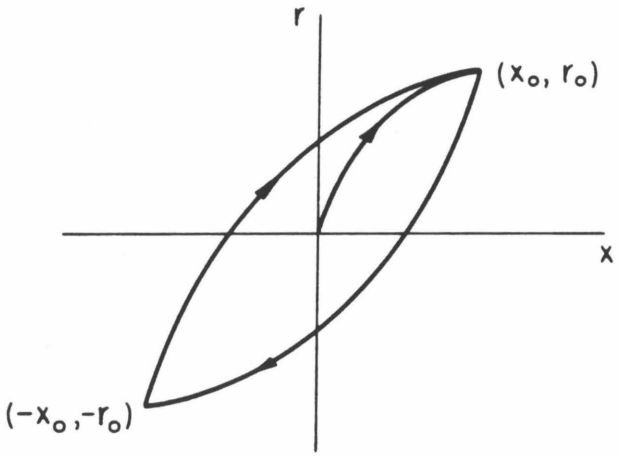

Fig. 5.2 Hysteretic Loop for Cyclic Loading

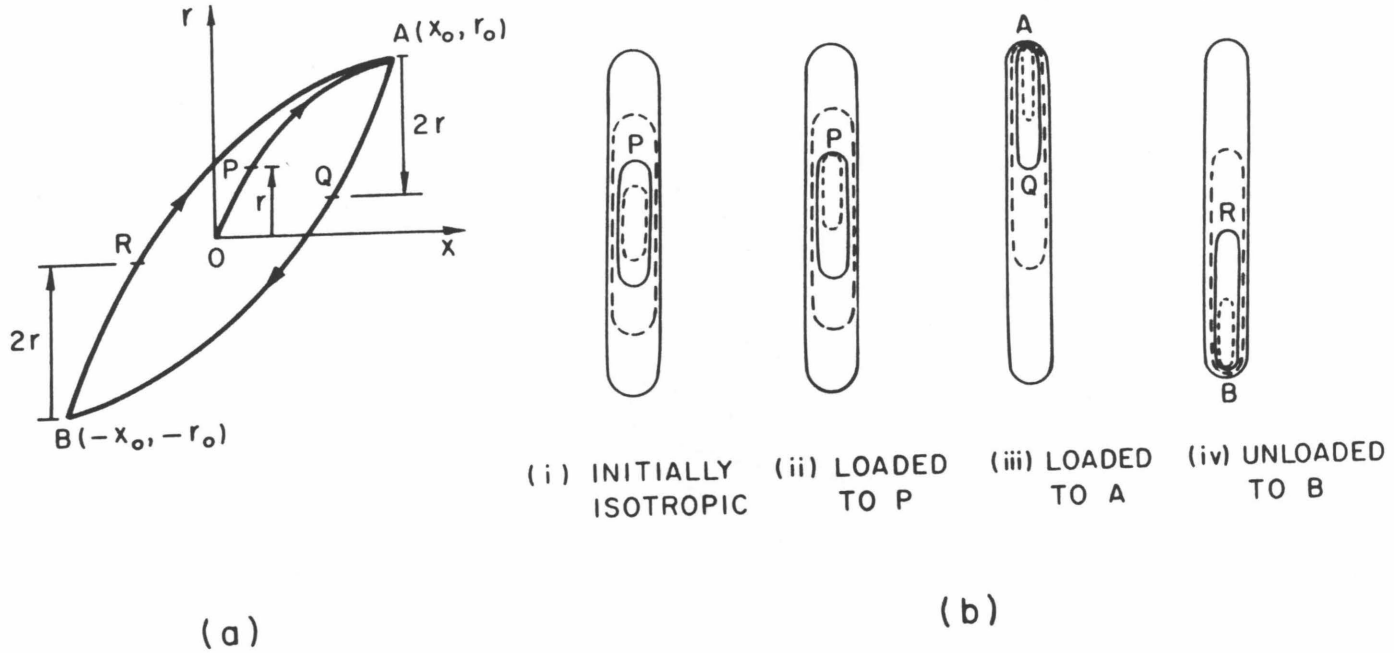

Fig. 5.3 (a) Masing Hysteresis Loop and (b) Multiple 'Stiffness' Surfaces

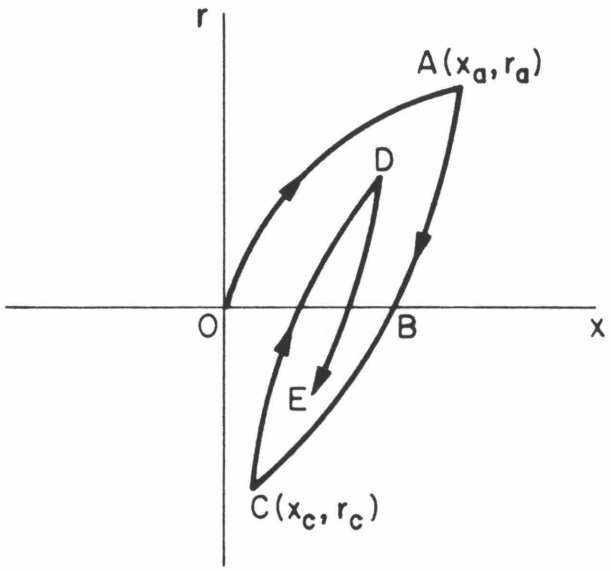

Fig. 5.4 Hysteretic Loop for Transient Loading

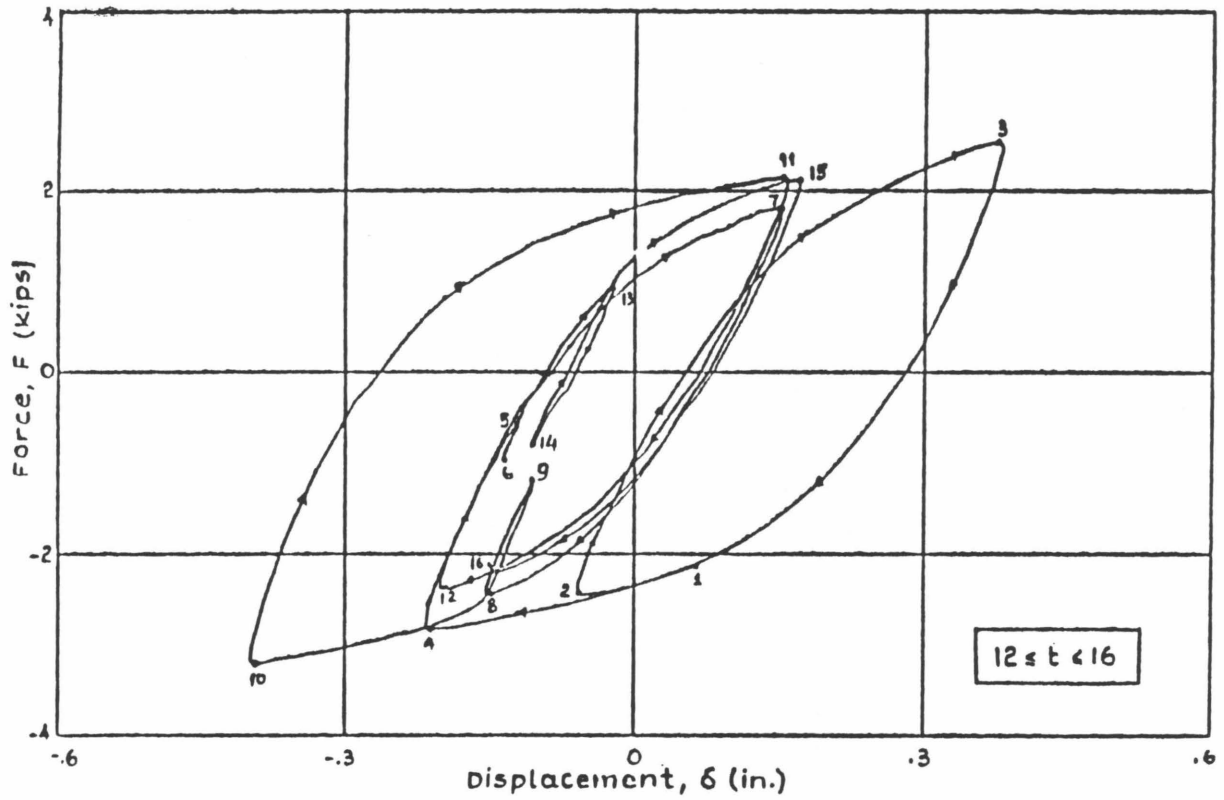

Fig. 5.5 Experimental Hysteresis Loops [3]

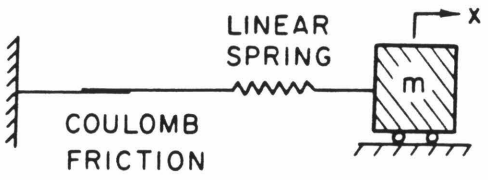

Fig. 5.6 Physical Interpretation of a Single Masing Element

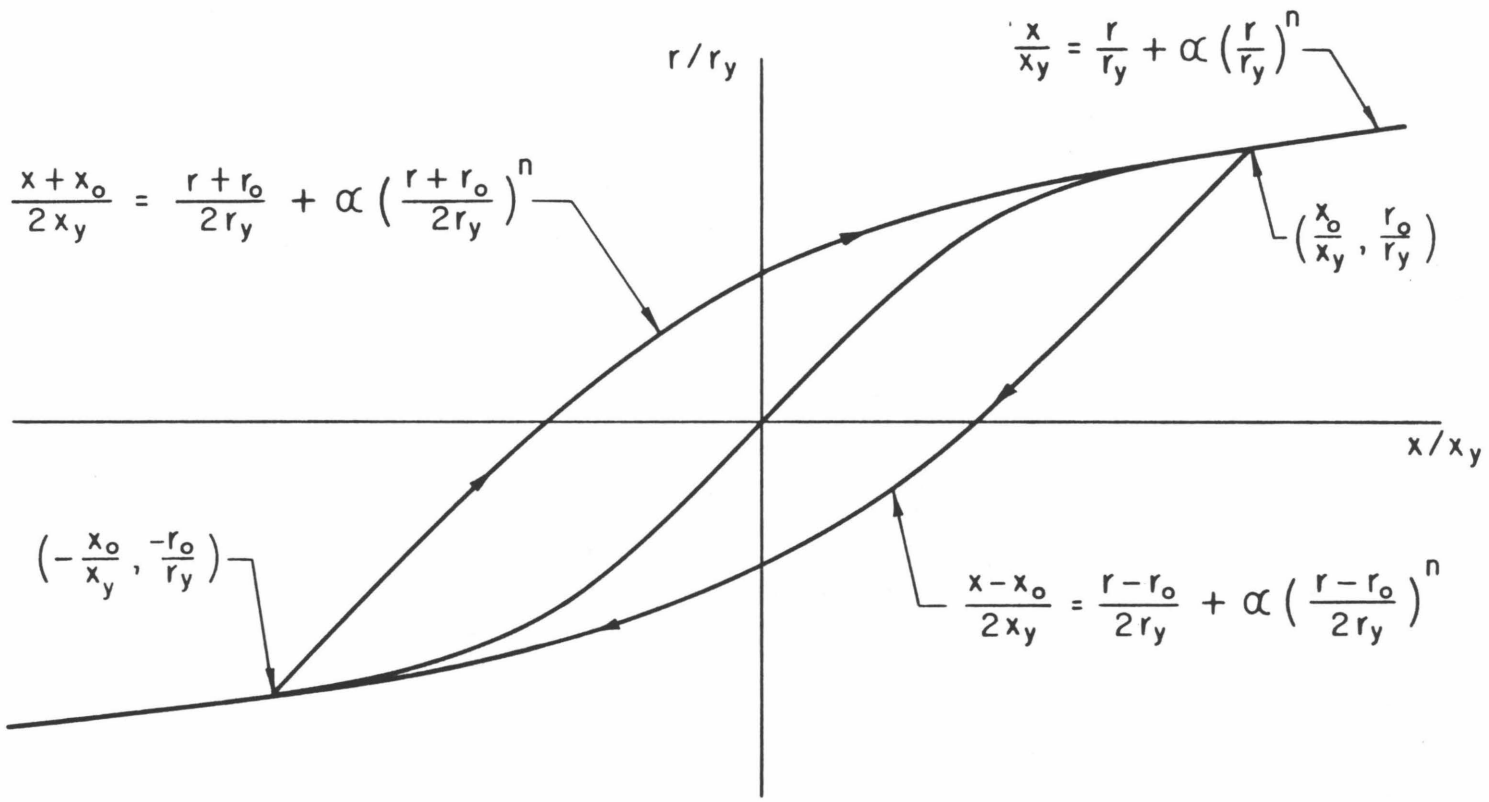

Fig. 5.7 Ramberg-Osgood Model [14]

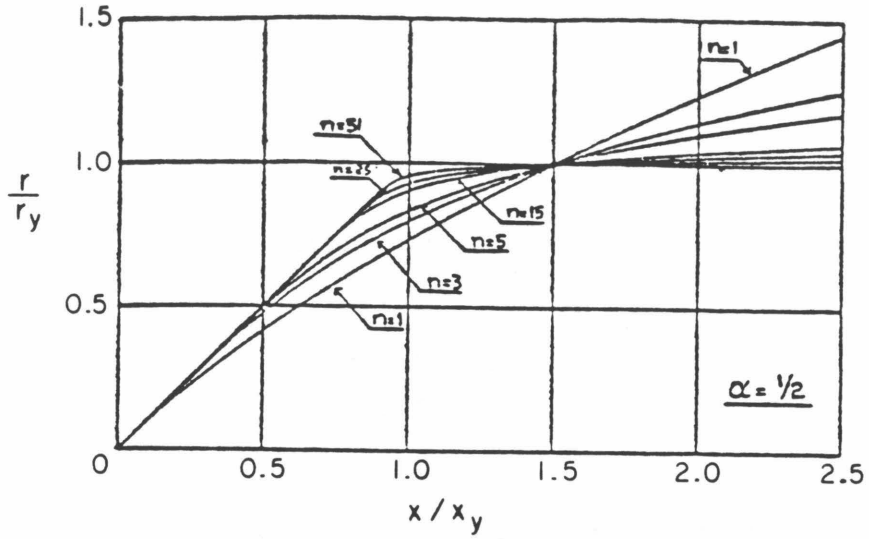

Fig. 5.8 Skeleton Curves Obtained via Ramberg-Osgood Relation [3]

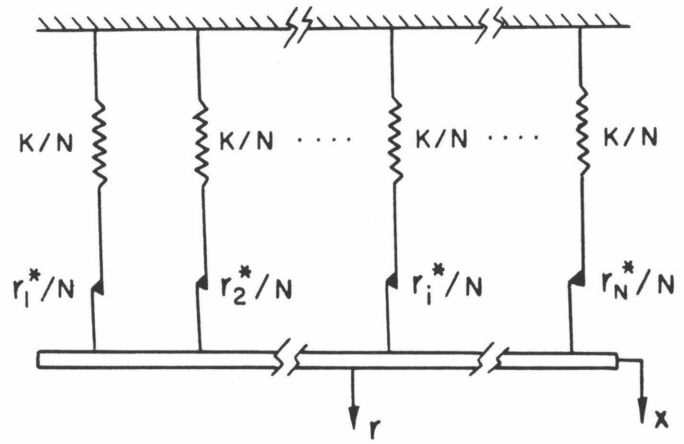

Fig. 5.9 Iwan's Model for a General Hysteretic System [11]

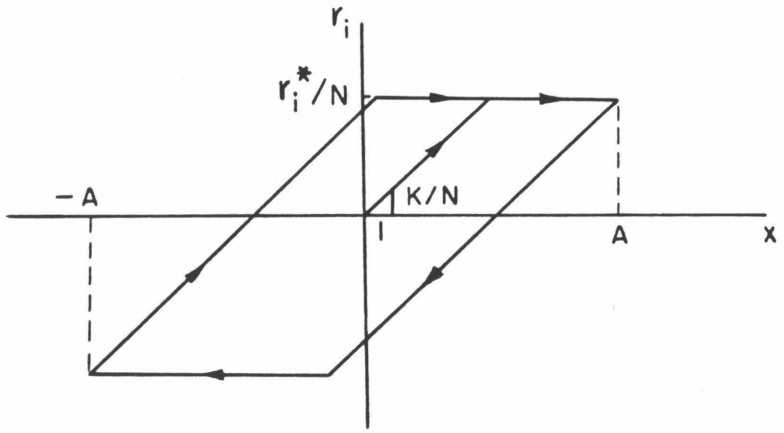

Fig. 5.10 Force-Displacement Relation of Each Elasto-Plastic Element in Fig. 5.9

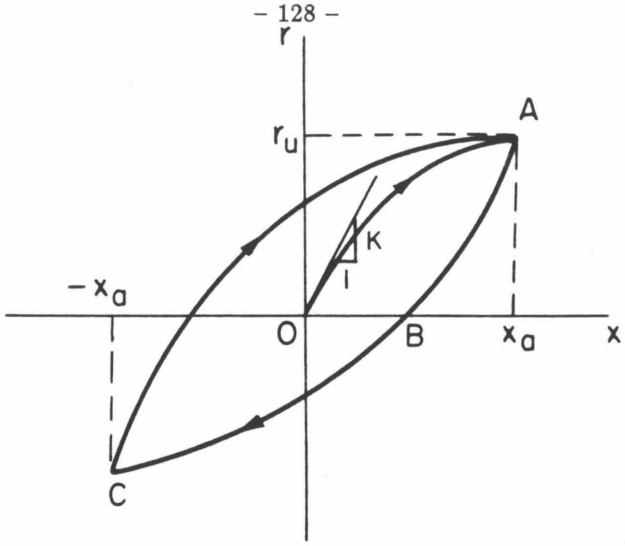

Fig. 5.11 Hysteresis Loop for Iwan's Model

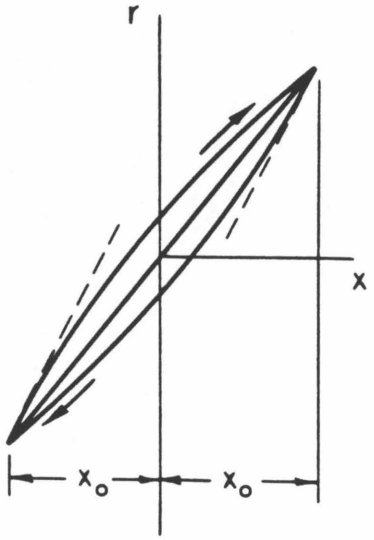

Fig. 5.12 Hysteresis Loop for the Model Studied by Pisarenko [22]

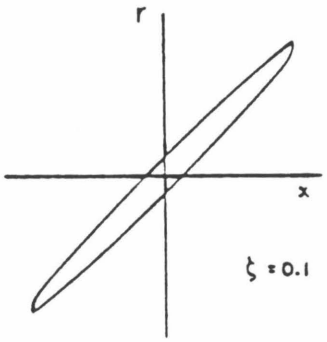

Fig. 5.13 Hysteresis Loop for Rosenblueth and Herrera's Model [24]

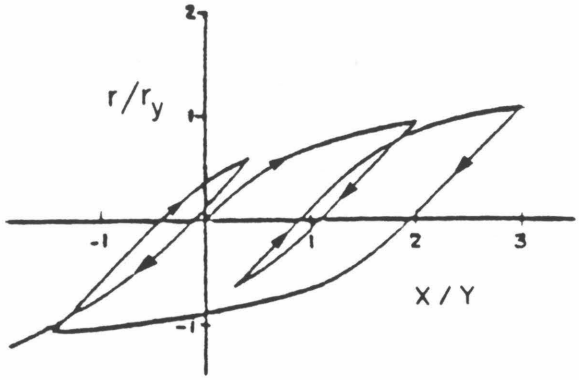

Fig. 5.14 Hysteretic Forces Corresponding to Random Displacements for Wen's Model [2]

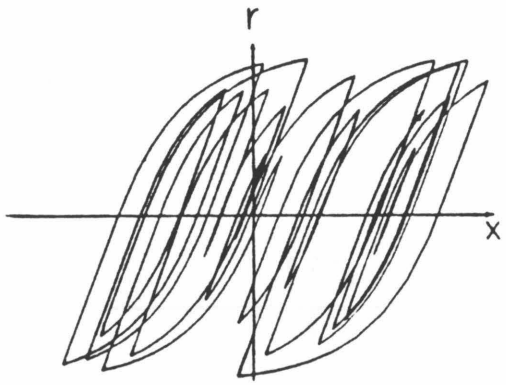

Fig. 5.15 Typical Force-Displacement Curves for Wen's Hysteretic Oscillator Subjected to White Noise Acceleration at Base [29]

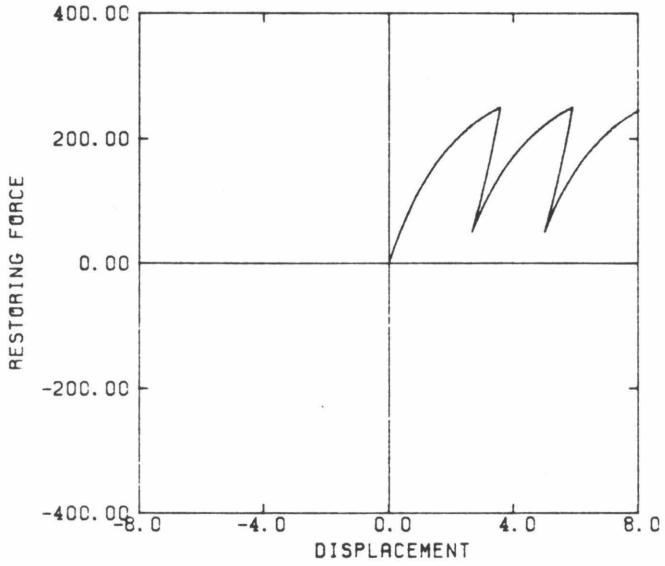

Fig. 5.16 Drifting Characteristic of Wen's Model

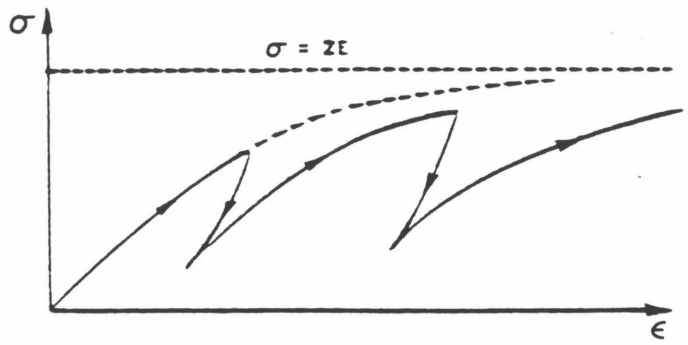

Fig. 5.17 Stress-Strain Behavior of a Simple Endochronic Model [31]

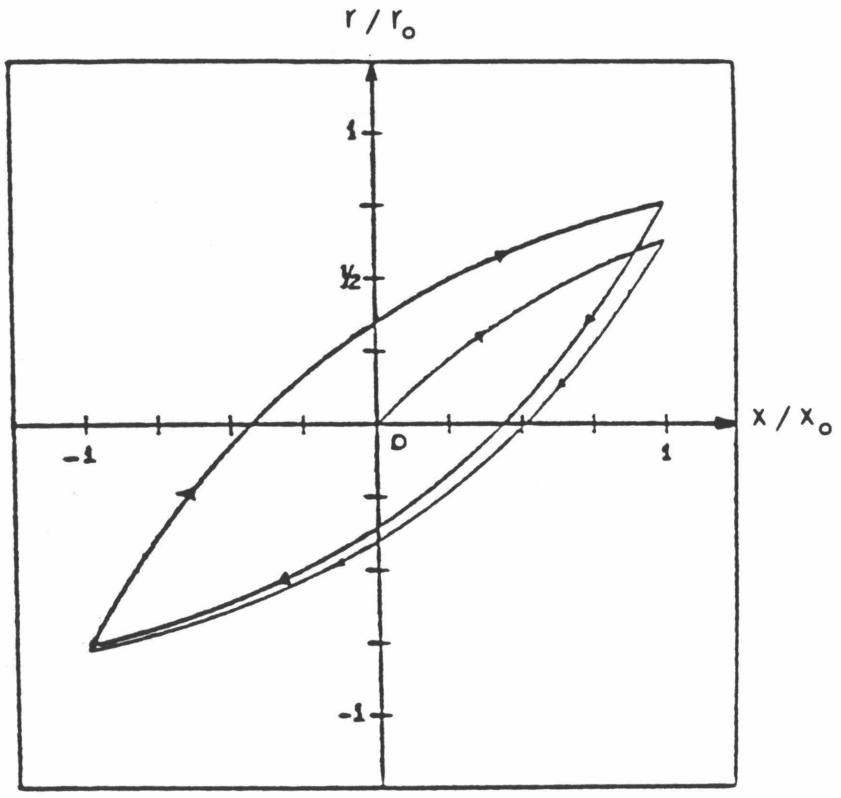

Fig. 5.18 Hysteresis Loop for Özdemir's Model [3]

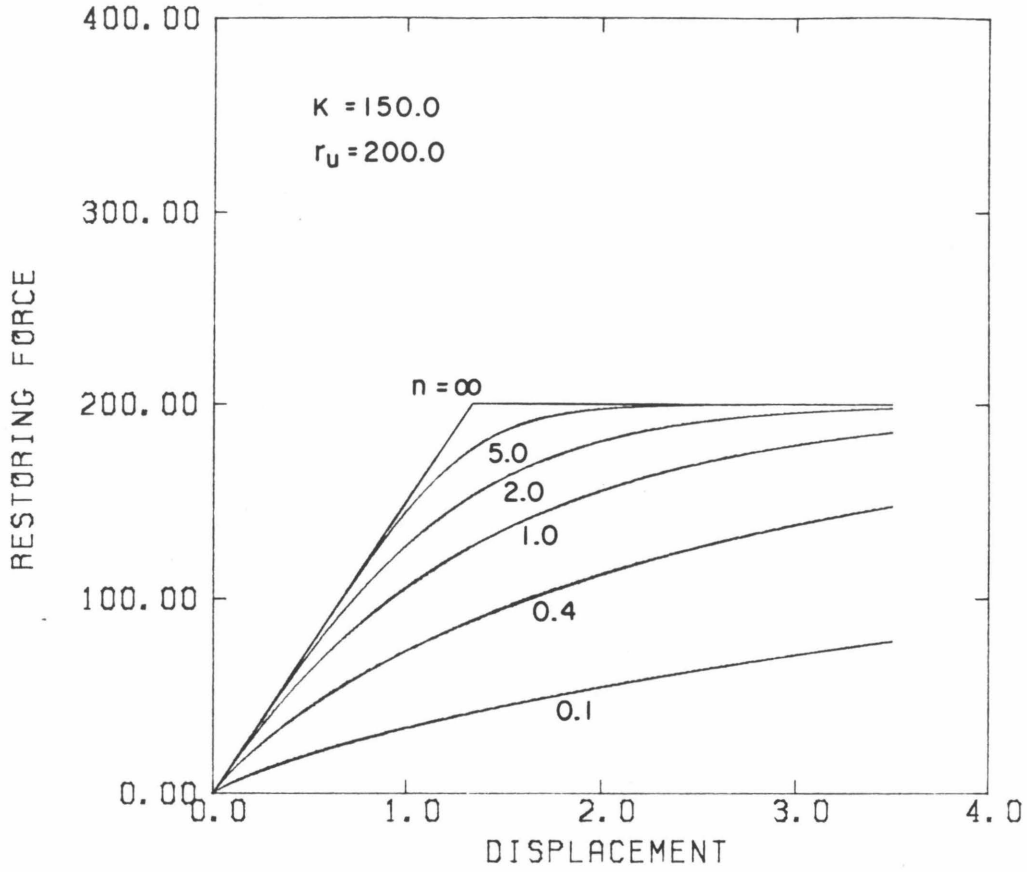

Fig. 5.19 Effect of n on the Force-Displacement Curve of Eq. 5.28

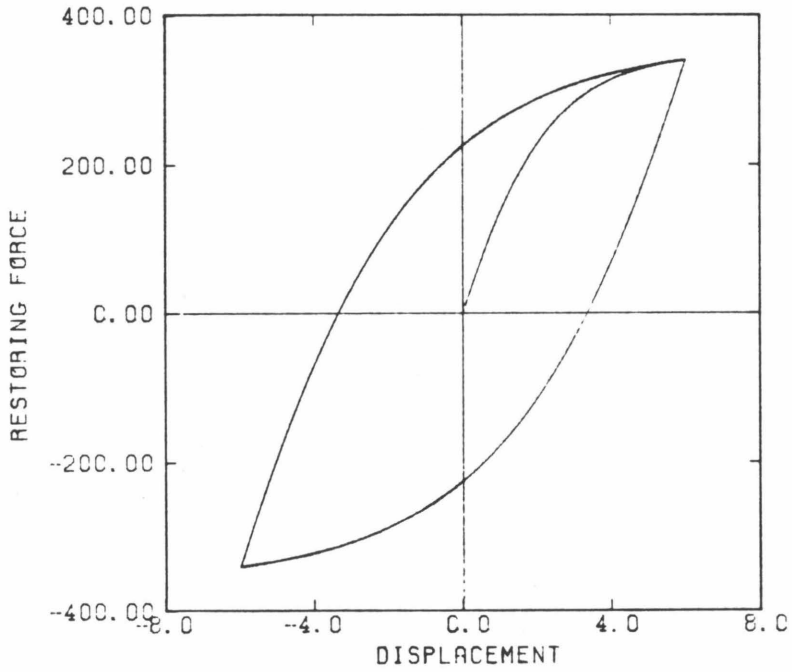

Fig. 5.20 Hysteresis Loop for Periodic Response of the Model in Eqs. 5.28 and 5.30

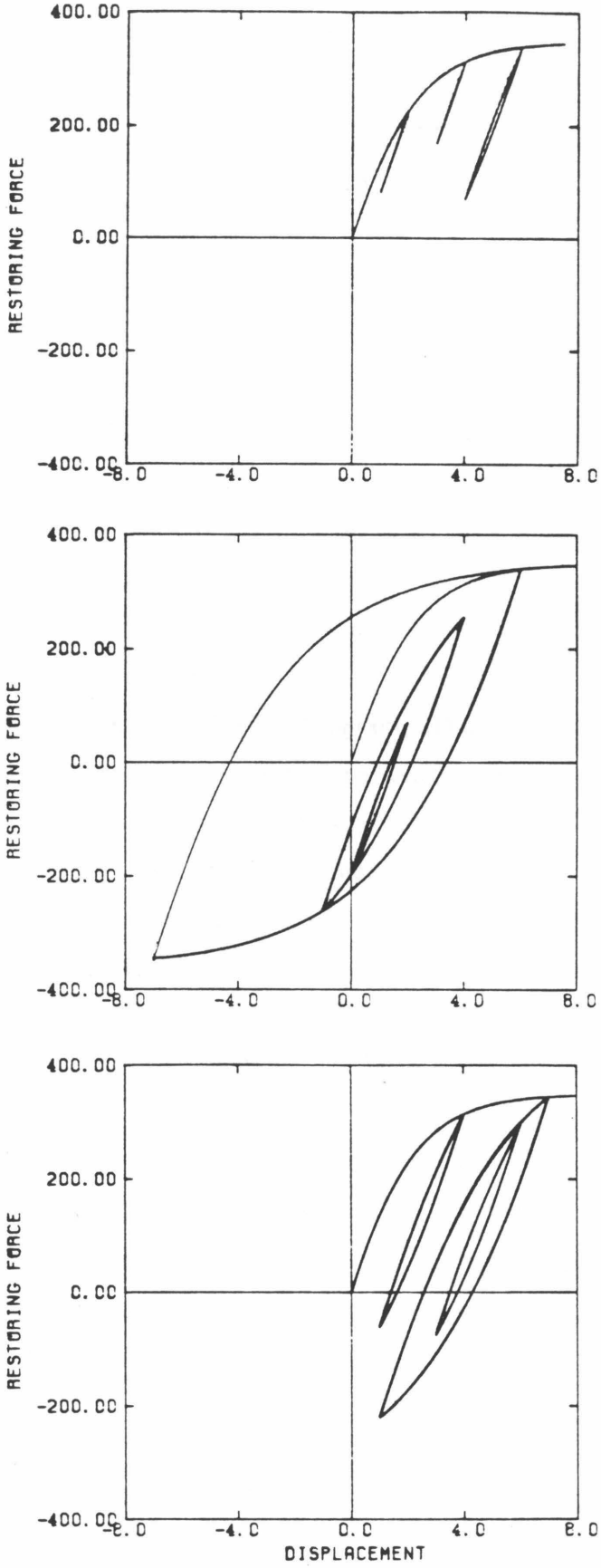

Fig. 5.21 Force-Displacement Curves for Arbitrary Loading of the Model in Eqs. 5.28 and 5.30

CHAPTER 6

SYSTEM IDENTIFICATION APPLIED TO THE INELASTIC PSEUDO-DYNAMIC TEST DATA

6.1 Introduction

In this chapter, it is shown how the restoring force-deformation relationship for a multi-degree-of-freedom structure excited by earthquake accelerations can be described using the new hysteretic model. For simplicity, the structure is then idealized as a shear building with the hysteretic model relating the story shears and story drifts. In particular, the pseudo-dynamic test structure, described in Chapter 2, which is a full-scale six-story steel-frame building, is modeled in this fashion, and methods are then given to estimate analytically the structural parameters involved in the modeling, such as the small-amplitude elastic stiffnesses and strengths of stories.

A hysteretic system identification program, HYSID, is developed to determine the optimal estimates of the hysteretic model parameters from experimental data. The optimization algorithm involves continual alternating between the steepest descent and the modified Gauss-Newton methods for the simultaneous identification of the optimal parameter values in a $(3N + 1)$-dimensional space where N is the number of degerees-of-freedom in the structure. This program is used to obtain the optimal estimates of 18 model parameters, resulting from the hysteretic modeling of the six-story test structure, by using the inelastic pseudo-dynamic test data. The prior estimates of the structural parameters described in the previous paragraph are used as the starting values for HYSID.

The prediction capability of the model obtained from the inelastic pseudo-dynamic test data is tested by subjecting it to the ground motion from the small-amplitude elastic pseudo-dynamic test and then comparing the model responses predicted with the measured structural responses. Conclusions are given concerning the prospects of using the hysteretic model in seismic analysis of structures.

6.2 Application of the Hysteretic Model to a Full-Scale Six-Story Steel Structure

6.2.1 Simplified Structural Model

The equation of motion of the N-story building in Fig. 2.1 can be written as:

$$M\ddot{\underset{\sim}{x}} + \underset{\sim}{R} = -M\ddot{z}(t)\,\underset{\sim}{1} \quad , \tag{6.1}$$

where $\underset{\sim}{R}$ is the vector of restoring forces at each degree of freedom. The restoring force R_i at the degree of freedom i stems from the interaction of that degree of freedom with all other degrees of freedom and with the ground. Therefore, the following relationship is assumed:

$$R_i = \sum_{\substack{j=0 \\ \neq i}}^{N} R_{ij} \quad , \tag{6.2}$$

in which R_{ij} $(j \neq 0)$ is the restoring force exerted at degree-of-freedom i by degree-of-freedom j due to the relative motion between the two, and R_{i0} is similar except it represents the interaction with the ground.

R_{ij} is hysteretic and depends on the history of relative displacement $(x_i - x_j)$, so R_{ij} is written in the following functional form:

$$R_{ij} = f_{ij}\,(x_i - x_j)\,, \qquad j = 0, 1, 2, \ldots, N; \quad j \neq i\,, \tag{6.3}$$

where $x_0 = 0$. The functionals f_{ij} are symmetric, i.e., $f_{ij}(x) = f_{ji}(x)$, and odd, i.e., $f_{ij}(-x) = -f_{ij}(x)$, so $R_{ji} = -R_{ij}$.

This model can be compared with the linear elastic case for which

$$R_{ij} = K_{ij} * (x_i - x_j) \quad , \tag{6.4}$$

where K_{ij} is the elastic stiffness of the spring between degrees of freedom i and j.

For the present hysteretic model which was introduced in Chapter 5, the virgin loading is given by the following nonlinear differential equation relating R_{ij} and $(x_i - x_j)$:

$$\dot{R}_{ij} = K_{ij}\,(\dot{x}_i - \dot{x}_j)\,\left[1 - \left|\frac{R_{ij}}{R_{u,\,ij}}\right|^{n_{ij}}\right] \quad , \tag{6.5}$$

where K_{ij} is the initial stiffness, $r_{u,\,ij}$ is the ultimate strength and n_{ij} is a model parameter, associated with the degrees-of-freedom i and j. The Masing model can be used to obtain any unloading and reloading branch curve.

6.2.1.1 Shear Building Approximation

By introducing a shear building approximation, it is assumed that the shear resistance to any degree of freedom comes only from its adjacent degrees of freedom,

$$\text{i.e.,} \quad R_{ij} = 0 \qquad \forall\, i,\, j \ni |i-j| > 1 \quad . \tag{6.6}$$

From Eq. 6.2,

$$R_i = R_{i,\,i-1} + R_{i,\,i+1} \quad . \tag{6.7}$$

With the introduction of story shears as shown in Fig. 6.1 in which $R_{i,i-1} = r_i$, $R_{i,i+1} = -r_{i+1}$, Eq. 6.7 becomes:

$$R_i = r_i - r_{i+1} \quad . \tag{6.8}$$

Equation 6.5 can be used to relate the story shear forces and story drifts in Fig. 6.1, according to which,

$$\dot{r}_i = K_i\,(\dot{x}_i - \dot{x}_{i-1}) \left[1 - \left|\frac{r_i}{r_{u,\,i}}\right|^{n_i}\right] \tag{6.9}$$

$$\dot{r}_{i+1} = K_{i+1}\,(\dot{x}_{i+1} - \dot{x}_i) \left[1 - \left|\frac{r_{i+1}}{r_{u,\,i+1}}\right|^{n_{i+1}}\right] \quad . \tag{6.10}$$

In the above hysteretic relationships, K_i and K_{i+1} are the initial stiffnesses, $r_{u,\,i}$ and $r_{u,\,i+1}$ are the ultimate strengths, and n_i and n_{i+1} are model parameters, of stories i and i+1, respectively. This shear building approximation will be used in the modeling of the pseudo-dynamic test structure described in the following section.

6.2.2 Structural Details of Test Building

As described in Section 2.5, a six-story, two-bay structure which would represent a portion of a complete building was adopted for the full-scale test. The floor plan of the test structure is shown in Fig. 2.7 and the elevations of the exterior and interior frames in Fig. 2.8. The material and structural properties of the members used are shown in Table 6.1, while the member sizes are presented in Figs. 6.2 and 6.3.

6.2.2.1 The Eccentrically-Braced Frame

Two of the most common structural systems used to resist seismically-induced forces are the moment-resisting frame and the concentrically-braced frame. However, a moment-resisting frame may not have enough elastic stiffness to control strong drift and nonstructural damage under service loads and minor earthquakes. The concentrically-braced frame

has excellent lateral elastic stiffness properties to control story drift and resist minor ground shaking, but the braces can repeatedly buckle under compressive cyclic loading and so can suffer a drastic decrease in their buckling strength and their ability to dissipate energy [2].

The eccentrically-braced frame has both the properties of high elastic lateral stiffness and good energy-dissipation capacity. By offsetting the braces a distance e as in Fig. 6.3, a link is formed between braces framing into a common girder. The performance of an eccentrically-braced frame during a major earthquake depends largely on the inelastic behavior of the links. In a well-designed eccentrically-braced frame, except for the plastic hinges at the ground level column bases, all the inelastic activity of the frame should be concentrated in the links. Also, the braces in the eccentric-bracing system can be designed not to buckle before the formation of active links in the girders, which is difficult to guarantee for concentrically-braced frames [2]. In the following section, a classification of active links is presented.

6.2.2.2 Active Links

The following classification has been developed [3,4] with reference to the behavior of active links, which strongly depends on their length. If they are sufficiently long, plastic moment hinges form at both ends of the links. On the other hand, if these links are short they tend to yield in shear with smaller end moments. The shear-moment interaction diagram shown in Fig. 6.4 can be used to illustrate the difference between the two kinds of active link behavior. The relevant parameters in reference to Fig. 6.5 are defined as follows:
The plastic moment capacity is:

$$M_p = f_y Z \quad , \tag{6.11}$$

in which the effect of shear is neglected, and f_y = yield stress of steel, and Z = plastic section modulus.
The plastic moment capacity reduced due to shear is:

$$M_p^* = f_y (b_f - t_w) t_f (d - t_f) \quad , \tag{6.12}$$

assuming that the web is in a plastic state and carries shear only.
The plastic shear capacity is:

$$V_p^* = \frac{f_y}{\sqrt{3}} (d - t_f) t_w \quad , \tag{6.13}$$

assuming that the web is yielding in shear and using the von Mises yield criterion.

At the balance point shown in Fig. 6.4, M_p^* and V_p^* are reached simultaneously. Then for the equilibrium of the link in Fig. 6.6 which is at the balance point,

$$e^* = \frac{2\,{M_p}^*}{{V_p}^*} \quad . \tag{6.14}$$

By comparing the actual lengths of links with e^*, the following conclusions can be reached:

(i) Active links whose lengths are equal to or shorter than e^* will yield predominantly in shear and are called shear links;

(ii) Links that are longer have moment-shear interaction;

(iii) The end moments of such long links will approach the plastic moment capacity M_p, and moment hinges will form at the ends of the links. These links are referred to as moment links.

Experimental results indicate that shear link action continues to predominate for lengths up to approximately $1.15e^*$ [5]. Also, it has been observed that shear links are more effective energy dissipators than moment links, although in frames shear links are likely to be subjected to larger ductility demands than longer moment links [3].

The analysis presented in this section is used later in this chapter to classify the links in the eccentrically-braced pseudo-dynamic test structure.

6.2.3 Prior Estimation of Structural Parameters

6.2.3.1 Story Stiffnesses by the First-Mode Approximation Method

In the first-mode approximation method (FMA) [6,7], the story stiffnesses for the shear-building model are calculated using known characteristics of the first mode, such as the fundamental frequency and the first-mode shape, of the structure being modeled. The modal properties may be from experiments in the case of an existing structure, or from a more detailed finite element model of the structure.

The modal equations of the shear-building model can be expressed as follows:

$$\mathrm{K}\,\underset{\sim}{\phi}^{(r)} = \omega_r^2\,\mathrm{M}\,\underset{\sim}{\phi}^{(r)} \tag{6.15}$$

where K is the stiffness matrix of the shear building, M is the diagonal mass matrix, ω_r is the natural frequency of the rth mode, and $\underset{\sim}{\phi}^{(r)}$ is the rth modeshape vector. Corresponding to the first mode, Eq. 6.15 becomes:

$$\mathrm{K}\,\underset{\sim}{\phi}^{(1)} = \omega_1^2\,\mathrm{M}\,\underset{\sim}{\phi}^{(1)} \quad . \tag{6.16}$$

For the test structure under consideration which is modeled as a six-story shear building, Eq. 6.16 could be expanded as follows:

$$\mathrm{K}\underset{\sim}{\phi}^{(1)} = \begin{bmatrix} \mathrm{K}_1+\mathrm{K}_2 & -\mathrm{K}_2 & & & \bigcirc & \\ -\mathrm{K}_2 & \mathrm{K}_2+\mathrm{K}_3 & -\mathrm{K}_3 & & & \\ & -\mathrm{K}_3 & \mathrm{K}_3+\mathrm{K}_4 & -\mathrm{K}_4 & & \\ & & -\mathrm{K}_4 & \mathrm{K}_4+\mathrm{K}_5 & -\mathrm{K}_5 & \\ & & & -\mathrm{K}_5 & \mathrm{K}_5+\mathrm{K}_6 & -\mathrm{K}_6 \\ & \bigcirc & & & -\mathrm{K}_6 & \mathrm{K}_6 \end{bmatrix} \begin{bmatrix} \phi_1^{(1)} \\ \phi_2^{(1)} \\ \phi_3^{(1)} \\ \phi_4^{(1)} \\ \phi_5^{(1)} \\ \phi_6^{(1)} \end{bmatrix}$$

$$= \omega_1^2 \, \mathrm{M}\underset{\sim}{\phi}^{(1)} \quad . \tag{6.17}$$

Equation 6.17 is now rearranged to give:

$$\begin{bmatrix} \phi_1^{(1)} & \phi_1^{(1)}-\phi_2^{(1)} & 0 & 0 & 0 & 0 \\ 0 & -\phi_1^{(1)}+\phi_2^{(1)} & \phi_2^{(1)}-\phi_3^{(1)} & 0 & 0 & 0 \\ 0 & 0 & -\phi_2^{(1)}+\phi_3^{(1)} & \phi_3^{(1)}-\phi_4^{(1)} & 0 & 0 \\ 0 & 0 & 0 & -\phi_3^{(1)}+\phi_4^{(1)} & \phi_4^{(1)}-\phi_5^{(1)} & 0 \\ 0 & 0 & 0 & 0 & -\phi_4^{(1)}+\phi_5^{(1)} & \phi_5^{(1)}-\phi_6^{(1)} \\ 0 & 0 & 0 & 0 & 0 & -\phi_5^{(1)}+\phi_6^{(1)} \end{bmatrix}$$

$$* \begin{bmatrix} \mathrm{K}_1 \\ \mathrm{K}_2 \\ \mathrm{K}_3 \\ \mathrm{K}_4 \\ \mathrm{K}_5 \\ \mathrm{K}_6 \end{bmatrix}$$

$$= \omega_1^2 \begin{bmatrix} \mathrm{m}_1 \, \phi_1^{(1)} \\ \mathrm{m}_2 \, \phi_2^{(1)} \\ \mathrm{m}_3 \, \phi_3^{(1)} \\ \mathrm{m}_4 \, \phi_4^{(1)} \\ \mathrm{m}_5 \, \phi_5^{(1)} \\ \mathrm{m}_6 \, \phi_6^{(1)} \end{bmatrix} \quad . \tag{6.18}$$

In the above formulation, $\mathrm{m_i}$ represents the mass associated with the ith degree-of-freedom, whereas $\phi_i^{(1)}$ is the component of the first mode at the ith degree-of-freedom.

The first-mode characteristics, as identified from the elastic pseudo-dynamic test data, are given in Table 4.1 of Chapter 4:

$$\omega_1 = 11.370 \text{ rad}/s, \text{ and}$$

$$\underset{\sim}{\phi}^{(1)} = [\,0.295,\ 0.531,\ 0.778,\ 1.012,\ 1.222,\ 1.403\,]^{\mathrm{T}} \, .$$

The mass matrix is taken to be the one given by Boutros and Goel [8]. Using these quantities, the system of linear equations (Eq. 6.18) can be solved for the story stiffnesses $K_1, K_2, \ldots, K_6$. The calculated story stiffnesses are given in Table 6.2, and their variation with story level is plotted in Fig. 6.7 where the stiffnesses are marked at the mid-points of the stories.

With the knowledge of the story stiffnesses, the stiffness matrix K of the shear building is constructed as in Eq. 6.17. Equation 6.15 is then solved for the natural frequencies and modeshapes corresponding to this stiffness matrix resulting from the first-mode approximation method. The calculated natural periods are given in Table 6.3 and the modeshapes are plotted in Fig. 6.8.

6.2.3.2 Story Stiffnesses Using Biggs' Formula

An approximate formula for the initial stiffness of a story in a multi-story frame, used by Anagnostopoulos [9] and reportedly from Biggs, is employed in this section. The stiffness of a particular story is estimated by making the following assumptions:

(a) column shears above and below a joint are equal;

(b) inflection points in columns above and below a joint are located symmetrically;

(c) rotation of all joints in a floor are equal.

With these assumptions and using slope-deflection equations, the following equation for the story stiffness was obtained:

$$K = \frac{24E}{h^2} \frac{1}{\sum \frac{2}{K_c} + \sum \frac{1}{K_{ga}} + \sum \frac{1}{K_{gb}}} \quad , \tag{6.19}$$

where

E = modulus of Elasticity,

h = story height,

l = beam length,

I = moment of Inertia,

$\sum K_c$ = $\sum (I/h)$ for all columns in the story,

$\sum K_{ga}$ = $\sum (I/l)$ for all beams in the floor above, and

$\sum K_{gb}$ = $\sum (I/l)$ for all beams in the floor below.

For braced frames one could use [9]:

$$K = K_{fr} + K_{br} \quad , \tag{6.20}$$

where K_{fr} is the story stiffness of the corresponding unbraced frame which is computed from Eq. 6.19, and K_{br} is the contribution by the braces to the story stiffness which is given by

$$K_{br} = \sum \frac{AE}{l} \cos^2 \alpha \quad , \tag{6.21}$$

where

A= area of bracing,

l = length of bracing,

α= angle between bracing and beam, and

Σ= summation over all the braces working in tension.

However, the braces of the test structure in the present study have been designed to resist both tension and compression, and in this eccentric bracing system the braces are not to buckle before the shear yielding of active links [1]. Hence, for the stiffness calculations following, the summation in Eq. 6.21 is taken over all the braces working in tension and also in compression.

Frames A and C of the test structure are unbraced moment-resisting frames with one column in each oriented for weak-axis bending, and their story stiffnesses are calculated using Eq. 6.19. Frame B of the test structure is also a moment-resisting frame, and in addition, it has eccentric K-bracings in its north bay. The story stiffnesses of frame B are calculated using Eqs. 6.19-21. The story stiffnesses of the test structure are then given by the sum of the story stiffnesses of all three frames A, B and C.

Stiffnesses of all the stories of the test structure are calculated in the above manner, and the results are presented in Table 6.2 and Fig. 6.7. With the knowledge of these story stiffnesses, the stiffness matrix K of the shear building is constructed as in Eq. 6.17. Equation 6.15 is then solved for the natural frequencies and modeshapes corresponding to this stiffness matrix resulting from Biggs' formula. The calculated natural periods are given in Table 6.3 and the modeshapes are plotted in Fig. 6.8.

6.2.3.3 Comparison of the First-Mode Approximation Method and Biggs' Formula

The initial story stiffnesses of the test structure have been estimated by the first-mode approximation method and also by using the Biggs' formula. The modal characteristics resulting from these approximations have also been computed.

Approximate values for the story stiffnesses are also measured directly from the hysteresis loops, obtained from the inelastic pseudo-dynamic test, which are shown in Fig. 6.9. Stiffness values from all three methods are now compared in Table 6.2 and Fig. 6.7. From Fig. 6.7, it is clearly seen that the first-mode approximation method gives rise to stiffnesses which are very close to the stiffness values measured directly from the test hysteresis loops. The Biggs' formula results in estimates of the story stiffnesses which are much too large except for the first story, confirming the observation of Lai and Vanmarcke [7]. This is not surprising since Anagnostopoulos [9] has already suggested that Biggs' formula for braced frames would not be as accurate as the formula for unbraced frames. It should be noted, though, that the Biggs' formula gives a purely theoretical result whereas the first-mode approximation method as used here utilized results derived from the structural tests.

The natural periods and modeshapes resulting from the first-mode approximation method and the Biggs' formula are compared in Table 6.3 and Fig. 6.8, respectively, along with the results from the system identification method applied to the 'elastic' pseudo-dynamic test data using the multiple-input multiple-output technique. In calculating the story stiffnesses by the first-mode approximation method, the shear building was assumed to have the same first-mode characteristics as that of the test structure estimated by the system identification method. Therefore, for this mode, the first-mode approximation method agrees exactly with the system identification results. However, for the other modes, it seems that Biggs' formula results in a slightly better comparison with the system identification results than the first-mode approximation method.

In summary, the first-mode approximation method results in better stifffness prediction though only the first-mode characteristics are reproduced well, while Biggs' formula does better with the higher modes. If the properties of the first mode can be estimated by reliable means such as experiments or detailed elastic finite element analyses, then it would be better to choose the first-mode approximation method to calculate story stiffnesses.

6.2.3.4 Estimation of Story Strengths

The strength of each story in the test structure is estimated by assuming that this story has been transformed into a mechanism. As shown in the following, the strength of each frame in the test structure is calculated separately, and the strengths of all three frames are then added in order to estimate the story strength.

(i) Plastic Moment Capacities of Columns and Girders

The plastic moment capacities of columns and the negative moment capacities of girders are calculated using the following equation:

$$M_p = f_y\, Z \tag{6.22}$$

where

f_y= yield stress of ASTM A36 steel, and

Z = plastic section modulus of steel member.

As mentioned above, only the negative moment capacities of composite girders can be calculated using Eq. 6.22 since slab concrete cracks in tension.

(ii) Plastic Positive Moment Capacity of Composite Girders

The positive moment capacities of girders are calculated by taking into account the composite action of steel girder and concrete slab [2,10].

(a) Effective Width of Composite Steel-Concrete Girders:

The effective width of concrete flange b_E (Fig. 6.10) is determined according to AISC: 1.11.1.

(b) Positive Moment Capacity

The procedure for determining the ultimate moment capacity depends on whether the neutral axis occurs within the concrete slab or within the steel girder. If the neutral axis occurs within the slab, the slab is said to be adequate, i.e., the slab is capable of resisting the total compressive force. If the neutral axis falls within the steel girder, the slab is considered inadequate, i.e., the slab is able to resist only a portion of the compressive force, the remainder being taken by the steel girder. In the following, full composite action is assumed, and also since any longitudinal reinforcement within the effective slab width usually makes little difference to the strength of a composite section, it is neglected.

- Case 1—Slab Adequate

From Fig. 6.11, the ultimate compressive force

$$C = 0.85 f'_c\, b_E\, a \tag{6.23}$$

and the ultimate tensile force

$$T = f_y A_s \quad . \tag{6.24}$$

Equating C and T for equilibrium gives

$$a = \frac{f_y \mathrm{A}_s}{0.85 f'_c \, \mathrm{b_E}} \quad . \tag{6.25}$$

According to AISC: 1.11.5.2-1, a from Eq. 6.25 has to satisfy the following:

$$a \leq t_c \quad , \tag{6.26}$$

where t_c is the concrete slab thickness above the steel deck.

The neutral axis distance x is calculated from

$$x = \frac{a}{\beta_1} \quad , \tag{6.27}$$

where β_1 is given by ACI: 10.2.7.3.

Full yield capacity of the steel girder is achieved when

$$\begin{aligned} x &< t_s \qquad \text{and} \\ \epsilon_s &\geq \epsilon_y \quad , \end{aligned} \tag{6.28}$$

where

$$\epsilon_s = 0.003 \left(\frac{t_s - x}{x} \right)$$

and (6.29)

$$\epsilon_y = \frac{f_y}{\mathrm{E_{steel}}} \quad .$$

Then the ultimate positive moment capacity M_u^+ becomes

$$\mathrm{M}_u^+ = \mathrm{T}l = f_y \mathrm{A}_s \left(\frac{d}{2} + t_s - \frac{a}{2} \right) \quad . \tag{6.30}$$

- Case 2—Slab Inadequate

If the depth a as determined in Eq. 6.25 exceeds the thickness t_c of the slab above the deck, the stress distribution will be as shown in Fig. 6.12, assuming the steel section accomodates plastic strain in both tension and compression at ultimate strength, i.e., a compact section.

The ultimate compressive force C_c in the slab is

$$\mathrm{C}_c = 0.85 f'_c \, \mathrm{b_E} \, t_c \quad . \tag{6.31}$$

The compressive force in the steel girder resulting from the portion of the girder above the neutral axis is shown in Fig. 6.12 as C_s.

The ultimate tensile force T satisfies

$$T = f_y A_s - C_s \quad . \tag{6.32}$$

For equilibrium,

$$T = C_c + C_s \quad . \tag{6.33}$$

From Eqs. 6.32 and 6.33,

$$C_s = \frac{f_y A_s - C_c}{2} \quad . \tag{6.34}$$

Assuming that the neutral axis is within the flange thickness of the girder,

$$C_s = f_y(b_f \delta) \tag{6.35}$$

from which δ can be calculated for the case $\delta \leq t_f$.

To determine h:

$$A_s \frac{d}{2} = (A_s - b_f \delta)h + (b_f \delta)(d - \frac{\delta}{2}) \quad . \tag{6.36}$$

The distances l_1 and l_2 in Fig. 6.12 are given by

$$\begin{aligned} l_1 &= d - h - \frac{\delta}{2} \qquad \text{and} \\ l_2 &= d + t_s - h - \frac{t_c}{2} \end{aligned} \quad . \tag{6.37}$$

The ultimate positive moment capacity M_u^+ for Case 2 is

$$M_u^+ = C_s l_1 + C_c l_2 \quad . \tag{6.38}$$

(iii) Capacity of Shear Links

Equations in Section 6.2.2.2 can be used to show that the portions of the girders between braces in the eccentrically K-braced frame B act as shear links. The shear capacity of these shear links, V_p^*, can be calculated using Eq. 6.13.

(iv) Behavior of Braces

At the ultimate capacity of a shear link, the shear force acting on that link is V_p^* ; then the maximum force acting on the brace will be

$$F_{br} = \frac{V_p^*}{\sin \alpha} \quad , \tag{6.39}$$

where α is the angle between the brace and the girder.

The brace forces corresponding to its yielding and buckling can be calculated, respectively, from

$$\begin{aligned} P_y &= f_{y,br}\, A_{br} \qquad \text{and} \\ P_e &= \frac{\pi^2 E I_{br}}{L^2} \quad . \end{aligned} \tag{6.40}$$

An effective column length factor of 1.0 [1] has been assumed in the calculation of the critical buckling load P_e in Eq. 6.40.

For all braces in the test structure, it can be shown that

$$F_{br} < P_e \text{ and } P_y \quad , \tag{6.41}$$

i.e., the braces neither yield nor buckle before the yielding of links in shear.

(v) Collapse Loads of Frames A, B and C

The story strength of each frame is calculated by applying the principle of virtual work to the corresponding story collapse mechanisms shown in Figs. 6.13 and 6.14. W and M's in these figures are the story collapse load and the plastic moment capacities of members, respectively.

According to the principle of virtual work,

$$\text{External Work} = \text{Internal Strain Energy} \quad . \tag{6.42}$$

- Frame A (C)

For the collapse mechanism of frame A(C) in Fig. 6.13, the virtual work principle gives

$$W h\phi = 2(M_1 + M_2 + M_3)\phi$$

$$W = \frac{2}{h}(M_1 + M_2 + M_3) \quad . \tag{6.43}$$

- Frame B

Similarly for frame B in Fig. 6.14,

$$W h\phi = (2M_1 + M_2 + M_3 + M_4 + M_5 + M_6)\phi \; + \; V_p^*(\theta + \phi)e$$

$$\theta + \phi = \frac{L}{e}\phi \qquad \text{gives}$$

$$W = \frac{1}{h}(2M_1 + M_2 + M_3 + M_4 + M_5 + M_6 + V_p^* L) \quad . \tag{6.44}$$

Once the story collapse loads of frames are calculated using Eqs. 6.43 and 6.44, the strength of the test structure is obtained by summing the collapse loads of all three frames at each story level. The results are shown in Table 6.4.

6.2.4 Optimal Estimation of Structural Parameters by System Identification

6.2.4.1 Hysteretic System Identification Technique, HYSID

An output-error approach for system identification called HYSID is used in conjunction with the steepest-descent and modified Gauss-Newton methods to determine the optimal estimates of the parameters for the hysteretic model from experimental data.

- **Output-Error Method**

The output-error $\underset{\sim}{e}$, defined in Eq. 3.1, is given by:

$$\underset{\sim}{e}(t;\underset{\sim}{\theta}) = [K_1(\underset{\sim}{x}_0 - \underset{\sim}{x}),\ K_2(\underset{\sim}{v}_0 - \underset{\sim}{\dot{x}}),\ K_3(\underset{\sim}{a}_0 - \underset{\sim}{\ddot{x}}),\ K_4(\underset{\sim}{r}_0 - \underset{\sim}{r})]^T \tag{6.45}$$

where each component is the output-error in the floor displacements, velocities, accelerations, relative to the ground, and story shears, respectively.
The model parameters are:

$$\underset{\sim}{\theta} = [\ldots, \{K_i,\ r_{u,i},\ n_i\}, \ldots]^T \quad i = 1, 2, \ldots, N \tag{6.46}$$

where N is the number of degrees of freedom in the structure, and K_i, $r_{u,i}$ and n_i are the story parameters described in Section 6.2.1.1.

The optimal values for the model parameters are calculated by minimizing a measure-of-fit $J(\underset{\sim}{\theta})$ which is obtained using the definition in Eq. 3.2 and the output-error $\underset{\sim}{e}$ in Eq. 6.45:

$$J(\underset{\sim}{\theta}) = K_1 V_1 \sum_{i=1}^{N} \int_{t_s}^{t_e} [x_{0,i} - x_i(\underset{\sim}{\theta})]^2 dt \ + \ K_2 V_2 \sum_{i=1}^{N} \int_{t_s}^{t_e} [v_{0,i} - \dot{x}_i(\underset{\sim}{\theta})]^2 dt$$

$$+ \ K_3 V_3 \sum_{i=1}^{N} \int_{t_s}^{t_e} [a_{0,i} - \ddot{x}_i(\underset{\sim}{\theta})]^2 dt \ + \ K_4 V_4 \sum_{i=1}^{N} \int_{t_s}^{t_e} [r_{0,i} - r_i(\underset{\sim}{\theta})]^2 dt \quad , \tag{6.47}$$

where the normalizing quantities are such that,

$$V_1^{-1} = \sum_{i=1}^{N} \int_{t_s}^{t_e} x_{0,i}^2 dt \quad , \qquad V_2^{-1} = \sum_{i=1}^{N} \int_{t_s}^{t_e} v_{0,i}^2 dt \quad ,$$

$$V_3^{-1} = \sum_{i=1}^{N} \int_{t_s}^{t_e} a_{0,i}^2 dt \quad \text{and} \qquad V_4^{-1} = \sum_{i=1}^{N} \int_{t_s}^{t_e} r_{0,i}^2 dt \quad .$$

- **Optimization Algorithm**

To determine the optimal estimates for the 3N model parameters which minimize the measure-of-fit $J(\underset{\sim}{\theta})$ in Eq. 6.47, a combination of the steepest-descent method and the modified Gauss-Newton method [11] is chosen because of its simplicity and computational efficiency over other gradient methods.

Steepest Descent Method:

The method of steepest descent is defined by the iterative algorithm

$$\underset{\sim}{\theta}_{k+1} = \underset{\sim}{\theta}_k - \rho_k \frac{\nabla J(\underset{\sim}{\theta}_k)}{\|\nabla J(\underset{\sim}{\theta}_k)\|_1} \quad , \tag{6.48}$$

where ρ_k is a nonnegative scalar minimizing $J\left(\underset{\sim}{\theta}_k - \rho \frac{\nabla J(\underset{\sim}{\theta}_k)}{\|\nabla J(\underset{\sim}{\theta}_k)\|_1}\right)$. In words, from the point $\underset{\sim}{\theta}_k$ we search along the direction of the negative gradient $\{-\nabla J(\underset{\sim}{\theta}_k)\}$ to a minimum point on this line; this minimum point is taken to be $\underset{\sim}{\theta}_{k+1}$.

Modified Gauss-Newton Method:

The measure-of-fit $J(\underset{\sim}{\theta})$ is approximated locally by a quadratic function and this approximate function is minimized exactly. If $\underset{\sim}{\theta}_k$ is the k-th estimate for the model parameters, J can be approximated by the truncated Taylor series near $\underset{\sim}{\theta}_k$ as:

$$J(\underset{\sim}{\theta}) \simeq J(\underset{\sim}{\theta}_k) + [\nabla J(\underset{\sim}{\theta}_k)]^T \, (\underset{\sim}{\theta} - \underset{\sim}{\theta}_k) + \frac{1}{2}(\underset{\sim}{\theta} - \underset{\sim}{\theta}_k)^T \, \nabla\nabla J(\underset{\sim}{\theta}_k) \, (\underset{\sim}{\theta} - \underset{\sim}{\theta}_k) \quad . \tag{6.49}$$

Then, $J(\underset{\sim}{\theta})$ is minimized at

$$\underset{\sim}{\theta}_{k+1} = \underset{\sim}{\theta}_k - [\nabla\nabla J(\underset{\sim}{\theta}_k)]^{-1} \, \nabla J(\underset{\sim}{\theta}_k) \quad . \tag{6.50}$$

If $J(\underset{\sim}{\theta})$ is twice continuously differentiable, then the algorithm is well-defined near the optimal estimates $\underset{\sim}{\hat{\theta}}$ since the Hessian matrix $\nabla\nabla J(\underset{\sim}{\theta})$ is positive definite. But for estimates remote from $\underset{\sim}{\hat{\theta}}$, this is not so, and the algorithm must be modified in order to guarantee convergence.

Since J is not quadratic in $\underset{\sim}{\theta}$ (Eqs. 6.9, 6.47), a stepsize $\rho > 0$ is introduced to ensure that the value of J decreases at every iteration step. For both the steepest descent and the

modified Gauss-Newton methods, the selection of step size is based on a one-dimensional line search in which a step size is doubled until the value of J no longer decreases. Then the step size corresponding to the minimum of the parabola which passes through the points bounding the minimum J is taken as the stepsize for the iteration. Also, the Hessian matrix may not be positive definite, or its inverse may not even exist, to yield a direction of descent in the multi-dimensional $J - \underset{\sim}{\theta}$ space. This is resolved by using an approximate Hessian $\nabla\tilde{\nabla}J(\underset{\sim}{\theta})$. These modifications to Eq. 6.50 give:

$$\underset{\sim}{\theta}_{k+1} = \underset{\sim}{\theta}_k - \rho_k \left[\nabla\tilde{\nabla}J(\underset{\sim}{\theta}_k)\right]^{-1} \nabla J(\underset{\sim}{\theta}_k) \quad . \tag{6.51}$$

∇J, $\nabla\tilde{\nabla}J$ which appear in Eqs. 6.48 and 6.51 can be calculated from Eq. 6.47 as follows:

$$(\nabla J(\underset{\sim}{\theta}))_j = -2K_1V_1 \sum_{i=1}^{N} \int_{t_s}^{t_e} (x_{0,i} - x_i) \frac{\partial x_i}{\partial \theta_j} dt - \ldots \qquad j = 1, 2, \ldots, 3N \quad . \tag{6.52}$$

The full Hessian is:

$$[\nabla\nabla J(\underset{\sim}{\theta})]_{jl} = -2K_1V_1 \sum_{i=1}^{N} \int_{t_s}^{t_e} (x_{0,i} - x_i) \frac{\partial^2 x_i}{\partial \theta_j \partial \theta_l} dt + 2K_1V_1 \sum_{i=1}^{N} \int_{t_s}^{t_e} \frac{\partial x_i}{\partial \theta_j} \frac{\partial x_i}{\partial \theta_l} dt$$

$$- \ldots \qquad j, l = 1, 2, \ldots, 3N \quad . \tag{6.53}$$

The integral terms containing the second derivatives of response quantities are dropped from the Hessian matrix, resulting in an approximate Hessian matrix:

$$[\nabla\tilde{\nabla}J(\underset{\sim}{\theta})]_{jl} = 2K_1V_1 \sum_{i=1}^{N} \int_{t_s}^{t_e} \frac{\partial x_i}{\partial \theta_j} \frac{\partial x_i}{\partial \theta_l} dt + \ldots \qquad j, l = 1, 2, \ldots, 3N \quad . \tag{6.54}$$

It can be shown that the scalar product:

$$< \underset{\sim}{y}, [\nabla\tilde{\nabla}J(\underset{\sim}{\theta})] \underset{\sim}{y} > \; = 2K_1V_1 \sum_{i=1}^{N} \int_{t_s}^{t_e} < \underset{\sim}{y}, \nabla x_i >^2 dt + \ldots \tag{6.55}$$

$$\geq 0 \quad \forall \underset{\sim}{y} \quad .$$

Therefore, the approximate Hessian is positive semi-definite. To ensure positive definiteness, a multiple λ of the identity matrix is added to the approximate Hessian whenever it is singular, where λ is a very small positive number. It can also be seen from Eqs. 6.53 and 6.54 that the approximate Hessian is close to the full Hessian near the optimal estimates.

In Eqs. 6.52-55, only the terms corresponding to the displacement output-error are shown for brevity.

The model responses and the sensitivity coefficients which appear in the expressions for J, ∇J and $\nabla\tilde{\nabla} J$ are calculated from the equation of motion of the structure together with the hysteretic relationship for the model using a fourth-order Runge-Kutta method. Figure 6.15 illustrates the process of parameter estimation in a very simplified flow diagram.

6.2.4.2 Analysis of Pseudo-Dynamic Inelastic Test Data

The pseudo-dynamic test structure was 'excited' by the Taft S21W accelerogram of the 1952 Kern County, California earthquake, scaled to a peak acceleration of 50% g (Fig. 6.16), to study the inelastic behavior of steel-frame structures during strong ground motions. This inelastic test data is analyzed using the hysteretic system identification technique, HYSID, described in the previous section, in order to determine the optimal estimates of the structural parameters which then enable prediction of the structural responses to other ground motions. In this study, the story shears are chosen for matching (i.e., $K_i = 0$, i = 1,2,3 and $K_4 = 1$, in Eq. 6.47) because of their significance in hysteretic modeling and the unique availability of measured shear forces due to the nature of the pseudo-dynamic test. The identification results are presented below.

- **Identification Results**

The hysteretic system identification program HYSID, described in the previous section, is used to estimate the optimal values of the structural parameters from the Phase II inelastic pseudo-dynamic test data. Several runs of the program HYSID were conducted, each with a different set of starting values for the model parameters, which are explained in Table 6.5. The value of measure-of-fit J at the begining of each run is also given in Table 6.5. The results of this investigation are presented in Table 6.6. The mean values of the optimal estimates from all nine runs are also calculated in Table 6.6. These optimal estimates of story stiffnesses, story strengths and n values are plotted in Fig. 6.18 along with their respective mean values to examine the reliability of the identified parameter values from different runs.

It should be expected that all the runs result in the same optimal estimates for the parameters. However, Fig. 6.18 shows that the parameters are not identified uniquely. This could be due to any presence of interaction between parameters which can result in a fairly flat region containing all the minimum points.

In spite of the diversity of the initial starting estimates for the different runs of HYSID as can be seen in Table 6.5, the optimal estimates are close in all cases, except for the story strengths of the top three stories which show a large scatter about their mean values in Fig. 6.18. This was expected because the structure did not experience any significant inelastic deformation at the top three stories (Fig. 6.9), and hence the determination of story strengths from these data is an ill-conditioned process since large changes in r_u make only small changes in the response. It is clear that a story strength cannot be estimated with any confidence if the story is not exercised well into its inelastic regime.

The mean values of the stiffnesses and strengths in Fig. 6.18 exhibit a decreasing trend with height, as expected, except for a lower first-story stiffness because of its higher flexibility; n takes values around 2.0. However, the fifth-story stiffness, strength of the fourth story and n values for stories 4 and 5 appear anomalous. The strength and n may be interacting because of the insignificant inelastic deformation of the top three stories during the test; stiffness of the fifth story is discussed below.

The stiffness matrix of the shear-building model whose story stiffnesses are the optimal estimates of stiffnesses of each case in Table 6.6, is calculated using Eq. 6.17 and then Eq. 6.15 is solved for the natural periods and modeshapes. The results are given in Table 6.7 and Fig. 6.19, respectively. Comparing Tables 6.3 and 6.7, it can be seen that the shear-building assumption in FMA and HYSID which made use of experimental results, causes the estimate for the third-mode period to be too high (0.13–0.14 sec) compared with the MI-MO result (of 0.10 sec) which is not based on such a model. The modest increase in the periods of the first two modes from HYSID compared to MI-MO may be the result of deterioration which causes period elongation. The interesting result is that the above modal characteristics for all the runs of HYSID are extremely close. For this reason, and also neglecting any small scatter of the optimal estimates about their mean values in Fig. 6.18, the mean values of the optimal estimates in Table 6.6 will be used for any further investigation. One final comment on the modeshapes is that the first mode has a kink at the fifth floor level as seen in Fig. 6.19. It is believed that this is an enlargement of a similar but milder kink in the MI-MO modeshape from the elastic test data. This kink may correspond to certain design features of the test structure which is not obvious from the design reports available to the author. This feature and possibly interaction between model parameters at the fourth and fifth story levels in HYSID are suspected to be reasons

for the surprisingly large stiffness for the 5th story in Fig. 6.18.

The time-histories of the optimal model responses at the roof level, mid-height and at floor 2 are compared with the test results in Fig. 6.20. The model predictions are excellent which is in agreement with the small values of measure-of-fit J in Table 6.6. Hysteresis curves obtained from the pseudo-dynamic test are compared with the curves 'predicted' by the optimal hysteretic model in Fig. 6.21. The hysteresis predictions are also very good.

A measure of the maximum amount of inelastic deformation each story has experienced during the test is defined by the 'fraction of inelasticity' as follows:

$$\text{Fraction of Inelasticity} = \frac{\text{Maximum Story Shear}}{\text{Story Strength}} \tag{6.56}$$

This fraction of inelasticity predicted by the optimal hysteretic model is calculated for each story of the test structure using the values of maximum story shear predicted by the model and the optimal estimates of the story strength, and the results are given in Table 6.8. These results suggest that the inelastic deformation experienced by the first three stories during the test should have been much larger compared to the top three stories which is indeed true as seen from the test hysteresis loops in Fig. 6.9. Also, that the fraction is close to unity in the first three stories demonstrates a strong nonlinear behavior and indicates that a linear model would have performed poorly.

6.3 Seismic Analysis of Structures Using the Hysteretic Model

The prediction capability of the hysteretic model is examined in this section in order to support the use of the model in seismic analysis of structures. It would be nice to test the optimal model discussed in the previous section using an independent inelastic test of the six-story structure. However, the only other pseudo-dynamic test data available to the author was the 'elastic' case where the test structure was subjected to the Taft S21W accelerogram with a scaled peak value of 6.5% g. These test data were therefore compared with the response calculated using the optimal model parameters identified from the pseudo-dynamic inelastic test data. The model responses predicted are compared with the measured elastic test data at the roof in Fig. 6.22. The time-histories of responses agree well over the duration of the test.

In addition, it also has to be noted that the optimal estimates of the model parameters, in general, do not differ very much from their prior estimates (Table 6.9) and therefore the latter also should give reasonably good response predictions. This is supported by the

small J-value of only 9% corresponding to the prior estimates. From Table 6.9, a value of 2 for the model parameter n seems reasonable for steel-frame structures, taking into account any possible interaction between the parameters of the fourth and fifth stories. This corresponds to the following force-deformation relationship on virgin loading:

$$\frac{r}{r_u} = \tanh\left(\frac{\mathrm{K}x}{r_u}\right) \tag{6.57}$$

It is planned to use the hysteretic model with other available earthquake data to estimate possible values of the model parameter n for different materials and structures. Thus, the hysteretic model could be used in the seismic analysis of structures using structural parameters estimated from the preliminary structural plans, thereby facilitating at the design stage an effective and iterative process to control structural responses to ground motions.

REFERENCES

[1] Askar, G., Lee, S.J. and Lu, L.-W., "Design Studies of the Six Story Steel Test Building: U.S.—Japan Cooperative Earthquake Research Program," Report No. 467.3, Fritz Engineering Laboratory, Lehigh University, Bethlehem, Pennsylvania, June, 1983.

[2] Ricles, J.M. and Popov, E.P., "Cyclic Behavior of Composite Floor Systems in Eccentrically Braced Frames," *Proceedings of the 6th Joint Technical Coordinating Committee Meeting*, U.S.—Japan Cooperative Research Program Utilizing Large-Scale Testing Facilities, Maui, Hawaii, June, 1985.

[3] Popov, E.P. and Malley, J.O., "Design of Links and Beam-to-Column Connections for Eccentrically Braced Steel Frames," Report No. UCB/EERC–83/03, Earthquake Engineering Research Center, University of California, Berkeley, California, January, 1983.

[4] Neal, B.G., "Effect of Shear Force on the Fully Plastic Moment of an I-Beam," *Journal of Mechanical Engineering Science*, Vol. 3(3), 258, 1961.

[5] Malley, J.O. and Popov, E.P., "Shear Links in Eccentrically Braced Frames," *Journal of Structural Engineering*, ASCE, Vol. 110(9), 2275-2295, September, 1984.

[6] Nielsen, N.N., "Dynamic Response of Multistory Buildings," Ph.D. Dissertation, California Institute of Technology, Pasadena, California, June, 1964.

[7] Lai, S.-S.P. and Vanmarcke, E.H. "Overall Safety Assessment of Multistory Steel Buildings Subjected to Earthquake Loads," Publication No. R80-26, Department of Civil Engineering, Massachusetts Institute of Technology, Cambridge, Massachusetts, June, 1980.

[8] Boutros, M.K. and Goel, S.C., "Pre-Test Analysis of the Six-Story Eccentric-Braced Steel Test Building," *Proceedings of the 5th Joint Technical Coordinating Committee Meeting*, U.S.—Japan Cooperative Research Program Utilizing Large-Scale Testing Facilities, Tsukuba, Japan, February, 1984.

[9] Anagnostopoulos, S.A., Roesset, J.M. and Biggs, J.M., "Non-Linear Dynamic Response and Ductility Requirements of Building Structures Subjected to Earthquakes," Publication No. R72-54, Department of Civil Engineering, Massachusetts Institute of Technology, Cambridge, Massachusetts, September, 1972.

[10] Salmon, C.G. and Johnson, J.E., *Steel Structures: Design and Behavior*, Harper & Row, Publishers, Inc., New York, 1980.

[11] Luenberger, D.G., *Introduction to Linear and Nonlinear Programming*, Addison-Wesley Publishing Co., Massachusetts, 1973.

Member	Property
Girders, Floor Beams and Columns	Wide-flange shapes made of ASTM A36 Steel
Braces	Rectangular tubes of ASTM A500 Grade B Steel
Slabs	$3\frac{1}{2}''$ lightweight concrete, approximate dry weight = 105 pcf, f'_c = 3000 psi
Decking	3" QL–99–16
Studs	$\frac{3}{4}''$ (19 Ø)

Table 6.1 Structural Properties of Members in the Test Structure [1]

Story	Elastic Stiffness (tonf/cm)		
	Test Hysteresis	FMA Method	Biggs' Formula
1	184.7	199.4	189.9
2	236.3	233.9	291.8
3	200.0	198.5	286.8
4	161.8	170.8	284.7
5	130.6	134.2	238.1
6	89.4	77.2	237.6

Table 6.2 Elastic Story Stiffnesses Estimated by Different Methods

Mode	Period (sec)		
	System Identification (MI–MO)	FMA Method	Biggs' Formula
1	0.553	0.553	0.489
2	0.191	0.218	0.170
3	0.104	0.142	0.105

Table 6.3 Natural Periods Estimated by Different Methods

Story	Strength (tonf)
1	295.1
2	323.8
3	264.9
4	255.5
5	183.1
6	172.1

Table 6.4 Story Strengths Estimated Using Collapse Mechanism

Case	Initial Estimate of $\underset{\sim}{\theta}$ (Eq. 6.46)	Initial J (%)
1	K for each story: prior estimates using the test hysteresis loops (Table 6.2) r_u for each story: prior estimates using collapse mechanism (Table 6.4) n for each story = 1.8: gives minimum value to the measure-of-fit J (Fig. 6.17) in which K and r_u used are the above prior estimates.	9.1
2	10% smaller than in Case 1	43.7
3	10% larger than in Case 1	65.9
4	+10%, -10%, +10%, -10%, ... larger than in Case 1	9.0
5	K, r_u: 15% larger than in Case 1 n : 15% smaller than in Case 1	56.0
6	K, r_u: 15% smaller than in Case 1 n : 15% larger than in Case 1	54.9
7	+20%, -20%, +20%, -20%, ... larger than in Case 1	8.5
8	25% smaller than in Case 1	106.7
9	25% larger than in Case 1	152.1

Table 6.5 Different Runs of the Program HYSID to Estimate the Optimal Values of the Structural Parameters from the Phase II Inelastic Test Data

Story	Parameter	Optimal Estimates									Mean Value
		Case 1	2	3	4	5	6	7	8	9	
1	K	188.0	190.1	183.0	194.3	190.4	189.4	201.0	192.1	195.1	191.5
	r_u	317.2	314.8	318.1	322.8	319.3	316.1	324.6	314.3	315.4	318.1
	n	1.6	1.6	1.6	1.5	1.6	1.6	1.4	1.6	1.7	1.6
2	K	214.4	215.6	216.3	210.3	216.5	214.7	204.0	212.6	214.9	213.3
	r_u	279.8	279.2	283.3	273.5	280.2	278.2	266.6	274.0	282.3	277.5
	n	1.7	1.7	1.7	1.9	1.7	1.7	2.2	1.8	1.7	1.8
3	K	172.2	171.9	175.4	169.2	168.9	172.5	171.9	174.4	169.6	171.8
	r_u	252.4	248.7	256.1	257.8	251.5	252.6	279.9	254.3	265.4	257.6
	n	2.3	2.3	2.3	2.3	2.5	2.3	1.8	2.1	2.0	2.2
4	K	155.9	153.2	160.0	154.9	155.9	154.3	151.2	147.7	144.6	153.1
	r_u	353.9	346.5	350.5	315.5	376.8	330.7	291.3	362.3	412.5	348.9
	n	3.1	3.1	2.9	3.4	3.0	3.2	3.4	3.2	3.4	3.2
5	K	257.8	254.0	256.5	267.2	268.8	251.7	251.5	233.9	239.5	253.4
	r_u	201.4	190.9	183.0	271.3	222.2	198.9	288.5	210.7	228.3	221.7
	n	1.0	1.1	1.2	0.7	0.8	1.2	0.9	1.4	1.4	1.1
6	K	109.8	109.8	102.9	113.7	116.1	106.6	110.1	125.4	104.7	111.0
	r_u	175.1	169.4	197.9	143.4	214.7	149.2	135.6	81.0	221.0	165.3
	n	1.9	1.8	2.2	2.0	1.7	2.2	2.2	1.9	2.5	2.0
J (%)		4.0	4.1	4.1	4.0	4.0	4.0	4.0	4.0	4.0	4.0

Table 6.6 Optimal Estimates of Structural Parameters from the Different Runs of HYSID

Case	Period (sec)					
	Mode 1	2	3	4	5	6
1	0.561	0.196	0.134	0.099	0.076	0.071
2	0.561	0.196	0.134	0.099	0.076	0.071
3	0.561	0.198	0.136	0.099	0.076	0.070
4	0.560	0.194	0.133	0.099	0.076	0.070
5	0.560	0.194	0.132	0.098	0.075	0.070
6	0.561	0.197	0.135	0.099	0.076	0.071
7	0.561	0.196	0.133	0.099	0.077	0.071
8	0.562	0.196	0.130	0.099	0.077	0.072
9	0.564	0.199	0.136	0.100	0.077	0.072

Table 6.7 Comparison of Modal Periods Corresponding to the Optimal Story Stiffnesses Resulting from the Different Runs of HYSID

Story	Fraction of Inelasicity, Predicted
1	0.92
2	0.93
3	0.85
4	0.56
5	0.64
6	0.41

Table 6.8 Predicted Values for the Extent of Inelastic Deformation

Story	Elastic Stiffness (tonf/cm)		Strength (tonf)		n	
	Prior	Optimal	Prior	Optimal	Prior	Optimal
1	184.7	191.5	295.1	318.1	1.8	1.6
2	236.3	213.3	323.8	277.5	1.8	1.8
3	200.0	171.8	264.9	257.6	1.8	2.2
4	161.8	153.1	255.5	348.9	1.8	3.2
5	130.6	253.4	183.1	221.7	1.8	1.1
6	89.4	111.0	172.1	165.3	1.8	2.0

Table 6.9 Comparison of the Prior and Optimal Estimates of the Structural Parameters

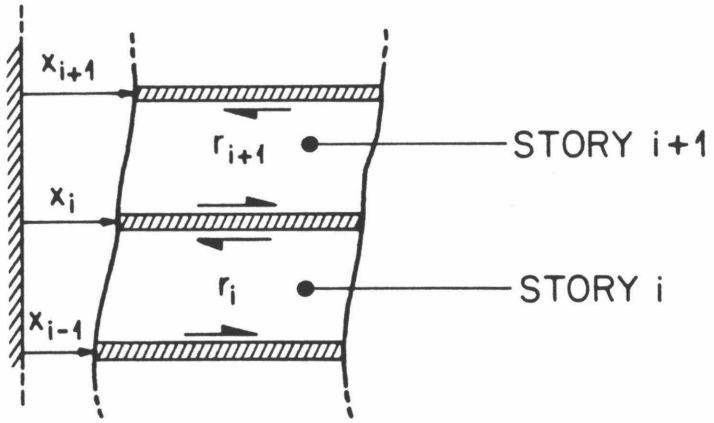

Fig. 6.1 Illustration of Story Shear Forces and Story Drifts

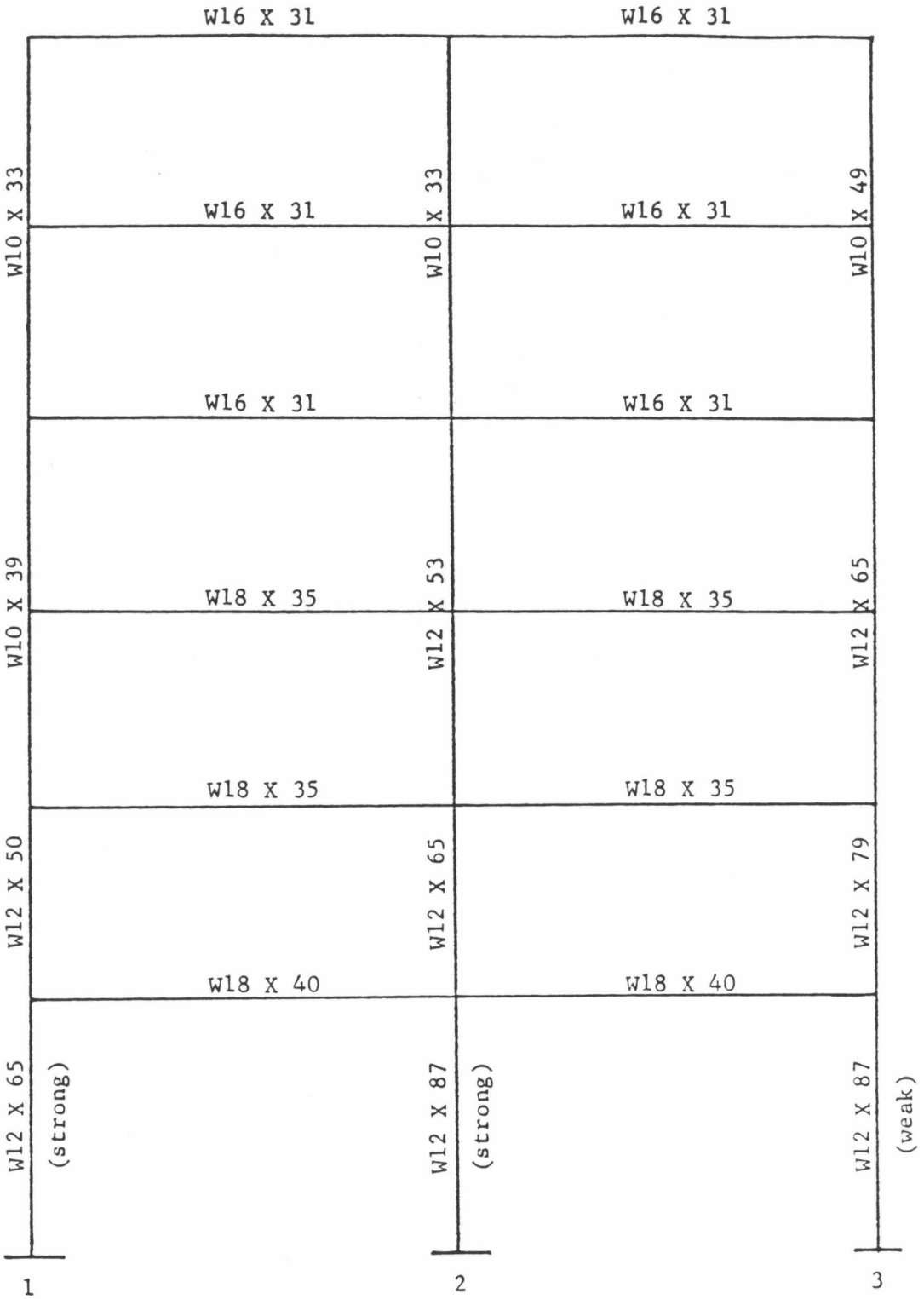

Note: Girders for lines 1 & 3, G_3 (all levels) W18 X 35
Girders for line 2, G_4 (all levels) W21 X 50
Floor beams (all levels) W16 X 31

Fig. 6.2 Member Sizes of Moment Frames A & C [1]

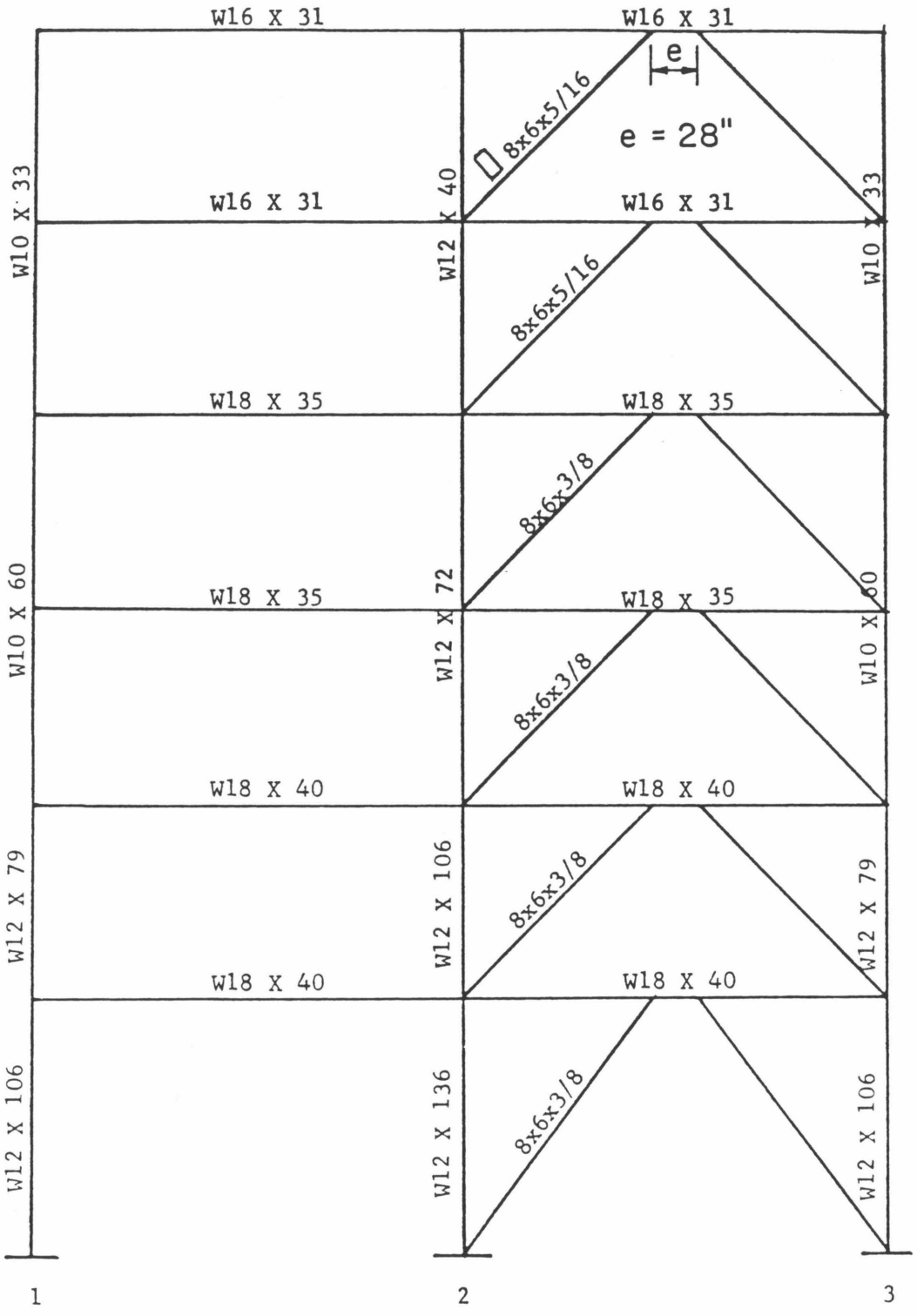

Fig. 6.3 Member Sizes of Braced Frame B with Eccentric Braces [1]

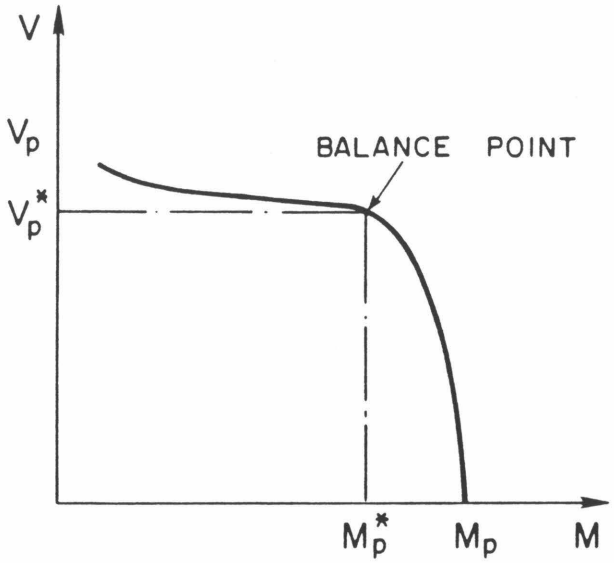

Fig. 6.4 Typical Shear-Moment Interaction Diagram for Wide Flange Sections [3]

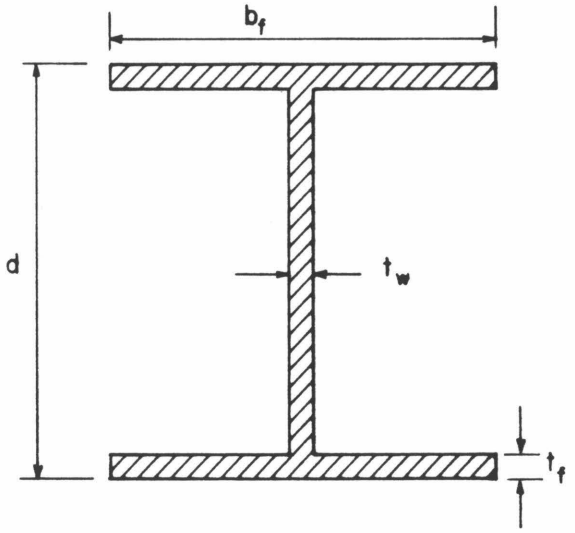

Fig. 6.5 Girder Dimensions

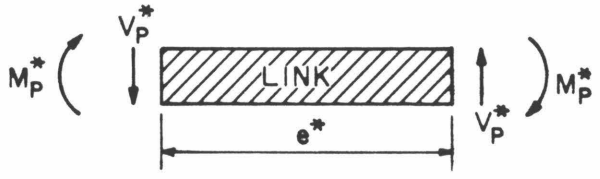

Fig. 6.6 An Active Link at the Balance Point

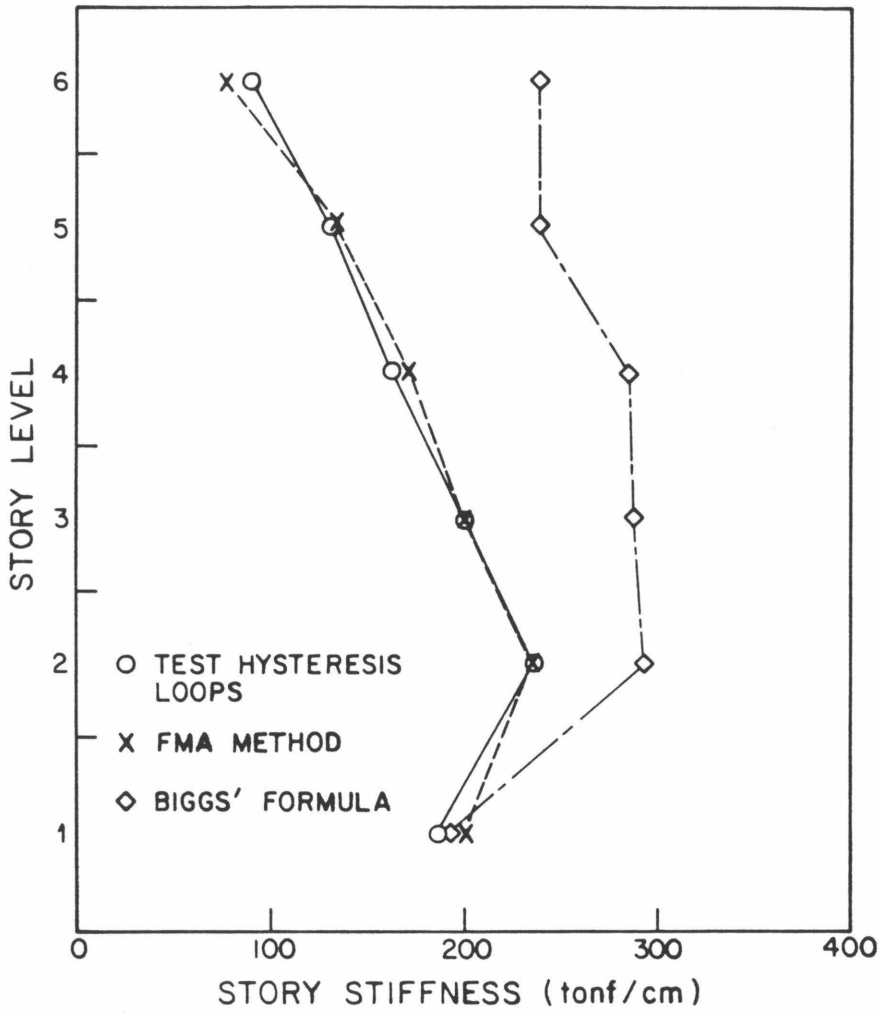

Fig. 6.7 Variation of Stiffness with Story Level Estimated by Different Methods

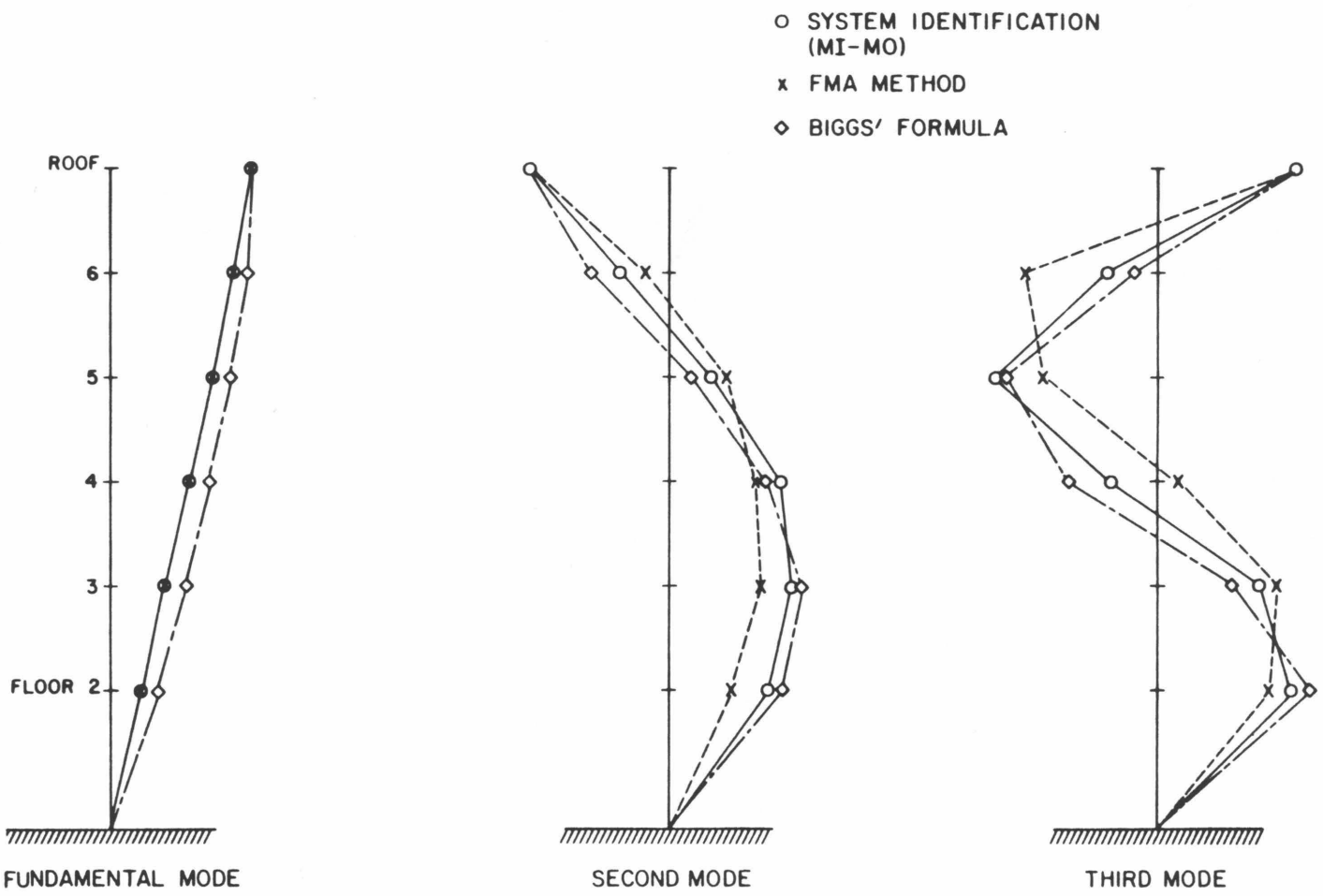

Fig. 6.8 Modeshapes Obtained by Different Methods

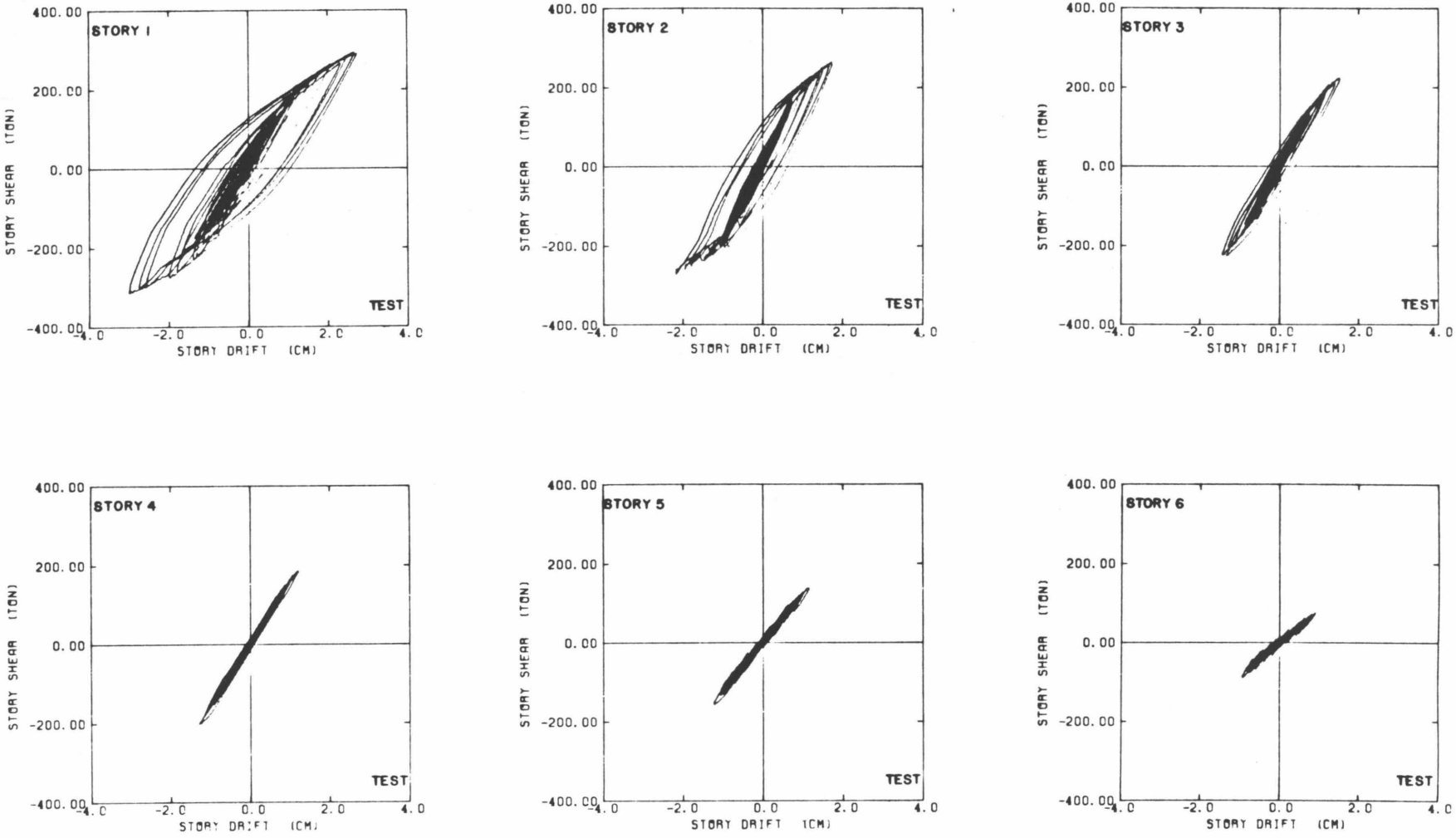

Fig. 6.9 Hysteresis Loops from the Inelastic Pseudo-Dynamic Test

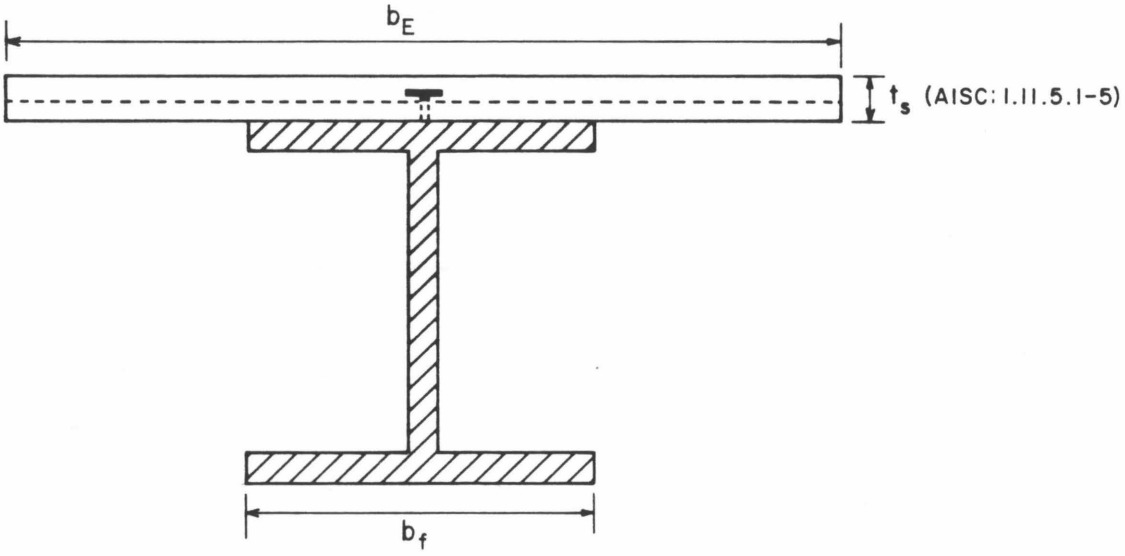

Fig. 6.10 Composite Steel-Concrete Section

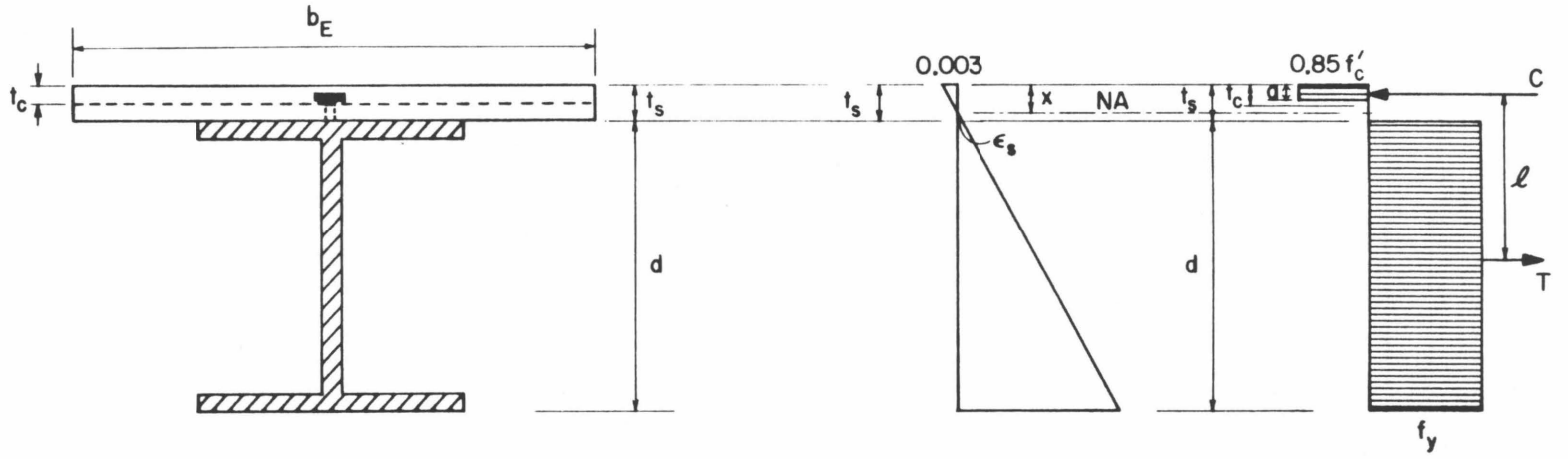

Fig. 6.11 Stress and Strain Distributions at Ultimate Moment Capacity for Case 1 - Slab Adequate

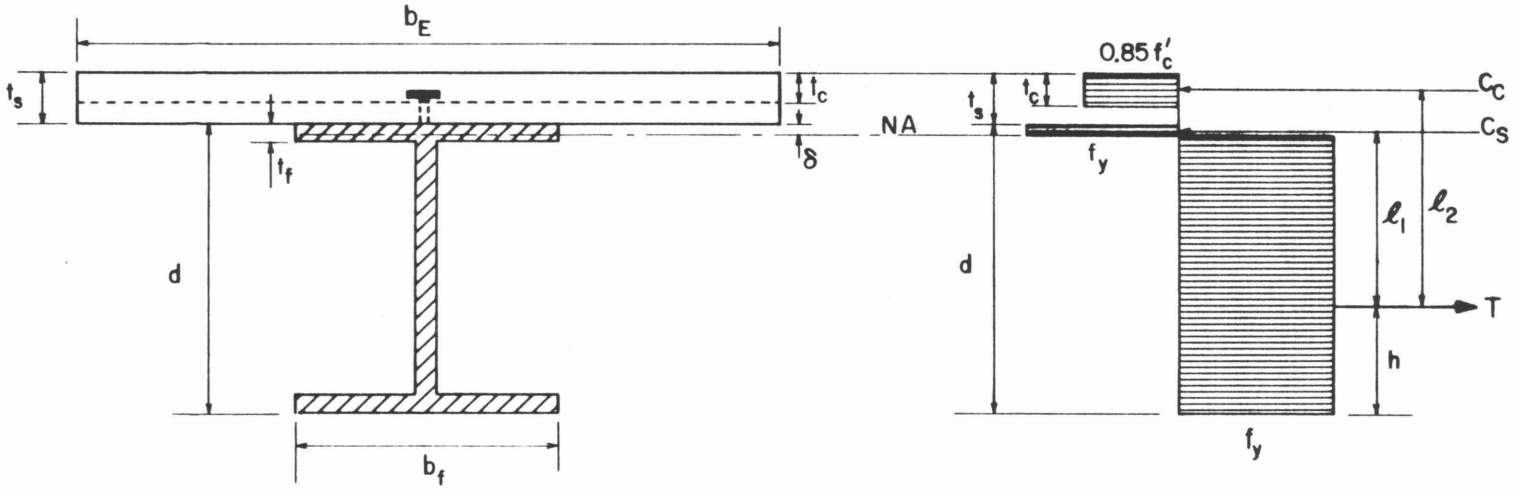

Fig. 6.12 Stress Distribution at Ultimate Moment Capacity for Case 2 - Slab Inadequate

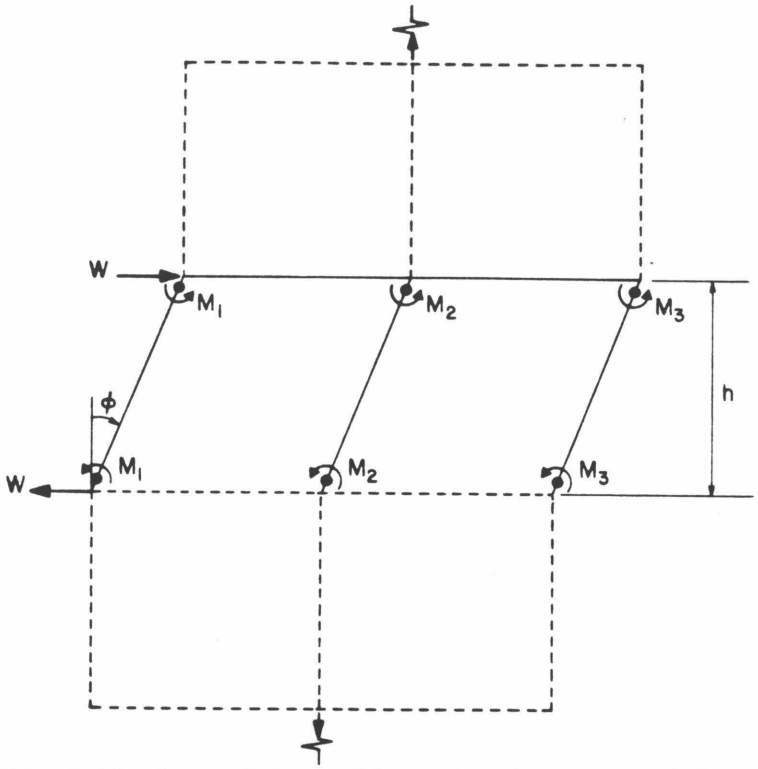

Fig. 6.13 Story Collapse Mechanism for Frame A(C)

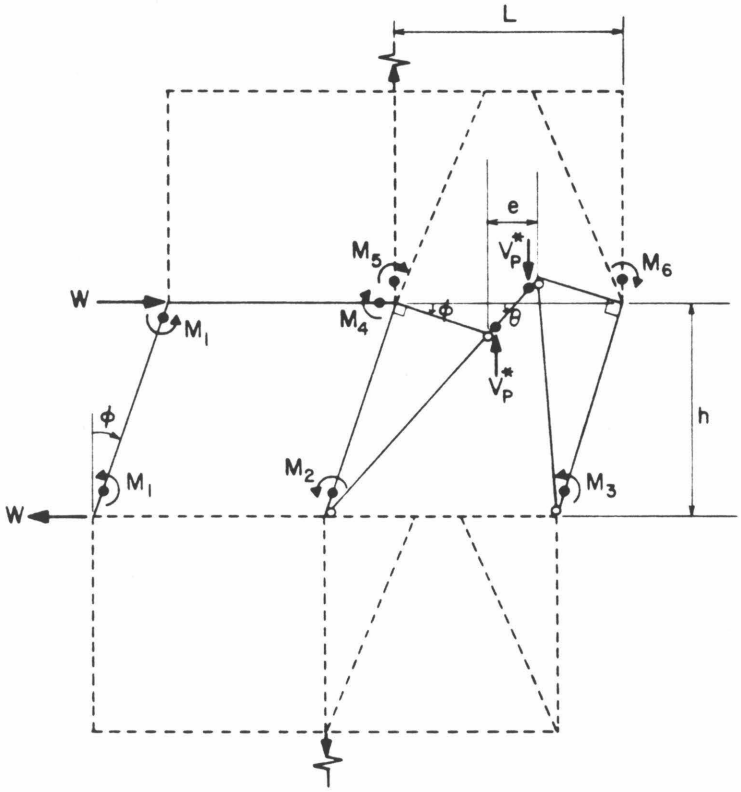

Fig. 6.14 Story Collapse Mechanism for Frame B

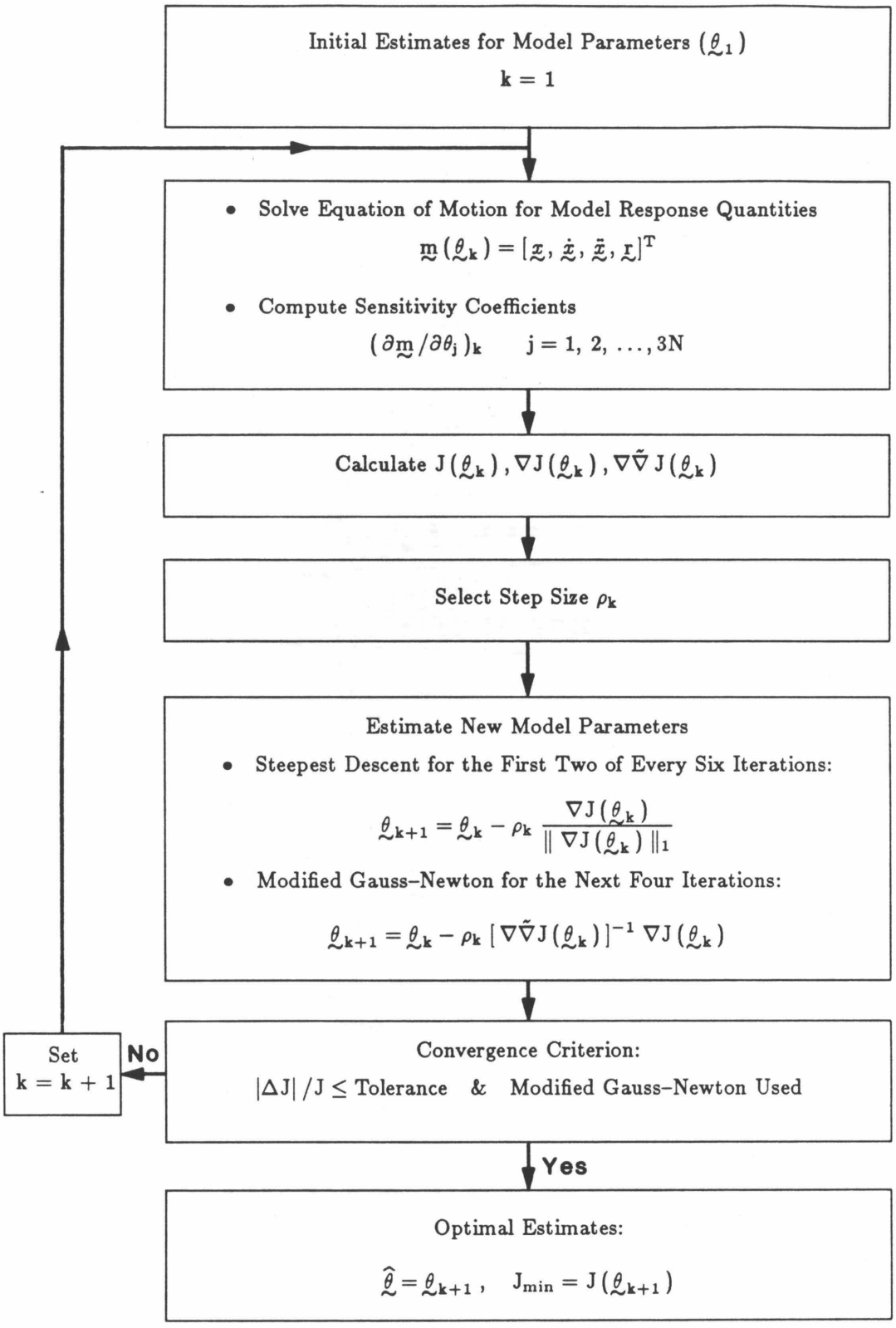

Fig. 6.15 Simplified Flow Diagram for HYSID

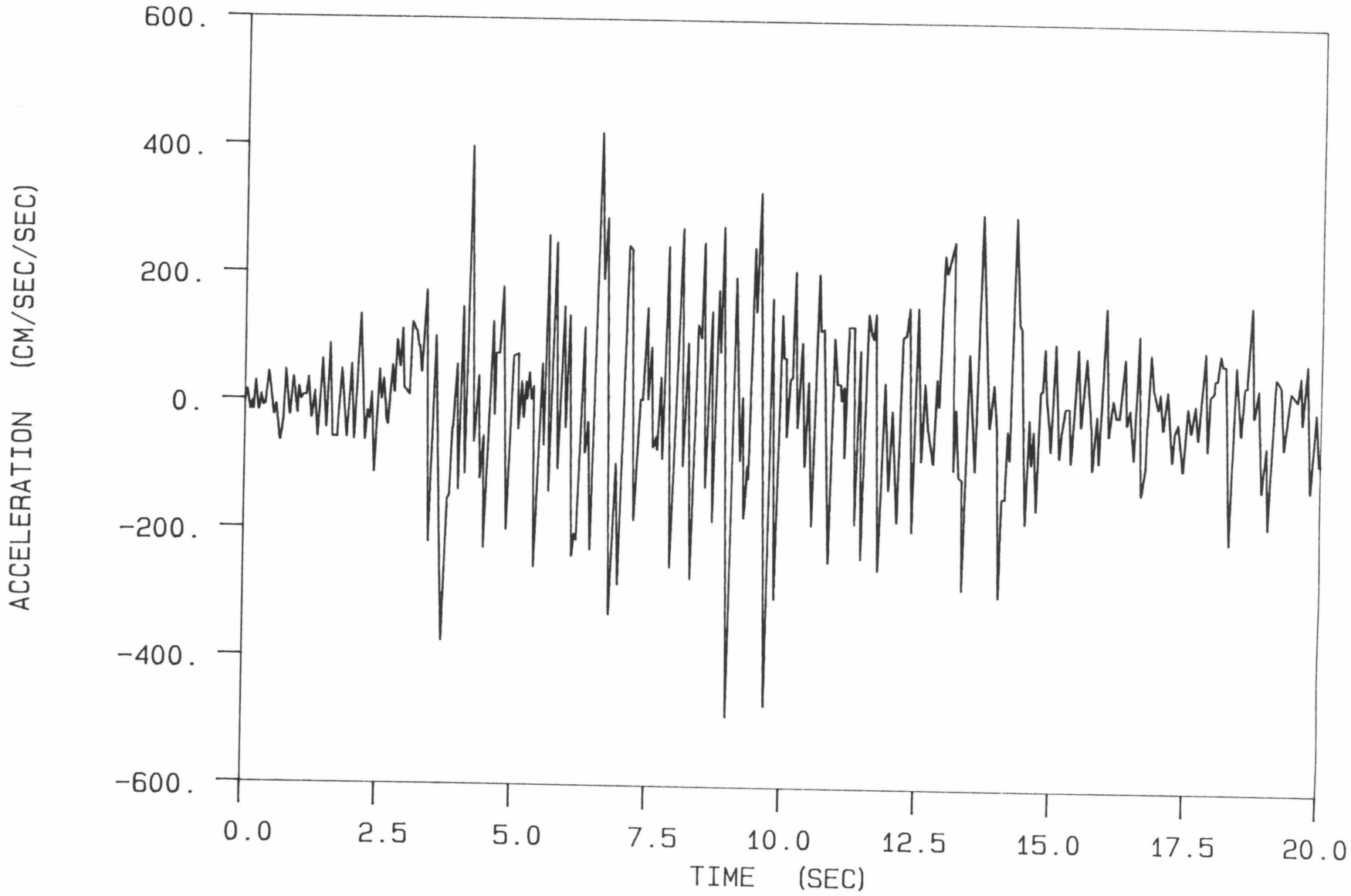

Fig. 6.16 Taft S21W Accelerogram, 1952 Kern County, California, Earthquake (peak scaled to 50% g)

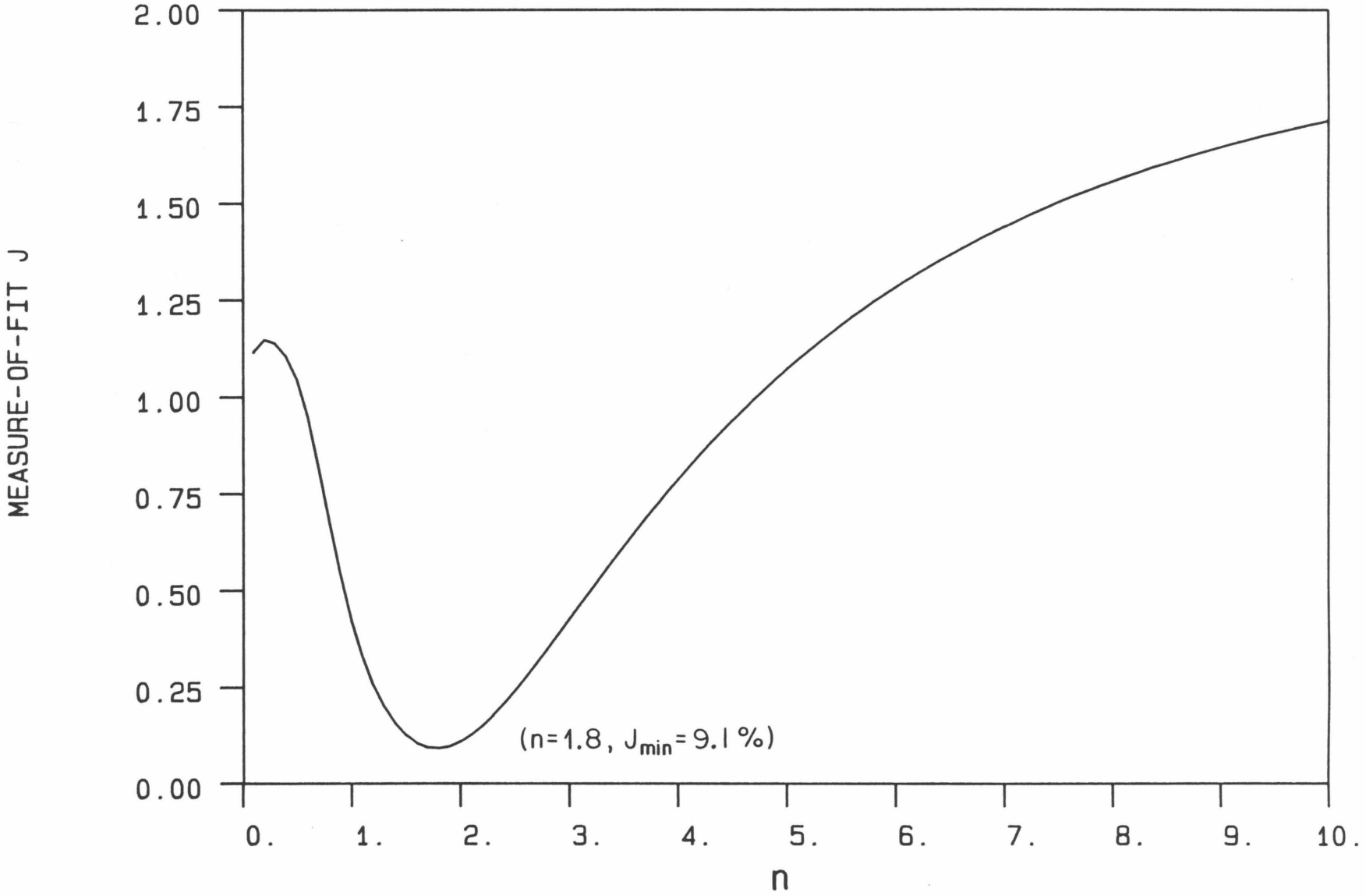

Fig. 6.17 Selection of Initial Estimate for n

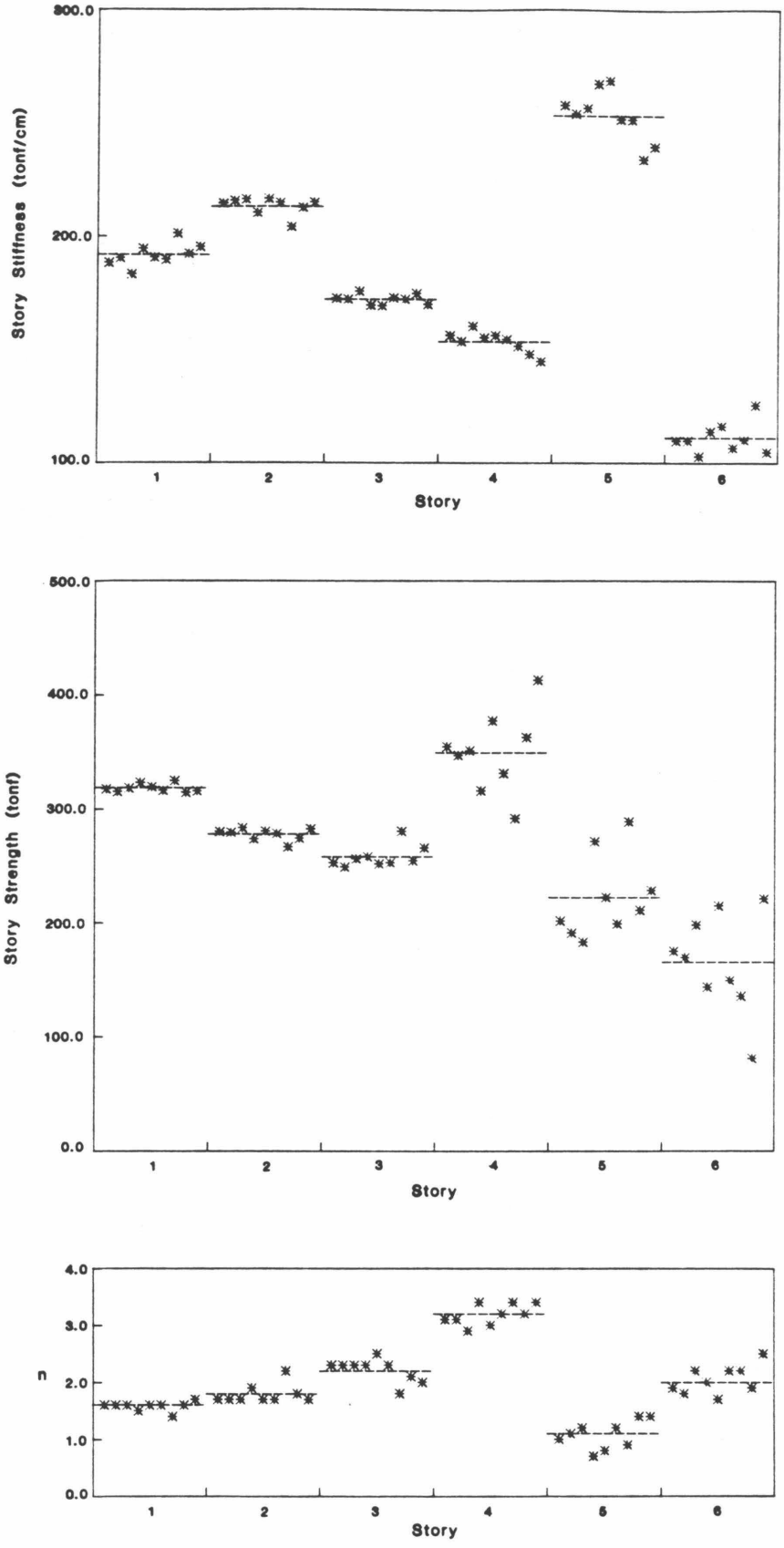

Fig. 6.18 Plots of Optimal Estimates and the Mean Values of Structural Parameters

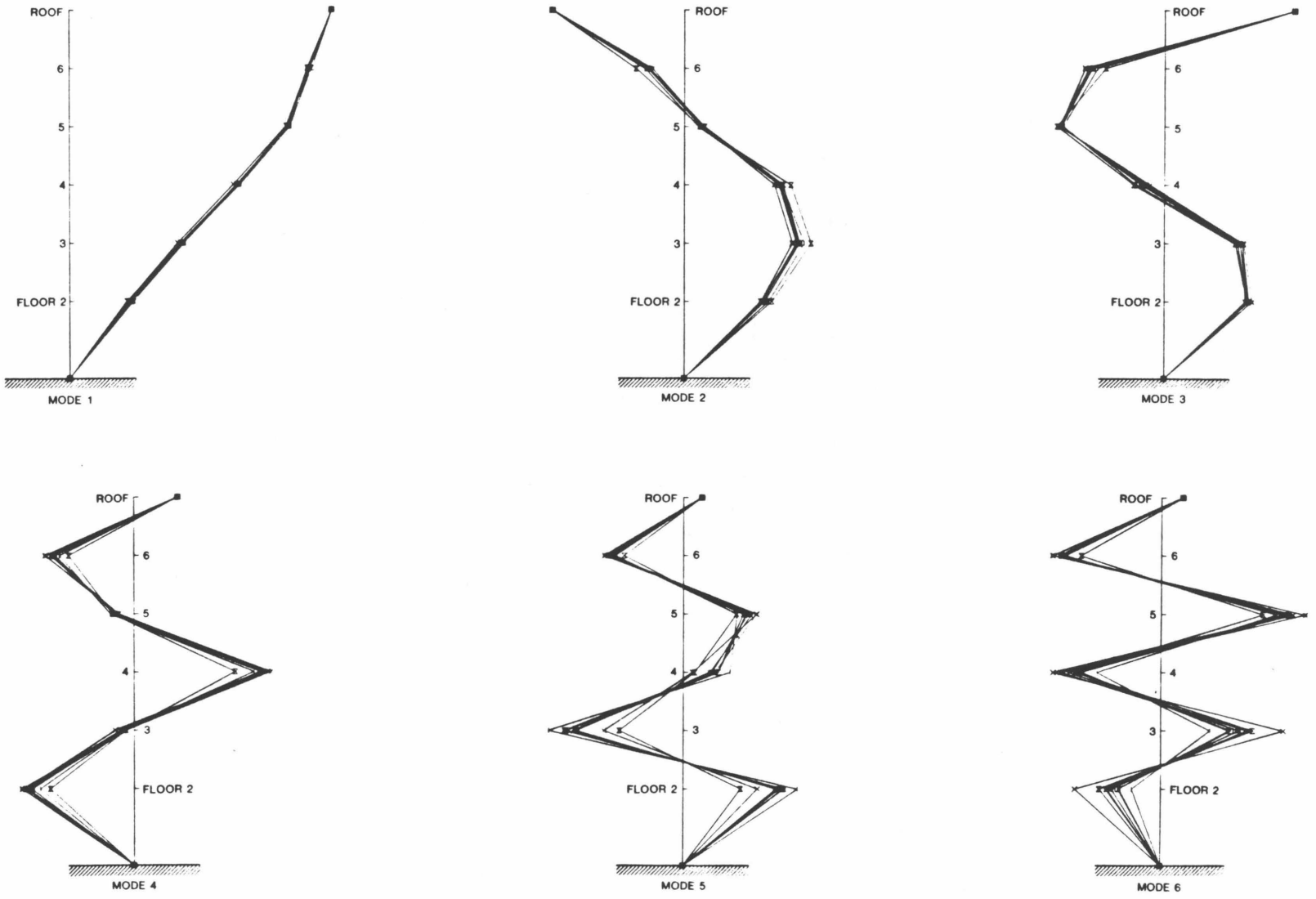

Fig. 6.19 Comparison of Modeshapes Corresponding to the Optimal Story Stiffnesses Resulting from the Different Runs of HYSID

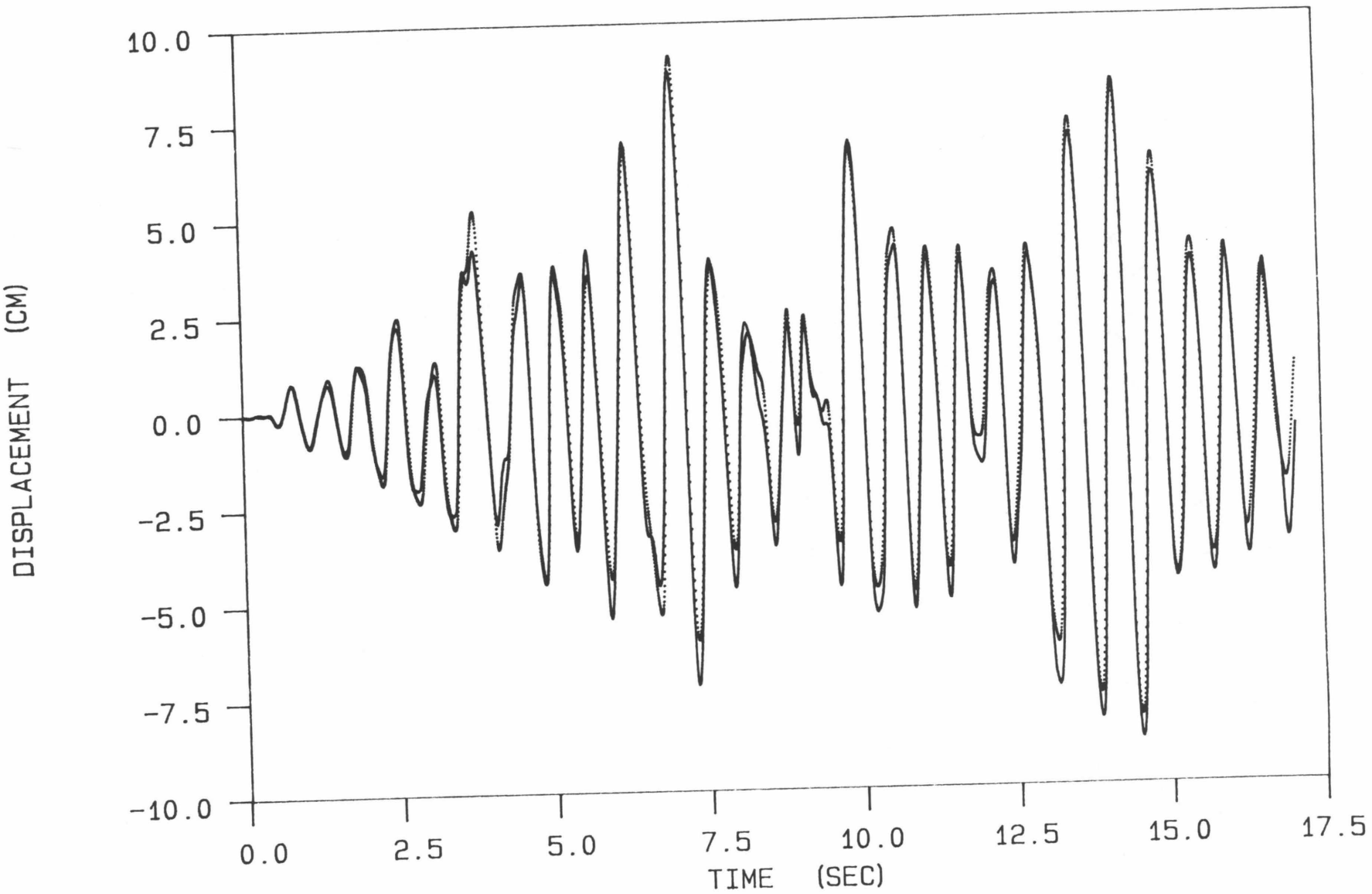

Fig. 6.20(a) Comparison of Roof Displacements (— *Inelastic* Pseudo-Dynamic Test; - - - Optimal Hysteretic Model)

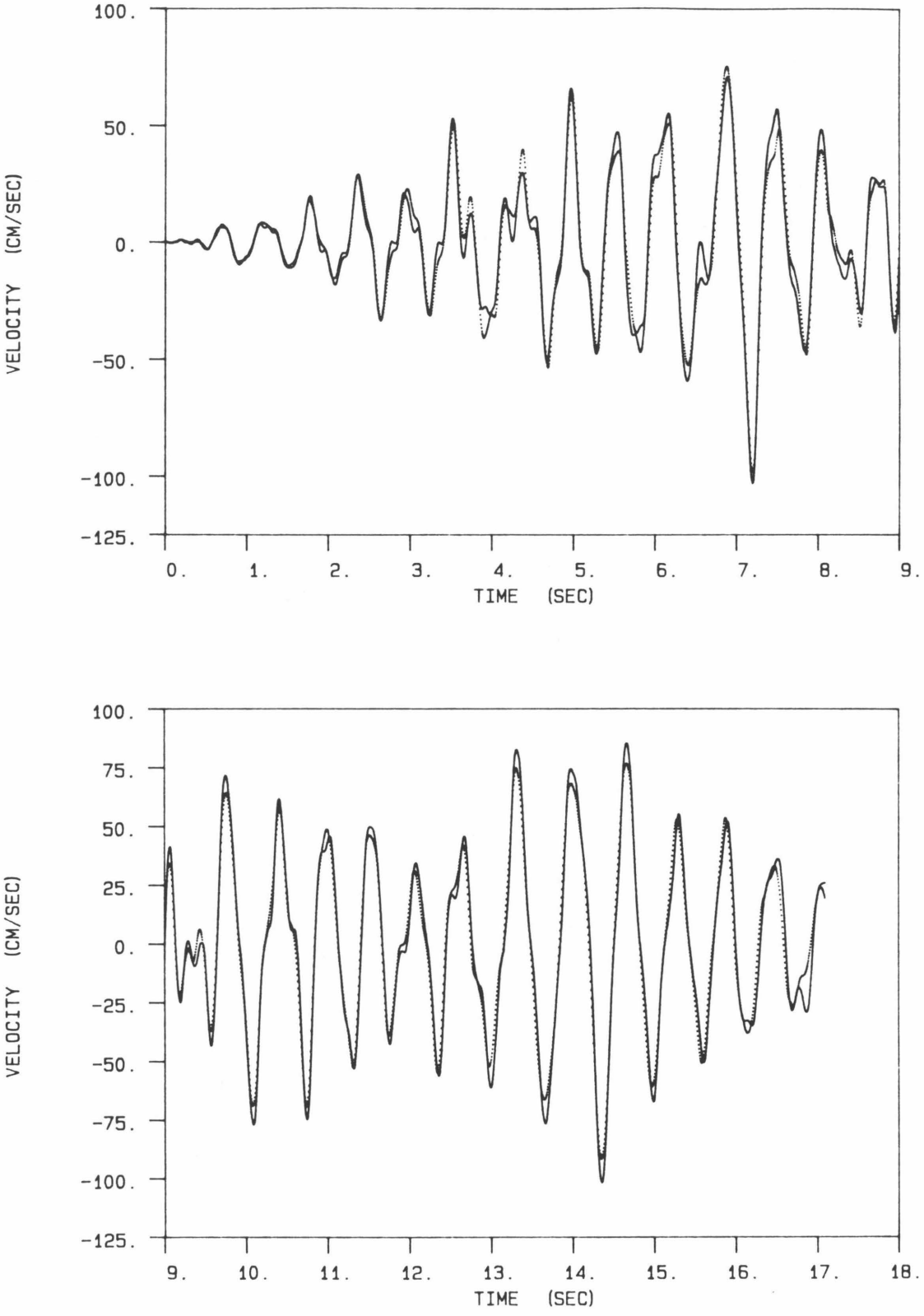

Fig. 6.20(b) Comparison of Roof Velocities (—— *Inelastic* Pseudo-Dynamic Test; - - - Optimal Hysteretic Model)

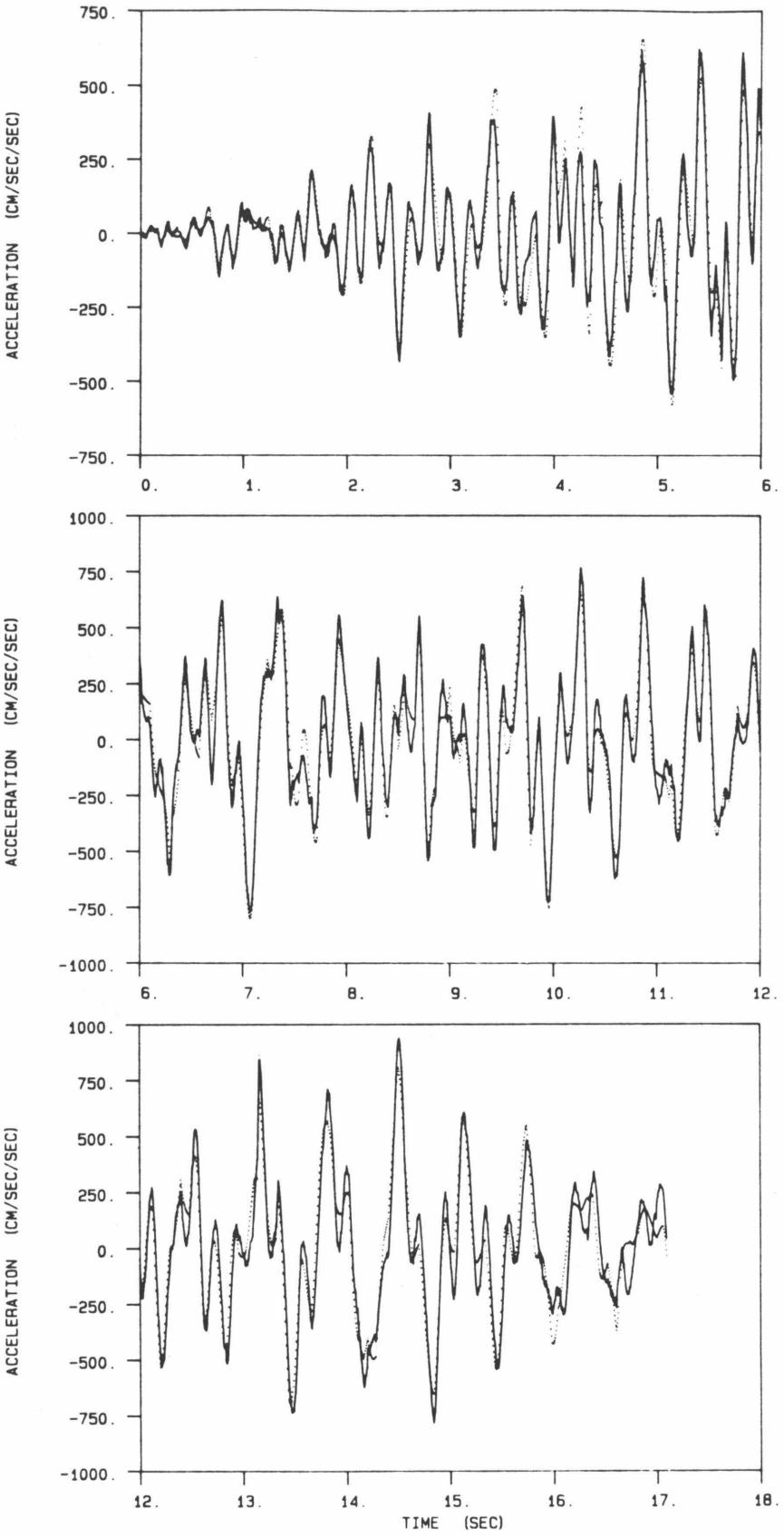

Fig.6.20(c) Comparison of Accelerations at Floor 4 (—— *Inelastic* Pseudo-Dynamic Test; - - - Optimal Hysteretic Model)

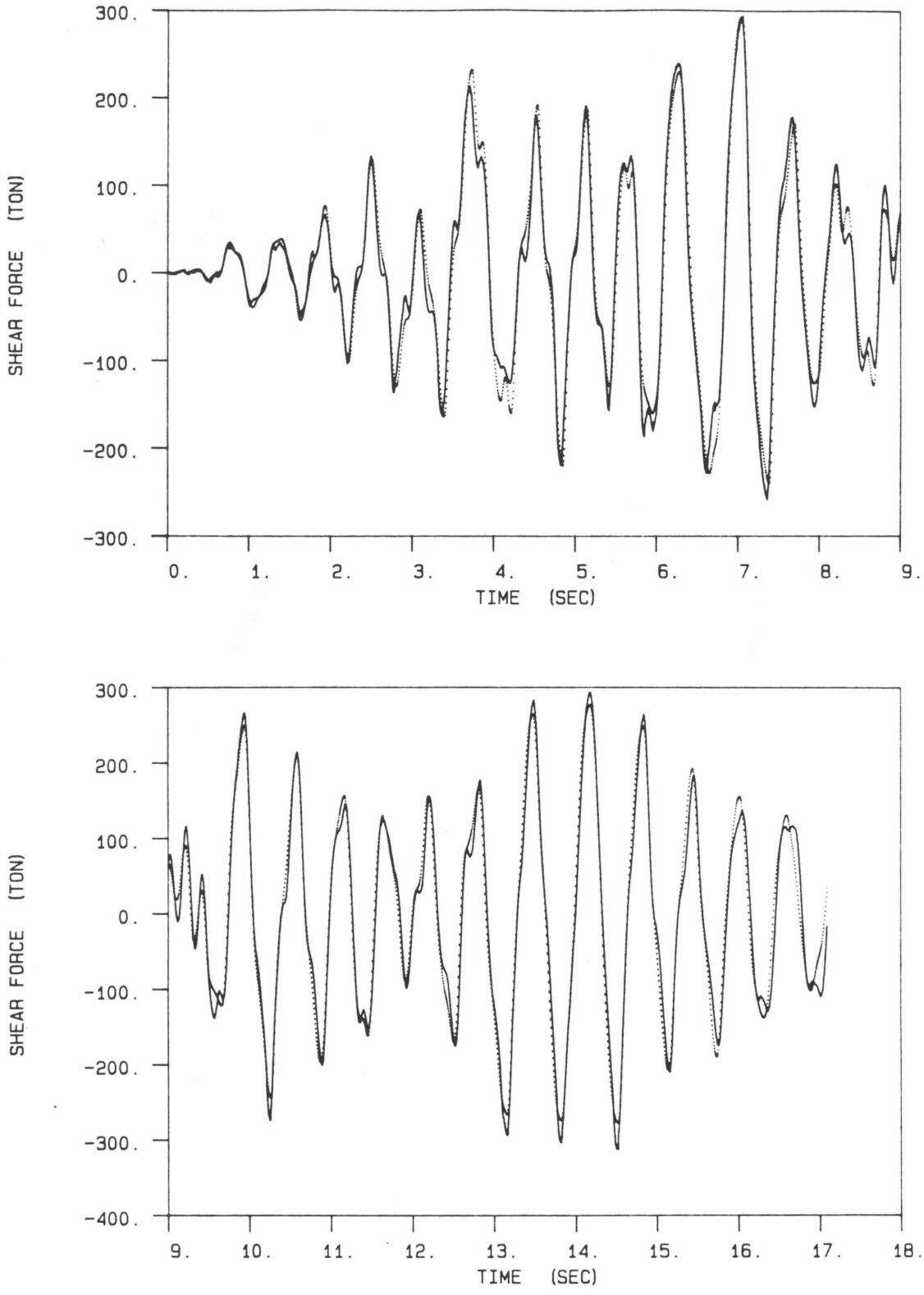

Fig. 6.20(d) Comparison of Base Shears (—— *Inelastic* Pseudo-Dynamic Test; - - - Optimal Hysteretic Model)

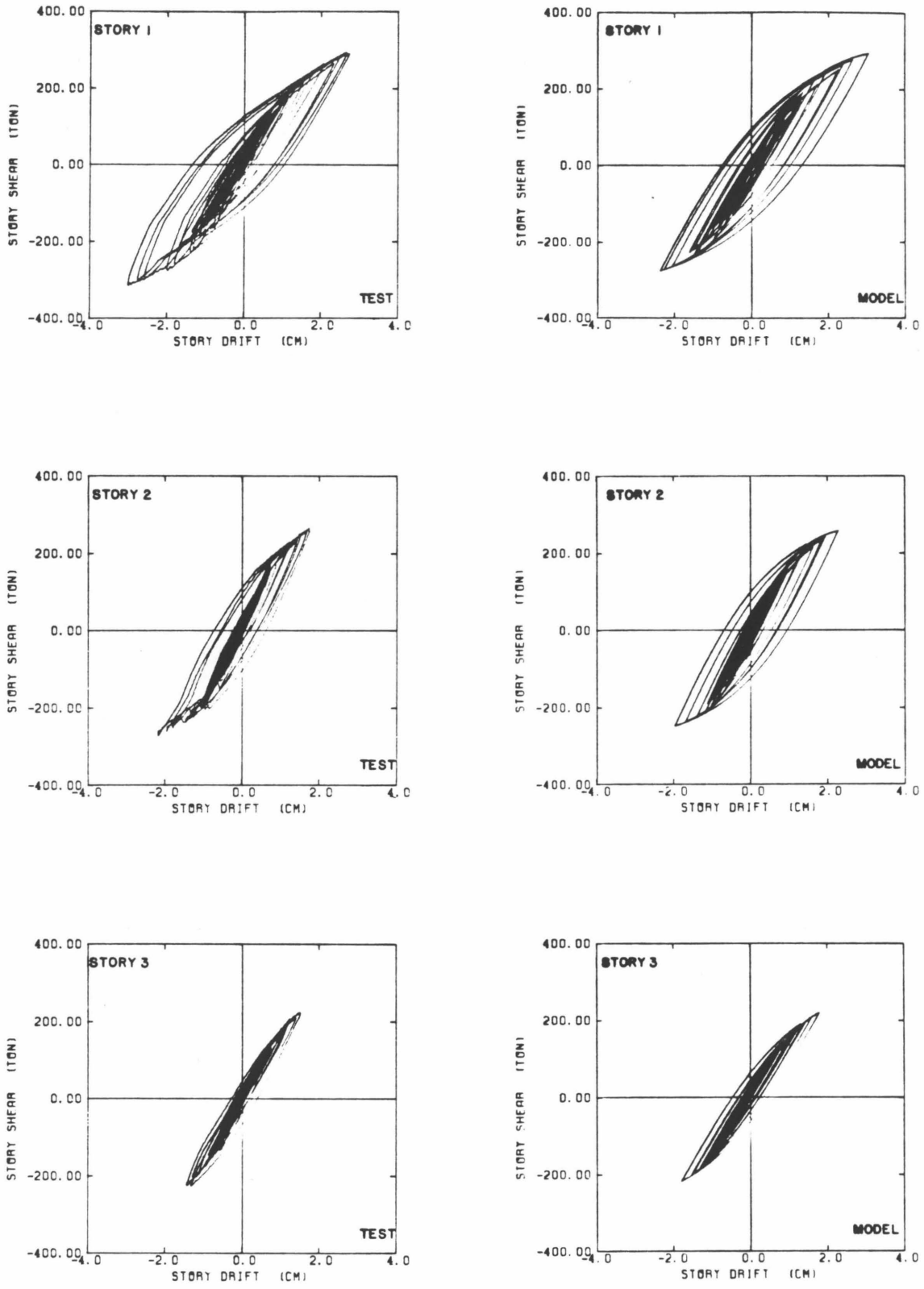

Fig. 6.21 Comparison of Hysteresis Behavior from the Inelastic Pseudo-Dynamic Test and the Optimal Hysteretic Model

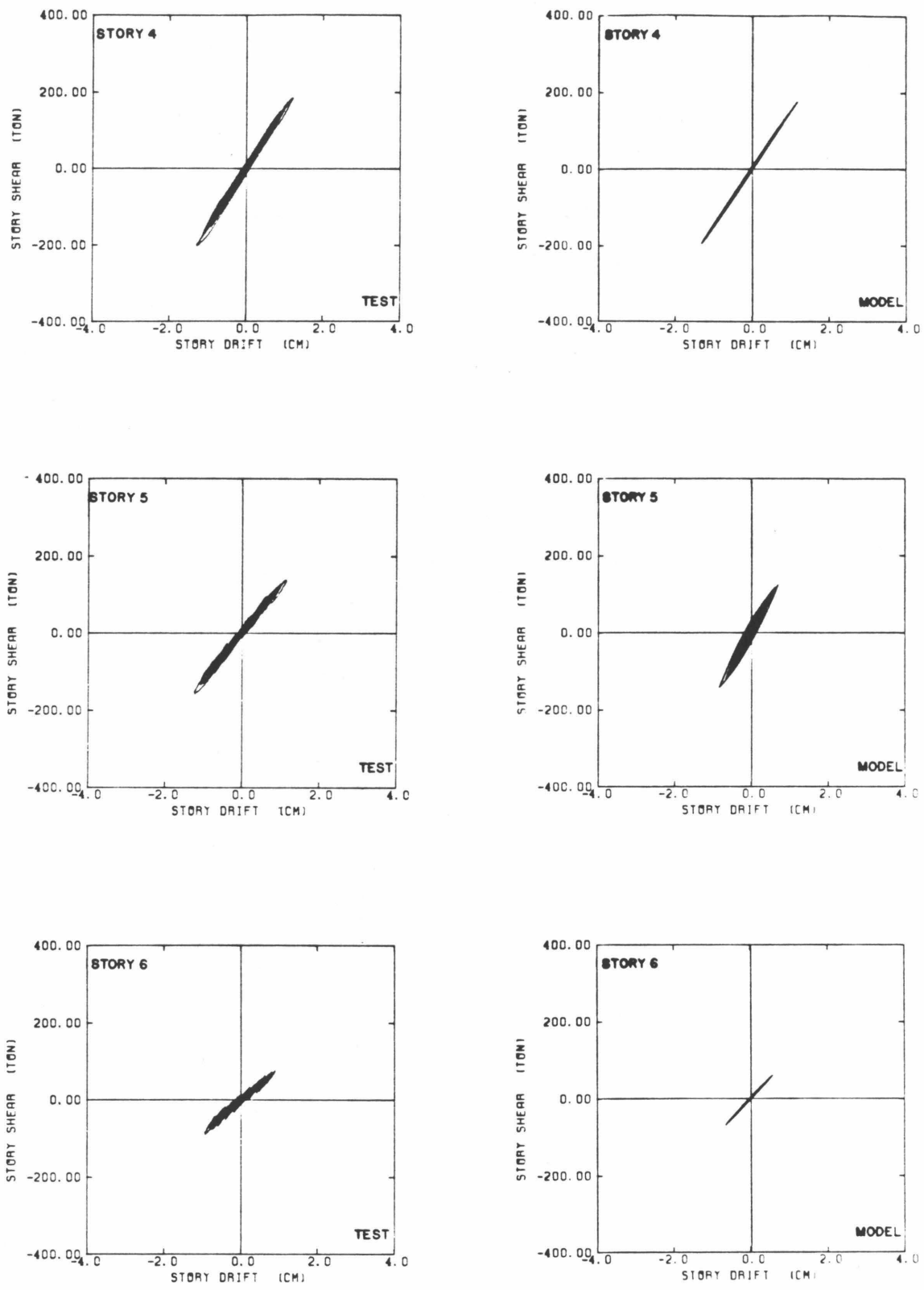

Fig. 6.21 (continued)
Comparison of Hysteresis Behavior from the Inelastic Pseudo-Dynamic Test and the Optimal Hysteretic Model

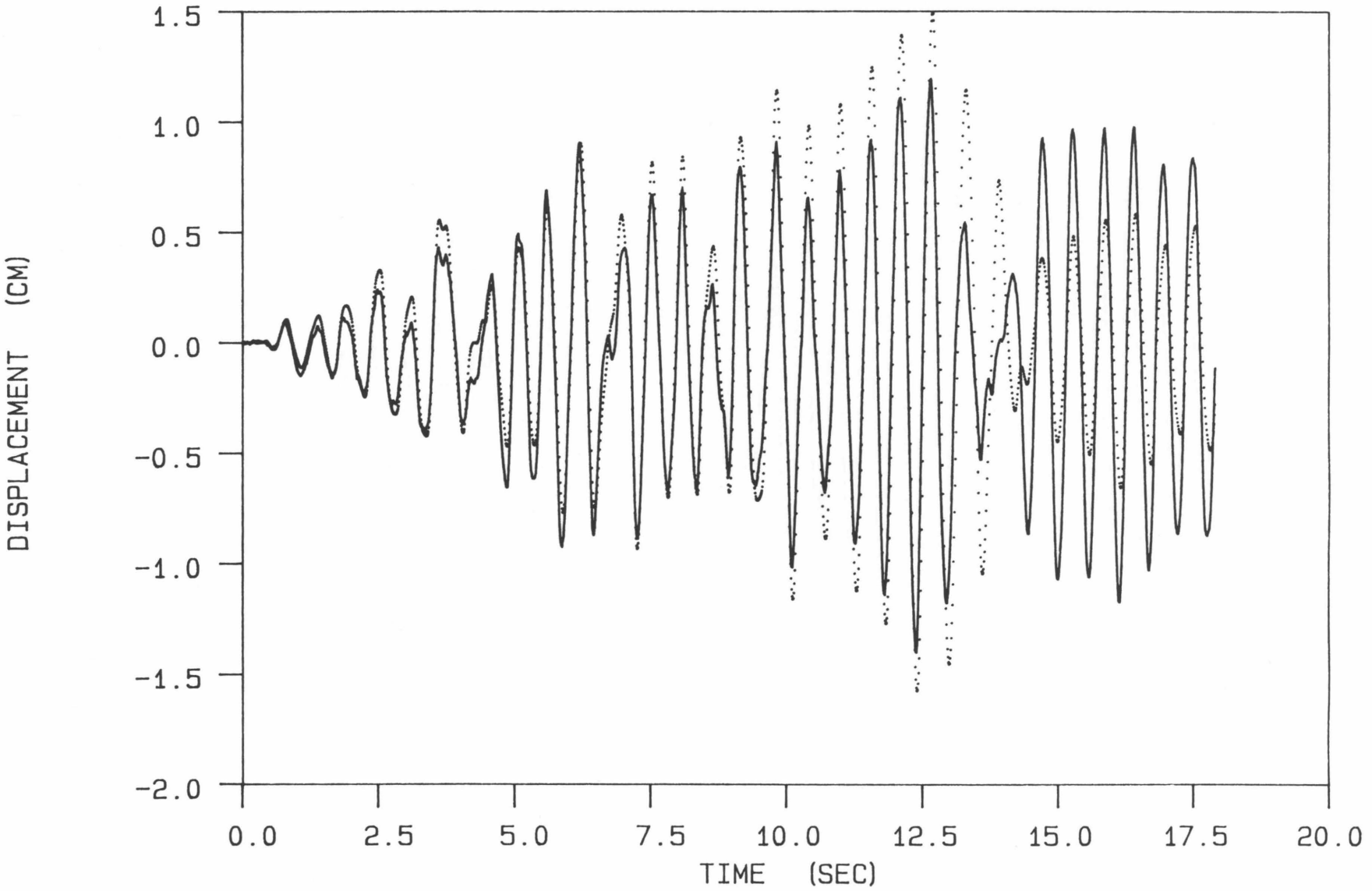

Fig. 6.22(a) Prediction of Roof Displacements (— *Elastic* Pseudo-Dynamic Test; - - - Optimal Hysteretic Model)

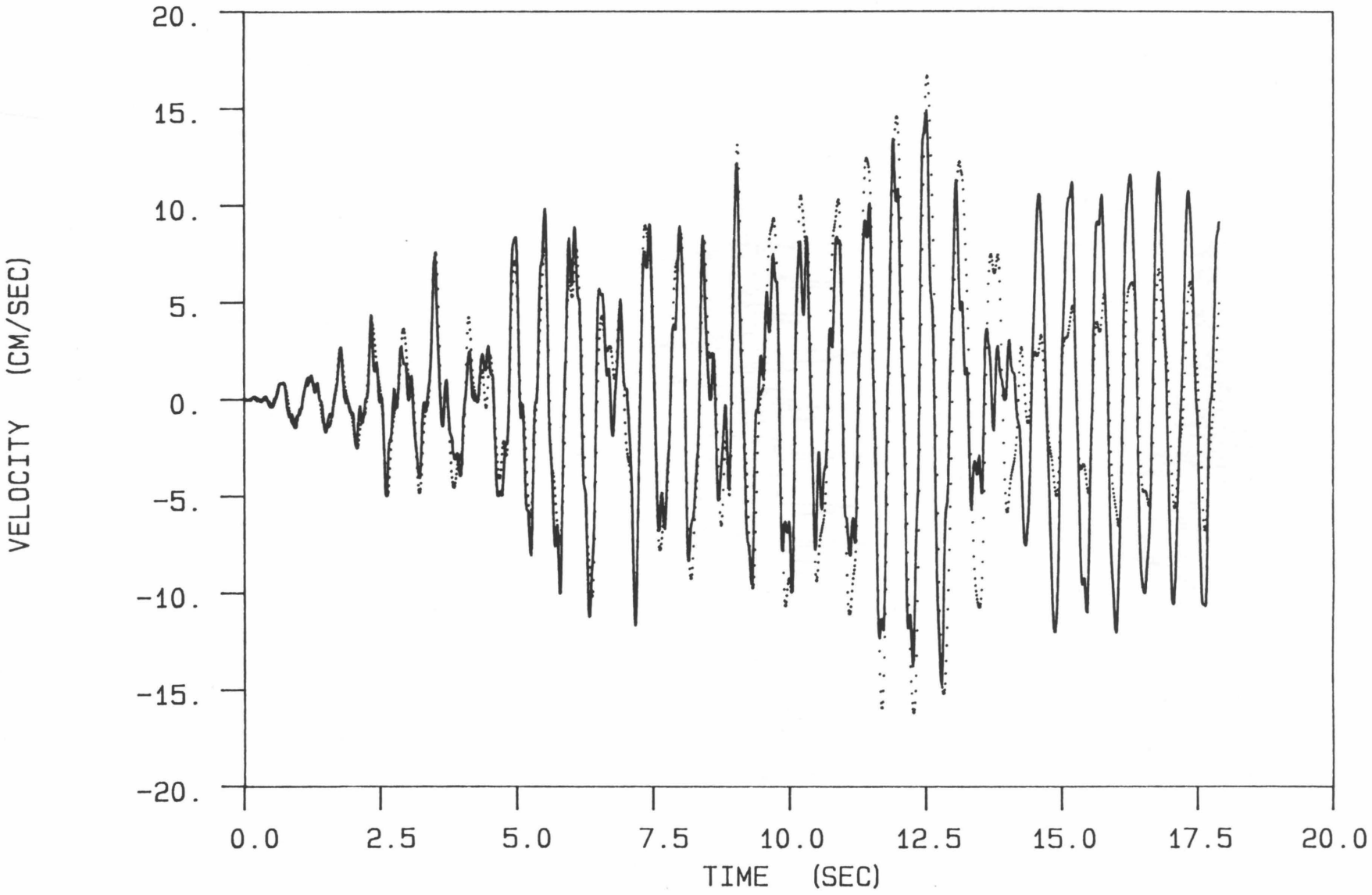

Fig. 6.22(b) Prediction of Roof Velocities (— *Elastic* Pseudo-Dynamic Test; - - - Optimal Hysteretic Model)

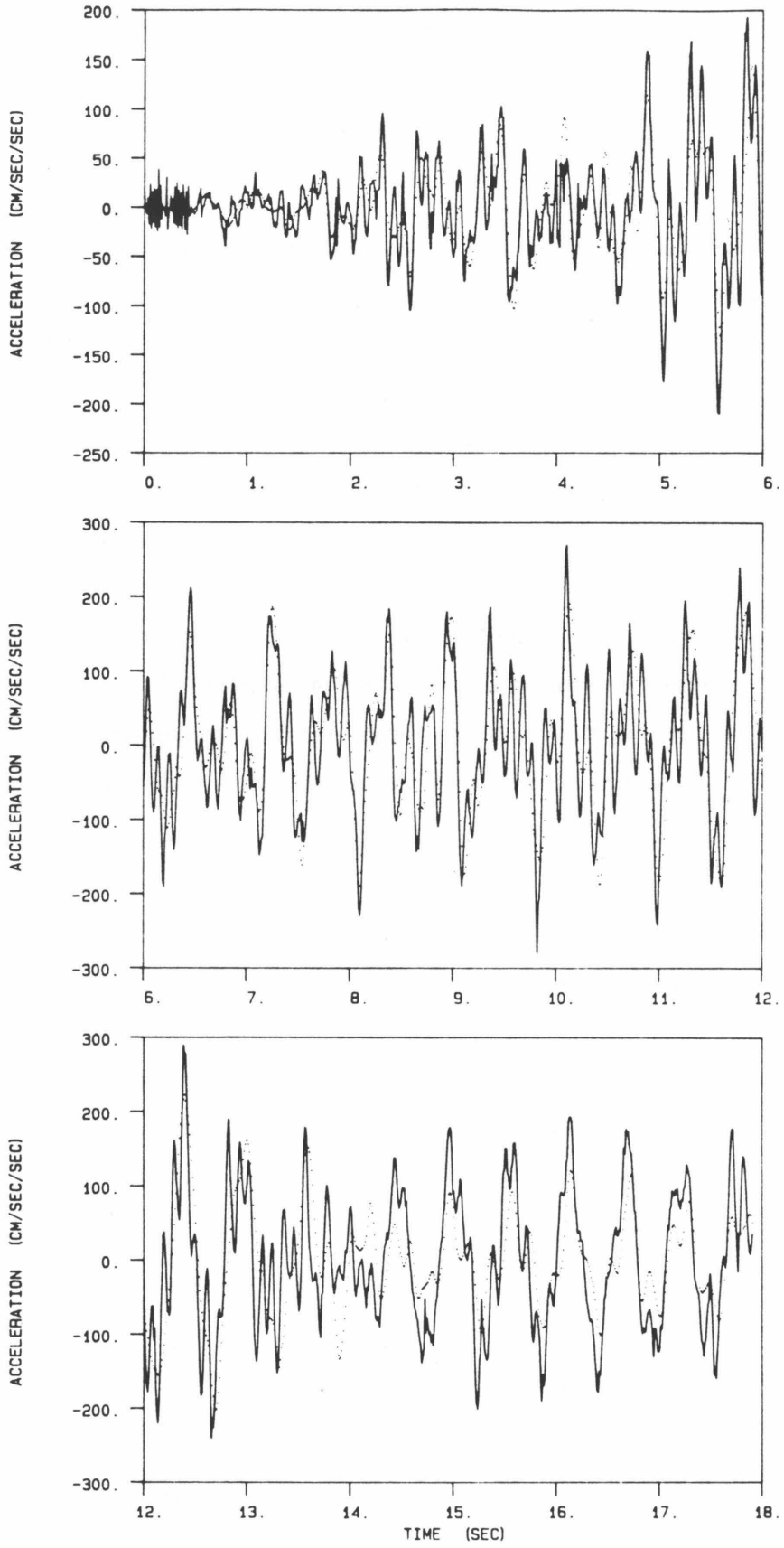

Fig. 6.22(c) Prediction of Roof Accelerations (—— *Elastic* Pseudo-Dynamic Test; - - - Optimal Hysteretic Model)

CHAPTER 7

CONCLUSIONS

Measuring the response of full-scale prototype structures, such as is done in the pseudo-dynamic method, remains the most realistic and reliable means to evaluate the inelastic seismic performance of structural systems and to devise structural details to improve their seismic performance. The important advantage of pseudo-dynamic testing over the traditional quasi-static test methods is that no assumption is made regarding the stiffness or restoring force characteristics of the test system. The actual restoring forces developed are measured during the test and used to compute the deformation response, in contrast to the *a priori* prediction of these forces using analytical models during ordinary quasi-static tests. This makes pseudo-dynamic testing a very powerful means of analyzing the dynamical behavior of structures in the inelastic region. Indeed, a better understanding of the inelastic behavior of structures gained from the pseudo-dynamic tests can be used to improve the current analytical modeling techniques, as has been done in this study.

As in all experimental methods, the pseudo-dynamic method also has errors inherently associated with it. The most serious error comes from the experimental system itself which gives rise to displacement-control and force-measurement errors. These errors were analyzed and were shown to act as effective excitations to the structure in addition to the ground motion. A modal analysis of the experimental errors proved that the control errors have a greater effect in the higher modes whereas the response of the lower modes is affected more by the measurement errors. A method of treatment of these errors was proposed by which the structural properties can be reliably estimated from the pseudo-dynamic test data.

A straightforward application of a single-input single-output system identification technique to estimate the modal properties of a full-scale six-story steel structure tested by the pseudo-dynamic method within its 'elastic' range at the Building Research Institute in Tsukuba, Japan, revealed negative damping for the third mode. An examination of the Fourier amplitude spectrum of the roof pseudo-acceleration record showed that the 'third-mode' signal near a frequency of 10 Hz is much too large relative to the first- and second-mode signals. This anomaly was also demonstrated when the Fourier amplitude spectra for the roof pseudo-accelerations and the accelerations of the three-mode model

identified from the pseudo-acceleration record from the roof were compared. Both spectra agree very well over a frequency range of the first two modes, but the third mode from the system identification procedure underestimates the apparent resonant amplitude from the test, despite the fact that the system identification procedure tried to make the third-mode response of the model larger by selecting a negative damping.

It was concluded that this strong signal around 10 Hz is not entirely due to the excitation of the third mode by the Taft earthquake record but is partly due to the cumulative effect of feedback of control and measurement errors during the pseudo-dynamic test. This unstable growth in the third mode produced the apparent negative damping when the system identification procedure tried to account for the strong signal solely from the earthquake excitation.

Using a multiple-input multiple-output system identification technique, namely MODE-ID, a linear model consisting of three classical normal modes was shown to be capable of reproducing the measured structural response within a mean-square error of 2%. Using MODE-ID, the effect of feedback errors was accounted for when estimating the modal parameters of the structure from the elastic test data by using the displacement-control errors, in addition to the ground motion, as inputs. This gave estimates of the equivalent viscous dampings for energy dissipated by the structure and for the apparent damping effect of the feedback errors on the structural modes. The identification results showed that the feedback errors added energy to the test structure in its third mode but damped the contributions of the first two modes during the elastic test.

The low structural damping values estimated as less than 1%, compared to field observations of 3% to 8% for the earthquake response of actual buildings, are presumably due to the absence of nonstructural components in the test structure and the absence of radiation damping during the pseudo-dynamic test because of its quasi-static nature.

The estimates for the modal parameters of the full-scale structure are in very good agreement with the corresponding results from a 0.3 scale model tested on the Berkeley shaking table, suggesting that scale-model testing is in fact a viable alternative to full-scale testing, at least with regard to reproducing the modal properties of full-scale structures.

The improvement of earthquake-resistant design of structures requires a knowledge of the nonlinear response of structures. This, in turn, requires a method for describing the dynamic force-deflection relation of structural systems. A smooth, nonlinear hysteretic

relation would be a realistic model for most applications.

A general class of Masing models is presented to represent this dynamic, hysteretic behavior. Masing assumed that a metal body consists of a system of elasto-plastic elements each with the same elastic stiffness but different yield limits, and asserted that the branches of the hysteresis loops for steady-state response are geometrically similar to the virgin loading curve and are described by the same basic equation but scaled with two-fold magnification. The resulting stiffness characteristics of the hysteretic system can be explained with the help of a continuous distribution of constant stiffness surfaces in the region of the restoring force space, an idea similar to the multiple yield surface representation with kinematic hardening in the incremental theory of plasticity.

Masing's hypothesis, which describes only the steady-state cyclic response, was considered by previous researchers to be of no help in the case of transient loading. However, it was shown in this study that Masing's original hypothesis can be extended for transient loading by the introduction of two simple hysteresis rules. A particular model within this general class of Masing models can be prescribed by giving its virgin loading curve. This class of models was shown, analytically and experimentally, to exhibit reasonable response behavior for arbitrary loading patterns.

Iwan also assumed that a general hysteretic system could be modeled as one consisting of 'Masing type' elements. He derived the force-deflection relationship of the entire system for both steady-state and transient response cases by keeping track of the fraction of elements in each of the yielded and unyielded categories. His results for the steady-state case agree with Masing's hypothesis.

In this study, it was shown that the same force-deformation relationships for both steady-state and transient responses can be obtained by the application of the general class of Masing models. The Masing models can be viewed as a simpler way of implementing Iwan's model which involves computing several integral terms in the force-deformation relationship. On the other hand, the fact that Iwan's model is based on physically realizable elements, provides additional support for the hysteresis rules chosen for the Masing models. The two classes of models are therefore mutually supportive.

Based on a study of some previous models, a simple virgin loading curve was chosen to prescribe a particular Masing model for modeling the nonlinear hysteretic behavior of steel structures. This gives a force-deflection relation which is general enough to be potentially

useful as a model for the hysteretic, dynamic behavior of a wide range of softening materials and structures. The model has three parameters: the initial stiffness, the ultimate strength and a parameter n to control the smoothness of the transition from elastic to fully plastic response in the force-displacement curve. An important feature of the model is that the model parameters can be estimated analytically based on the structural plans, since two of the parameters are directly related to the physical system under investigation. Also, by testing the model sufficiently with available experimental data, a set of feasible values for the parameter n for different materials and structures can be obtained. This is necessary if the model is to have the potential of predicting structural response prior to a structure being built and tested.

This hysteretic model was examined for its applicability to real structures. It was shown how it could be used to model the restoring force-deformation relationship for a multi-degree-of-freedom structure excited by an earthquake. For simplicity, the structure was idealized as a shear building with the hysteretic model relating the story shears and story drifts. In particular, the pseudo-dynamic test structure, which is a full-scale six-story steel-frame building, was modeled in this fashion.

Methods were given to estimate the structural parameters involved in the modeling from the structural plans, except for the parameter n. The initial story stiffnesses of the test structure were estimated by the first-mode approximation method and by Biggs' formula. The first-mode approximation method resulted in better stiffness prediction, although only the first-mode characteristics were reproduced well, while Biggs' formula did better with the higher modes. Hence, it can be said that if the properties of the first mode can be estimated by reliable means such as experiments or detailed elastic finite element analyses, then the choice of the first-mode approximation method is better to calculate story stiffnesses. The strength of each story in the test structure was estimated by assuming that the story was transformed into a collapse mechanism.

A hysteretic system identification program, HYSID, which employs an output-error approach, was developed to determine the optimal estimates of the hysteretic model parameters from experimental data. The optimization algorithm involves continual alternating between the steepest-descent method and the modified Gauss-Newton method for the simultaneous identification of the optimal parameter values in a (3N+1)-dimensional space, where N is the number of degrees of freedom in the structure.

The inelastic pseudo-dynamic test data were analysed using HYSID, in order to examine the applicability of the new hysteretic model to a real structure and to determine whether the optimal estimates of the initial stiffnesses and ultimate strengths were consistent with the theoretical values determined for the six-story test structure. This also gave an opportunity to examine suitable values for n since this parameter cannot be determined theoretically. In this study, the story shears were chosen for matching when estimating the parameters because of their significance in hysteretic modeling and their unique availability due to the nature of the pseudo-dynamic test. The theoretical estimates of the initial stiffnesses and ultimate strengths, and some perturbations of these, were used as the starting values for the different runs of HYSID.

In spite of the diversity of the initial starting estimates for the different runs of HYSID, the identified model parameters were in good agreement except for the strengths of the top three stories which showed a large scatter about their mean values. This was expected because the structure did not experience any significant inelastic deformation at the top three stories, and the determination of story strengths from elastic or nearly elastic test data is an ill-conditioned process.

The modal characteristics calculated from the optimal estimates of story stiffnesses corresponding to different runs of HYSID were found to be extremely close. For this reason, and also because of the small scatter of the optimal estimates about their mean values, the mean values were used for further study.

The time-histories of the optimal model responses were compared with the measured responses of the test structure and were found to be in excellent agreement. Experimental hysteresis loops obtained from the pseudo-dynamic test were also predicted well by the optimal hysteretic model. The simple three-parameter model for each story shear-deformation relationship appears to be sufficient to capture the essential features of the nonlinear behavior of the steel frame test structure.

A measure of the maximum amount of inelastic deformation any story experienced during the test, as predicted by the optimal hysteretic model, suggests that the inelastic deformation experienced by the first three stories during the test was substantially larger than that in the top three stories, which agrees with what was observed from the test hysteresis loops.

The prediction capability of the hysteretic model was tested in order to assess the use of

the model in seismic analysis of structures. Since there were no other independent inelastic test data available, the response from the elastic pseudo-dynamic test was predicted by the optimal nonlinear model identified from the inelastic test data. The predicted response agreed very well with the measured elastic test response time-histories over the duration of the test.

The prior theoretical estimates of the model parameters seem to be a good approximation to the optimal estimates, suggesting that the hysteretic model has the potential to be used in the seismic analysis of structures. In this case, structural parameters estimated from the structural plans would be used during design to facilitate an effective iterative procedure to limit maximum structural responses to prescribed ground motions. It is tentatively suggested, based on the structure studied, that a value of 2 for parameter n should be appropriate when predicting the inelastic, undamaged behavior of steel-frame structures. Interestingly enough, this corresponds to the case where the force-deformation relation is hyperbolic tangent.

With these encouraging results, further exploration of the nonlinear model is planned, such as the generalization of the hysteretic model to problems in continuum mechanics using a multiple-yield surface plasticity theory, application to damage detection in structures, further experimental verification using shaking-table tests, modeling of deterioration of material properties such as stiffness and strength during strong ground motions and the development of a seismic design methodology using the hysteretic model.

APPENDIX A

RESPONSE STATISTICS BY THE METHOD OF OPERATIONAL CALCULUS

The transient and steady-state response statistics of the difference equation 2.17 in Chapter 2 are obtained by the method of operational calculus [1] in this section.

Suppressing the superscript r, Eq. 2.17 can be written as:

$$\xi_i - \phi_1 \xi_{i-1} + \phi_2 \xi_{i-2} = a_{i-1} \qquad i = 1, 2, \ldots \tag{A.1}$$

with the initial conditions of $\xi_{-1} = 0$ and $\xi_0 = 0$.

From Operational Calculus,

$$\xi_{i-k} = e^{-ks} \xi_i \quad . \tag{A.2}$$

Substituting Eq. A.2 into Eq. A.1 gives the following:

$$[1 - \phi_1 e^{-s} + \phi_2 e^{-2s}] \xi_i = a_{i-1} \quad . \tag{A.3}$$

By decomposition in partial fractions and subsequent expansion, it can be shown that:

$$[1 - \phi_1 e^{-s} + \phi_2 e^{-2s}]^{-1} = \sum_{n=0}^{\infty} \frac{\lambda^{n+1} - \mu^{n+1}}{\lambda - \mu} e^{-ns} \tag{A.4}$$

where λ and μ are the eigenvalues corresponding to the homogeneous part of Eq. A.1.

The application of this expansion yields the solution of the difference equation as:

$$\xi_i = \sum_{n=0}^{\infty} \frac{\lambda^{n+1} - \mu^{n+1}}{\lambda - \mu} e^{-ns} a_{i-1} \quad . \tag{A.5}$$

Use of Eq. A.2 gives:

$$\xi_i = \sum_{n=0}^{i-1} \frac{\lambda^{n+1} - \mu^{n+1}}{\lambda - \mu} a_{i-1-n} \tag{A.6}$$

$$\xi_i^2 = \left(\sum_{n=0}^{i-1} \frac{\lambda^{n+1} - \mu^{n+1}}{\lambda - \mu} a_{i-1-n} \right)^2 \quad . \tag{A.7}$$

If a_i's have zero mean and are uncorrelated $\ni$ $E[a_i a_j] = 0 \quad \forall\, i \neq j$, then

$$E[\xi_i^2] = \sum_{n=0}^{i-1} \left(\frac{\lambda^{n+1} - \mu^{n+1}}{\lambda - \mu} \right)^2 E[a_{i-1-n}^2] \quad . \tag{A.8}$$

In addition, the ξ_i's have zero mean (taking expectation of Eq. A.6). If the input process a_i has a constant standard deviation $\sigma_a \; \forall \, i$, then

$$\sigma_{\xi_i}^2 \;=\; A_i \, \sigma_a^2 \tag{A.9}$$

where $$A_i \;=\; \sum_{n=0}^{i-1} \left(\frac{\lambda^{n+1} - \mu^{n+1}}{\lambda - \mu} \right)^2 \quad .$$

From Eq. 2.17:

$$a_i = -\alpha \, \eta_i - \beta f_i \quad . \tag{A.10}$$

Therefore,

$$E[\, a_i^2 \,] \;=\; \alpha^2 \, E[\, \eta_i^2 \,] \;+\; \beta^2 \, E[\, f_i^2 \,] \quad , \tag{A.11}$$

if η_i and f_i have zero mean and are uncorrelated.

Furthermore, if η_i and f_i have constant standard deviations σ_η and σ_f, respectively, $\forall \, i$, then

$$\sigma_a^2 = (\alpha \sigma_\eta)^2 + (\beta \sigma_f)^2 \quad . \tag{A.12}$$

In fact, the assumptions of zero mean and constant standard deviation for the input process a_i are implied by similar assumptions on η_i and f_i and Eq. A.10.

From Eqs. A.9 and A.12:

$$\sigma_{\xi_i}^2 = A_i \, [\, (\alpha \sigma_\eta)^2 + (\beta \sigma_f)^2 \,] \quad . \tag{A.13}$$

Back-substituting for A_i, α and β:

$$\begin{aligned} \sigma_{\xi_i}^2 = & \left\{ \sum_{n=0}^{i-1} \left(\frac{\lambda^{n+1} - \mu^{n+1}}{\lambda - \mu} \right)^2 \right\} \\ & * \left[\frac{(\Delta t \, \omega_r)^4}{(1 + \Delta t \, \zeta_r \, \omega_r)^2} \, \sigma_\eta^2 + \frac{(\Delta t)^4}{(1 + \Delta t \, \zeta_r \, \omega_r)^2} \, \sigma_f^2 \right] \quad . \end{aligned} \tag{A.14}$$

Equation A.14 defines the variance for the transient response corresponding to the difference equation A.1.

Steady state response statistics are obtained by letting $i \rightarrow \infty$ in Eq. A.13:

$$\sigma_{\xi_\infty}^2 = A_\infty \, [\, (\alpha \sigma_\eta)^2 + (\beta \sigma_f)^2 \,] \quad , \tag{A.15}$$

in which

$$A_\infty = \sum_{n=0}^{\infty} \left(\frac{\lambda^{n+1} - \mu^{n+1}}{\lambda - \mu} \right)^2$$

$$= \frac{1}{(\lambda - \mu)^2} \sum_{n=0}^{\infty} [\lambda^{2(n+1)} + \mu^{2(n+1)} - 2(\lambda\mu)^{n+1}] \quad .$$

If the system is stable, then $|\lambda| < 1$ and $|\mu| < 1$, and so:

$$A_\infty = \frac{1}{(\lambda - \mu)^2} \left[\frac{\lambda^2}{1 - \lambda^2} + \frac{\mu^2}{1 - \mu^2} - \frac{2\lambda\mu}{1 - \lambda\mu} \right] \quad ,$$

which simplifies to:

$$A_\infty = \frac{(1 + \lambda\mu)}{(1 - \lambda^2)(1 - \mu^2)(1 - \lambda\mu)} \quad . \tag{A.16}$$

Therefore, the steady state response variance is given by:

$$\sigma^2_{\xi\infty} = \frac{(1 + \lambda\mu)}{(1 - \lambda^2)(1 - \mu^2)(1 - \lambda\mu)} * \left[\frac{(\Delta t\, \omega_r)^4}{(1 + \Delta t\, \zeta_r\, \omega_r)^2} \sigma^2_\eta + \frac{(\Delta t)^4}{(1 + \Delta t\, \zeta_r\, \omega_r)^2} \sigma^2_f \right] \quad , \tag{A.17}$$

provided that $|\lambda| < 1$ and $|\mu| < 1$.

The eigenvalues of the difference equation A.1 are calculated as follows:

$$\lambda^2 - \phi_1 \lambda + \phi_2 = 0 \quad , \tag{A.18}$$

and the eigenvalues are:

$$\lambda, \mu = \frac{1}{2} \left[\phi_1 \pm \sqrt{\phi_1^2 - 4\phi_2} \right] \tag{A.19}$$

where ϕ_1 and ϕ_2 are given by Eq. 2.17.

Case (i) $\phi_1^2 - 4\phi_2 < 0 \qquad \left(\omega_r < \frac{2}{\Delta t} \sqrt{1 - \zeta_r^2} \right)$

i.e., the eigenvalues are complex conjugates.

$$|\lambda| = |\mu| = \frac{1}{2} [\phi_1^2 + (4\phi_2 - \phi_1^2)]^{1/2}$$

$$= [\phi_2]^{1/2}$$

$$= \left[\frac{1 - \Delta t\, \zeta_r\, \omega_r}{1 + \Delta t\, \zeta_r\, \omega_r} \right]^{1/2} < 1 \tag{A.20}$$

Case (ii) $\phi_1^2 - 4\phi_2 = 0 \qquad \left(\omega_r = \frac{2}{\Delta t}\sqrt{1-\zeta_r^2}\right)$

i.e., the eigenvalues are real and coincident.

$$\lambda = \mu = \frac{1}{2}\phi_1$$

$$= \frac{1 - \frac{1}{2}(\Delta t\,\omega_r)^2}{1 + \Delta t\,\zeta_r\,\omega_r} \quad , \tag{A.21}$$

so $|\lambda|$, $|\mu| < 1$ if $\Delta t\,\omega_r < 2$.

Case (iii) $\phi_1^2 - 4\phi_2 > 0 \qquad \left(\omega_r > \frac{2}{\Delta t}\sqrt{1-\zeta_r^2}\right)$

i.e., the eigenvalues are real and distinct.

$$\lambda,\ \mu = \frac{1}{2}\left[\phi_1 \pm \sqrt{\phi_1^2 - 4\phi_2}\right]$$

$$= \frac{1}{(1 + \Delta t\,\zeta_r\,\omega_r)}\left[1 - \frac{1}{2}(\Delta t\,\omega_r)^2\left\{1 \mp \sqrt{1 - \frac{4(1-\zeta_r^2)}{(\Delta t\,\omega_r)^2}}\right\}\right] \quad , \tag{A.22}$$

so $|\lambda|$, $|\mu| < 1$ if $\Delta t\,\omega_r < \sqrt{2}$.

- **Example Problem**

For Case (i) described previously,

$$\lambda = \frac{1}{2}\left[\phi_1 + i\sqrt{4\phi_2 - \phi_1^2}\right]$$

$$\mu = \frac{1}{2}\left[\phi_1 - i\sqrt{4\phi_2 - \phi_1^2}\right] \quad . \tag{A.23}$$

Using Eqs. 2.17, A.23 and A.16:

$$A_\infty = \frac{(1 + \Delta t\,\zeta_r\,\omega_r)^2}{(\Delta t\,\omega_r)^3\,\zeta_r\left[4 - (\Delta t\,\omega_r)^2\right]} \quad . \tag{A.24}$$

Then from Eq. A.17:

$$\sigma^2_{\xi_\infty} = \frac{(1 + \Delta t\,\zeta_r\,\omega_r)^2}{(\Delta t\,\omega_r)^3\,\zeta_r\left[4 - (\Delta t\,\omega_r)^2\right]}\left[\frac{(\Delta t\,\omega_r)^4}{(1 + \Delta t\,\zeta_r\,\omega_r)^2}\,\sigma_\eta^2 + \frac{(\Delta t)^4}{(1 + \Delta t\,\zeta_r\,\omega_r)^2}\,\sigma_f^2\right] \quad .$$

Therefore,

$$\sigma^2_{\xi^{(r)}_\infty} = \frac{\Delta t}{\zeta_r\left[4 - (\Delta t\,\omega_r)^2\right]}\left[\omega_r\,\sigma^2_{\eta(r)} + \frac{1}{\omega_r^3}\,\sigma^2_{f(r)}\right] \quad . \tag{A.25}$$

REFERENCE

[1] Erdélyi, A., *Operational Calculus and Generalized Functions*, Holt, Rinehart and Winston, Inc., 1962.